



HAL
open science

Prévision et contrôle du bruit de roulement dans les bâtiments

Matthew Edwards

► **To cite this version:**

Matthew Edwards. Prévision et contrôle du bruit de roulement dans les bâtiments. Acoustics [physics.class-ph]. Université de Lyon, 2020. English. NNT : 2020LYSEI097 . tel-03178824

HAL Id: tel-03178824

<https://theses.hal.science/tel-03178824>

Submitted on 24 Mar 2021

HAL is a multi-disciplinary open access archive for the deposit and dissemination of scientific research documents, whether they are published or not. The documents may come from teaching and research institutions in France or abroad, or from public or private research centers.

L'archive ouverte pluridisciplinaire **HAL**, est destinée au dépôt et à la diffusion de documents scientifiques de niveau recherche, publiés ou non, émanant des établissements d'enseignement et de recherche français ou étrangers, des laboratoires publics ou privés.



INSA

N° d'ordre NNT : 2020LYSEI097

THÈSE de DOCTORAT **DE L'UNIVERSITE DE LYON**
opérée au sein de
I'INSA Lyon

École Doctorale ED 162
MEGA (Mécanique, Energétique, Génie Civil, Acoustique)

Spécialité/ discipline de doctorat : Acoustique

Soutenue publiquement le 3/11/2020, par :
Matthew Ryan EDWARDS

Prediction and Control of Rolling Noise in Buildings

Devant le jury composé de :

LE BOT, Alain, Directeur de Recherche, École Centrale de Lyon

Président

KROPP, Wolfgang, Professeur des Universités, l'Université de Technologie de Chalmers

Rapporteur

DUHAMEL, Denis, Professeur des Universités, École des Ponts ParisTech

Rapporteur

GUIGOU-CARTER, Catherine, Docteur, CSTB

Examinatrice

TOTARO, Nicolas, Professeur des Universités, INSA-Lyon

Directeur de thèse

CHEVILLOTTE, Fabien, Ingénieur de Recherche, Matelys Research Lab

Invité

Département FEDORA – INSA Lyon - Ecoles Doctorales – Quinquennal 2016-2020

SIGLE	ECOLE DOCTORALE	NOM ET COORDONNEES DU RESPONSABLE
CHIMIE	CHIMIE DE LYON http://www.edchimie-lyon.fr Sec : Renée EL MELHEM Bat Blaise Pascal 3 ^e étage secretariat@edchimie-lyon.fr Insa : R. GOURDON	M. Stéphane DANIELE Institut de Recherches sur la Catalyse et l'Environnement de Lyon IRCELYON-UMR 5256 Équipe CDFA 2 avenue Albert Einstein 69626 Villeurbanne cedex directeur@edchimie-lyon.fr
E.E.A.	ELECTRONIQUE, ELECTROTECHNIQUE, AUTOMATIQUE http://edeea.ec-lyon.fr Sec : M.C. HAVGOUDOUKIAN Ecole-Doctorale.eea@ec-lyon.fr	M. Gérard SCORLETTI Ecole Centrale de Lyon 36 avenue Guy de Collongue 69134 ECULLY Tél : 04.72.18 60.97 Fax : 04 78 43 37 17 Gerard.scorletti@ec-lyon.fr
E2M2	EVOLUTION, ECOSYSTEME, MICROBIOLOGIE, MODELISATION http://e2m2.universite-lyon.fr Sec : Safia AIT CHALAL Bat Darwin - UCB Lyon 1 04.72.43.28.91 Insa : H. CHARLES Safia.ait-chalal@univ-lyon1.fr	Mme Gudrun BORNETTE CNRS UMR 5023 LEHNA Université Claude Bernard Lyon 1 Bât Forel 43 bd du 11 novembre 1918 69622 VILLEURBANNE Cédex Tél : 06.07.53.89.13 e2m2@univ-lyon1.fr
EDISS	INTERDISCIPLINAIRE SCIENCES-SANTE http://www.ediss-lyon.fr Sec : Safia AIT CHALAL Hôpital Louis Pradel - Bron 04 72 68 49 09 Insa : M. LAGARDE Safia.ait-chalal@univ-lyon1.fr	Mme Emmanuelle CANET-SOULAS INSERM U1060, CarMeN lab, Univ. Lyon 1 Bâtiment IMBL 11 avenue Jean Capelle INSA de Lyon 696621 Villeurbanne Tél : 04.72.68.49.09 Fax :04 72 68 49 16 Emmanuelle.canet@univ-lyon1.fr
INFOMATHS	INFORMATIQUE ET MATHEMATIQUES http://infomaths.univ-lyon1.fr Sec : Renée EL MELHEM Bat Blaise Pascal 3 ^e étage infomaths@univ-lyon1.fr	Mme Sylvie CALABRETTO LIRIS – INSA de Lyon Bat Blaise Pascal 7 avenue Jean Capelle 69622 VILLEURBANNE Cedex Tél : 04.72. 43. 80. 46 Fax 04 72 43 16 87 Sylvie.calabretto@insa-lyon.fr
Matériaux	MATERIAUX DE LYON http://ed34.universite-lyon.fr Sec : M. LABOUNE PM : 71.70 –Fax : 87.12 Bat. Saint Exupéry Ed.materiaux@insa-lyon.fr	M. Jean-Yves BUFFIERE INSA de Lyon MATEIS Bâtiment Saint Exupéry 7 avenue Jean Capelle 69621 VILLEURBANNE Cedex Tél : 04.72.43 71.70 Fax 04 72 43 85 28 Ed.materiaux@insa-lyon.fr
MEGA	MECANIQUE, ENERGETIQUE, GENIE CIVIL, ACOUSTIQUE http://mega.universite-lyon.fr Sec : M. LABOUNE PM : 71.70 –Fax : 87.12 Bat. Saint Exupéry mega@insa-lyon.fr	M. Philippe BOISSE INSA de Lyon Laboratoire LAMCOS Bâtiment Jacquard 25 bis avenue Jean Capelle 69621 VILLEURBANNE Cedex Tél : 04.72 .43.71.70 Fax : 04 72 43 72 37 Philippe.boisse@insa-lyon.fr
ScSo	ScSo* http://recherche.univ-lyon2.fr/scso/ Sec : Viviane POLSINELLI Brigitte DUBOIS Insa : J.Y. TOUSSAINT viviane.polsinelli@univ-lyon2.fr	Mme Isabelle VON BUELTZINGLOEWEN Université Lyon 2 86 rue Pasteur 69365 LYON Cedex 07 Tél : 04.78.77.23.86 Fax : 04.37.28.04.48

*ScSo : Histoire, Géographie, Aménagement, Urbanisme, Archéologie, Science politique, Sociologie, Anthropologie

Acknowledgments

This work was done as part of Acoutect: an innovative training network composed of five academic and seven non-academic participants. This consortium comprises various disciplines and sectors within building acoustics and beyond, promoting intersectoral, interdisciplinary and innovative training and mobility of the researchers within the project. This project has received funding from the European Union's Horizon 2020 research and innovation program under grant agreement No 721536.

This work was also performed within the framework of the Labex CeLyA of L'Université de Lyon, operated by the French National Research Agency (ANR-10-LABX-0060/ANR-11-IDEX-0007).

To my colleagues at Matelys Research Lab, who helped me along the way to not only complete my research, but also to settle into Lyon and make the city feel like home. In particular to François-Xavier Bécot, Fabien Chevillotte, and Luc Jaouen. The level of professionalism and down-to-earth sensibility that I experienced working with them is not easy to find, and I am grateful for it.

To my colleagues in the Acoutect innovative training network. The friendships formed throughout the course of our journey together will undoubtedly stay with me for many years to come. Getting to experience this adventure with you all was a blessing and an honor.

To Nicolas Totaro and the rest of the team at LVA, who provided me invaluable guidance, as well as many resources which I needed to complete key aspects of my research.

To my parents Steve and Linda Edwards, for being forever supportive of my decision to move so far away in pursuit of this dream. Though an ocean may separate us, the love I feel from them has not diminished one bit.

To Samuel Stafl, who provided me with the greatest gift any friend has ever given me. His selfless act at the start of this adventure helped me in more ways than could have ever been foreseen.

*Life is not tried, it is merely survived,
if you're standing outside the fire.*

GARTH BROOKS

Résumé

Cette thèse concerne le développement d'un modèle numérique pour prédire le niveau de pression acoustique normalisé généré par un chariot roulant dans un environnement intérieur de bâtiment. Un exemple d'un tel scénario est un chariot de livraison qui roule sur le sol lorsque les marchandises sont déplacées dans un espace commercial. Le son généré se propage facilement aux étages adjacents de la structure à plusieurs niveaux. Les objectifs principaux de cette thèse sont de développer un modèle de bruit de roulement qui peut estimer l'avantage relatif fourni par un revêtement de sol pour réduire le niveau sonore rayonné d'un chariot de livraison ou d'un autre dispositif de roulement intérieur, ainsi que de représenter avec précision les phénomènes physiques présents dans le contact de roulement intérieur. Le modèle est spécifiquement adapté aux caractéristiques des chariots dans les bâtiments à plusieurs étages.

Le premier chapitre présente une synthèse bibliographique qui fait le point sur la modélisation du bruit de roulement dans les domaines précédemment explorés du contact roue/rail et pneu/route des véhicules. Des comparaisons sont établies concernant les techniques de modélisation de ces domaines adjacents qui peuvent être adaptées pour le bruit de roulement à l'intérieur. Un bref résumé de l'état de l'art de l'excitation mécanique dans les bâtiments est également donné.

Le deuxième chapitre présente le modèle du bruit de roulement, y compris un contexte théorique de la mécanique de contact sur laquelle le modèle est basé. Le modèle utilise les propriétés géométriques et matérielles de la roue et du sol, ainsi que les profils de rugosité à petite échelle des deux surfaces en contact afin de prédire la force de contact et le niveau sonore rayonné qui en résulte. Le modèle fonctionne dans le domaine temporel afin d'estimer la force de contact à chaque instant avant de passer au domaine fréquentiel, où les spectres de force de contact résultants sont convertis en un niveau de pression acoustique normalisé par l'utilisation de la méthode de la matrice de transfert.

Une attention particulière est accordée à la modélisation des irrégularités discrètes, telles que les méplats de roues et les joints de sol. Ces irrégularités génèrent des forces d'impact chaque fois qu'elles se déplacent dans la zone de contact, dont l'ampleur dépasse de loin la force de contact nominale en raison de la rugosité à petite échelle. Leur présence entraîne donc des niveaux de pression acoustique très élevés qui ont un intérêt particulier à être modélisés avec précision. En calculant le profil de la roue et du plancher à chaque instant et en les superposant au profil de rugosité à petite échelle, le comportement du système roue/sol prenant en compte une de ces irrégularités discrètes peut être simulé.

Dans le troisième chapitre, une technique originale pour estimer la rigidité d'une roue cylindrique pleine est présentée. Une étude paramétrique a été menée afin d'identifier la dépendance de la rigidité de la roue à chacune des variables pertinentes : le rayon et la largeur de la roue, la taille du rayon de l'axe de la roue, la charge appliquée et les propriétés du matériau. La méthodologie est utilisée pour estimer la rigidité de nouveaux types de roues (c'est-à-dire différentes géométries et matériaux) sans avoir besoin de résoudre un modèle d'éléments finis à chaque fois. Une telle méthodologie a des applications au-delà du domaine de l'acoustique, car la caractérisation de formes avec des sections transversales non constantes peut être utile dans le domaine plus large de la science des matériaux. Elle est utilisée ici dans le modèle de roulement pour représenter la rigidité effective de la roue du chariot.

Dans le quatrième chapitre, une série de résultats d'essais expérimentaux relatifs au bruit de roulement à l'intérieur sont présentés. Les profils de rugosité à petite échelle de plusieurs matériaux usuels de roues et de planchers ont été mesurés. Comme la rugosité à petite échelle de la roue et du sol est un paramètre d'influence important dans le bruit de roulement intérieur, ces profils servent non seulement à analyser les spectres d'excitation typiques du roulement, mais aussi à alimenter le modèle. En outre, une série de tests de bruit de roulement a été réalisée à deux endroits : un partenaire industriel en France et un second aux Pays-Bas. Les deux sites contenaient des salles d'essai de laboratoire à deux niveaux où le chariot pouvait être roulé dans la salle supérieure et le son mesuré dans la salle inférieure. Les résultats ainsi qu'une analyse de la manière dont chacun des autres paramètres d'influence (vitesse du chariot, charge supplémentaire, etc.) affecte le niveau sonore rayonné sont présentés.

Dans le cinquième chapitre, le modèle de bruit de roulement est validé par une comparaison approfondie des résultats du modèle et des résultats expérimentaux. Les phénomènes identifiés au cours des essais expérimentaux sont vérifiés dans le modèle de roulement et une analyse des capacités et des applications du modèle est présentée.

Mots clés: roulement, bruit, modèle, acoustique, son, hertzien, contact, multicouche, bâtiment à plusieurs étages.

Abstract

This thesis concerns the development of a numerical model for predicting the normalized sound pressure level generated by a rolling trolley in an indoor building environment. An example of such a scenario is a delivery trolley, which rolls across the floor as merchandise is moved throughout a commercial space. The sound generated propagates easily to the adjacent floors of the multi-level structure. The primary objectives of this thesis are to develop a rolling noise model that can estimate the relative benefit provided by a floor covering at reducing the radiated sound level of a delivery trolley or other indoor rolling device, as well as accurately represent the physical phenomena present in indoor rolling contact. The model is specifically adapted for the characteristics of rolling trolleys in multi-story buildings.

In the first chapter a thorough literature review is presented, giving a state of the art of rolling noise modeling in the previously explored domains of train wheel/rail and vehicle tire/road contact. Comparisons are drawn regarding the modeling techniques of these adjacent domains which may be adapted for indoor rolling noise. A brief review of the state of the art of mechanical excitation in buildings is also given.

In the second chapter the rolling noise model is presented, including a theoretical background of the contact mechanics upon which the model is based. The model uses the geometrical and material properties of the wheel and floor, as well as the small-scale roughness profiles of the two surfaces in contact, in order to predict the contact force and resulting radiated sound level. The model operates in the time domain in order to estimate the contact force at each discretized moment in the rolling event before transitioning to the frequency domain, where the resulting contact force spectra is converted to a normalized sound pressure level through use of the transfer matrix method.

A particular focus is given to the modeling of discrete irregularities, such as wheel flats and floor joints. These features generate impact forces each time they move through the area of contact whose magnitudes far exceed the nominal contact force due to small scale roughness. As such, their presence results in highly elevated sound pressure levels which have a particular interest in being accurately modeled. By calculating the wheel and floor profile at each discretized moment in time and superimposing them onto the small scale roughness profile, the behavior of the wheel/floor system as one of these discrete irregularities is encountered may be estimated.

In the third chapter, an original technique for estimating the stiffness of a solid cylindrical wheel is presented. A parametric study was conducted in order to identify the dependence of

the wheel stiffness on each of the relevant variables: including the wheel's radius, axle size, width, applied load, and material properties. The methodology is used to estimate the stiffness of new wheel types (i.e. different geometries and materials) without needing to solve a finite element model each time. Such a methodology has application beyond the field of acoustics, as the characterization of shapes with non-constant cross sections may be useful in the wider field of materials science. It is used here in the rolling model to represent the effective stiffness of the trolley wheel.

In the fourth chapter, a series of experimental test results related to indoor rolling noise are presented. The small scale roughness profiles of several common wheel and floor materials were measured. As the small scale roughness of the wheel and the floor is an important influencing parameter in indoor rolling noise, these profiles serve not only as a means of analyzing typical rolling excitation spectra, but also as inputs to the model. Additionally, a series of rolling noise tests were conducted at two locations: an industrial partner in France and a second in the Netherlands. Both locations contained two-level laboratory test rooms where the trolley could be rolled in the upper room and the sound measured in the lower room. Their results are presented, including an analysis of how each of the other influencing parameters (trolley speed, added load, etc.) affect the radiated sound level.

In the fifth chapter, the rolling noise model is validated via a thorough comparison of model and experimental results. The phenomena identified during the experimental tests are verified in the rolling model, and an analysis of model capabilities and applications is presented.

Keywords: rolling, noise, model, building, acoustics, sound, Hertzian, contact, multi layer, multi story

Introduction	25
1 Literature Review	31
1.1 Contact modeling	31
1.1.1 Train wheel/rail contact modeling	32
1.1.2 Automotive tire/road contact modeling	37
1.1.3 Contact model summary	39
1.2 Discrete irregularities	40
1.3 The contact filter	40
1.4 Roughness	41
1.5 Wheel radiation	43
1.5.1 Train wheel radiation	43
1.5.2 Automotive tire radiation	44
1.5.3 Indoor wheel radiation	44
1.6 Ground radiation	45
1.6.1 Train rail radiation	45
1.6.2 Automotive road radiation	46
1.6.3 Sound radiation in buildings	47
1.7 Conclusion	48
2 Rolling Noise Model	51
2.1 Contact model	52
2.1.1 Hertzian contact	52
2.1.2 Equivalent spring foundation	58

2.2	Implementation into the rolling noise model	64
2.3	Discrete irregularities	66
2.3.1	Wheel flats	68
2.3.2	Floor joints	72
2.4	Contact dimensionality	73
2.4.1	Two-dimensional model	74
2.4.2	One-dimensional model	75
2.5	Dynamic model	76
2.6	Propagation model	79
2.6.1	Transfer matrix method	79
2.6.2	Application in the rolling noise model	80
2.7	Preliminary model	82
2.7.1	Key differences between the preliminary and improved models	85
2.8	Conclusion	86
3	Wheel Stiffness	89
3.1	Background	89
3.2	FE model development	91
3.2.1	Mesh definition	92
3.2.2	Re-meshing	95
3.3	Parametric study	96
3.3.1	Investigated variables	96
3.4	Parametric study results	98
3.5	Generation of the abacus	101
3.5.1	Normalized wheel stiffness	101
3.5.2	Lookup table	102
3.5.3	Series of one-dimensional polynomials	103
3.5.4	Two-dimensional polynomial	103
3.6	Comparison of the three methods	105
3.7	Comparison with analytical methods	107
3.7.1	Equivalent beam	108
3.7.2	Equivalent trapezoidal prism	109
3.8	Discussion	110
3.8.1	Implementation into a rolling noise model	110
3.8.2	Scope of the method's applicability	111

3.9	Conclusion	112
4	Experimental Testing	115
4.1	Roughness measurement	115
4.1.1	Measurement of the small-scale roughness profile	116
4.1.2	Roughness parameters	121
4.1.3	Directionality	124
4.2	The test trolley	130
4.3	Rolling noise location one: Industrial partner in France	131
4.3.1	Rolling noise: Test trolley	133
4.3.2	Comparison with a second trolley	139
4.3.3	Global indicators	141
4.3.4	Test conclusion	144
4.4	Rolling noise location two: Industrial partner in the Netherlands	144
4.4.1	Floor transmission loss	145
4.4.2	Rolling noise: Test trolley	148
4.4.3	Rolling noise: Three-wheeled trolley	154
4.4.4	Influence of floor mobility	158
4.4.5	Global indicators	159
4.4.6	Test conclusion	163
4.5	Test location comparison	164
4.6	Conclusion	166
5	Model Validation	169
5.1	Default parameters	169
5.2	Floor admittance	170
5.3	Wheel stiffness: comparison of the proposed methods	171
5.4	Roughness profiles	174
5.5	Radiated sound level: Model versus experimental results	174
5.5.1	Level Acoustics & Vibration	175
5.5.2	Industrial partner in France	179
5.6	Global indicators: Model versus experimental results	182
5.6.1	Level Acoustics & Vibration	182
5.6.2	Industrial partner in France	185
5.7	Investigation of the contact force	187

5.7.1	Contact force spectrum	190
5.7.2	Wheel impedance	190
5.8	Contact dimensionality	191
5.9	Comparison with the preliminary model	192
5.10	Conclusion	197
General Conclusions and Perspectives		201
Bibliography		205
A Appendix A		219
A.1	Recommendation for a standard rolling noise machine	219
A.1.1	Introduction	219
A.1.2	The standard tapping machine: A history	221
A.1.3	Proposed development process	233
A.1.4	Conclusion	234
A.1.5	Acknowledgments	234
B Wheel Diagrams		237
C Wheel Stiffness Abacus		241
C.1	Parametric study	241
C.2	Lookup table	242
C.3	One-dimensional polynomials	244
C.4	Two-dimensional polynomial	246

List of Abbreviations

BE: Boundary element
BPM: Beats per minute
CAD: Computer-aided design
CPSD: Cross power spectral density
DPRS: Distributed point reacting spring
FDTD: Finite difference time domain
FE: Finite element
HyRoNE: Hybrid rolling noise estimation
IL: Insertion loss
ISO: International Organization for Standardization
INRETS: L'Institut national de recherche sur les transports et leur sécurité
LVA: Laboratoire Vibrations Acoustique de l'INSA Lyon
LVDT: Linear variable displacement transducer
MDF: Medium-density fiberwood
PSD: Power spectral density
RMS: Root mean square
SEA: Statistical energy analysis
SNR: Signal to noise ratio
SPERoN: Statistical physical explanation of rolling noise
TL: Transmission loss
TWINS: Track-wheel interaction noise software

MULTI-USE, multi-story buildings are a ubiquitous feature of urban areas. Buildings with commercial shops on the ground floors and private residencies on the upper floors allow easy access for people to do their shopping while still allowing them to live in a high density urban area. However, these areas have a high number of noise sources, making acoustic-oriented designs and solutions of ever increasing importance. There are multiple types of noise which can be a nuisance in multi-story urban buildings: traffic noise, floor impact noise, rain noise, general noise from neighbors, etc. Most of these have long been topics of investigation in the world of acoustics. When looking specifically at vertical transfer paths (i.e. from floor to ceiling or vice versa), impact noise is generally regarded as the main concern. A common example of this is footfall noise, caused by people walking across the floor. However, there is another source of noise that has yet to be investigated in the context of building acoustics: rolling noise.

General context

The commercial stores that exist on the ground floors of many of these multi-story buildings receive deliveries on a regular basis (in some cases daily) to restock their inventory. These deliveries are typically done using rolling trolleys, and often happen when the residencies are occupied (e.g. early in the morning). An example of one is shown in Figure 1. These trolleys generate low frequency noise as they roll across the floor, which propagates easily throughout the building structure and up into the private residencies on the upper stories. The low frequency nature and time of day at which it typically occurs means this noise can be a nuisance to the inhabitants of these apartments.



Figure 1: A typical delivery trolley

As shown in Figure 2, delivery trolleys are not the only sources of rolling noise in multi-story building environments. In office spaces (and residential buildings too), rolling chairs generate noise as they move across the floor. Even rolling children's toys have the potential to cause a nuisance to inhabitants of adjacent apartments. In these scenarios, the transfer path is usually downward: from the apartment above to the apartment below.



Figure 2: Examples of potential indoor rolling noise sources. From left to right: office chair, delivery cart, push dolly, children's toy, suitcase.

The tapping machine is the most widely used device for assessing the performance of the flooring construction used in multi-story buildings. This use is justified, to be sure, as impact noise is often given as one of the greatest sources of annoyance to multi-story building inhabitants [1]. As shown in Figure 3, it consists of five hammers controlled by an AC motor on a cam system. The hammers rise and fall in succession to generate impact events with the floor upon which the machine rests.

While being effective at replicating impact noise, tapping machines do not accurately assess a floor's ability at attenuating rolling noise. As shown in Figure 4, the sound signature of impact noise is quite different than that of rolling noise in both the temporal and spectral domains. One would not likely confuse the sound of a neighbor walking around on the floor above in an apartment complex with that of said neighbor rolling their office chair across the same floor. Considering the prevalence of tapping machines (and their regulation [2, 3, 4]), this mismatch means that focus is rarely given to the effects of rolling noise when designing acoustic treatment



Figure 3: A typical tapping machine. The five hammers repeatedly drop in succession to generate impacts with the floor at a rate of 10 Hz.

systems for floors, resulting in a gap in performance. The physics of sound transmission are blisteringly complex; there is no guarantee that solutions which have been developed to reduce tapping noise will necessarily be effective at reducing rolling noise. Unfortunately, this often means that each type of noise has to be tackled individually.

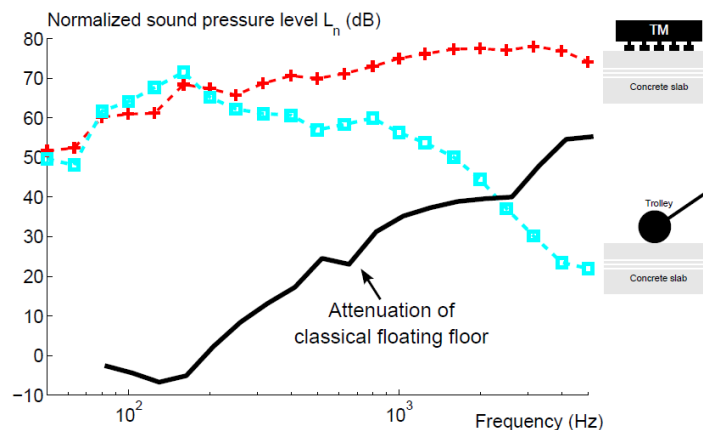


Figure 4: Comparison of the spectra of tapping noise and rolling noise of a classical concrete floor, as well as the attenuation of a classical floating floor (140 mm concrete slab + a decoupling layer + 40 mm screed). [5]

Looking at impact noise, the generation mechanism is relatively clear: an object with some velocity strikes another object, and this impact results in their vibration, which can either radiate sound to the air, propagate vibration to other structures, or both. Rolling noise, on the other hand, may not seem so clear. There is no impact that can be seen occurring to the naked eye: so what is causing the sound to be generated? In reality the two objects, in this case a wheel (or wheels) and the floor, are still vibrating. This vibration is still what is causing the sound radiation. The difference lies in what is causing these objects to vibrate in the first place. Rolling noise is generated by the small scale relative roughness between the wheel and the

surface that wheel is rolling on. As represented in Figure 5, even surfaces which appear visually smooth can be quite rough on the micro level. As the wheel rolls across the floor, this relative roughness excites the two bodies. This causes them to vibrate and radiate sound. There exists a need to develop solutions for rolling noise in buildings. An effective first step in discovering these solutions is to simulate the noise numerically.

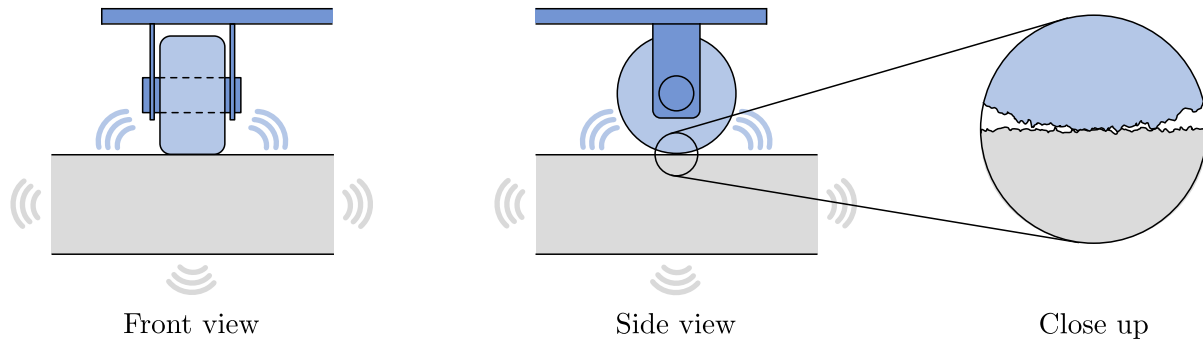


Figure 5: Schematic of a trolley rolling across the floor. The excitation is caused by the relative small-scale roughness between the two bodies.

Rolling noise has been thoroughly investigated for decades. However, until Chevillotte et al. in 2015 [6, 7], this was done uniquely in the context of vehicle tire/road and train wheel/rail contact. Models which aim at predicting these types of noise exist (e.g. [8, 9, 10] for tire and [11, 12, 13, 14] for train), but they cannot be easily adapted to work for indoor rolling noise due to differences in the underlying phenomena which cause such noise (mainly the propagation of the sound to the surrounding environment, which is quite different between roads, train tracks, and indoor buildings). There exists a need for rolling noise models which can handle the unique case of an indoor rolling scenario.

Scientific objectives and approach of the thesis

In the field of building acoustics, solutions are often quantified in terms of the benefit they provide over a reference configuration. Doing so allows one to visualize the relative benefit that a floor covering provides in reducing a given type of excitation. The primary objectives of this thesis are to develop a rolling noise model that can estimate the relative benefit provided by a floor covering at reducing the radiated sound level of a delivery trolley or other indoor rolling device, as well as accurately represent the physical phenomena present in indoor rolling contact. The model should be specifically adapted for the characteristics of rolling trolleys in multi-story buildings, which train and automotive models cannot replicate. This is a domain which has hereto been left unexplored. As such, this thesis serves as a ground-breaking look into the problem of indoor rolling noise. The goal is that this thesis shall serve as a platform

which spurs further exploration into the field of indoor rolling noise by other researchers.

This thesis begins with a thorough overview of the existing literature on train and automotive rolling noise. In first investigating the techniques which have already been developed for a similar domain, one may identify those which have the potential to be adapted for the indoor scenario. Furthermore, this overview shall also serve to highlight the differences between indoor and outdoor rolling noise. This will aid in identifying the areas in which new developments will need to be made in order to account for the unique challenges of rolling noise in multi-story buildings.

The numerical rolling noise model developed in this thesis is presented in Chapter 2. This includes a unique estimation of the elastic stiffness of the trolley wheel, which is subsequently presented in Chapter 3. These two chapters make up the bulk of the theoretical and analytical components of the development.

A numerical model is only as good as the data which is fed into it, and rolling noise is no exception. An explanation of the experimental testing, including the measurement of real small-scale roughness profiles and the radiated sound level of rolling test trolleys in a laboratory environment is presented in Chapter 4. These provide the link between computer simulation and the real world. They are used both as input into the model and as a means of a validation of model results, which is done in Chapter 5. Finally, the appendix includes additional numerical information relevant to the model development, as well as a proposition for a standard rolling device, which may become the rolling noise equivalent of the standard tapping machine.

COMPUTER simulations can be developed for solving all sorts of problems, as they allow engineers to try multiple iterations of the same scenario quickly, without having to build or test anything in physical space. A computer model which could accurately predict the noise generated by a wheeled cart rolling in a building would be extremely useful to assist in the development of new indoor noise control solutions. An ideal model would be able to use different wheel and floor materials as inputs in order to identify how each one affects the radiated noise. This chapter presents the feasibility of developing such a model by giving an overview of models which have been developed for predicting rolling noise in other domains.

The subject of rolling noise generation has been a topic of investigation for many decades. Dozens of models have been developed, each with their own unique focus, in an attempt to simulate the forces that are at play in the area of contact between the two bodies. The following chapter is not an attempt to summarize them all, as doing so would require a lifetime of work and understanding. Instead, a number of works which are the most relevant to the topic of rolling noise in buildings will be discussed, with focus given to the similarities and differences between the techniques and underlying assumptions used in these models, versus those which exist for indoor rolling noise.

1.1 Contact modeling

Perhaps the first researcher to investigate the phenomenon of contact modeling was Henrich Hertz, who published his first works on contact mechanics in 1885 [15]. In this series of papers, Hertz describes the pressure distributions of various shapes in contact with one another. This work formed the basis of what is now known as *Hertzian contact theory*. Models which follow this theory assume the contacting bodies to be elastic half spaces with frictionless surfaces, that the contact strains are small and within the elastic limits of the respective materials, and that

the characteristic dimensions of the bodies are large compared to the area of contact between them. An elastic half space is a surface which is treated as being infinite in all directions except for the one which is outward normal to the surface itself.

Following the work of Hertz came additional pioneering works from researchers such as Love [16], Timoshenko [17], Boussinesq [18], and Johnson [19], who all explored and found analytical solutions to a wide range of contact problems. These sources tackle contact mechanics from a very high level perspective, and do not dive into the specifics of noise radiation in real world examples. Still, because the underlying mathematics are largely the same, their work continues to serve as the bedrock for even the most modern contact models of today.

A highly comprehensive exploration of rolling contact of three dimensional bodies was published by Kalker [20]. This is considered by many to be one of the most advanced and generalized formulation on rolling contact. However much of the specificity of this work goes beyond the scope of this thesis (e.g. exploring phenomena such as friction, adhesion, and creepage). Thus it will not be discussed here in great detail.

Models for this kind of contact fall into one of three categories: frequency domain, time domain, or hybrid. Frequency and time domain models operate as their names imply, while hybrid models use a combination of performing calculations in both domains at different stages of the modeling process. Which approach is used depends on the techniques used to develop the model, as well as the priorities of what the model is trying to achieve. Frequency domain models are typically more simplified, but offer a lower degree of precision in their results. Time domain models have the benefit of being able to offer a higher degree of precision and/or incorporate nonlinear effects without sacrificing too much computational efficiency. Hybrid models attempt to offer a balance of robustness and efficiency by using both techniques selectively.

There exists two main areas where rolling contact noise modeling has been researched the most: automotive tire/road and train wheel/rail contact. Both are scenarios where the overall noise environment is largely contributed to by wheels rolling on a surface, and both occur in environments where excessive noise can be an issue (particularly when the roads and/or rails pass through heavily populated urban environments). The sections that follow will examine some of the models that exist in each of these fields.

1.1.1 Train wheel/rail contact modeling

Rolling noise in the context of train wheel/rail contact has been a major topic of interest for many decades. The small scale surface roughness between the wheel and rail is the primary cause of this noise [21]. One of the first attempts at quantifying this phenomenon was done in

1976 by Remington, Rudd, Vér, et al. [22, 23, 24, 25]. This series of works investigated the phenomenon of train wheel/rail contact in four parts: characterizing the wheel/rail system, noise due to wheel squeal, noise due to discontinuities, and noise due to roughness. Here, the wheel was modeled as a simple rigid mass, equal to that of the wheel plus one-third the mass of the axle (i.e. the axle is considered as a massive spring), having impedance $Z_{\text{wheel}} = i\omega m$. The rail was modeled as an infinitely long beam in bending, having impedance of a beam on an elastic foundation. Remington used their impedances to analytically predict the force interaction of the two surfaces. The relative wheel/rail roughness was then coupled with the impedances in order to calculate their forced responses.

In a later model [26], Remington refined the methodology to include the influence of Hertzian contact stiffness, which was not present in the earlier version. This model (and others [27, 28, 29, 30, 31, 32]) exemplifies one kind of methodology for estimating the interaction between the two surfaces: a spring placed between a point-contact. This contact spring (which is often represented as two springs in series positioned on either side of the roughness strip) serves as the representation of how the roughness affects the two surfaces through the form of a changing spring stiffness. The forcing is again taken as the roughness spectra, but instead of influencing the impedances of the wheel and rail directly, it now interacts with the contact spring. An example of such an interaction is shown in Figure 1.1. By including the presence of a contact spring, Hertzian contact theory is used to incorporate the influence of local deformations on the wheel/rail responses. These one-dimensional models can be thought of as a strip of roughness sandwiched between the static wheel and rail, which is then “pulled through” to excite the coupled bodies via the contact spring.

The method proposed by Feldmann [27, 28] uses the same contact spring approach, but removes the assumption that the roughness excitation source is perfectly rigid inside the contact patch. It allows the roughness profile to elastically deform, leading to treating it as a “force source” rather than a “velocity source”. However, difficulties in estimating these forces have caused others to doubt the practicality of such an approach [21]. The method proposed by Thompson [29, 30, 31, 32] builds off of Remington’s work: providing an in depth investigation into the excitation and subsequent vibration of train wheels and rails through the use of their frequency response functions.

These models operate in the frequency domain, allowing for simplified computation, but limited by the assumptions that must be made. As such, the contact springs are considered linear, and any non-linearities known to exist in the real world (e.g. a contact stiffness which changes with the roughness passing through it) are linearly approximated. However, it is worth noting

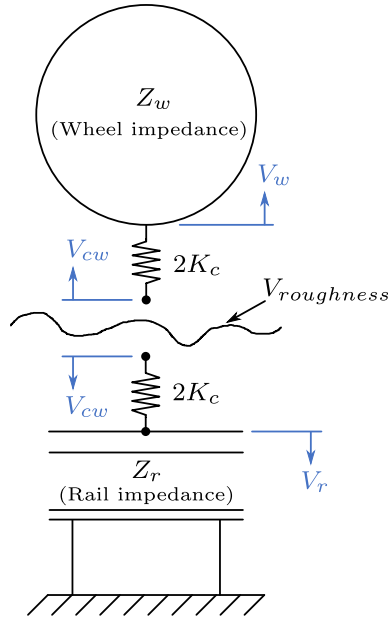


Figure 1.1: Example of the point-contact model used in [25].

that Wu and Thompson [33] found that the non-linear effects of train wheel/rail interaction are negligible for high static pre-loads, low frequencies (below 100 Hz), and high frequencies (above 1 000 Hz). The latter two points prove fruitful for the applicability of a linear indoor rolling noise model, as preliminary measurements have found the acoustic energy of indoor rolling noise to mostly exist in the sub 100 Hz range [5].

When modeling train wheel/rail contact in three dimensions, the contact point is expanded to become a contact area. A typical methodology involves splitting up the contact area into a grid of discrete cells, with each cell having its own contact stress to be found. Good examples of such a model can be found in work by Remington and Webb [11], as well as additional work by Thompson [34]. Here, a bed of independent, non-linear springs forms the interaction between the wheel and rail. This is based on a Winkler bedding [35, 36], a concept first proposed by Winkler in 1871 to replace a continuous support with a bed of springs. An example of such an interaction is shown in Figure 1.2. Known as the *distributed point reacting spring* (DPRS) method, this allows Hertzian deformation of the wheel and rail to be represented in a way which still allows for calculation in the frequency domain. The springs are made non-linear by setting them to deform with the square root of their deflection in order to ensure agreement with Hertzian contact theory. Additionally, to account for the fact that the springs are assumed to be independent from one another, modified *equivalent radii* of the wheel and rail are calculated and used.

The DPRS method is actually a simplified version of a method that was first proposed by Boussinesq in 1885 [18]. Many models consider the Boussinesq method to be “the standard”

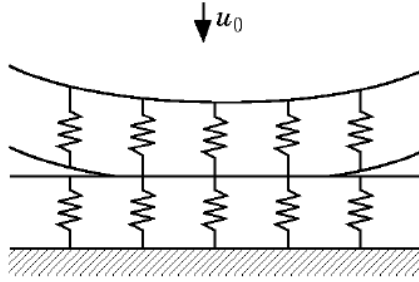


Figure 1.2: Example of a 2D contact model using a bed of independent, non-linear springs. Reproduced from [11].

against which their precision is judged [34, 37]. If a model's results agree well with an equivalent calculation done using the Boussinesq method, that model is generally considered good. The further a model's results deviate from an equivalent Boussinesq calculation, generally the greater number of simplifications are made to decrease the computation time. It recognizes that the contact area and the surface deflection (within and without) the contact area are dependent upon one another. If the two surfaces are treated as elastic half spaces in contact with one another (rather than placing contact springs in between like previously discussed methods), one cannot be computed first in order to then find the other. Thus an iterative approach is taken to calculate the two unknowns simultaneously. Once the iteration converges, and once the displacement at each point in the region is known, the contact forces can be calculated.

The Boussinesq method is more computationally taxing than the DPRS method, but it has the added benefit that it accounts for the fact that the displacement of any given point in the area of contact is dependent on the displacement of all other points in the area of contact as well (an artifact that is ignored in the independent spring models). However, Thompson, Hemsworth, and Vincent [13, 12] found the results when using the DPRS method to be sufficiently similar to the results when using the Boussinesq method, that they decided to incorporate the former into a software package they developed, called the "Track-wheel interaction noise software" (TWINS). The two procedures give results for the stress distribution in the contact area which are nearly identical when the roughness wavelength is long compared to the dimensions of the contact area, but which differ greatly when that wavelength becomes small compared to the dimensions of the contact area. However, when the resulting blocked force is calculated from each of these stress distributions, the results remain similar for both wavelength scenarios. This was achieved by adding what essentially amounts to a high pass filter to the results of the DPRS procedure, which effectively simulates the actual tendency of the wheel to follow the roughness at long wavelengths, but remain fixed with respect to the roughness at shorter wavelengths.

Different models prioritize different assumptions based on the varying applications they were

designed for. An example of this can be seen in the transition from a 3D frequency domain model to a 2D time domain model. While a full three-dimensional model is indeed robust, it is not always necessary or feasible. In any given model that wishes to use real-world roughness data as an input, that data must come from some measured source. In many situations, measured roughness data is only available for a single line along the longitudinal direction of a rail surface (or along the circumferential direction of the wheel surface). For situations such as these, two-dimensional contact models exist. Ford and Thompson [38] developed such a model by adapting the DPRS method to be suitable for 2D applications. As in the 3D DPRS procedure, a bed of springs is placed between the wheel and rail. However, This bed is two-dimensional, consisting of only one line of springs which are allowed to deflect vertically. Ford and Thompson further simplified the model by making the springs linear, but replaced the radius of the wheel R with an equivalent radius R_m in order to correct for these simplifications. This results in a simplified 2D procedure which still agrees with Hertzian contact theory.

Due to the efficient nature of the 2D DPRS procedure, Ford and Thompson were able to incorporate it into a rolling noise prediction model which operates in the time domain rather than the frequency domain. If the scenario is again thought of as two smooth surfaces (the wheel and rail) in contact with one another, where a strip of relative roughness is “pulled” between the two to derive the resulting contact forces, then a time domain model becomes straightforward to visualize. The total time that the roughness strip is spent being pulled through the contact area is split up into a series of discrete steps, allowing the deflections, stiffnesses, and resulting contact forces in the line of contact springs to be calculated incrementally.

This incremental time stepping forms the basis of other time-domain contact models as well. Pieringer, Kropp, and Thompson [39] developed a time domain model that works with either two or three-dimensional contact. The 2D version uses a simplified Winkler bedding, while the 3D version uses the more robust (but more complex) elastic half space approach. Pieringer et al. found that their 3D model gives results for the contact force that are “several dB lower than the 2D model”, which they attribute to meaning the 2D model is over-predicting the result (rather than the 3D model under-predicting). This work highlights the fact that 2D models decrease in accuracy as the transverse variance in roughness increases. It suggests that it may be necessary to investigate whether trolley wheels have a tendency to vary in roughness in their transverse direction.

Mazilu [40] and Nordberg [41] each developed time domain point contact models using Green’s functions to describe the response of the rail. This use of Green’s functions is an interesting development, though it was primarily used as a method of describing the behavior of the rail due

to the presence of periodically spaced supports called *sleepers*. Neilsen on the other hand used finite element (FE) modeling to represent the rail with supports [42]. Considering how different this type of a support system is from the floor of a building, it may not prove applicable in the case of indoor rolling noise.

Lundberg et al. [14, 43, 37] developed an interesting model which combines aspects of several of the methodologies discussed above. The model reduces the full 3D geometry of the contact area to a point contact to increase computational efficiency while still retaining relatively high accuracy through use of pre-calculated filters. These computations are done in the frequency domain to find the non-linear contact stiffness and effect of the non-linear contact filtering. These parameters are then used as inputs in the time domain wheel/rail dynamic model. Green's functions are also incorporated to describe the impulse responses of the wheel and rail. The state dependent filtering may prove useful in indoor rolling noise modeling, due to its ability to operate the time-domain dynamic model as a point contact while still retaining more accuracy than previously developed 1D models. Further discussion of the contact filter effect, which is an artifact of other previously examined models as well, is given in Section 1.3.

1.1.2 Automotive tire/road contact modeling

As the discussion in the previous section shows, much work has been done to model the complex force interactions occurring in the area of train wheel/rail rolling contact. This is primarily driven by the fact that there has long been a clear consensus that this roughness induced excitation serves as the main source of train wheel/rail noise [21]. In the world of automotive tire/road noise, however, this consensus does not exist. According to Wullens [44], there is still no clear agreement as to how much the various sound generation mechanisms contribute to the overall noise level. These include mechanisms such as tire vibration, the stick-slip & stick-snap effect, flow induced noise, air pumping, the horn effect, air resonance radiation, and roughness in the contact patch. As the names imply, the stick-slip and stick-snap effects are caused by the tire treads modulating between adhesion and release from the road, which generates noise. Flow induced noise is caused by air turbulence due to air moving in the small channels of the tire tread outside the contact area. Air pumping is described in [8] as a "fluctuating air flow into and out of volume in the tyre/road surface". It also describes the horn effect as causing a sound amplification on the order of 10-25 dB due to the horn-like geometry formed by the road and tire. Only the last of these, the roughness in the contact patch, is of concern in the application of indoor rolling noise. As such, a fragmentation of efforts has occurred. The focus in automotive rolling noise analysis has been split up across many domains.

Just as it is common to model the train wheel as an elastic half space, many automotive models which use the elastic half space approach have been developed as well (e.g. [45, 46, 44, 47, 48]). This underlines its prominence as an effective contact modeling technique. von Meier, van Blokland and Descornet [49] developed an early empirical model which estimates the penetration between the tire and road surface, though it does not estimate the contact force between the two. A single estimated stiffness value is calculated using this empirical model in order to estimate the relationship between the tire/road texture and the generated noise [50]. Clapp [51] developed a physical model based on a similar envelopment procedure which appears to be somewhat similar in methodology to the Boussinesq method of calculating the indentation of a rigid surface (the road texture) into an elastic body (the tire). However, as it is not iterative, it does not reach the full estimated contact, but only an approximation. Klein and Hamet [50] used these as their main source of reference when developing a model with L’Institut national de recherche sur les transports et leur sécurité (INRETS). As opposed to some other models which require the roughness profiles of both surfaces (the wheel and ground) to estimate the noise generated, the INRETS model uses a sample of the road roughness, but only the elastic properties (Young’s modulus and Poisson’s ratio) of the tire.

The above highlights another difference between automotive and indoor rolling noise. With automotive tire/road contact, the tire is much softer than the road, so the road is typically assumed perfectly rigid in most automotive contact models. With indoor rolling noise however, the material of the floor and of the wheel can be sufficiently similar in rigidity that this condition cannot be confidently assumed. That is, with indoor rolling noise, both bodies are assumed to deform and interpenetrate, as opposed to just one penetrating into the other.

Pacejka and Sharp [52] developed a tire model which is based on the previously discussed Winkler bedding. They extended the bedding (calling the extended version a “wire brush”) to include forces acting in the transverse and tangential directions. These additional forces are important for tire modeling, though they are not expected to be of significant concern for indoor rolling noise. Similar to the TWINS model for train rolling noise, (in that it was developed for practical commercial use), the statistical physical explanation of rolling noise (SPERoN) and hybrid rolling noise estimation (HyRoNE) models were developed by Beckenbauer, Klein, Kropp, and Hamet [53, 54] for automotive rolling noise. These models solve the contact problem in both the time and frequency domains by use of a linearized hybrid model that is part physical (time domain) and part statistical (frequency domain). These 3D models again use the micro-scale roughness of the road, but only macro-scale geometry (i.e. the tread pattern) of the tire. They have the benefit of being able to solve for the pass-by noise of a vehicle in a much shorter amount

of time than some of the more detailed models which operate completely in the time domain. An illustration of the envelopment procedure used in the SPERoN and HyRoNE models is shown in Figure 1.3. However, it is worth noting that some researchers consider the envelopment procedure to be a band-aid of sorts: a method to be avoided in contact modeling if possible.

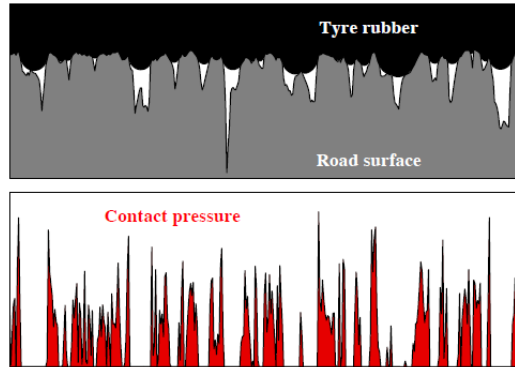


Figure 1.3: Illustration of the envelopment procedure used in the SPERoN and HyRoNE tire/road contact models. Reproduced from [53].

Andersson and Kropp [9] developed a 3D model which, similar to the Winkler bedding, calculates the unique spring stiffness at each tire/road contact point in the discretized interface between the two. It captures the roughness profile of the road down to the millimeter scale, which is quite good compared to the size of a typical tire. Though it would still be too large for indoor rolling noise, who's contact dimensions are often on the order of 1–2 millimeters in total. While the approach of using smaller length scales has been validated, the model as a whole (with respect to experimental data) has not. Kropp has also been involved in other recent work with Wullens [55], Hoever [56], and others [57], though these models more-so focus on the other aspects of rolling tire noise (such as tire vibration) which are not directly applicable to indoor rolling noise.

1.1.3 Contact model summary

Though many years old at this point, the works by Remington [58, 26] and Thompson [29, 30, 31, 32] still form the basis of even the most complex train wheel/rail models today. The body of knowledge in automotive rolling contact is a bit more fragmented in origin, likely due to the fact that there does not exist a long standing consensus on whether or not roughness contact is the primary source of tire/road noise, like there does with train wheel/rail contact. A lot of the development that has occurred in recent years has been in the areas of rolling noise prediction that deviate from application to indoor rolling noise: notably with regards to wheel/tire vibration and radiation, rail/road vibration and radiation, and sound propagation from the sources. Application of these aspects is discussed further in Sections 1.5, 1.6 and 1.6.3,

respectively. While intuition may suggest that 3D contact models will always be the best tools available, there are situations where simplicity and computational efficiency are considered sufficiently valuable that 2D or even 1D models are better suited. Furthermore, developments in roughness and contact stiffness pre-filtering have allowed even modern 1D models to retain good accuracy in their results.

1.2 Discrete irregularities

In the context of wheel roughness (whether train or automotive), a discrete irregularity refers to any imperfection on either surface which is sufficiently large that it may not be considered as simply part of the roughness profile. For train rails, this would be a rail joint or turnout (the latter being a particular issue in ground-borne noise problems due to their unavoidable prevalence). For train wheels, flat spots are typically considered. For automotive scenarios, tire discontinuities are typically not investigated, as the high flexibility of the tire does not lend itself to producing flat spots (this is different than the entire tire going flat due to a puncture, though that is also outside the scope of automotive rolling noise modeling). Road discontinuities, on the other hand, can be incorporated into models similarly to rail imperfections.

Vér, Ventres, and Myles [24] studied the effects of discontinuities on train rolling noise in a multitude of scenarios. Their findings showed that the noise generated due to a discrete irregularity is more akin to impact noise rather than roughness induced rolling noise. They were able to mimic the discrete irregularity noise using a simple wheel drop test. Wu and Thompson [59] investigated the effects of wheel flats on train wheel/rail rolling noise, and found that the noise due to wheel flats is greater than the noise generated by the relative roughness alone for speeds up to 200 km/h. These models generally operate in the time domain. In regards to indoor rolling noise, discontinuities are manifested as floor joints and wheel flats. Both of these may be able to be accounted for via adaptation of existing techniques in train wheel/rail discrete irregularity contact.

1.3 The contact filter

The use of filtering has been mentioned multiple times so far as a method of modifying roughness spectra. This may be used to account for non-linear effects in a linear model, as was done by Lundberg et al. in [14]. It also applies to a phenomenon that is inherent to rolling noise, referred to as *the contact filter* or *the contact filter effect*. Because the area of contact between the two surfaces is finite, roughness asperities with wavelengths that are short

compared to the size of this area are essentially “filtered out” and not seen (or excited) by the system [38]. While some earlier models [22, 23, 24, 25] did not incorporate this filter into the processing of the roughness spectra, it has since become a relatively common feature of train wheel/rail contact modeling. Interestingly, there is very little discussion of the contact filter effect in automotive contact models, though some do briefly mention its existence (e.g. [60, 9]). Models which operate in two or three dimensions (i.e. models which do not use a simple point contact) naturally contain a contact filter and thus do not require additional model features or roughness pre-processing to account for it.

1.4 Roughness

Any model which is attempting to predict the radiated sound power due to the roughness between two surfaces will require some estimation of the roughness itself as an input. There are two ways of estimating this roughness, either analytically or empirically. Early researchers such as Bender and Remington [61] developed formulas to analytically estimate the wheel/rail roughness spectra. These spectra were used as the forcing to find the response of the train wheel and rail. In fact, because any roughness profile (measured or not) needs to be digitized into order to be input into the model anyway, many works (e.g. [33, 40, 40, 38]) incorporate a “first pass” validation by using a simple artificial roughness profile, such as a sine wave.

Multiple methods have been used to measure real roughness data. An accelerometer or displacement transducer can be passed over the surface in question at a constant speed to measure the roughness profile, with the latter being more accurate due to its ability to move more slowly (thus avoiding a possible loss of contact during measurement) [34]. For 3D data, multiple parallel lines of roughness data are typically captured. In the TWINS program [12], Thompson used a linear variable displacement transducer (LVDT) to measure train wheel roughness on 20 parallel lines, separated by 2.5 mm, along the entire circumference of the wheel. Rail roughness was measured on 11 parallel lines along a 1.2 m section of the rail. Pieringer et al. [39] also measured roughness data on parallel lines for their 3D model, but did so with a transverse spacing of 1 mm on an 8 m total length. Today BS EN 15610 exists as a standard method for measuring roughness profiles on train wheels and rails [62].

As mentioned in Section 1.1.2, automotive tire/road contact models typically use real world roughness data for the road, but not the tire, due to the high elasticity of the tire material, and the focus on the effect of the tread pattern instead. Klein and Hamet [50] used 150 mm sample sections for the road roughness data source, though it does not appear to specify the sample spacing. A very precise method was used in [44]. Fifteen parallel lines of roughness data, each

spaced 10 mm apart, were measured on an ISO replica road surface. Roughness amplitude was measured every 0.2 mm.

Lundberg et al. [14] note that there is an inherent difficulty in incorporating measured roughness data into any model. High precision models require a roughness profile with very fine spatial resolution, but such data is very difficult to gather and thus is not often available: neither for the researchers developing the models, nor for the beneficiaries who end up applying them in industry. As Thompson explains, there is a trade off between spatial resolution and overall measurement length [12]. A large overall measurement length is needed in order to fully capture the low frequency components of the roughness.

The small circumference of the trolley wheel may be beneficial for roughness measurements, as a much higher spatial resolution could theoretically be used versus that of a train wheel or automotive tire while still retaining the same overall data-set size. However, measuring the roughness of a typical floor presents the same challenges of whether to prioritize overall measurement length or spatial resolution. Of course, the phrase “typical floor” raises another issue altogether. Compared to roads and rails (which are almost always either made of asphalt or steel, respectively), there are dozens of different materials that may be used in floors where trolleys would typically be found. A large variance in roughness spectra across different kinds of floors would pose challenges for ensuring broad application of a indoor rolling noise models. The same may also be said for wheels, which also come in a variety of materials.

The scale of these roughness profiles poses a higher variance as well in indoor rolling noise. The smooth wheels and rails seen in train contact usually have relatively low-amplitude roughness profiles. The coarse asphalt roads and tire treads seen in automotive contact usually have relatively large-amplitude roughness profiles. The wheels and floors seen in indoor contact, on the other hand, may exhibit both high and low amplitude roughness profiles. This variance is unique to indoor rolling noise.

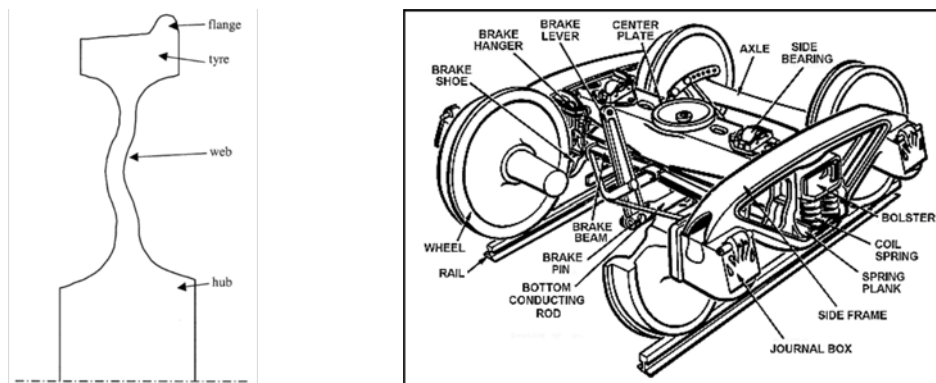
One technique for measuring the contact force in train wheel/rail contact is to place accelerometers and/or strain gauges on the axle box during testing [63]. Doing so allows a closer estimation of the influence of the roughness profile on the resulting excitation than measuring the radiated sound level. Such a technique could be used for indoor rolling noise: placing an accelerometers on the trolley frame during rolling may be able to provide an understanding of the link between roughness and resulting wheel excitation, as well as validate the force modeling of an indoor rolling contact model.

1.5 Wheel radiation

In general, wheel radiation is the area where the greatest amount of deviation occurs between the train, automotive, and indoor rolling contact. Because of their large size and complex response to forcing, a good deal of effort has been put into accurately modeling the response of both train wheels and automotive tires.

1.5.1 Train wheel radiation

Train wheels have a very high mass and rigidity, but possess a complex geometry. This is made even more complicated when considering the influence of the *car trucks*, which encase the wheels and contribute to sound radiation. Example of these are shown in Figure 1.4.



(a) Cross section of UIC 920 mm freight wheel.
Reproduced from [64].

(b) A typical train car truck.

Figure 1.4: Diagrams of typical train wheel constructions.

Remington [22] treated the train wheel as a rigid, un baffled disk radiating in the transverse direction. This is straightforward, but neglects the effects of mode shapes on vibration. Others [65, 66] have incorporated this through use of the Rayleigh integral technique [67], though this leads to errors at low frequencies. The boundary element (BE) method was used by Thompson and Jones [64] to achieve a more robust approximation of the wheel vibration. They found that use of this method results in radiation levels which can be quite a bit lower than those predicted by the Rayleigh integral technique at very low frequencies. Zhang and Jonasson [68] investigated the directivity of wheel radiation on sound propagation, and found that while it does lead to increased accuracy in determining the sound pressure level observed at a specific location next to a passing train, its incorporation into the wheel radiation model is not necessary to achieve the average sound pressure level of a passing train, which is often all that is desired.

1.5.2 Automotive tire radiation

Automotive tires, while not being as massive as train wheels, are significantly less rigid, and thus vibrate in irregular ways under forced excitation. Additional phenomena such as air pumping and the horn effect further contribute to tire sound radiation, but are not present in indoor rolling noise. The shape of a tire is a toroid, and several different approaches have been taken to model its vibration. The tire can be treated analytically as a vibrating cylindrical ring, such as was done by Kindt, Sas, and Desmet in [69]. The ring can be unfolded and represented as a vibrating plate, such as was done by Larsson and Kropp in [70]. FE models, such as the one developed by Brinkmeier et al. [71], have seen increasing popularity in recent years as computing power has increased exponentially. An example of the complexity of some of these vibrational modes is shown in Figure 1.5. A less conventional method involves representing the tire as a wave-guide to identify the vibration modes of the cavity within, such as was used by Hoever and Kropp [56]. Similarly to train wheel models, the BE method was also used in an automotive model by González and Abscal [72] to simulate the vibration of the tire. This 2D approach was found to have good agreement with other models using the elastic half space approach.

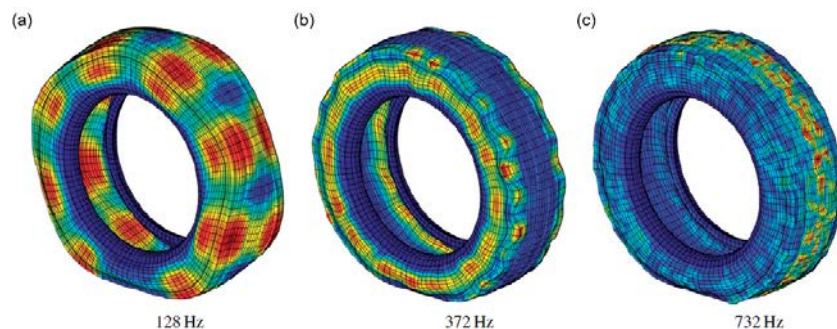


Figure 1.5: An example of truck tire eigenforms. Reproduced from [71].

1.5.3 Indoor wheel radiation

Compared to train wheels and automotive tires, trolley wheels are significantly more simple in their geometry, and more importantly, much smaller in size. This is beneficial in that it allows many of the complicating factors of existing rolling noise models to be ignored. The horn effect and air pumping do not produce any real effect due to the wheel's small size and low speed. Furthermore, the contribution from wheel radiation to the overall generated sound power in the reception room is likely negligible as well. As a simple comparison, if the wheel is treated as a circular piston source (i.e. vibrating in the transverse direction), the sound pressure amplitude generated will increase with the square of the radius [73]. Similarly, the radiated sound pressure level of the vibrating floor will increase linearly with its surface area (and thus with the square

of its radius for a circular floor). In a simplified comparison between the radiation of a trolley wheel with a radius of 5 cm to a circular floor of radius 1.5 m (which would be a rather small room), the sound pressure level generated by the vibrating floor will be $900\times$ greater than that of the vibrating wheel. If the trolley is assumed to have four wheels vibrating as incoherent sources, then the vibrating floor will still generate a pressure amplitude which is $450\times$ greater than that of the vibrating wheels. For indoor structure-borne noise, the radiation of the floor plays the dominant role.

Finally, the sound radiation of the trolley occurs in the emission room (which is of less interest than the reception room), and would thus be treated as an air-borne source. This is already taken into account in insulation treatment of buildings, whereas the rolling excitation of the floor in the reception room is not yet taken into account (being the focus of this thesis). For these reasons, it is not necessary to include effects of wheel radiation in an indoor rolling noise model.

1.6 Ground radiation

1.6.1 Train rail radiation

As was mentioned in Section 1.1.1, much of the work surrounding train rail radiation involves modeling the complex foundation upon which rails are constructed, including the rails, clips, sleepers, ballast, and subgrade. An example diagram is shown in Figure 1.6. Indoor floor construction is of course very different, and for this reason, much of the work surrounding train rail radiation does not have a direct application for indoor rolling noise.

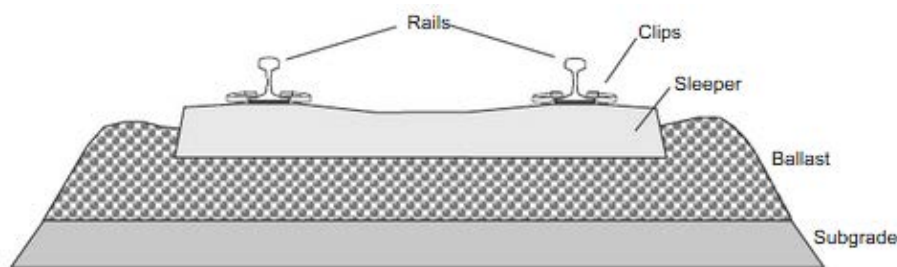


Figure 1.6: A typical train track construction. Reproduced from [74].

Remington [22] modeled the sound radiation of the rail differently depending on whether the forcing was vertical or horizontal. For lateral forcing, the rail was modeled as an infinite cylinder with a diameter equal to the height of the rail. For vertical forcing, the rail was modeled as two independently vibrating infinite cylinders, with diameters equal to those of the rail head and foot. Other models (e.g. [75]) represent the rail as an infinite Timoshenko beam. Thompson

[12] used both continuous and periodic supports in the TWINS program, represented by a series of spring-mass-spring systems connecting the rail to the ballast. To find the resulting radiation due to this vibration, the TWINS program treats the rail and supports separately as vibrating two-dimensional structures. However, simple line sources (e.g. in [25]) have also been used.

1.6.2 Automotive road radiation

Road sound radiation tends to be more straightforward than rail sound radiation due to its simpler construction. The roads are typically treated as a slab of material and thus do not require complex modeling to derive their influence on sound propagation. Some models (e.g. [76, 54]) incorporate the presence of the road in order to calculate its influence on the sound radiation of the tire. Keulen and Duškov [60] compiled a very thorough report which gives a summary of how various road parameters influence sound radiation. Some of these insights are summarized in Figure 1.7. Texture (what is being called *roughness* in this thesis) and mechanical impedance are usually accounted for in the contact model. Porosity, and also sometimes acoustic absorption, are also sometimes included to identify their effects on airborne radiated sound. Keulen and Duškov agree with Wullens [44] that while the effect of road parameters on each mechanism is known, the contribution of each mechanism to the overall sound radiation still has no clear consensus.

mechanism	road parameter		
	texture	porosity	mech. impedance
vibrations	strong	weak	strong
side wall vibrations	strong	weak	strong
stick-slip	strong	mediate	?
stick-snap	strong	mediate	?
air turbulence	weak	weak	weak
resonance in tyre	mediate	weak	?
air-pumping	mediate	strong	?
resonance in profile	mediate	strong	?
horn effect	weak	strong	weak
Absorption of tyre/road noise	weak	strong	weak
Absorption of propulsion noise	weak	strong	weak

Figure 1.7: Summary of how road parameters affect various sound propagation mechanisms for cars. Reproduced from [60].

1.6.3 Sound radiation in buildings

Calculating the sound propagation from source to receiver differs greatly in indoor rolling noise from train and automotive noise. For the latter two, the propagation path is horizontal, and airborne sound is the primary concern. For the former, the propagation path is vertical, and structure-borne sound is the primary concern. Thus, propagation techniques for train or automotive rolling noise are not readily applicable. Instead, propagation models developed for predicting other sources of indoor structure-borne noise are of greater relevancy.

An interesting method which currently exists for measuring the structure-borne radiated sound power of a stationary machine, but which could be extended to be applicable for indoor rolling noise, is the reception plate method [77]. This method works on the assumption that “when a vibrating source is connected to a simple plate structure, under a steady-state condition, then the source power equals the plate power” [78]. Any losses which occur between the machine and the plate can be accounted for by the loss factor η_{total} . As an example, Späh and Gibbs [79] measured the structure-borne sound power of a floor-mounted whirlpool bath tub and a wall-mounted cistern. They were able to achieve agreement between measured and predicted sound pressure levels using the reception plate method within 5 dB for frequencies above 125 Hz. Considering the simplicity of the technique, and the relative accuracy of the results that are able to be achieved, its applicability in measuring the sound power of a rolling cart could be considered. However, a difficulty still exists due to the fact that the source would be moving across the reception plate in the case of rolling noise. Because of the nature of a rolling wheel, it is not possible to use transducers to measure the forces acting in the contact area directly. As such, other techniques must be used for measuring other quantities (such as the sound pressure level) indirectly and back calculating to find the estimated forcing.

The transfer matrix method (TMM) [80] appears to show promise in its ability to be incorporated into an indoor rolling noise model. It is a well known technique which is often used for modeling the propagation of airborne sound through multi-layered porous media. Rhazi and Atalla [81] extended the method to be able to successfully model the propagation of structure-borne sound as well. This was done using several different methods, though the wave-based approach yielded the most promising results. In application of this method, once the generated contact force from rolling is found, it can be used as the injected force into the multi-layered system (e.g. a concrete slab with a soft floor covering) to calculate the radiated sound power. This methodology is particularly attractive because of the prevalence of multi-layered flooring as a noise control solution in buildings. The ability to identify how different floor layers affect the radiated sound from indoor rolling noise would be a valuable tool in building acoustic design.

Sound radiation in buildings is a topic which has been explored previously, but not in the context of rolling noise. Prediction of downward radiation from mechanical excitation exists for sources such as impact noise [3], the rubber ball [82] (see appendix F), walking noise [83], and even rainfall noise [82]. Recommendations for prediction of upward and lateral radiation from airborne and structure-borne excitation in heavy-weight buildings exist as well [84]. However, no standard currently exists for transmission to adjacent rooms for light-weight buildings.

In the world of building acoustics, a standard tapping machine has long existed for the purpose of replicating and regulating impact noise. This device, which was originally designed to mimic the sound of human footfall [85], consists of five hammers which rise and fall automatically in succession to generate impact events with the floor upon which the machine rests [82].

Work on the rainfall excitation of multi-layer systems has been developed by Guigou-Carter et al. [86, 87] and Chéné et al. [88]. In these models (which can be both analytical and numerical), the source is a randomly distributed fixed point excitation. That is, the locations of each raindrop impact are random, but the impact event for a given rain drop is still fixed in space over the short duration of the impact. This is different than impact noise from a tapping machine, which is a single fixed point excitation (i.e. all impacts occur at a single fixed point in space: there is no force distribution)[†]. Both of these however differ from rolling noise, which is a single moving point excitation. The injected force into the floor continuously moves in a line across the floor.

The TMM used for prediction of mechanical excitation is used due to the benefit it provides over alternative methods such as FE modeling and statistical energy analysis (SEA). FE modeling is typically too detailed and computationally expensive, requiring a large amount of information about the setup. SEA on the other hand poses the opposite problem: it often does not provide enough detail for the case of mechanical excitation to yield useful results. The TMM strikes a balance between the two, and is thus what is often used for indoor mechanical sound propagation. Software packages have been developed which implement the TMM for various forms of mechanical excitation, such as AlphaCell [89]. The addition of rolling excitation to these types of software could widen the number of use cases in which they may be applied.

1.7 Conclusion

This chapter reviews a sampling of the vast amount of literature which exists in the modeling of rolling noise. Focus was given to automotive tire/road and train wheel/rail contact, as those

[†]Technically the hammer impacts of a tapping machine are distributed as each of the five hammers do not impact exactly the same spot on the floor, but are spaced adjacent to one another. However, they are sufficiently close that for modeling purposes, they are treated as all impacting the same point on the floor.

are the areas which have seen the majority of devoted research in years past. The state of the art of indoor mechanical excitation was also reviewed.

Hertzian contact is an assumption which is found in the vast majority of the rolling models reviewed. The point-contact spring, 2D Winkler bedding, and 3D elastic half space methods of estimating the contact between surfaces are all methods which are used regularly in automotive and train rolling noise modeling which can have application in modeling indoor rolling noise as well. The trade offs between time domain and frequency domain, as well as between 1D, 2D, or 3D modeling, are aspects which continue to depend on the particular goals of the model application, despite vast improvements in computing power over the years. While the underlying phenomenon of roughness induced sound radiation is shared between automotive, train, and indoor scenarios, there still exist many differences which will need to be adapted for in order to develop an accurate indoor rolling noise model. Nevertheless, because of the increasing emphasis that is being placed on quiet building design, the necessity for a model which can accurately predict this kind of noise is only likely to increase in the future.

Following this literature review, the rolling noise model developed in this thesis is presented next in Chapter 2. This includes a theoretical background of the contact mechanics which form the basis of the model, as well as an explanation of how the force generated during rolling is converted to wheel/floor movement and eventually a radiated sound pressure level. Chapter 3 provides an explanation of how the wheel stiffness is calculated, which is used in the rolling noise model to estimate the vertical movement of the trolley wheel in response to the rolling excitation. Chapter 4 presents a series of experimental tests conducted regarding rolling noise, and Chapter 5 compares the results of these tests to model predictions in order to validate the model, identify model capabilities, and applications.

THIS chapter presents the rolling noise model used to estimate the radiated sound level of an indoor trolley rolling across a floor. The theory behind the Hertzian contact of the wheel/floor interaction is first presented in Section 2.1, followed by an expansion of the model's applicability through the inclusion of discrete irregularities in Section 2.3. The sections thereafter describe how the dimensionality of the model affects its formulation Section 2.4, how the calculation of the contact force due to the local wheel/floor interaction is translated to the response of the wheel (Section 2.5), and the resulting sound propagation (Section 2.6).

This thesis comes about as a result of a preliminary rolling noise model which was developed prior to the start of this work. This preliminary model, originating from [5], is presented in Section 2.7 as a means of comparing the improvements made between it and the current rolling noise model. Further comparison between the preliminary and improved models will be given in Chapter 5.

The general outline of the improved rolling noise model is shown in Figure 2.1. Operating in the time domain, the model uses the influencing properties of the wheel and floor to calculate the contact force between the two bodies for each discretized moment in time throughout the rolling event. These include the wheel and floor roughness profiles, the wheel and floor material properties (Young's modulus and Poisson's ratio), the speed of the trolley, mass of the trolley (plus added load), and geometric profiles of the wheel and floor. Such profiles include not only the dimensions of the wheel, but also any discrete irregularities such as wheel flats or floor joints.

The contact force at each moment in time is used as input into the dynamic model, where the resulting movement of the wheel and floor are calculated in response to the excitation's injected force. This influences what the exact roughness profile will be for the following time step, as the wheel and floor continuously move in relation to one another, influencing how much (or how little) contact exists between them. Once the contact force has been calculated for each time

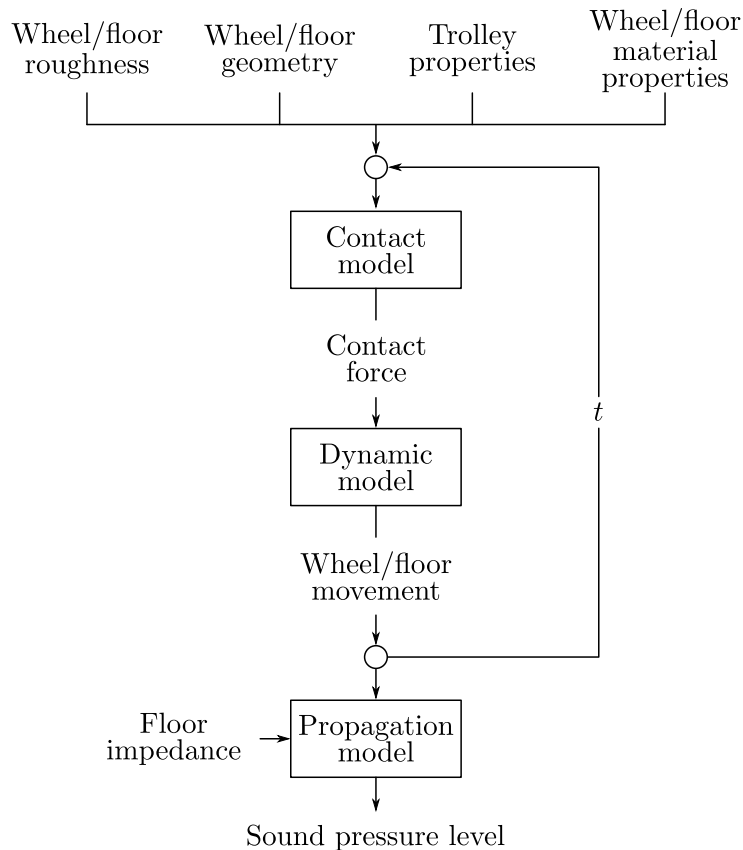


Figure 2.1: General outline of the rolling noise model.

step in the rolling event, the model is converted to the frequency domain, where the blocked force spectra is used in conjunction with the wheel and floor impedances to convert the blocked force to a flexural force. From there the sound pressure level may be calculated in the reception room below.

2.1 Contact model

In order to estimate the contact force for each time step, an equivalent spring foundation is used (sometimes called a Winkler bedding [35]). This has been used in other rolling noise models (for example [34, 90]), and has proven to be a good estimation when compared to the more physically accurate Boussinesq method [18]. The equivalent spring foundation, as with most methods of estimating the contact force between two bodies, is based on Hertzian contact mechanics.

2.1.1 Hertzian contact

Let us consider the case of two arbitrary ellipsoidal bodies in contact with one another, the geometry of which is given by Figure 2.2. Hertz showed in 1896 that as the two bodies are

brought close to one another, they first touch at a point, which then grows to form an ellipse, as the relative compressive load increases [15]. The theory for this phenomenon is based on the following four assumptions:

- The strains are small enough that they remain within the elastic limit of deformation for the two bodies. No plastic deformation occurs in the vicinity of contact.
- The area of contact is small compared to the size of the bodies, such that they may be both considered as elastic half spaces with non-conforming surfaces.
- The two bodies are perfectly smooth. No surface roughness exists.
- The two bodies are frictionless. Only normal pressure is considered in the vicinity of contact.

Under these assumptions, the ellipse which defines the area of contact has a major axis of length $2a$ and a minor axis of length $2b$, as shown in Figure 2.3.

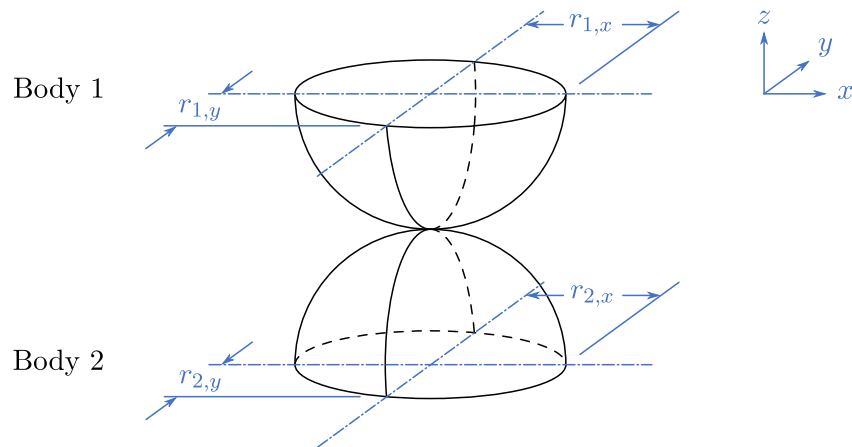


Figure 2.2: Contact between two ellipsoidal solids

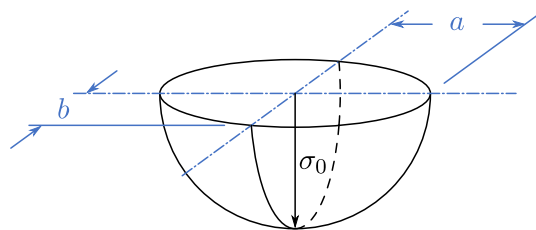


Figure 2.3: Ellipsoidal stress profile formed by two ellipsoidal bodies in contact under load

The stress distribution within the contact area of the smooth bodies was found by Hertz to be [15]

$$\sigma = \sigma_0 \sqrt{\left(\frac{x}{a}\right)^2 + \left(\frac{y}{b}\right)^2} \quad (2.1)$$

where x and y are distances from the center of the ellipse, and σ_0 is the maximum stress, given by

$$\sigma_0 = \frac{3Q}{2\pi ab} \quad (2.2)$$

where Q is the vertical compressive load between the two bodies in Newtons.

In order to determine the stress distribution, the size of the contact area, which is a function of the load and material parameters, must first be found. To do so, it is useful to first define some characteristics of the interaction between the two bodies. Under the plane stress assumption, the apparent relative elasticity E' between the two bodies is given by

$$E' = \left(\frac{1-\nu_1}{E_1} + \frac{1-\nu_2}{E_2} \right)^{-1} \quad (2.3)$$

where ν and E are the Poisson's ratio and Young's modulus of each body, denoted by the appropriate subscripts.

The curvature sum, which accounts for the geometry of both bodies and is equal to the inverse of the equivalent radius of interaction, can be found by

$$\Sigma\rho = \frac{1}{r_{\text{eq}}} = \frac{1}{r_{1,x}} + \frac{1}{r_{1,y}} + \frac{1}{r_{2,x}} + \frac{1}{r_{2,y}} \quad (2.4)$$

Similarly, the curvature difference is defined as

$$\mathcal{C} = \frac{\left(\frac{1}{r_{1,x}} - \frac{1}{r_{1,y}} \right) + \left(\frac{1}{r_{2,x}} - \frac{1}{r_{2,y}} \right)}{\Sigma\rho} \quad (2.5)$$

With these definitions, the contact area dimensions can now be found for the general case. Harris demonstrated the following quantities [91].

$$a = a^* \left(\frac{3Q}{2E'\Sigma\rho} \right)^{1/3} \quad (2.6)$$

$$b = b^* \left(\frac{3Q}{2E'\Sigma\rho} \right)^{1/3} \quad (2.7)$$

$$u_0 = \frac{u^*\Sigma\rho}{2} \left(\frac{3Q}{2E'\Sigma\rho} \right)^{2/3} \quad (2.8)$$

Here u_0 is the interpenetration between the two bodies. This is a displacement which represents the small amount of deformation that the two bodies experience in the vicinity of contact due to being pressed into one another. The dimensionless quantities a^* , b^* , and u^* are functions of

only the body geometries and material properties [91]

$$a^* = \left(\frac{2\kappa^2 \mathcal{E}}{\pi} \right)^{1/3} \quad (2.9)$$

$$b^* = \left(\frac{2\mathcal{E}}{\pi\kappa} \right)^{1/3} \quad (2.10)$$

$$u^* = \frac{2\mathcal{F}}{\pi} \left(\frac{\pi}{2\kappa^2 \mathcal{E}} \right)^{1/3} \quad (2.11)$$

where κ is the eccentricity parameter

$$\kappa = a/b \quad (2.12)$$

and \mathcal{F} and \mathcal{E} are the complete elliptic integrals of the first and second kind, respectively.

$$\mathcal{F} = \int_0^{\pi/2} \left[1 - \left(1 - \frac{1}{\kappa^2} \right) \sin^2 \phi \right]^{-1/2} d\phi \quad (2.13)$$

$$\mathcal{E} = \int_0^{\pi/2} \left[1 - \left(1 - \frac{1}{\kappa^2} \right) \sin^2 \phi \right]^{1/2} d\phi \quad (2.14)$$

In order to eliminate the circular dependence of Equations (2.6) to (2.12), the known body geometries may be related to the eccentricity parameter through

$$\mathcal{C} = \frac{(\kappa^2 + 1)\mathcal{E} - 2\mathcal{F}}{(\kappa^2 - 1)\mathcal{E}} \quad (2.15)$$

which is equal to the definition of \mathcal{C} given in Equation (2.5).

Equations (2.5) and (2.9) to (2.15) can be combined to solve for the desired dimensionless contact parameters. Tabulated values for a^* , b^* , and u^* for various values for \mathcal{C} were found by Harris [91]. They have been reproduced in Table 2.1. They offer enough resolution that linear interpolation may be used to find the dimensionless contact parameters corresponding to any combination of body geometries with sufficient accuracy. The complete contact stress profile can now be found between any two ellipsoidal solids.

Table 2.1: Dimensionless contact parameters, reproduced from [91]

\mathcal{E}	a^*	b^*	u^*
0	1	1	1
0.1075	1.076	0.9318	0.9974
0.3204	1.2623	0.8114	0.9761
0.4795	1.4556	0.7278	0.9429
0.5916	1.644	0.6687	0.9077
0.6716	1.8258	0.6245	0.8733
0.7332	2.011	0.5881	0.8394
0.7948	2.265	0.548	0.7961
0.83495	2.494	0.5186	0.7602
0.87366	2.8	0.4863	0.7169
0.90999	3.233	0.4499	0.6636
0.93657	3.738	0.4166	0.6112
0.95738	4.395	0.383	0.5551
0.9729	5.267	0.349	0.496
0.983797	6.448	0.315	0.4352
0.990902	8.062	0.2814	0.3745
0.995112	10.222	0.2497	0.3176
0.9973	12.789	0.2232	0.2705
0.9981847	14.839	0.2072	0.2427
0.9989156	17.974	0.18822	0.2106
0.9994785	23.55	0.16442	0.17167
0.9998527	37.38	0.1305	0.11995
1	∞	0	0

If body 2 is assumed to be a half space rather than an ellipsoid (such as that show in Figure 2.4), then $r_{2,x} = r_{2,y} = \infty$, and several simplifications can be made. In this case, the contact stress profile is still ellipsoidal in shape, but the numerical notation may be dropped from the subscripts and Equations (2.4) and (2.5) reduce to

$$\Sigma\rho = \frac{1}{r_x} + \frac{1}{r_y} \quad (2.16)$$

$$\mathcal{E} = \frac{\left(\frac{1}{r_x} - \frac{1}{r_y}\right)}{\Sigma\rho} \quad (2.17)$$

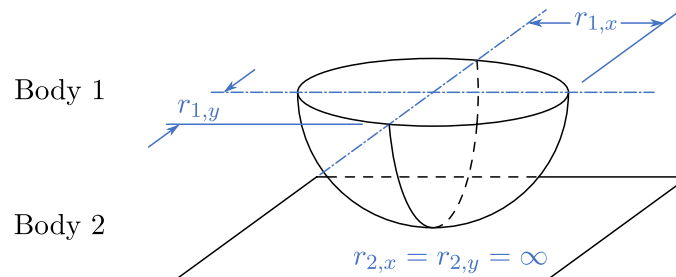


Figure 2.4: Contact between a solid of revolution and a half space

If the transverse radius of body 1 is also set to infinity, then contact devolves to a line of zero length in the x direction, infinite width in the y direction, and an interpenetration of zero (thus no contact stress), due to the mathematical implication that body 1 is now infinitely wide. By making body 1 a cylinder and assuming body 2 to have the same width w as body 1 (shown in Figure 2.5), ideal line contact develops, and the contact area becomes a rectangle of length $2a$ and width w . The contact stress profile becomes semi-cylindrical in shape, as shown in Figure 2.6.

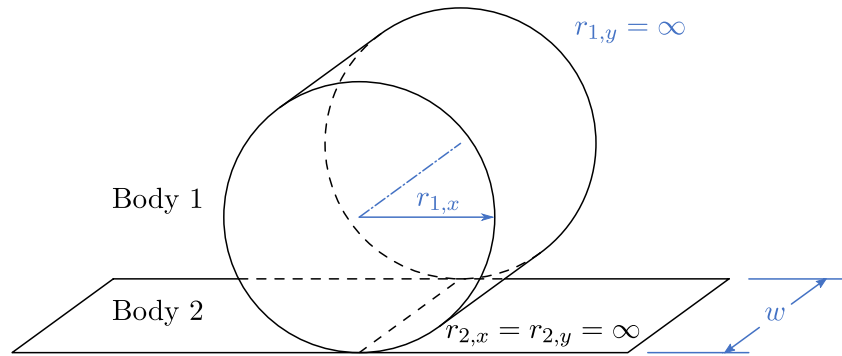


Figure 2.5: Contact between a cylinder and a half space of equal width

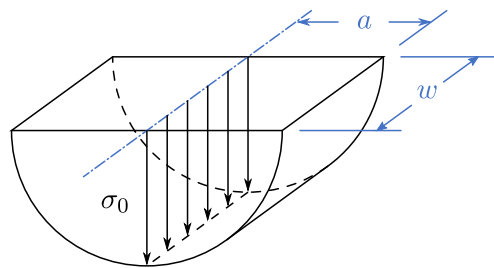


Figure 2.6: Semi-cylindrical contact profile formed by a cylinder and a half space of equal width under load

The Hertzian equations for σ_0 , a , and u_0 become

$$\sigma_0 = \frac{2Q}{\pi w a} \quad (2.18)$$

$$a = \sqrt{\frac{4Q}{\pi w E' \Sigma \rho}} \quad (2.19)$$

$$u_0 = \frac{4Q}{\pi w E'} \quad (2.20)$$

The stress profile is now only a function of x

$$\sigma = \sigma_0 \sqrt{1 - \left(\frac{x}{a}\right)^2} \quad (2.21)$$

The complete contact stress profile can now be found between a cylinder and a half space. In reality, a half space which is wider than the cylinder will produce edge loading, but these effects are assumed negligible for the case of indoor rolling noise due to the low static loads at play.

2.1.2 Equivalent spring foundation

The equations in the previous section are useful when the surfaces of the two bodies are perfectly smooth. In reality, this is never the case, and the presence of roughness requires an alternative approach be taken in order to calculate the contact force. This is where the equivalent spring foundation comes into play. A bed of independent springs is placed in the interface between the two bodies. They are independent in the sense that the deflection of one does not affect the deflection of its neighbors. In reality, this is not the case, when a surface deforms, the deflection at a given point affects the deflection in the surrounding area. However, as will be seen shortly, the behavior of the springs may be modified to account for this discrepancy and offset the majority of the error it causes.

The ellipsoidal wheel

Let us examine the second case explored in the previous section, with body 2 being a half space (Perhaps analyzing the rolling noise of a skate boarder in a half pipe may be of use to others, but it is unfortunately not the focus of this study). We will define x to be positive in the direction of rolling, and z to be positive normal from the floor. As shown in Figure 2.7, when the two bodies are brought together under zero load, they first touch at a single point o , where we will place the origin of our axes.

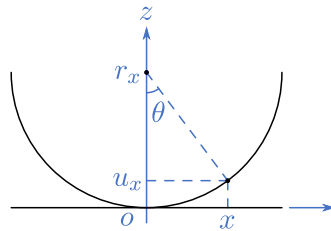


Figure 2.7: Geometry of the wheel/floor interface in the xz plane. The situation is identical for the yz plane, simply by swapping x for y .

The position of an arbitrary point (x, u_x) on the wheel in the xz plane is

$$u_x = r_x(1 - \cos\theta) \quad (2.22)$$

$$x = r_x \sin\theta \quad (2.23)$$

In the vicinity of contact, the small angle approximation may be applied ($\sin\theta \approx \theta$, $\cos\theta \approx 1 - \theta^2/2$), yielding

$$u_x \approx \frac{r_x \theta^2}{2} \quad (2.24)$$

$$x \approx r_x \theta \quad (2.25)$$

Since we are interested in using x as our dependent variable rather than θ , these two equations may be combined to yield

$$u_x \approx \frac{x^2}{2r_x} \quad (2.26)$$

similarly for the yz plane

$$u_y \approx \frac{y^2}{2r_y} \quad (2.27)$$

The above equations may be used to find the normal stress at any arbitrary point in the wheel/floor interface.

Let us now return to the bed of independent springs. If the springs are assumed linear, the contact stress profile of the wheel/floor interface can be written as [11]

$$\sigma = \sigma_0 \left[1 - \left(\frac{x^2}{2r_x u_0} + \frac{y^2}{2r_y u_0} \right) \right] \quad (2.28)$$

where u_0 is the maximum deflection (which is the same for both x and y due to symmetry), and σ_0 is the maximum normal stress, occurring at $(x, y) = (0, 0)$. This does not appear to be of the same form as the Hertzian stress profile from Equation (2.1): there is a missing square root. Indeed, the force in the springs (i.e. the contact force) in Equation (2.28) will increase with the square of their deflection. This does not agree with Hertzian theory, which predicts that the contact force will increase with $u_0^{1.5}$. To correct for this, the springs can be made non-linear by setting them to deflect with the square root of the deflection. Thus the contact stress profile becomes

$$\sigma = \sigma_0 \sqrt{1 - \left(\frac{x^2}{2r_x u_0} + \frac{y^2}{2r_y u_0} \right)} \quad (2.29)$$

If we define the following equalities

$$a = \sqrt{2r_x u_0} \quad (2.30)$$

$$b = \sqrt{2r_y u_0} \quad (2.31)$$

then equations Equations (2.1) and (2.29) are identical, and our bed of springs (shown in Figure 2.8) agrees exactly with Hertzian theory.

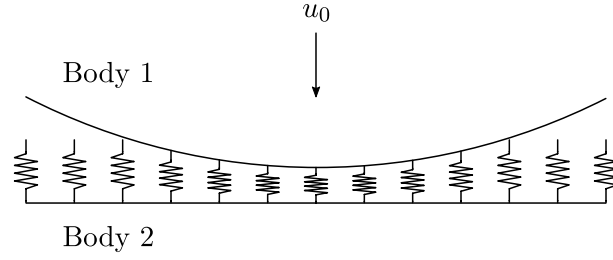


Figure 2.8: A bed of independent springs placed between the floor and wheel

There is one more issue to deal with. The dimensions for the contact area predicted by Equations (2.30) and (2.31) are incorrect. This is due to the independent nature of the springs, exemplified in Figure 2.9. As they do not account for the interaction with one another, the contact area is predicted to be larger than reality. To account for this, we shall define *equivalent* radii which will yield the appropriate contact area dimensions.

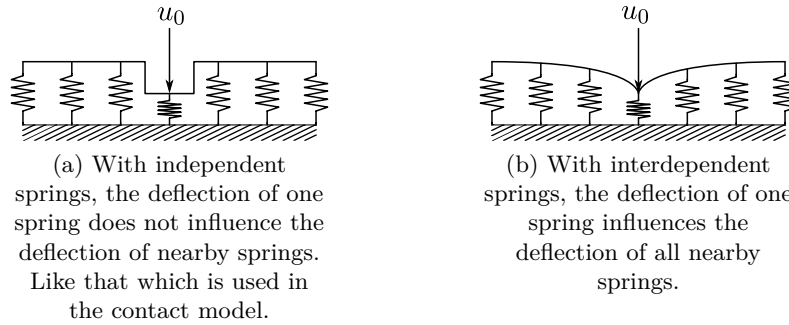


Figure 2.9: Bed of springs under a point load.

If we combine Equations (2.6) and (2.7) with their respective Equations (2.30) and (2.31), we may define our equivalent radii r'_x and r'_y , such that

$$a = a^* \left(\frac{3Q}{2E'\Sigma\rho} \right)^{1/3} = \sqrt{2r'_x u_0} \quad (2.32)$$

$$b = b^* \left(\frac{3Q}{2E'\Sigma\rho} \right)^{1/3} = \sqrt{2r'_y u_0} \quad (2.33)$$

by substituting Equation (2.8) into the above formulations and solving for r'_x and r'_y , we obtain

$$r'_x = \frac{(a^*)^2}{u^* \Sigma\rho} \quad (2.34)$$

$$r'_y = \frac{(b^*)^2}{u^* \Sigma\rho} \quad (2.35)$$

which still only depend on the geometry of the wheel, not the load or the material properties of the wheel or floor.

Equation (2.29), with the wheel radii replaced with the equivalent radii defined in Equations (2.34) and (2.35), yields the complete stress profile in the vicinity of contact. The stress profile is integrated across the entire contact area, but only for those points which are found to have a positive stress. A negative stress implies that the two bodies are in tension at that point, which is not physically possible (adhesion effects are ignored in the contact model), thus we conclude that this point is outside the area of contact. This is summarized by

$$\sigma(x, y) = \begin{cases} \sigma_0 \sqrt{1 - \left(\frac{x^2}{2r'_x u_0} + \frac{y^2}{2r'_y u_0} \right)} & \text{if } \frac{x^2}{2r'_x u_0} + \frac{y^2}{2r'_y u_0} < 1 \\ 0 & \text{if } \frac{x^2}{2r'_x u_0} + \frac{y^2}{2r'_y u_0} \geq 1 \end{cases} \quad (2.36)$$

and the total contact force is

$$F = \iint \sigma(x, y) dx dy \quad (2.37)$$

In practice the contact area is discretized, as shown in Figure 2.10, in order to numerically calculate the contact force integral.

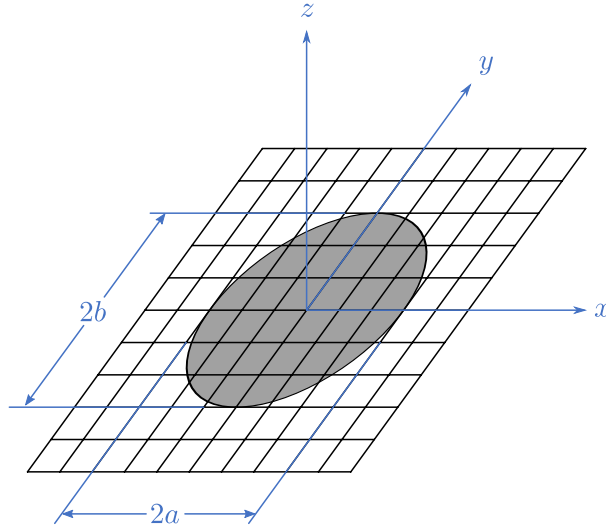


Figure 2.10: Discretized area of contact, the dimensions of which are defined by the lengths $2a$ and $2b$ in the longitudinal and transverse directions.

Let us consider an example for the purpose of verifying the validity of this formulation. An ellipsoidal wheel is placed on a flat floor and placed under load. The parameters used for this example are given in Table 2.2.

Table 2.3 shows the calculated values for the Hertzian contact dimensions and interpenetration for five different loads, alongside the contact dimensions and contact force found using the bed of springs method. A 50×50 grid spacing across an area of $10 \times 10 \text{ mm}^2$ was used for the numerical integration. The two formulations provide identical results for the Hertzian contact lengths, and extremely close results for the estimated contact force.

Table 2.2: Example parameters

Parameter	Unit	Variable	Value
Wheel radius	(mm)	r_x	50
Wheel transverse radius	(mm)	r_y	100
Wheel Young's modulus	(GPa)	E_1	0.2
Wheel Poisson's ratio	(-)	ν_1	0.3
Floor Young's modulus	(GPa)	E_2	30
Floor Poisson's ratio	(-)	ν_2	0.2

Table 2.3: Ellipsoidal example results

Q (N)	Hertzian		Bed of Springs		
	a (mm)	b (mm)	a (mm)	b (mm)	F (N)
50	2.88	1.81	2.88	1.81	49.8
100	3.63	2.28	3.63	2.28	100.0
150	4.15	2.62	4.15	2.62	149.2
200	4.57	2.88	4.57	2.88	200.5

The stress profile for the case of $Q = 50$ N is shown in Figure 2.11. The ellipsoidal stress profile can be seen.

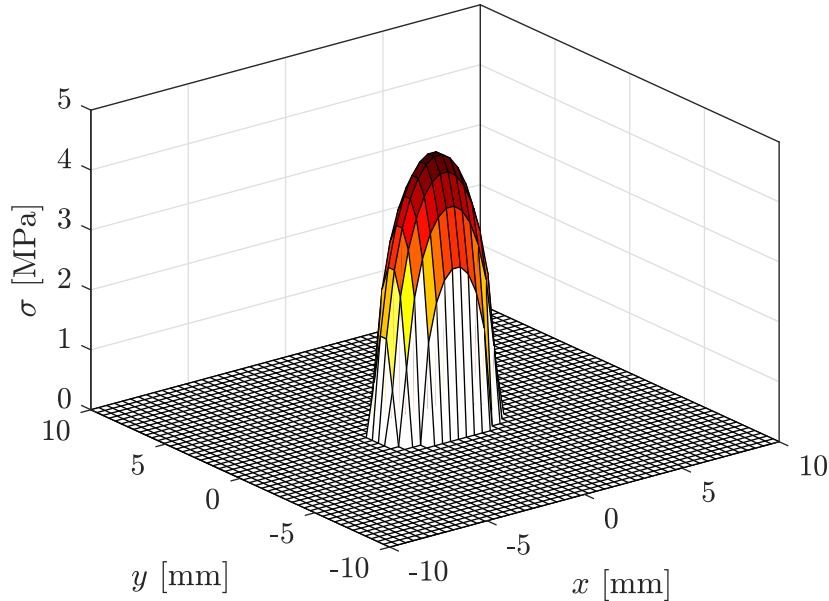


Figure 2.11: Contact stress profile for a smooth ellipsoidal wheel ($r_x = 50$ mm, $r_y = 100$ mm) under a 50 N load, calculated with the bed of springs method.

The Cylindrical Wheel

In the case of a cylindrical wheel and flat floor, the same process described in Section 2.1.2 may be used, replacing the ellipsoidal equations with those for the cylindrical case. As before, ideal line contact is assumed, so the width of the wheel and floor are assumed equal. In the

absence of curvature in the transverse direction, the y dependency is dropped from the smooth stress profile. Equation (2.36) becomes

$$\sigma(x) = \begin{cases} \sigma_0 \sqrt{1 - \frac{x^2}{2r'u_0}} & \text{if } \frac{x^2}{2r'u_0} < 1 \\ 0 & \text{if } \frac{x^2}{2r'u_0} \geq 1 \end{cases} \quad (2.38)$$

As before, Equation (2.38) may be made to agree with Hertzian theory by defining an equivalent radius such that

$$a = \sqrt{\frac{4Qr}{\pi w E'}} = \sqrt{2r'u_0} \quad (2.39)$$

which, when combined with Equation (2.20) and solved for r' , yields

$$r' = \frac{r}{2} \quad (2.40)$$

For the cylindrical wheel, the equivalent radius is simply half the true wheel radius.

If the same example parameters from Table 2.2 are used (with the exception of r_y , which may be replaced by the wheel width $w = 20$ mm), then the Hertzian and bed of springs results may once again be compared with one another for the case of the cylindrical wheel. The results are shown in Table 2.4. Once again, very good agreement can be seen between the two methods.

Table 2.4: Cylindrical example results

Q (N)	Hertzian	Bed of Springs	
	a (mm)	a (mm)	F (N)
50	0.85	0.85	50.8
100	1.21	1.21	102.5
150	1.48	1.48	152.0
200	1.71	1.71	199.4

The stress profile for the case of $Q = 50$ N is shown in Figure 2.12. The semicircular stress profile can be seen. For easy comparison, the axis limits are the same as those used in Figure 2.11. While the profile is of course significantly wider for the cylindrical wheel than for the elliptical wheel, spanning the entire width of the wheel, it is consequently much shorter in length. All else being equal (save for the difference in transverse curvature), the contact lengths calculated for the elliptical wheel are roughly $3\times$ longer than those of its equivalent cylindrical counterpart.

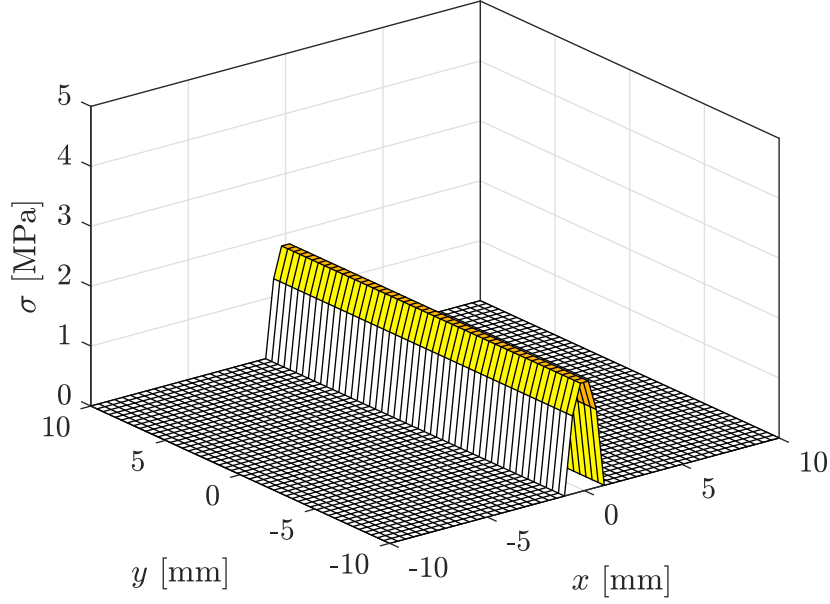


Figure 2.12: Contact stress profile for a smooth cylindrical wheel ($r = 50$ mm, $w = 20$ mm) under a 50 N load, calculated with the bed of springs method.

2.2 Implementation into the rolling noise model

Before describing the implementation of the equations of contact into the rolling noise model, it is helpful to first define the coordinate systems used. Shown in Figure 2.13, the global coordinate system (x, y, z) remains fixed throughout the rolling event, with the wheel first being placed such that the wheel center is located at the center of the xy plane. The origin of the z axis is located at the position of contact between the wheel and the floor in the absence of roughness. As the wheel rolls across the floor, a local coordinate system (x', y', z') follows, whose origin remains at the location of the wheel center in x and y . $z' = z$ for all time.

The two coordinate systems are coupled at a given moment in time t via the speed of the trolley v ,

$$x = vt \quad (2.41)$$

such that $x' = 0$ at $x = vt$.

Figure 2.14 shows a diagram of how the equivalent bed of springs is used in the contact model. The interpenetration of the wheel and floor u_R is calculated using

$$u_R(x, x', y') = u_0 - z_W(x) + \varsigma(x, x', y') - \xi_W(x, x', y') + \xi_F(x, x') \quad (2.42)$$

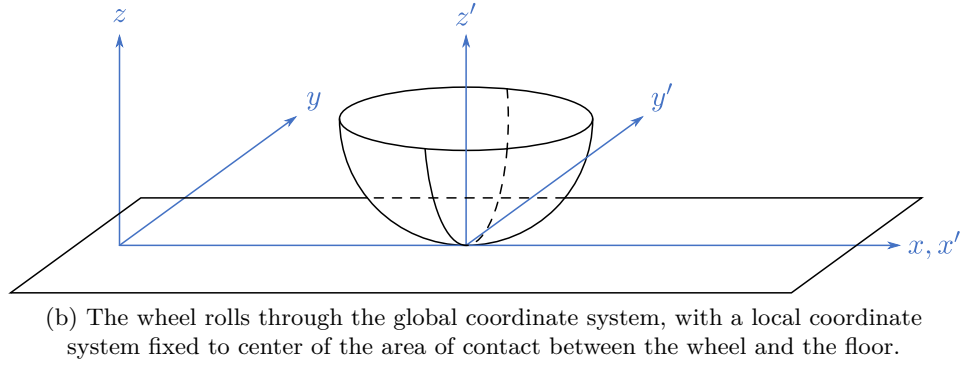
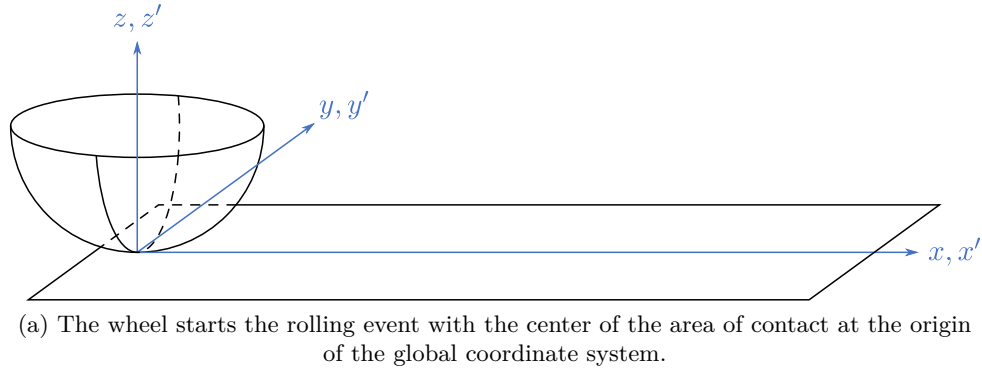


Figure 2.13: Coordinate systems used in the rolling noise model.

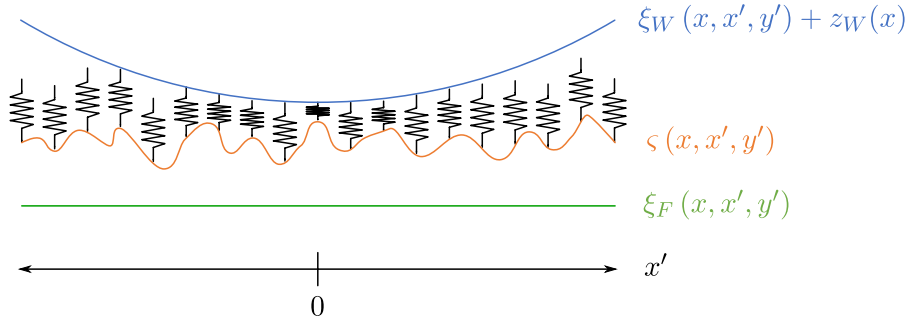


Figure 2.14: Contact model used for estimating the contact stresses between the wheel and the floor

Here u_0 is the Hertzian deflection in the absence of roughness, defined by either Equation (2.8) or Equation (2.20) depending on the geometry of the wheel. z_W is the vertical position of the wheel center, ζ is the relative roughness profile between the wheel ζ_W and the floor ζ_F ,

$$\zeta(x, x', y') = \zeta_F(x, x', y') - \zeta_W(x, x', y') \quad (2.43)$$

which is positive for an asperity on the floor. Finally, ξ_W and ξ_F are the geometric profiles of the wheel and the floor respectively.

For a given x , the roughness profile ς , wheel profile ξ_W and floor profile ξ_F are re-defined for the local coordinate system. Typically, the wheel profile will be simply defined by its radii of curvature (in the direction of rolling x , as well as the transverse direction y)

$$\xi_W(x, x', y') = \frac{x'^2}{2r'_x} + \frac{y'^2}{2r'_y} \quad (2.44)$$

where r'_x and r'_y are the modified wheel radii described in the previous sections. The floor profile will typically be zero for all x . However, they may differ in the presence of discrete irregularities such as wheel flat spots or floor joints. The profiles would then need to be updated at each x as a flat spot or floor joint moves through the vicinity of contact. The process for defining these more complex profiles is given in Section 2.3.

In order to account for the presence of roughness and the vertical movement of the wheel center, Equations (2.36) and (2.38) need only be slightly modified. They may be summarized by the general contact stress equation

$$\sigma_R(x, x', y') = \begin{cases} \sigma_0 \sqrt{\frac{u_R(x, x', y')}{u_0}} & u_R(x, x', y') > 0 \\ 0 & u_R(x, x', y') \leq 0 \end{cases} \quad (2.45)$$

As before, any points in the discretized calculation area which are found to have negative interpenetrations are assumed to be out of contact, and the stresses at those points are set to zero.

Once the stress profile is known, it may then be integrated across the entire contact area to obtain the full contact force due to roughness

$$F_R(x) = \int \int \sigma_R(x, x', y') dx' dy' \quad (2.46)$$

Care must be taken to ensure the integration is carried out over a sufficiently large area so as to encompass the entire area of contact, which will not be exactly equal to $2a \times 2b$ in the presence of roughness. When performing the integration numerically, the presence of any nonzero values on the edges of the stress matrix prior to integration indicates that the limits are too small.

2.3 Discrete irregularities

The rolling noise model is not, strictly speaking, continuously dynamic in nature. In its discretized form, it is actually a series of static snapshots, each pieced together to form the rolling event in the time domain. As such, it may be thought of not as a rough wheel rolling forward in

the $+x$ direction across a rough stationary floor, but rather as a smooth stationary wheel sitting on a smooth stationary floor, and a flat “roughness strip” pulled in the $-x$ direction between the two. Inherent in this formulation is the assumption that the contact area stays centered below the wheel center, such that the wheel axis and contact area center are both located at $x' = 0$ in the local coordinate system. However, in the presence of discrete irregularities, this ceases to be the case.

Discrete irregularities are variations in the profile of the wheel and/or floor which deviate from the small scale asperities found in the roughness profiles. They cause both the vertical and horizontal position of the wheel center to vary greatly from its neutral location, which is typically at a distance of r_x directly above the center of the area of contact (or in the case of the model with equivalent radii, a distance of r'_x directly above the center of the area of contact). Consequently, they may not be simply included in the roughness profiles ζ_W & ζ_F , and must be considered separately. This is also why the local coordinate system (x', y', z') is said to follow the wheel center and not the center of the area of contact in the xy plane.

Ignoring small scale roughness for the time being, let us consider a smooth wheel with a single flat spot, as shown in Figure 2.15. As the flat spot moves into the vicinity of contact, the position of the contact area will first shift backwards to be behind the wheel center. At the moment that the flat spot is in full contact with the floor, the contact area is equal in length to the length of the wheel flat, and is again centered below the wheel center. Immediately thereafter, the flat spot begins to leave the vicinity of contact, and the contact area now shifts forward to be slightly ahead of the wheel center.

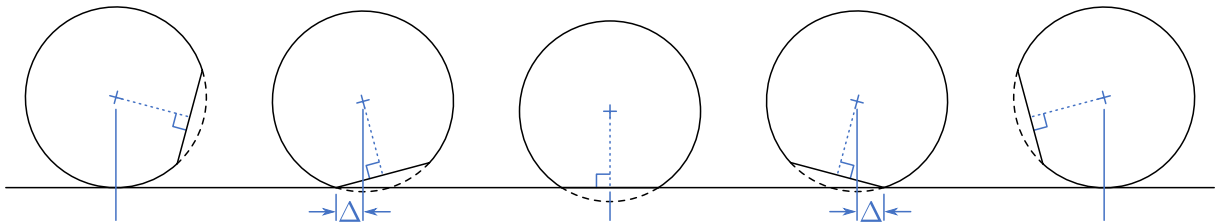


Figure 2.15: Example of a wheel flat moving through the vicinity of contact. Not drawn to scale.

Similarly for a floor joint (as shown in Figure 2.16), the position of the contact area shifts behind the wheel center as the wheel enters the floor joint. At the moment of impact with the far side, a second contact zone appears ahead of the wheel center[†]. As the wheel continues forward and out of the joint, the rear contact zone disappears, and the front contact zone returns to center.

[†]A scenario in which the wheel contacts the bottom of the floor joint before contacting the far side is not considered here. The joint would need to be unreasonably wide and/or shallow for such a situation to occur, and thus outside the realm of typical floor joint geometries.

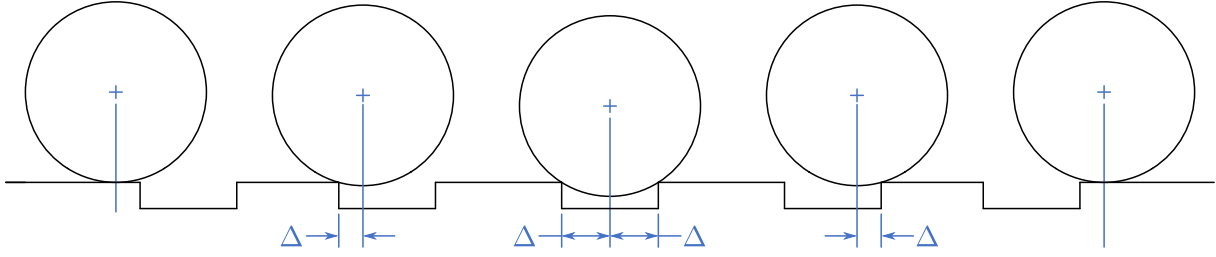


Figure 2.16: Example of a floor joint moving through the vicinity of contact. Not drawn to scale.

The following sections will explain the process by which wheel flats and floor joints are accounted for in the rolling noise model.

2.3.1 Wheel flats

Wheel flats (or flat spots) are a possible artifact of indoor trolley wheels. A wheel which gets stuck for a period of time and slides across the floor may generate a flat spot due to friction. Alternatively, a large impact due to a drop or fall may cause a wheel to generate a flat spot as well. In both cases, the presence of the flat spot results in an impact occurring each time it completes a revolution, which has the potential to have a significantly higher sound level than that which is caused by the small scale roughness alone.

For a wheel of radius r , an ideal wheel flat may be modeled as a chord of the wheel circumference, as shown in Figure 2.17. The flat depth h_W , ideal flat length $l_{0,W}$, and ideal center angle Φ_0 are related by [92]

$$\frac{\Phi_0}{2} = \sin^{-1}\left(\frac{l_{0,W}}{2r}\right) = \cos^{-1}\left(1 - \frac{h_W}{r}\right) \quad (2.47)$$

The profile of such a wheel may be described by

$$R_{0,\phi}(\phi) = \begin{cases} r & |\phi| > \left|\frac{\Phi_0}{2}\right| \\ \frac{r \cos \frac{\Phi_0}{2}}{\cos \phi} & |\phi| < \left|\frac{\Phi_0}{2}\right| \end{cases} \quad (2.48)$$

where ϕ is evaluated over the interval $[-\pi, \pi]$.

Alternatively, some rolling noise models have had success using a rounded wheel flat profile, which replaces the hard corner transition between flat and curved with one which is more gentle profile [92, 93, 59]. This is intended to represent a wheel flat which has been in place for a period of time, and which has had its edges “worn down” from its ideal profile. These profiles are generally not based on any physical measurement of real rounded flat spots, but are simply mathematical approximations of what the creators believed a rounded wheel flat may look like.

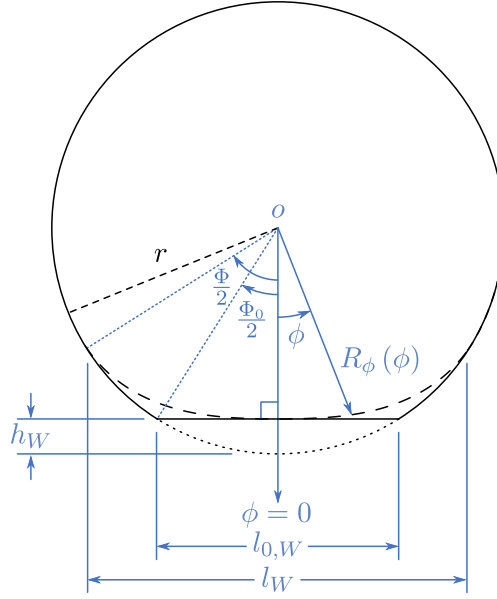


Figure 2.17: Geometry of an ideal and rounded wheel flat.

Such a rounded profile may be represented by [92]

$$\frac{\Phi}{2} = \sin^{-1} \left(\frac{l_W}{2r} \right) = \cos^{-1} \left(1 - \frac{h_W}{r} \right) \quad (2.49)$$

$$R_\phi(\phi) = \begin{cases} r & |\phi| > \left| \frac{\Phi}{2} \right| \\ r - \frac{h_W}{2} \left[1 + \cos \left(\frac{2\pi\phi}{\Phi} \right) \right] & |\phi| < \left| \frac{\Phi}{2} \right| \end{cases} \quad (2.50)$$

One may recall that the wheel radius r_x in the contact model is modified in order to keep agreement with Hertzian contact mechanics and account for the non-linear deflection of the contact springs. Consequently, in order to map the flat spot to the wheel of reduced radius r'_x , we shall reduce the flat height by the same amount.

$$h'_W = h_W \frac{r'_x}{r_x} \quad (2.51)$$

In order to allow for multiple wheel flats at arbitrary radial positions, Equations (2.48) and (2.50) may be modified by introducing θ , which is the position of the center of the wheel flat in the angular domain. Shown in Figure 2.18, the profile of a wheel with k ideal flat spots

is described by

$$R_{0,\phi}(\phi) = \begin{cases} r'_x & 0 < \phi < \theta_1 - \frac{\Phi_0}{2} \\ \frac{r'_x \cos \frac{\Phi_0}{2}}{\cos(\theta_1 - \phi)} & \theta_1 - \frac{\Phi_0}{2} \leq \phi \leq \theta_1 + \frac{\Phi_0}{2} \\ r'_x & \theta_1 + \frac{\Phi_0}{2} < \phi < \theta_2 - \frac{\Phi_0}{2} \\ \frac{r'_x \cos \frac{\Phi_0}{2}}{\cos(\theta_2 - \phi)} & \theta_2 - \frac{\Phi_0}{2} \leq \phi \leq \theta_2 + \frac{\Phi_0}{2} \\ \vdots & \vdots \\ r'_x & \theta_{k-1} + \frac{\Phi_0}{2} < \phi < \theta_k - \frac{\Phi_0}{2} \\ \frac{r'_x \cos \frac{\Phi_0}{2}}{\cos(\theta_k - \phi)} & \theta_k - \frac{\Phi_0}{2} \leq \phi \leq \theta_k + \frac{\Phi_0}{2} \\ r'_x & \theta_k + \frac{\Phi_0}{2} < \phi < 2\pi \end{cases} \quad (2.52)$$

and for k rounded flat spots

$$R_\phi(\phi) = \begin{cases} r'_x & 0 < \phi < \theta_1 - \frac{\Phi}{2} \\ r'_x - \frac{h'_W}{2} \left[1 + \cos \left(2\pi \frac{\theta_1 - \phi}{\Phi} \right) \right] & \theta_1 - \frac{\Phi}{2} \leq \phi \leq \theta_1 + \frac{\Phi}{2} \\ r'_x & \theta_1 + \frac{\Phi}{2} < \phi < \theta_2 - \frac{\Phi}{2} \\ r'_x - \frac{h'_W}{2} \left[1 + \cos \left(2\pi \frac{\theta_2 - \phi}{\Phi} \right) \right] & \theta_2 - \frac{\Phi}{2} \leq \phi \leq \theta_2 + \frac{\Phi}{2} \\ \vdots & \vdots \\ r'_x & \theta_{k-1} + \frac{\Phi}{2} < \phi < \theta_k - \frac{\Phi}{2} \\ r'_x - \frac{h'_W}{2} \left[1 + \cos \left(2\pi \frac{\theta_k - \phi}{\Phi} \right) \right] & \theta_k - \frac{\Phi}{2} \leq \phi \leq \theta_k + \frac{\Phi}{2} \\ r'_x & \theta_k + \frac{\Phi}{2} < \phi < 2\pi \end{cases} \quad (2.53)$$

where ϕ is now evaluated over the interval $[0, 2\pi]$.

The reduction of the wheel radius implicitly means that the the wheel will make a greater number of revolutions across the floor for a given rolling event than what occurs in reality. Normal this would not pose a problem. However, in the presence of wheel flats, this will result in an increase in the number of impacts over a given rolling distance (in the case of cylindrical wheel, the number of impacts will increase by a factor of two), implicitly changing the impact frequency of the wheel flats. This will indeed have an effect on the radiated sound level, and thus needs to be corrected for. This ensures that the correct number of flat spots are placed on the wheel profile even with a reduced radius.

$$\Delta\phi = \frac{\Delta x}{r_x} \quad (2.54)$$

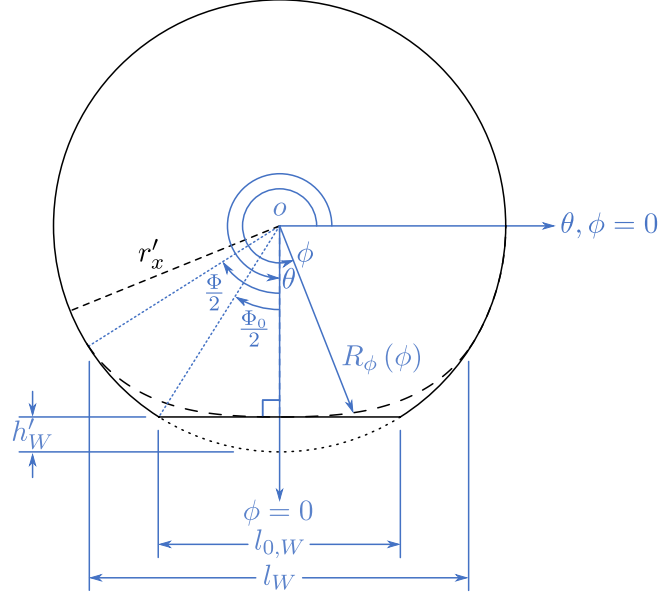


Figure 2.18: Geometry of the wheel flat with reduced wheel radius and flat height, located at an arbitrary angular position θ around the wheel.

The rolling noise model operates in Cartesian coordinates, thus the wheel profile ξ_W must be converted to the moving coordinate system (x', z') in order to be implemented into the model. To do this, the wheel profile is first converted to an intermediate rotating coordinate system (x'', z'') , as shown in Figure 2.19,

$$R_{x''}(x'') = R_\phi(\phi) \left[\cos \phi \hat{i}'' + \sin \phi \hat{k}'' \right] \quad (2.55)$$

where \hat{i}'' and \hat{k}'' are the unit vectors for the x'' and z'' directions respectively.

This coordinate system is offset by vertical distance r'_x and angle ψ from the local coordinate system (x', z')

$$\psi = \frac{x}{r'_x} \quad (2.56)$$

which is a function of the wheel's position in the global coordinate system. The wheel profile is converted to the local coordinate system (x', z') via

$$\xi_W(x, x') = R_{x''}(x'') \left[(\cos \psi + \sin \psi) \hat{i}' + (r'_x - \sin \psi + \cos \psi) \hat{k}' \right] \quad (2.57)$$

where \hat{i}' and \hat{k}' are the unit vectors for the x' and z' directions respectively. This is the formulation for ξ_W used in Equation (2.42) in the rolling noise model in the presence of wheel flats.

Care must be taken to evaluate Equation (2.57) over a sufficiently large interval so as to capture the full length of the flat spot when it is in full contact with the floor (e.g. as it is shown

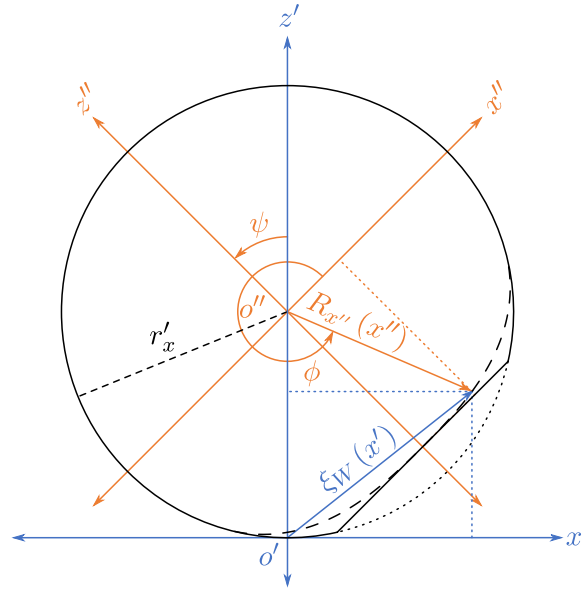


Figure 2.19: Intermediate rotating coordinate system (x'', z'') , offset by angle ψ and vertical distance r_x from the local coordinate system (x', z') . The origin is fixed to the wheel center and rotates with the wheel, such that the wheel profile in this coordinate system remains unchanged for all t in the global rolling event.

in Figure 2.17). In practice, this means that the interval $[-x', x']$ in the rolling noise model should be slightly longer than l_W when a wheel with flat spots is considered: much larger than the Hertzian contact length $2a$. Though the previous criteria still stands: the presence of any nonzero values on the edges of the stress matrix prior to integration of Equation (2.46) indicates that the limits are too small.

2.3.2 Floor joints

The formulation for the floor joints used in the rolling noise model is much simpler than the formulation for the wheel flats: consisting of only a step down, as shown in Figure 2.20. This may be added directly into the rolling model by defining the floor profile in the global coordinate system (x, z) as the joint depth $-h_F$ within $\pm l_F/2$ of the joint center, and zero everywhere else. The joint centers are known based on the total rolling distance L and the length of an individual floor tile L_t .

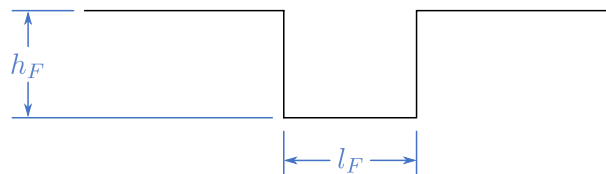


Figure 2.20: Geometry of a simple floor joint.

Just as the wheel flat height was multiplied by r'_x/r_x in order to correctly map the flat profile

to the reduced wheel radius, the same procedure may be applied to the floor joint. This ensures that the floor joint encountered by the wheel in the model is not relatively longer than that which occurs in reality. This is done using

$$l'_F = l_F \frac{r'_x}{r_x} \quad (2.58)$$

In the global coordinate system (x, z) , the profile of a floor with k joints, each having center position $x_{j,k}$, may be given by

$$\xi_F(x) = \begin{cases} 0 & x < x_{j,1} - \frac{l'_F}{2} \\ -h_F & x_{j,1} - \frac{l'_F}{2} \leq x \leq x_{j,1} + \frac{l'_F}{2} \\ 0 & x_{j,1} + \frac{l'_F}{2} < x < x_{j,2} - \frac{l'_F}{2} \\ -h_F & x_{j,2} - \frac{l'_F}{2} \leq x \leq x_{j,2} + \frac{l'_F}{2} \\ \vdots & \vdots \\ 0 & x_{j,k-1} + \frac{l'_F}{2} < x < x_{j,k} - \frac{l'_F}{2} \\ -h_F & x_{j,k} - \frac{l'_F}{2} \leq x \leq x_{j,k} + \frac{l'_F}{2} \\ 0 & x > x_{j,k} + \frac{l'_F}{2} \end{cases} \quad (2.59)$$

which is evaluated over the interval $[0, L]$. For each time t in the rolling model, the section of the floor profile ξ_F within the range $[-x', x']$ is used in Equation (2.42) in the presence of floor joints for calculating the interpenetration of the wheel and floor.

Care must again be taken to evaluate Equation (2.59) over a sufficiently large interval so as to capture the full length of the floor joint when it is centered directly at $x' = 0$. In practice, this means that the interval $[-x', x']$ in the rolling noise model should be slightly longer than l'_F when floor with joints is considered. In the event that a wheel with flat spots and jointed floor are both being considered, the interval would be the larger of the two lengths l'_W and l'_F .

2.4 Contact dimensionality

The contact model is designed to operate in three dimensions: allowing for varying roughness and contact stress in the longitudinal x and transverse y directions (the third dimension z being the magnitudes of the roughness and contact stress themselves). However, it may be reduced to two or one dimension if desired. This provides a shorter computation time at the expense of reduced accuracy. A two dimensional model (one which uses a contact line in the x dimension

only, rather than a contact area) accounts for neither transverse variations in the roughness profile, nor a transverse wheel radius. A one dimensional model (one which uses a single contact point between the wheel and floor) takes this a step further, removing the effect of the contact filter. Considering the speed at which the three dimensional model runs (the calculation takes less than two minutes to complete when using a spatial resolution of $55 \mu\text{m}$ and total rolling distance of 1 m on a laptop computer with an Intel i5-6300HQ 2.3 GHz processor and 16 GB of RAM), its use is not particularly burdensome, and therefore would likely be sufficient for most cases. Nevertheless, the ability to change the dimensionality of the model is included for the purpose of demonstrating their differences. This comparison will be made in Chapter 5.

2.4.1 Two-dimensional model

In order to reduce the model to two dimensions, a small number of minor changes need only be made to the equations used in Section 2.2. Equations (2.42) to (2.45), lose their dependency on y' , being now only functions of x and x' .

$$u_R(x, x') = u_0 - z_W(x) + \varsigma(x, x') - \xi_W(x, x') + \xi_F(x, x') \quad (2.60)$$

$$\varsigma(x, x') = \varsigma_F(x, x') - \varsigma_W(x, x') \quad (2.61)$$

$$\xi_W(x, x') = \frac{x'^2}{2r'_x} \quad (2.62)$$

$$\sigma_R(x, x') = \begin{cases} \sigma_0 \sqrt{\frac{u_R(x, x')}{u_0}} & u_R(x, x') > 0 \\ 0 & u_R(x, x') \leq 0 \end{cases} \quad (2.63)$$

In the presence of discrete irregularities, the wheel and floor profiles ξ_W and ξ_F remain unchanged, as they are already two-dimensional. Numerically, this results in a reduction from an $N \times M$ array to an $N \times 1$ vector, where M is the size of the discretized roughness profile in the y direction. Equation (2.46) becomes a single integral of the form

$$F_R(x) = 2b \int \sigma_R(x, x') dx' \quad (2.64)$$

Here the integration is now performed over a line rather than an area, and the resulting force per unit width multiplied by the Hertzian contact width $2b$ to get the full contact force.

2.4.2 One-dimensional model

In order to further reduce the model to one dimension, additional changes are required. In a 1D model, an equivalent spring foundation no longer exists between the wheel and the floor. Only a single contact spring exists, and its governing equations may be taken directly from those used in Hertzian contact theory.

As before, the interpenetration becomes one dimensional, depending now only on x . Equations (2.42), (2.43) and (2.45) become

$$u_R(x) = u_0 - z_W(x) + \varsigma(x) - \xi_W(x) + \xi_F(x) \quad (2.65)$$

$$\varsigma(x) = \varsigma_F(x) - \varsigma_W(x) \quad (2.66)$$

$$\sigma_R(x) = \begin{cases} \sigma_0 \sqrt{\frac{u_R(x)}{u_0}} & u_R(x) > 0 \\ 0 & u_R(x) \leq 0 \end{cases} \quad (2.67)$$

As the curvature of the wheel profile is no longer taken into account, Equation (2.44) becomes zero for all x in the absence of wheel flats.

The contact force is found for the ellipsoidal and cylindrical wheels by rearranging Equation (2.8) and Equation (2.20) respectively to solve for the load Q . Replacing the Hertzian interpenetration u_0 by u_R , one obtains for the ellipsoidal wheel

$$F_R(x) = \frac{2}{3} E' \Sigma \rho \left(\frac{2u_R(x)}{u^* \Sigma \rho} \right)^{3/2} \quad (2.68)$$

and for the cylindrical wheel

$$F_R(x) = \frac{\pi}{4} w E' u_R(x); \quad (2.69)$$

These formulations replace Equation (2.46) in the 1D case.

Due to their inherent two-dimensional nature, the calculated wheel and floor profiles for the discrete irregularities must still be initially calculated as described in Section 2.3 for each time t . In order to reduce them to one dimension for use in Equation (2.65), the center value of each vector is taken, as this corresponds to the profile value at the point of contact. This process is illustrated in Figure 2.21 for the case of a wheel flat. The 2D profile in the vicinity of contact $[-x', x']$ is emboldened, with the center point taken for the 1D case shown in red.

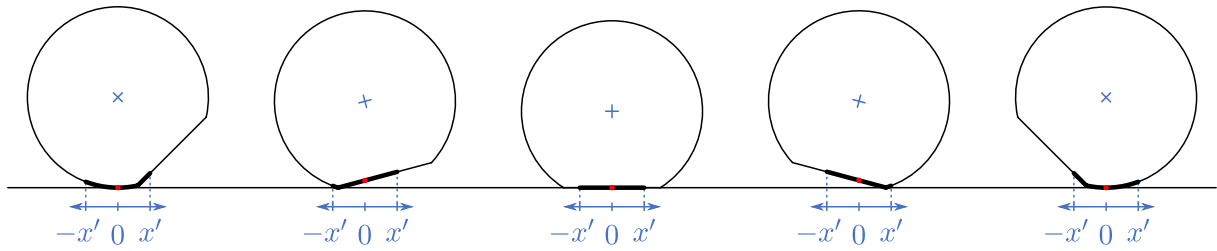


Figure 2.21: Example procedure of removing the center value of the wheel profile vector for use in the 1D model

2.5 Dynamic model

The dynamic model, shown in Figure 2.22, is based on a wheel modeled as a spring-mass-damper system resting on a rigid floor. The mass M is the mass of the trolley plus added load, divided by the total number of wheels on the trolley. For a vehicle with a built-in suspension system, the stiffness used in the dynamic model is straightforward to calculate: it is simply the stiffness of the suspension spring. However, most trolleys do not have suspension systems: they are made up of a wheel turning about a rigid axle. In such a scenario, the stiffness used in the dynamic model is instead the stiffness of the wheel itself. The stiffness K here is the equivalent elastic stiffness of the wheel, which is a function of the wheel's geometry and elastic properties. A presentation of how such a stiffness is calculated is given in Chapter 3. A small amount of damping C is added to be able to tune the model and avoid instabilities. The two balancing forces on the system are the mass load of the trolley from above and the contact force due to roughness F_R from below.

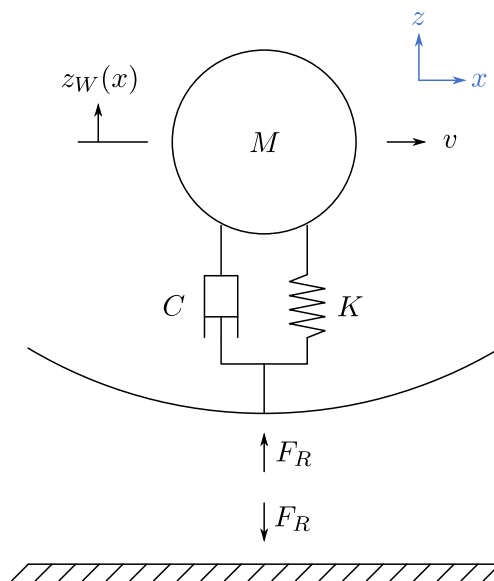


Figure 2.22: Dynamic model of the wheel/floor contact.

The wheel may be represented by its receptance $G_W(f)$ and impulse response function $g_W(t)$.

$$G_W(f) = \frac{1}{-(2\pi f)^2 M + i(2\pi f)C + K} \quad (2.70)$$

$$\tilde{g}_W(t) = \mathcal{F}^{-1}(G_W(f)) \quad (2.71)$$

where \mathcal{F}^{-1} represents the inverse Fourier transform.

Figure 2.23 shows the wheel response for an exemplary trolley having total mass $M = 17$ kg, wheel stiffness $K = 953$ kN/m, and damping factor $C = 2.3$ kNm. The impulse response is assumed to have decayed to zero when the peak amplitude drops below 1% of the amplitude of the initial peak. In the developed rolling noise model, the viscous damping ratio was set to $\zeta = 0.4$. The viscous damping ratio and viscous damping factor are related via

$$\zeta = \frac{C}{2\sqrt{KM}} \quad (2.72)$$

This, in combination with the wheel stiffness, are included to ensure stability in the model (the model would otherwise have a tendency to go unstable when encountering moderate roughness asperities).

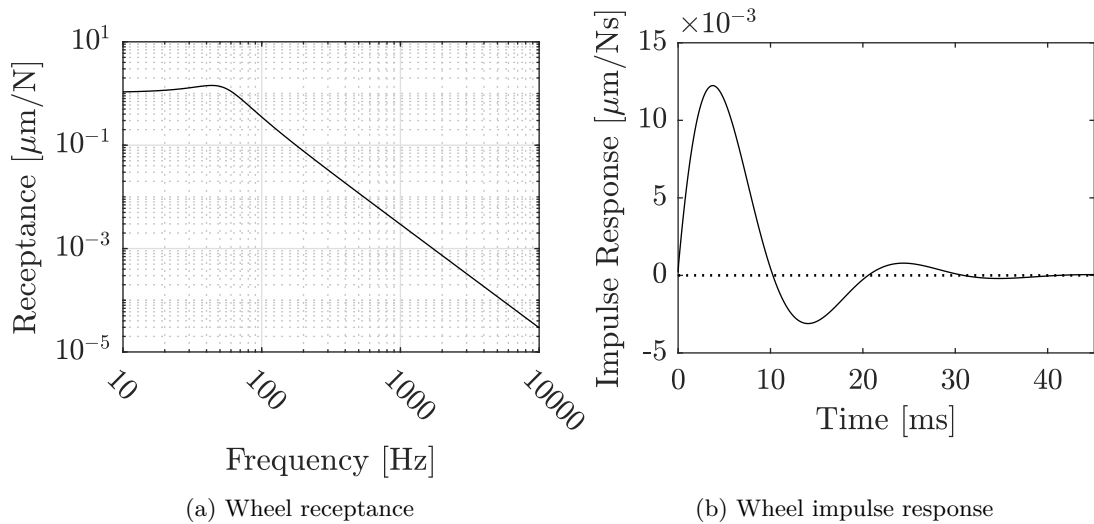


Figure 2.23: Example wheel response for the case of $M = 17$ kg, wheel stiffness $K = 953$ kN/m, and damping factor $C = 2.3$ kNm.

The equivalent spring foundation in the contact model calculates the deflection of the wheel and floor in the area of contact. This Hertzian evaluation does not account for the macro-level movement of the wheel (i.e. its center position z_W), thus it must be calculated separately and

added in. To do so at a given x , a discretized form of the wheel Green's function is used [94]

$$\begin{aligned} g_W(1) &= \frac{1}{2}\Delta t \cdot \tilde{g}_W(0) \\ g_W(n) &= \Delta t \cdot \tilde{g}_W(n-1) \quad \text{for } n = 2, 3, \dots, N-1 \\ g_W(N) &= \frac{1}{2}\Delta t \cdot \tilde{g}_W([N-1]\Delta t) \end{aligned} \quad (2.73)$$

where the discretization is defined by

$$t(n) = (n-1)\Delta t \quad \text{for } n = 1, 2, \dots, N \quad (2.74)$$

The change in vertical wheel position at step n is calculated using the contact force and the discretized wheel Green's function.

$$\Delta z_W(n) = g_W(1)(F_R(n) - Q) \quad (2.75)$$

The vertical position of the wheel from the start of the rolling event up to step n is calculated as a convolution of the wheel Green's function and the contact force history (represented by the symbol $*$).

$$z_W^{old}(0 \rightarrow n) = g_W * (F_R(0 \rightarrow n) - Q) \quad (2.76)$$

The convolution is defined by

$$\tilde{g}_W(t) * (F_R(0 \rightarrow t) - Q) = \int_0^t (F_R(\tau) - Q) \tilde{g}_W(t - \tau) d\tau \quad (2.77)$$

Or the discretized version

$$g_W(n) * (F_R(0 \rightarrow n) - Q) = \sum_{k=1}^K (F_R(k) - Q) g_W(n - k + 1) \quad (2.78)$$

Thus the vertical wheel position at step n is

$$z_W(n) = \Delta z_W(n) + z_W^{old}(n) \quad (2.79)$$

This results in an interdependence of Equations (2.42), (2.45), (2.46) and (2.79). To alleviate this, the vertical wheel position at step n is used to calculate the total interpenetration profile at step $n+1$. For the initial step $n=0$, a vertical wheel position of $z_W(0) = 0$ is assumed.

The use of discretized Green's functions provides a more accurate estimation over another popular method of numerically solving differential equations: the finite difference time domain

method (FDTD). While the latter estimates the wheel position at time $t + \Delta t$ based on the wheel movement at time t , the former estimates the wheel position at time $t + \Delta t$ based on the wheel movement at time $0 \rightarrow t$.

Using this procedure, the wheel/floor interpenetration, contact force, and resulting wheel movement may be calculated for each position. At the end of the rolling event, the entire response history of the wheel and the floor is known.

2.6 Propagation model

Once the contact force is known for the entire rolling event, the only step left is to convert this force to a radiated sound power. This is done through use of the transfer matrix method (TMM).

2.6.1 Transfer matrix method

The TMM is used in the field of acoustics to calculate the propagation of an acoustic wave through a multi-layered structure. It does so by reducing the problem from three dimensions down to two, allowing for variation (and consequently, sound propagation) in two spatial directions (compression and bending) rather than all three, as shown in Figure 2.24. This simplifies the problem without compromising accuracy for scenarios where the propagation media are more or less homogeneous in one of the three dimensions.

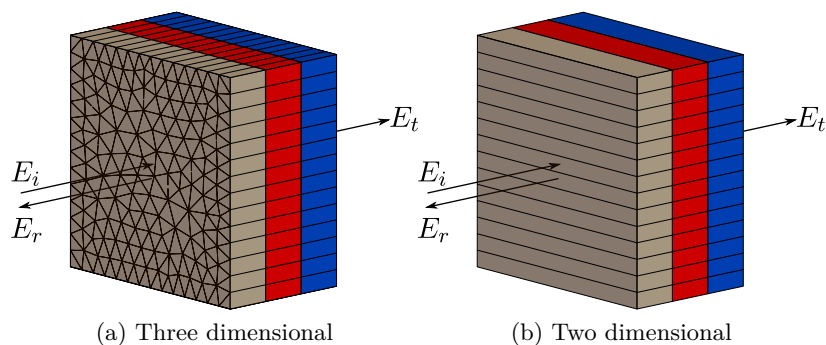


Figure 2.24: Reduction in dimensionality of the transfer matrix method. Knowing the incident energy E_i , the reflected energy E_r and transmitted energy E_t may be calculated for the multi-layered system.

While examples of the use of the TMM in acoustics are plentiful for the case of airborne sound (e.g. [95, 96, 80, 97]), examples of the use of the TMM for structure-borne sound are much more sparse. A ground breaking work was done by Rhazi and Atalla to develop formulae which use the TMM for mechanical excitation [81]. The main limit here is the hypothesis of

infinite lateral dimensions. The finite dimension is taken into account using the finite TMM (fTMM) [98, 99], which corrects for the radiation of the plate. However, the modal behavior of the floor is still not taken into account. These formulae have been adapted for use in this rolling noise model.

2.6.2 Application in the rolling noise model

The method used to calculate the propagation into the room below uses a wave-based approach. The floor is assumed to be infinite in the x and y dimensions, separating two semi-infinite fluids (those of the two rooms), and excited by a point load. Both this load and the floor's response are assumed to be harmonic, which means they may be represented by an infinite series of plane waves using the spatial Fourier integral transform [81]. This method is often viewed as a simple multiplication of four-poles (2×2) matrices but is, in fact, a resolution of all the waves propagating through planar layers. The number of waves propagating through a layer depends on its nature: fluid (1), isotropic solid (2), isotropic poro-elastic (3), orthotropic solid (3) or orthotropic poro-elastic type (4). The appropriate coupling conditions are implemented at the interfaces. The assembly can be done according to [80] or with the recent improvements by [100]. After assembly, the multi-layer can be represented for each plane wave, by a relationship between the pressure p and velocity v on the emission and reception sides

$$\begin{pmatrix} p \\ v \end{pmatrix}_{x=0} = \mathbf{T} \begin{pmatrix} p \\ v \end{pmatrix}_{x=h} \quad (2.80)$$

where h is the thickness of the layer. Here \mathbf{T} is the layer's transfer matrix, which is a function of the continuity equations between layers, as well as the properties of wave propagation within the layer [95]. The multi-layer system is worked through one layer at a time to obtain the global transfer matrix. This is used to obtain the impedance of the multi-layer floor $Z_{s\text{TMM}}$.

The propagation model operates in the frequency domain to convert the previously calculated contact force and wheel response to a radiated sound power. This is done using [81]

$$\Pi_{rad} = \frac{1}{8\pi^2} \int_0^{2\pi} \int_0^\infty \left| \frac{F_{\text{flex}}(f)}{F_{\text{ref}}} \right|^2 \frac{Z_0 \sigma_{\text{finite}}}{|Z_{s\text{TMM}}(f) + Z_{B,\infty}(f)|^2} k_r dk_r d\phi \quad (2.81)$$

where F_{flex} is the injected force, F_{ref} is a reference force of 1 Newton, Z_0 is the acoustical impedance of air, $Z_{B,\infty}$ is the radiation impedance, and σ_{finite} is the "finite size" radiation efficiency. The TMM is used to calculate the impedance of the multilayered floor $Z_{s\text{TMM}}$ for each wavenumber couple (k_x, k_y) or (k_r, ϕ) . In essence, the radiated power of an infinite plate is

calculated, then spatially windowed to achieve the effective radiation of a plate with size equal to the actual floor.

The finite size radiation efficiency is given by

$$\sigma_{\text{finite}} = \frac{Re(Z_R)}{Z_0 S} \quad (2.82)$$

where S is the surface of the multi-layer, and Z_R is the radiation impedance considering the finite size. The wave approach does not yield good results for the sound radiated by a planar structure (e.g. a multi-layer floor) under mechanical excitation below the floor's critical frequency [101]. In reality, the finite area of the floor will play a role in its radiation efficiency, thus the need for a correction term. This technique is sometimes referred to as *spatial windowing*. Here the TMM is extended to take into account the floor's size, as well and corrections for the radiation efficiency at low frequencies.

The injected flexural force F_{flex} depends on the blocked force, which is taken to be the contact force $F_R(f)$. This takes into account the impedance of both the wheel and floor, using

$$|F_{\text{flex}}(f)|^2 = \left| \frac{1}{1 + Re[Y_{\text{sTMM}}(f)] Z_{\text{exc}}(f)} \right|^2 |F_R(f)|^2 \quad (2.83)$$

Where Z_{exc} is the wheel impedance, estimated as the blocked force divided by the time derivative of the vertical wheel position, and $Y_{\text{sTMM}} = 1/Z_{\text{sTMM}}$ the floor admittance.

Only the real part of the floor admittance is used in Equation (2.83) to calculate the injected flexural force due to rolling noise. While it is not fully understood why, it has been found that use of only the real part of the floor admittance yields results which are more in line with reality when modeling indoor rolling noise. It is believed that considering the imaginary part in the injected force would involve taking into account the dissipation twice for this scenario. As such, omitting the imaginary term in Equation (2.83) yields a more accurate estimation of the injected flexural force due to rolling contact.

As with the wheel impedance, the floor impedance may theoretically be calculated by dividing the injected force by the floor velocity. However, as the injected force is calculated from the contact force found in the contact model, it may appear that it cannot be known ahead of time. To alleviate this problem, the floor impedance is pre-calculated using an injected point force of 1 N. This essentially yields a unit floor impedance, which when used in Equation (2.83) in conjugation with the blocked force, will yield the correct injected flexural force.

In the above equations, the flexural force is the estimation of the forcing which is occurring by the wheel into the floor with the response of the floor taken into account. If it were theoretically

possible to place a force transducer between the wheel and the floor in such a way which did not modify the measured force, F_{flex} is what it would measure[†].

The radiated power calculated in Equation (2.81) is the sound power in the reception room below: a measure of the acoustic energy per unit time emitted by the rolling trolley. However, Equation (2.81) was calculated using a sphere of unit surface area, so it is also equal to sound intensity (the sound intensity of a source being its sound power per unit area). The normalized sound pressure level in the reception room is thus calculated using [3],

$$L_n = 10\log_{10}(\Pi_{\text{rad}}) + 10\log_{10}\left(\frac{4S}{A_0\Pi_{\text{ref}}}\right) \quad (2.84)$$

where $A_0 = 10 \text{ m}^2$ is the reference equivalent absorption area and $\Pi_{\text{ref}} = 10^{-12} \text{ W}$ is the reference sound pressure.

This normalized sound pressure takes into account the absorption of the reception room. It provides a direct link for comparison with impact sound, which is computed using the same metric.

2.7 Preliminary model

As stated previously, the rolling noise model presented in this chapter builds upon a preliminary model which had been developed as a pilot study in years prior [6]. At the time that the preliminary model was created, no measured roughness profiles were available. Instead artificial profiles were used. These were first represented as a sinusoidal waveform whose period was based on the perimeter of the wheel

$$\varsigma_W(x) = A\sin(r_x x) \quad (2.85)$$

where A is an arbitrary roughness amplitude, generally chosen to be on the same order of magnitude as the static Hertzian interpenetration u_0 . This may seem reasonable at first, as a given point on the wheel encounters the contact area once per revolution as the wheel rolls across the floor. However, representing this behavior as a sinusoid is incorrect, as the relative distance between the wheel and the floor does not follow a sinusoidal path. A roughness profile represented as a sinusoid is actually akin to a sinusoidal profile which has been wrapped around the wheel. The profile appears sinusoidal in a radial reference frame (i.e. the the viewpoint of an observer who is rotating around the perimeter of the wheel, constantly facing the the wheel center), but not in a Cartesian one (i.e. the viewpoint of an observer who is moving linearly in

[†]Such a measurement is not physically possible. The presence of the force transducer would change the contact condition and thus change the resulting force between the two bodies.

the direction of rolling, constantly facing the lateral face of the wheel).

The preliminary model, which operates in the time domain, is also based on Hertzian contact theory. The model treats the contact between the wheel and the floor as two cylinders in contact, with the radius of the floor tending to infinity. In Section 2.1, the interpenetration of the bodies in the absence of roughness was shown to be

$$Q = \frac{\pi}{4} E' w u_0 \quad (2.86)$$

where the apparent Young's modulus is computed similarly as in the improved model using Equation (2.3). The preliminary model assumes that the interpenetration u_0 may be summed with the roughness profile ς to achieve the contact force due to roughness:

$$F_R(x) = \frac{\pi}{4} E' w [\varsigma(x) - z_W(x)] \quad (2.87)$$

Similarly to how two relative points on the wheel and floor are assumed to be out of contact if the contact stress at that location is calculated to be negative in the improved model, the total contact force in the preliminary model was set to zero any time a negative value was calculated. Also, here ς is only a function of the total rolling distance x , as the model operates in only one dimension. The relative roughness profile is the floor roughness minus the wheel roughness. If the interpenetration is less than zero then the two bodies are assumed to be out of contact.

The rolling distance and elapsed time are once again coupled via the trolley speed v

$$x = vt \quad (2.88)$$

No wheel radius reduction is used in the preliminary model, so the contact area half-length is calculated directly as

$$a = \sqrt{r_x u_0} \quad (2.89)$$

At each moment in time t , the contact force is calculated as a function of the static wheel properties and the relative roughness between the wheel and the floor.

Figure 2.25 shows a schematic of the dynamic model used in the preliminary rolling noise model. Similarly to the improved model, the wheel is represented as a simple spring-mass-damper system. The floor is considered rigid. As opposed to the improved model, which uses a Green's function to represent the response of the wheel, the preliminary model calculates the

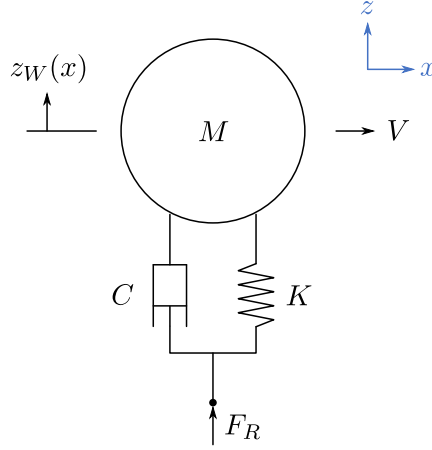


Figure 2.25: Dynamic model used in the preliminary rolling noise model

wheel response directly from its equation of motion using the FDTD method.

$$\left(M + \frac{M_W}{3}\right) \ddot{z}_W(t) + C\dot{z}_W(t) + Kz_W(t) = F_R(t) \quad (2.90)$$

The preliminary model used the mass of the trolley (including added load) plus one third of the wheel mass. Typically the mass of the spring is not taken into account. However, if it is considered (as is done here), only one third of its mass has an effect.

At each moment in time t , the equation of motion is solved for the vertical acceleration \ddot{z}_W by using the contact force at time t to find the vertical wheel acceleration at time $t + \Delta t$. The resulting vertical wheel velocity and displacement are then found with the FDTD method using

$$\dot{z}_W(t + \Delta t) = \dot{z}_W(t) + \ddot{z}_W(t)\Delta t \quad (2.91)$$

$$z_W(t + \Delta t) = z_W(t) + \dot{z}_W(t)\Delta t \quad (2.92)$$

At the end of the rolling event, the contact force is known for all t .

In order to estimate the wheel stiffness, the preliminary model uses the elastic stiffness of an equivalent beam. This beam, being a rectangular prism with height $r_x - u_0$ and cross sectional area $2aw$, yields the equivalent wheel stiffness as

$$K = \frac{2awE_1}{(1 - \nu_1^2)(r_x - u_0)} \quad (2.93)$$

As will be shown in Chapter 3, this representation of a wheel as an equivalent beam is not entirely accurate. It has a tendency to under-estimate the actual wheel stiffness, particularly for very small contact area half-length values.

Similar to the improved model, the sound propagation is derived from the contact force by

converting to the frequency domain and using the TMM to calculate the radiated sound power level in the reception room with Equation (2.81). However, as opposed to using the real part of the floor impedance to obtain the injected flexural force (which is done in the improved model as it has been found to yield more accurate results), both real and complex parts of the floor impedance are used in the preliminary model [81].

$$|F_{\text{flex}}|^2 = \left| \frac{Z_{\text{sTMM}}}{Z_{\text{sTMM}} + Z_{\text{exc}}} \right|^2 |F_i|^2 \quad (2.94)$$

2.7.1 Key differences between the preliminary and improved models

A major difference between the preliminary and improved model is the expansion to three dimensions via the use of a Winkler bedding. Not only does this allow for variations in the roughness profile in the transverse direction to be taken into account, it also provides a natural way of implementing the effect of the contact filter. As introduced in Chapter 1, the contact between the wheel and floor will naturally filter out the components of the relative roughness profile whose wavelengths are shorter than the dimensions of the contact area. If the contact area has no physical size (as is the case with a one-dimensional model), no filtering can occur. This results in an overestimation of the contact force spectrum (and consequently the radiated sound level) at higher frequencies. Additionally, while the improved model uses pre-calculated Green's functions to estimate the wheel response, the preliminary model uses the more simplified FDTD method. The use of Green's functions has been found to yield a dynamic system which is less susceptible to small changes in the values of the wheel stiffness K and damping factor C .

Another major difference is the estimation of the wheel stiffness. The preliminary model uses an equivalent beam to estimate the wheel stiffness, which could be inaccurate. For the improved model, a parametric study was conducted using a series of finite element models in order to generate polynomial expressions which yield accurate estimations of the wheel stiffness for a variety of wheel geometries. This topic is expanded upon at length in Chapter 3.

As the preliminary model operates in one dimension and does not account for the curvature of the wheel, discrete irregularities must be included in the roughness profile rather than being implemented separately through the terms ξ_W and ξ_F . The preliminary model does not account for the shifting of the contact area relative to the wheel center, resulting in an inaccurate estimation of the wheel behavior when rolling through a wheel flat or floor joint. The improved model, on the other hand, is able to more accurately estimate the impact force from discrete irregularities. This greatly improves the applicability of the rolling noise model, as the presence of a wheel flat or floor joint can overwhelm any effect that the small scale roughness would have

on the radiated sound level. Thus, being able to fully capture its effect is of high importance.

2.8 Conclusion

This chapter presents the methodology used in the rolling noise model to calculate the interaction force between the wheel and floor as a result of their Hertzian contact. A bed of non-linear, point-reacting independent springs is placed between the two bodies, which may be used to calculate the contact stress profile by discretizing the area of contact and calculating the spring force at each discrete point. Using this technique, both the detailed stress profile and the total contact force are able to be accurately computed. Equivalent radii are used in the place of the true wheel radii in order to retain agreement with Hertzian contact theory, correcting for the non-linear nature of the springs. When roughness is added to the interface between the two bodies, the actual size of the contact area changes. Depending on the position of the peaks and troughs in the roughness profile, sections of the two bodies in the vicinity of contact may come out of contact with one another in locations where they otherwise would have been touching in the absence of roughness. What is important to observe is that, with this method, no matter what the conditions (wheel geometry, wheel/floor material properties, or applied load, relative roughness profile), whenever the roughness profile is removed, the contact area dimensions predicted by the bed of springs method return to once again being in agreement with those predicted by the Hertzian equations.

IN Chapter 2, the wheel is modeled as a spring-mass-damper system, with the spring stiffness representing the bulk deformation of the wheel itself. Calculating the value of such stiffness is no trivial task, as the wheel is a complex shape whose geometry changes as it deforms. For this reason, a parametric study using a finite element (FE) approach was conducted in order to develop a method for estimating this wheel stiffness. By solving FE models for multiple wheel geometries and material configurations, trends may be determined which guide how each parameter influences the overall stiffness. The development of this parametric study and resulting wheel stiffness abacus are presented in this chapter. Part of this work has been published in [102].

3.1 Background

The scenario of a delivery trolley rolling on a floor inside a commercial space presents unique challenges for dynamic modeling which are not present in automotive tire/road or train wheel/rail rolling contact. One of these differences is that of the relative stiffnesses of the two contacting bodies. In the dynamic models of train wheel/rail rolling contact, the wheel and rail themselves are generally considered mechanically rigid, due to their metallic construction and thus extremely high stiffnesses [11]. Instead, the train bogie suspension and railroad sleepers are modeled as dynamic systems which respond to the contact force as their input [12, 75, 40, 39]. In the dynamic models used in automotive tire/road rolling contact, the road is generally considered mechanically rigid, its vibration contributing minimally to the propagation of sound [46, 8, 103, 57]. Calculation of the complex motion of the tire is instead given priority. In a dynamic model used for indoor trolley wheel/floor rolling contact, neither the wheel nor the floor may be considered mechanically rigid. They both move and deform on a bulk level in response to the forces in the area of contact between them, due to their relatively low elasticities.

For a vehicle with a built-in suspension system, the stiffness used in the equivalent spring-mass-damper system of the dynamic model is straightforward to calculate: it is simply the stiffness of the suspension spring. However, most trolleys do not have suspension systems: they are made up of a wheel turning about a rigid axle. In such a scenario, the stiffness used in the dynamic model is instead the stiffness of the wheel itself. Considering the vast range of sizes and materials that trolley wheels come in, this presents a challenge for incorporation into a sound prediction model that wishes to be widely applicable for a range of indoor rolling scenarios.

One option may be to build an FE model for a given wheel, but this is costly, as it requires a new FE model to be run for every single unique geometry/material composition. Additionally, a further problem exists in the fact that the geometry of the wheel in a rolling event is dependent on the motion of the wheel itself. As was explained in greater detail in Chapter 2, according to Hertzian contact theory the size of the contact area formed between a cylindrical wheel and a flat floor is a function of the wheel radius, wheel width, the compressional load on the wheel, and the elastic properties (Young’s modulus and Poisson’s ratio) of the wheel and floor [15]. In a static scenario, the load is constant, and the size of the contact area may be easily calculated. In a dynamic scenario, the load changes continuously as the motions of the wheel and floor respond to their relative interaction. Consequently, the “flat spot” formed on the bottom of the wheel by the contact area (and thus the effective geometry of the wheel itself) also changes continuously. If FE modeling were to be used in the calculation of each unique wheel’s stiffness, either the dynamic phenomenon of the wheel geometry would need to be neglected, or an FE model would need to be run at each individual time step in the dynamic model. Here we seek to avoid this problem by development of an alternative method.

A second option would be to run a series of FE models in the form of a parametric study, extract trends in the data, and develop a system for estimating the stiffness of any geometry or material composition, without the need to solve a new FE model each time. In this chapter, a straightforward method is proposed to characterize the compressional stiffness of a cylindrical wheel in contact with a flat surface, including how it changes with time throughout the course of the rolling event. This is inspired by the methodology used by Sim and Kim to estimate the elastic properties of viscoelastic materials [104]. Polynomial relations are derived from high order FE models of a cylindrical wheel under static vertical compression, linking the wheel/axle radii ratio and contact area half-length. A series of one dimensional polynomials or a single two dimensional polynomial may be found which completely describe how a cylindrical wheel’s stiffness changes as a function of its changing geometry. Such polynomial functions, or alternatively a classical lookup table, may be incorporated into an indoor rolling noise model, allowing

the wheel stiffness to be calculated throughout the rolling event. This allows for a more precise estimation of the movement of the wheel, leading to increased accuracy in sound predictions.

3.2 FE model development

Before a parametric study could begin, it was first necessary to determine the type of shape to be used in the FE model. Three basic designs were investigated, which are shown in Figure 3.1: a half cylinder, and half cylinder with an axle cut-out, and a full cylinder with an axle cut-out. To investigate the influence of the flat spot which develops on the bottom of the wheel in the area of contact due to local Hertzian deformation when the wheel and floor are brought into contact under load, a flat area was added to the bottom of the shapes as well. The convention of half-length is adopted from Hertzian contact theory, and simply refers to half the length of the contact area in the direction of rolling (the full contact area having length $2a$).

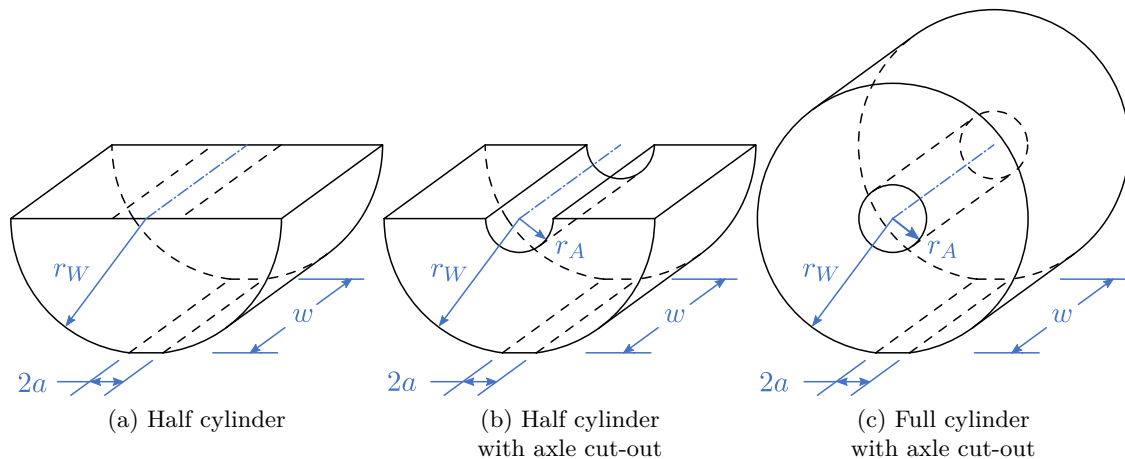


Figure 3.1: The three shapes used in the initial phase of the parametric study.

With this formulation, the geometry of the FE model remains a function of only four parameters: the wheel radius r_W , axle radius r_A , wheel width w , and contact area half-length a . Additionally, Young's modulus E and Poisson's ratio ν of the wheel material, as well as the input displacement u_0 , were also included. In Hertzian contact, u_0 is the interpenetration between the wheel and the floor. This value is represented here as the vertical distance that the wheel axle is pushed downward. Thus by dividing the resulting calculated force on the surface of the axle in the FE model by this input displacement, the effective stiffness of the wheel may be estimated.

3.2.1 Mesh definition

The geometries were constructed using pythonOCC [105]. Initial meshing was done using Tetgen [106]. Table 3.1 shows the switches that were used for specifying the mesh definition. As the geometry built with pythonOCC defines the shape in terms of its boundaries, boundary conformity was used to build the mesh thereafter. A minimum allowable radius-edge ratio of 1.4 was used to ensure no sharp-edged tetrahedra were generated. The mesh densities of the FE models were defined based on the width of the wheel, having a maximum edge length of $w/7$. Finally, region attributes were added to allow for applying constraints of different surfaces in the mesh solving process.

Table 3.1: Switches used with Tetgen for FE mesh generation

Name	Description	Switch	Value
Boundary conformity	Reads a boundary description of a piece-wise linear complex for mesh generation.	-p	-
Quality mesh generation	Defines a minimum allowable radius-edge ratio.	-q	1.4
Adaptive mesh generation	Imposes a maximum volume constraint on all tetrahedra.	-a	$V = \frac{1}{3} \left(\frac{w}{7}\right)^3$
Assigning region attributes	Adds an integer number attribute to each tetrahedron to define the region it belongs to.	-AA	-

Finally, the mesh files were modified to include surface labels. This was done to allow FreeFem++ [107], which was used for solving the FE model, to know upon which surface nodes to impose the appropriate boundary conditions: fixed on the bottom flat spot, displacement on the axle surface, and free elsewhere.

Figure 3.2 shows a schematic of the boundary conditions imposed on the meshed bodies. To solve the FE model, the flat contact area surface on the bottom of the wheel was fixed in place. A uniform displacement in the downward vertical direction was imposed on the axle surface, simulating the mass of the trolley which is borne by the wheel under load. A glued condition between the axle and the wheel was assumed for the purpose of the FE calculations. Thus, for the half cylinder with axle cut-out, the displacement was applied on the half-cylindrical axle surface. For the full cylinder with axle cut-out, the displacement was applied on the full cylindrical axle surface. For the half cylinder, the displacement was applied on the nodes located in a flat rectangular surface on the top of the half cylinder, with width equal to the cylinder width and length equal to what would be the axle diameter if it were there.

In experimenting with different application conditions for the input displacement on the FE meshes, it was found that applying the displacement on only the bottom half of the full cylinder

with axle cut out (similar to the two half cylinders) resulted in behavior which deviated from that which is predicted by theory. When the displacement is applied only on the bottom half of the axle for the full cylinder, high wheel/axle radii ratios can cause the top half of the wheel to buckle, deforming the shape of the axle cutout to that of a flattened cylinder. Applying the input displacement on the full axle surface alleviated this problem, as the axle surface would no longer buckle at high wheel/axle radii ratio. Thus it was chosen to be the application condition for the parametric study.

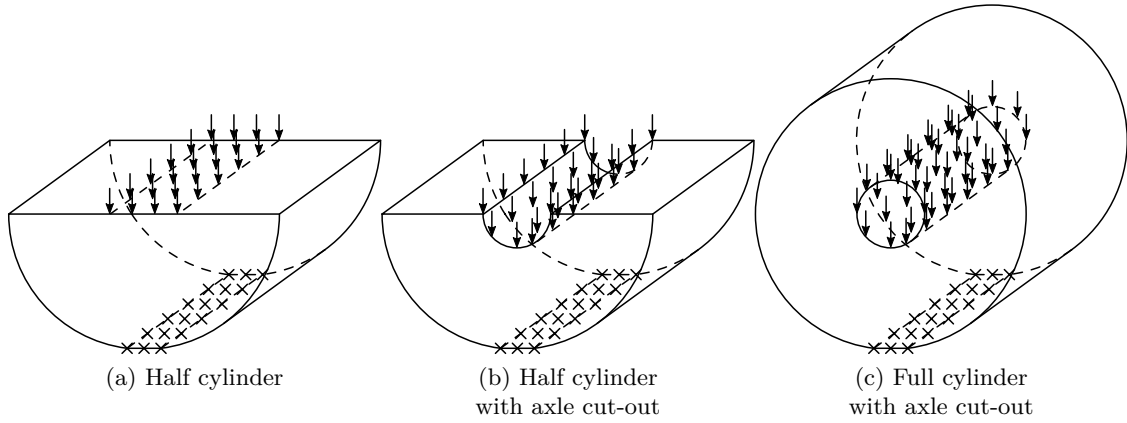


Figure 3.2: The boundary conditions imposed on the three meshed bodies. The movement of the contact area on the bottom of the wheel was fixed (\times) while a uniform displacement was applied to the axle surface in the downward vertical direction (\downarrow). All other surfaces were given a free boundary condition.

FreeFem++ calculates the force on each mesh element under the given restrictions in response to the applied displacement. From there, the equivalent stiffness of the wheel is calculated by dividing the force on the axle surface by the displacement of the axle surface

$$K_{\text{eq}} = \left(\frac{F_z}{U_z} \right)_{\text{axle surface}} \quad (3.1)$$

where the vertical normal stress σ_{zz} and vertical displacement u_z are integrated across the whole axle surface to find its overall force.

$$F_z = \int \sigma_{zz} dA \quad (3.2)$$

$$U_z = \frac{1}{A} \int u_z dA \quad (3.3)$$

A Windows 10 PC with an AMD Ryden Threadripper 1950X 16-Core 3.40 GHz processor and 64 GB of RAM was used for all calculations. The FE model was solved in FreeFem++ with the UMFPACK direct solver, using arbitrarily chosen values (though within the range of typical

indoor wheel sizes) for the wheel properties for all three geometries, then their calculation times and resulting stiffnesses compared. Table 3.2 shows the parameters chosen.

Table 3.2: Summary of the parameters used for the three comparative FE models

Parameter	Variable	Unit	Value
Wheel radius	r_{wheel}	(mm)	50
Axle radius	r_{axle}	(mm)	6.5
Wheel Width	w	(mm)	35
Contact area half-length	a	(mm)	1
Young's modulus	E	(MPa)	200
Poisson's ratio	ν	(-)	0.3
Input displacement	u_0	(mm)	0.01

A note of clarification is worth mentioning here. In the FE model, both the contact area half-length a and the input displacement u_0 are defined independently. In reality, the two are linked to one another by the Hertzian equation

$$a = \sqrt{r_W u_0} \quad (3.4)$$

Thus, for the FE model, the values for a and u_0 were chosen such that they are both in agreement with Equation (3.4). In practice, that meant choosing a value for a and then calculating the necessary input displacement to apply which, in a real scenario, would result in the aforementioned contact area half-length. A value of $a = 1$ mm was chosen as it is considered reasonable for a wheel of the given parameters: the load which would need to be applied to achieve such a value is neither improbably large nor improbably small. This results in an input displacement of $u_0 = 0.01$ mm.

Table 3.3 shows the results of the three FE calculations. Going into the study, the hypothesis was that time could be saved by using the half cylinder geometries, as the smaller number of nodes (roughly half that of the full cylinder) would result in much shorter calculation times while still yielding similar results. Because the nodes in the top half of the full cylinder geometry exist outside the field of compression formed between the axle and the flat spot on the bottom, the theory was that their presence would not contribute in a significant way to the calculated stiffness. That is, they would be in tension, effectively providing no resistance against the input displacement, rather than being in compression and resisting the downward displacement of the axle. However, this was not found to be the case. The calculated stiffness of the full cylinder with axle cut-out was roughly 55% that of the half cylinder and 30% that of the half cylinder with axle cut-out. Additionally, while there was a 40%–60% reduction in calculation time between the half-cylinder geometries and the full cylinder, even the calculation time of the full cylinder

was still not prohibitively high. Thus, the full cylinder with axle cut-out was chosen as the geometry to be used for the parametric study.

Table 3.3: Summary of results comparing the FE models for the three geometries

Geometry	Stiffness (kN/m)	Calculation Time (s)
Half cylinder	1803	30
Half cylinder with axle cut-out	3037	46
Full cylinder with axle cut-out	989	76

3.2.2 Re-meshing

Finite element meshing programs will typically automatically increase the number of nodes near sharp geometric features, such as corners or edges, in order to ensure the shape of the final mesh remains the same as the shape of the input geometry, within a margin of error. However, the issue with the geometry in question here, particularly the flat spot on the bottom of the wheel, is that it is not the type of situation that would automatically trigger the meshing process to increase the node density in the vicinity. Since the angle between the flat spot and the curved wheel is obtuse (and nearly 180° for extremely small contact area half-lengths), the meshing process will typically only give the contact area a length of a single tetrahedron. This can be overridden by specifying a maximum edge length that is smaller than this distance. However, this would also result in an unnecessarily fine mesh across the rest of the body's surface.

To alleviate this problem, the meshing process used in the preliminary runs was modified to specifically add extra nodes in the vicinity of the contact area. The mesh was first generated as normal, then re-meshed, this time defining the maximum tetrahedron size based on the contact area half-length (rather than the wheel width) for the tetrahedra in the vicinity of the contact area. This ensured the contact area had at least 4 nodes along its length. Additionally, an increased optimization level of 9 was specified (the default level of 2 was used in the first meshing process) to ensure good mesh quality after the re-meshing process. A summary of the switches used during re-meshing is shown in Table 3.4, and an example of the FE model before and after re-meshing is shown in Figure 3.3. Depending on the geometry, mesh sizes ranged between 1.0×10^4 and 5.3×10^4 nodes, having degrees of freedom between 2.1×10^6 and 1.1×10^7 .

Table 3.4: Switches used with Tetgen for FE re-meshing

Name	Description	Switch	Value
Tetrahedral mesh reconstruction	Reconstructs an existing tetrahedral mesh	-r	-
Mesh sizing function	Applies a user-defined mesh sizing function which specifies the desired edge lengths for each node in the final mesh	-m	-
Quality mesh generation	Defines a minimum allowable radius-edge ratio.	-q	1.4
Mesh optimization	Specifies a mesh optimization level.	-O	9

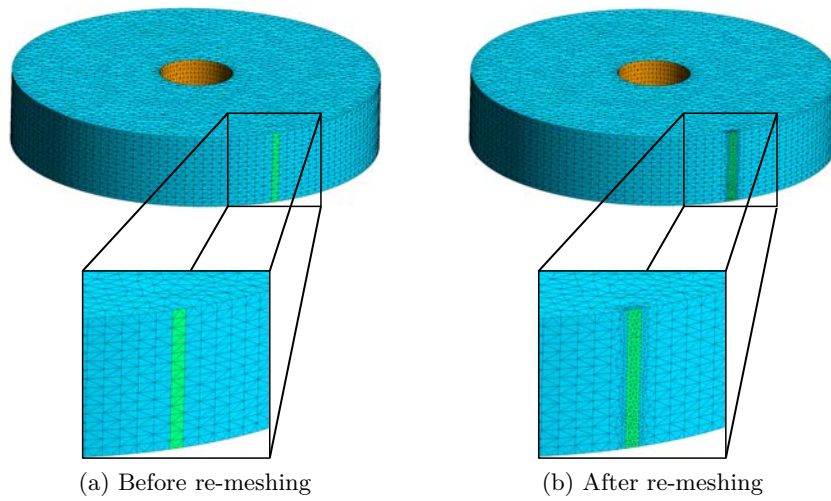


Figure 3.3: Example FE model before and after the re-meshing process. Extra nodes were added in the vicinity of the contact area.

3.3 Parametric study

A parametric study was conducted in order to identify the degree of influence that each parameter has on the wheel stiffness. A series of FE models were run for cylindrical wheels of various geometries and material compositions, from which trends were identified.

3.3.1 Investigated variables

For each of the variables chosen to be investigated, a range was selected which encompasses the full scope of any trolley wheel which may be reasonably expected to be found in the real world. Table 3.5 summarizes the range of values that were chosen for each variable. The values for the input displacement u_0 , wheel radius r_W , and wheel width w were all regularly spaced. The values for Young's modulus E were logarithmically spaced (base 10), in order to cover a

wider range of values. The remaining variables (Poisson’s ratio ν , relative axle radius r_A/r_W , and relative contact area half-length a/r_W) were mostly linearly spaced, but also had additional points added to the beginning or end of their respective range in order to get a finer spacing in those areas. A full list of the exact values used may be found in Appendix C. The axle radius, wheel width, and contact area half-length are expressed as ratios: relative to the wheel radius. This nomenclature allows for ease of comparison due to the use of dimensionless quantities. Due to limitations with the meshing software, relative contact area half-length values below 0.003 were not able to be reliably meshed.

Table 3.5: Range of values used for each parameter

Parameter	Variable	Unit	Value
Input displacement	u_0	(mm)	0.1 – 10
Young’s modulus	E	(GPa)	0.01 – 200
Poisson’s ratio	ν	(-)	0 – 0.495
Wheel radius	r_W	(mm)	10 – 100
Relative axle radius	r_A/r_W	(-)	0.05 – 0.95
Relative wheel width	w/r_W	(-)	0.1 – 1
Relative contact area half-length	a/r_W	(-)	0.003 – 0.1

In lieu of running a calculation for every possible permutation of the values of all six parameters (which would have resulted in over four billion individual runs), each parameter was given its own investigation. Thus for a given parameter, all the others were fixed at a constant value, and the stiffness calculated for each value of the parameter in question. For example, for the runs investigating the effect of the wheel width, all other parameters remained constant, and only the wheel width was varied from one run to another. The only exception to this was Poisson’s ratio, which was investigated for all eleven of its values across all parameter investigations. Table 3.6 shows the constant values chosen for the parametric study. For a given parameter with N possible values, $11N$ runs were conducted. This resulted in 1 342 runs overall.

Table 3.6: Values used for the default variables

Variable	Unit	Value
u_0	(mm)	0.4
E	(GPa)	0.2
r_W	(mm)	50
r_A/r_W	(-)	0.2
w/r_W	(-)	0.4
a/r_W	(-)	0.02

3.4 Parametric study results

After all the desired conditions were solved, the results were analyzed, and the calculated stiffness of the wheel plotted against each parameter in question. The results of the FE simulations reveal patterns in how the wheel stiffness is influenced by each of the various parameters: some expected, some not. For each plot, default parameters (those which are identical for all data points) are shown in the bottom right hand corner. Points having the same x coordinate are for varying values of Poisson's ratio (0–0.495). Schematics of the extreme wheel geometries on each plot are shown for reference: drawn to scale with respect to one another.

The parameters having a linear influence on the wheel stiffness, shown in Figure 3.4, are Young's modulus and the wheel width. For a given FE model, a change in either of these values results in a proportional change to the wheel stiffness. Since Young's modulus of a material is essentially a measure of that material's intrinsic stiffness independent of shape, logic follows that it would be linearly proportional to the actual wheel stiffness. Similarly, increasing the width of the wheel essentially acts like adding springs in parallel, thus increasing the stiffness in a linear fashion.

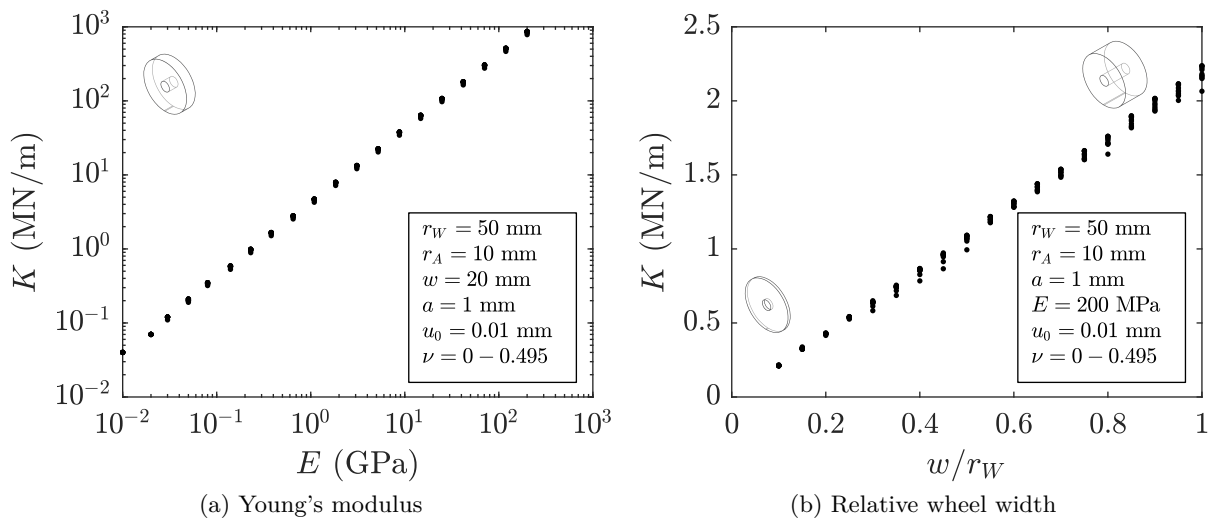


Figure 3.4: Results of the parametric study. Points having the same x coordinate (but a different y coordinate) are for varying values of Poisson's ratio ν . Schematics of the extreme wheel geometries are shown for reference (drawn to scale with respect to one another).

The two parameters exhibiting unique relationships with the wheel stiffness, shown in Figure 3.5, are the axle radius and the contact area half-length. Neither may be described by a simple expression, and will thus become the topic of further investigation in Section 3.5. For the axle radius: as the ratio between the axle radius and the wheel radius approaches unity, the stiffness approaches infinity. Since the axle is considered rigid in the FE models, as the volume

of wheel material approaches zero, the compressed wheel gets closer and closer to exhibiting that of a rigid connection: having infinite stiffness. For the contact area half-length: as the size of the contact area approaches zero, the stiffness begins to drop off exponentially. While not able to be directly calculated, it is believed that with even smaller contact areas, the stiffness would continue to fall towards zero at an ever increasing rate.

Looking on the right side of Figure 3.5(a), it may not appear at first glance to be a reasonable geometry for a trolley wheel. After all, an axle that makes up 96% of the volume of the wheel/axle assembly may hardly be considered realistic. Indeed, this is *not* the type of scenario being exemplified by these high axle/wheel radii ratios. They are instead exemplifying the scenario of a two-piece construction wheel, where a hard wheel core is wrapped in a softer outer layer. Such a situation is relatively common for indoor trolley wheels. Here the core is sufficiently stiffer than the softer outer layer that it may be considered mechanically rigid. Thus, for the purpose of the FE models, the inner wheel core and axle may be considered one-in-the-same. Schematics of these kinds of wheels are shown in Figure 3.6. Here, wheels (a) and (c) are being exhibited by the FE models, *not* wheel (b).

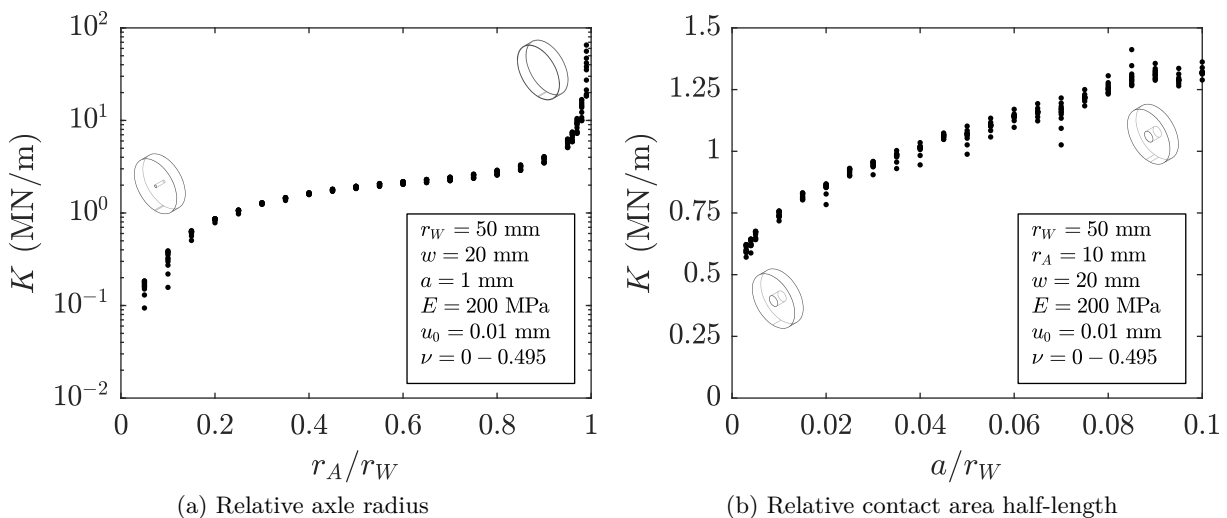


Figure 3.5: Results of the parametric study. Points having the same x coordinate (but a different y coordinate) are for varying values of Poisson's ratio ν . Schematics of the extreme wheel geometries are shown for reference (drawn to scale with respect to one another).

Figure 3.7 shows two parameters which have no influence on the wheel stiffness: the wheel radius and input displacement. The first comes with a caveat, as the ratio between the axle radius and the wheel radius does indeed have a strong effect on the wheel stiffness. However, when this ratio is held constant, increasing the wheel radius does not result in any change in wheel stiffness. So perhaps it is better to say that the wheel radius *does* have an effect on the stiffness, but that this effect can be fully described by the changing axle/wheel radii ratio. In

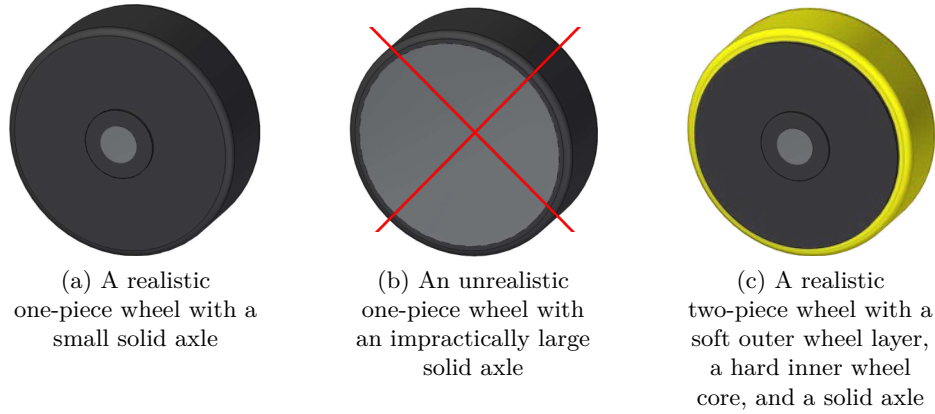


Figure 3.6: Three example wheels. In the scenario of a high wheel/axle ratio, wheel (c) is being exhibited, not wheel (b).

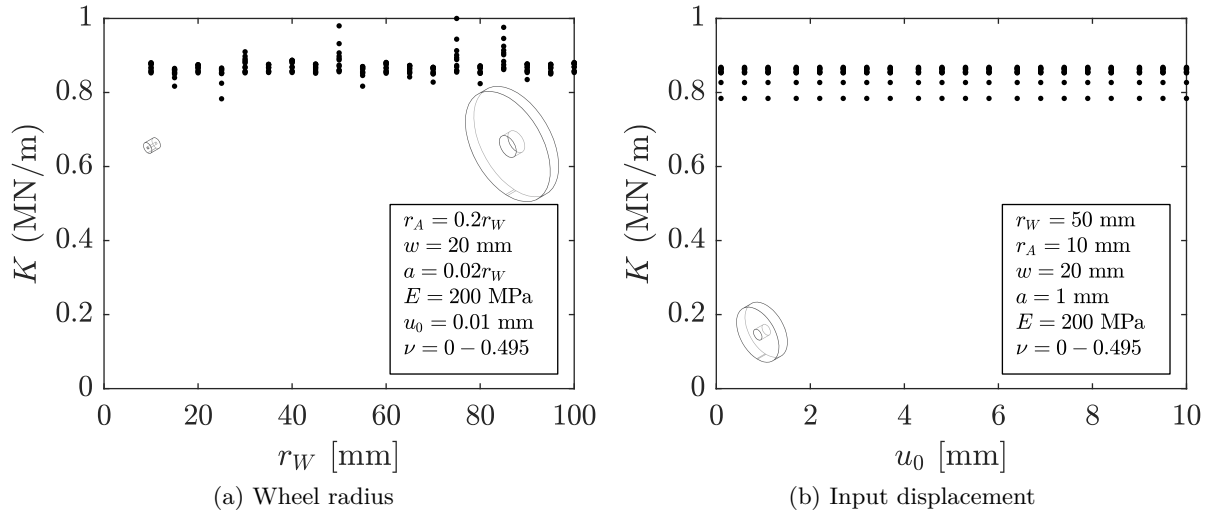


Figure 3.7: Results of the parametric study. Points having the same x coordinate (but a different y coordinate) are for varying values of Poisson's ratio ν . Schematics of the extreme wheel geometries are shown for reference (drawn to scale with respect to one another).

regards to input displacement, the lack of dependence is in accordance with the use of a linear material in the FE models, where increasing compression does not result in increased stiffness.

Finally, there is one more parameter which deserves discussion: Poisson's ratio. An elastic solid of uniform cylindrical or rectangular prism shape, compressed in the axial direction, is known to have a high dependency on Poisson's ratio [104]. However, looking across all six plots in Figures 3.4, 3.5 and 3.7, a change in Poisson's ratio results in essentially no change in stiffness (all else held constant). The points which exhibit the largest deviation are all for the highest values of Poisson's ratio (above 0.49), and they do not occur in a consistent fashion (i.e. not always an increase and not always a decrease). In essence, the stiffness is remaining nearly unchanged for all values of Poisson's ratio all the way up until around 0.49, where only then the modeling instability that exists when approaching $\nu = 0.5$ starts to have a minor effect. This

near lack of dependence on Poisson’s ratio was certainly unexpected. In fact, when loaded in the vertical direction, it is the effect of the wheel shape which dominates. The cylindrical form allows the wheel material to “move out of the way” under compression into the horn-shaped free spaces between the wheel and the floor. A visualization of this is shown in Figure 3.8. The shape of the geometry itself is linking the movement of the two transverse directions to that of the longitudinal direction in a way that negates any influence that the Poisson effect may have.

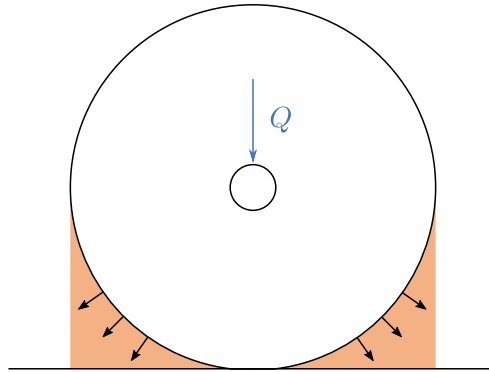


Figure 3.8: Diagram of the wheel compression under an arbitrary load Q . The movement of the wheel into the areas formed between the wheel and the floor overrides any effect a change in Poisson’s ratio may have on the stiffness.

3.5 Generation of the abacus

To generate the abacus, a second series of FE models were run for the two chosen non-linearly dependent variables: the axle radius and the contact area half-length (both normalized by the wheel radius). Nineteen values between 0.05 and 0.98 were chosen for the axle/wheel radii ratio r_A/r_W . Eighteen values between 0.003 and 0.1 were chosen for the relative contact area half-length a/r_W . Constant values of $w/r_W = 0.4$, $E = 1$ Pa, $\nu = 0.3$, and $u_0 = 0.1$ mm were chosen for the wheel width, Young’s modulus, Poisson’s ratio, and vertical displacement respectively. Though it should be noted that, due to their relationship with the wheel stiffness (linear for w and E , and independent for ν and u_0), their choice is arbitrary.

3.5.1 Normalized wheel stiffness

Figure 3.9 shows the results of the second series of FE calculations. Equation (3.5) was first used to find the normalized wheel stiffness by dividing by Young’s modulus and the wheel width.

$$K_{\text{norm}} = \frac{K}{wE} \quad (3.5)$$

The normalized stiffness was then plotted as a function of the axle/wheel radii ratio and relative contact area half-length. The data is plotted with a logarithmic z -scale (base 10) in order to visualize how the stiffness changes for both low and high values of r_A/r_W . As the axle/wheel radii ratio grows, so does the influence of the size of the contact area on the stiffness. For ratios 0–0.8, there is a $1.5\times$ factor in the change in normalized stiffness. Above 0.8 the stiffness increases exponentially, up to a factor of nearly $16\times$.

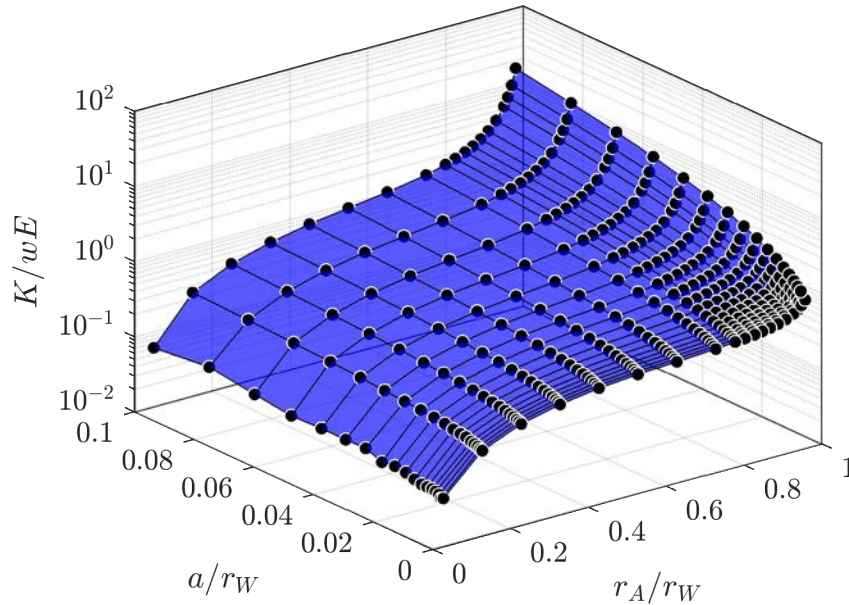


Figure 3.9: Normalized wheel stiffness as a function of axle/wheel radii ratio and relative contact area half-length. Plotted on a logarithmic z -scale (base 10).

Three methods have been developed for implementing the data from the abacus into a rolling noise model: a lookup table, a series of one-dimensional polynomials, and a single two-dimensional polynomial. They are described in detail in the following sections. The exact values of the abacus are given in Appendix C.

3.5.2 Lookup table

A straightforward method of implementing the wheel stiffness abacus is to use the data points in Figure 3.9 as a lookup table. The normalized wheel stiffness for a wheel of any reasonable size (i.e. for $0.05 \leq r_A/r_W \leq 1$ and $0.003 \leq a/r_W \leq 0.1$) may be calculated via two-dimensional linear interpolation of the data points. This encompasses nearly every type of cylindrical solid wheel which would be expected to be found on an indoor trolley.

3.5.3 Series of one-dimensional polynomials

In lieu of using a lookup table, polynomial relations may instead be generated to characterize the relationship between the influencing parameters and the wheel stiffness. This has the benefit of simplifying the implementation procedure into a rolling noise model. To do so, univariate 9th order exponential polynomials following the form of Equation (3.6) were first fitted to the data in Figure 3.9 with r_A/r_W as the dependent variable: giving one polynomial P for each relative contact area half-length

$$P_{a/r_W}(r_A/r_W) = \frac{K}{wE} = \exp\left(\sum_{i=1}^9 C_i^{a/r_W} (r_A/r_W)^i\right) \quad (3.6)$$

where C_i^{a/r_W} is the i^{th} polynomial coefficient. This was chosen as it is the highest order polynomial for which a close fit is observed. Equation (3.6) produces polynomials having coefficient of determination $R^2 > 0.998$ for all a/r_W . Higher order polynomials began to exhibit unstable behavior (large peaks and troughs started to emerge between the known data points) and no longer accurately mapped to the data sets. These polynomials characterize how the normalized stiffness changes with varying axle/wheel radii ratio for a given contact area half-length.

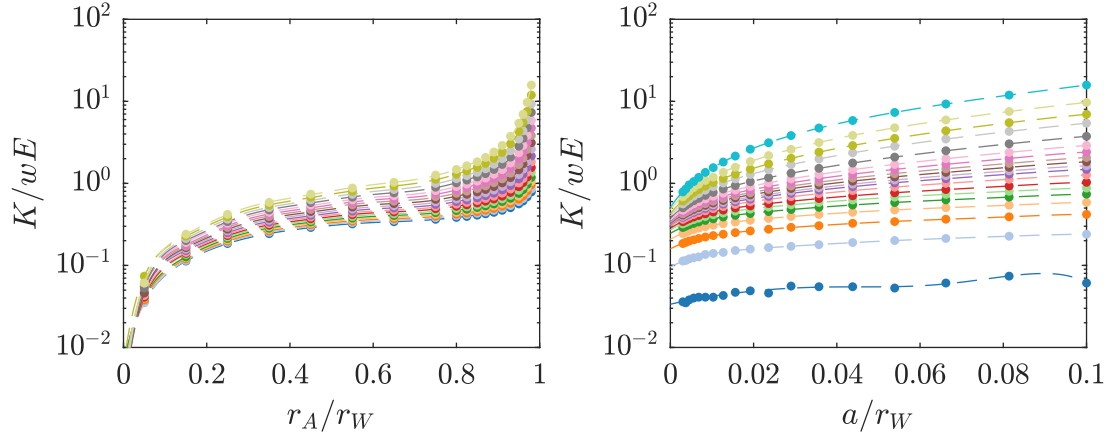
A second series of univariate 6th order polynomials were then fitted to data with a/r_W as the dependent variable: giving one polynomial for each axle/wheel radii ratio. These polynomials, following the form of Equation (3.7), characterize how the normalized stiffness changes with varying contact area half-length for a given axle/wheel radii ratio.

$$P_{r_A/r_W}(a/r_W) = \frac{K}{wE} = \sum_{i=1}^6 C_i^{r_A/r_W} (a/r_W)^i \quad (3.7)$$

Figure 3.10 shows the generated one-dimensional polynomials for both varying axle/wheel radii ratio and contact area half-length. Together, they may be used to calculate the stiffness of a wheel of nearly any geometry. The procedure for how this is done in practice is shown in Section 3.6.

3.5.4 Two-dimensional polynomial

The third characterization method developed involves fitting a single two-dimensional polynomial to the entire data set. This greatly simplifies the implementation process by reducing the entire calculation procedure to a single step. A homogeneous bivariate exponential polynomial



(a) 9th order 1D polynomials for normalized wheel stiffness as a function of axle/wheel radii ratio. (b) 6th order 1D polynomials for normalized wheel stiffness as a function of contact area half-length.

Figure 3.10: 1D polynomials. Plotted on a logarithmic y -scale (base 10).

of the form shown in Equation (3.8) was fit to the data points.

$$P(f, g) = \frac{K}{wE} = \exp \left[\sum_{N=0}^5 \left(\sum_{i=1}^N C_{i, N-i} f^i g^{N-i} \right) \right] \quad (3.8)$$

For ease of display, the expressions for axle/wheel radii ratio and contact area half-length have been replaced by functions f and g , such that

$$f = r_A/r_W \quad (3.9)$$

$$g = a/r_W \quad (3.10)$$

The fitting process was done in MATLAB using the function *fit*, which is part of the Curve Fitting Toolbox. This function fits a curve or surface to a data set (in this case a surface) using a non-linear least squares method. As this method works by iteratively fitting a function to the data, a maximum number of 10 000 function evaluations and a maximum number of 100 000 iterations were imposed.

The resulting 2D polynomial is given by Equation (3.11). Note that the coefficients have been rounded here for ease of display. Exact coefficient values are given in Appendix C.

$$\begin{aligned}
P(f, g) = \frac{K}{wE} = \exp \left(95.4f^5 + 280.4f^4g - 1\,319.1f^3g^2 + 4\,004.4f^2g^3 - 9\,965.2fg^4 \right. \\
+ 1\,052\,707.6g^5 - 249.3f^4 - 352.0f^3g + 1\,109.0f^2g^2 + 75.9fg^3 \\
- 305\,716.2g^4 + 246.5f^3 + 123.1f^2g - 454.0fg^2 + 33\,012.8g^3 \\
\left. - 117.0f^2 + 7.3fg - 1\,625.3g^2 + 28.7f + 42.6g - 4.6 \right) \quad (3.11)
\end{aligned}$$

The 2D polynomial is plotted with the FE model results in Figure 3.11. It has an extremely good fit, with a coefficient of determination of $R^2 = 0.996$. This polynomial fully characterizes how the normalized stiffness changes with nearly any geometry.

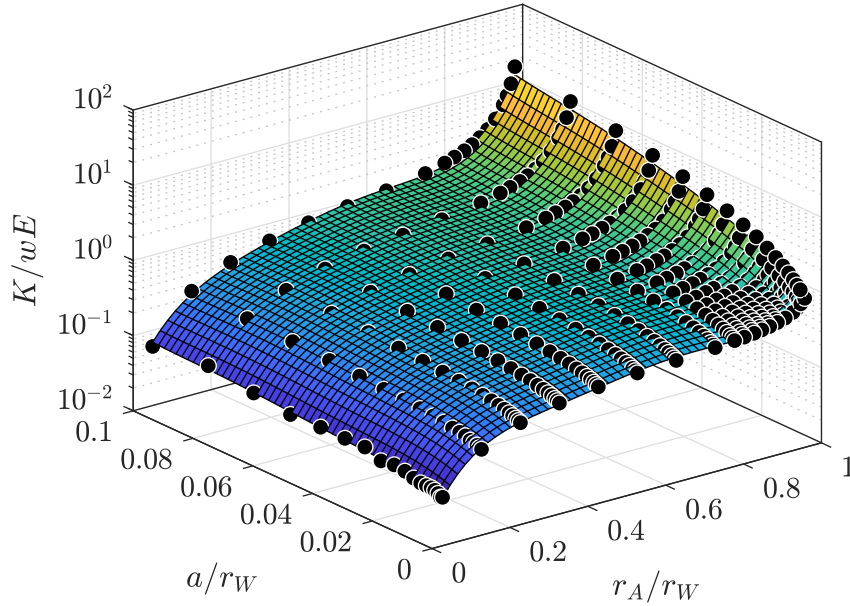


Figure 3.11: 5th order homogeneous bivariate polynomial for normalized wheel stiffness as a function of both axle/wheel radii ratio and relative contact area half-length. Plotted on a logarithmic z -scale (base 10).

3.6 Comparison of the three methods

In order to compare the three methods, as well as demonstrate how each may be used to calculate the stiffness of a given wheel, an example characterization is performed. Let us take two wheels with properties given in Table 3.7.

Table 3.7: Example wheel parameters

Variable	Unit	Wheel 1	Wheel 2
E	(MPa)	760	105
ν	(-)	0.3	0.25
r_W	(mm)	42	64
r_A	(mm)	12.5	57.4
w	(mm)	25	45

For a cylindrical wheel, the size of the contact area according to Hertzian contact theory is given by Equation (2.19). For the example, we will use a concrete floor ($E_{\text{floor}} = 3.3$ GPa, $\nu_{\text{floor}} = 0.2$). If the wheel is put under a static load of $Q = 200$ N, Equation (2.19) estimates a contact area half-length of $a_1 = 0.80$ mm and $a_2 = 1.83$ mm for each wheel. Thus the dimensionless geometric quantities necessary to calculate the stiffnesses are $r_A/r_{W_1} = 0.300$ and $a/r_{W_1} = 0.020$ for wheel 1 and $r_A/r_{W_2} = 0.897$ and $a/r_{W_2} = 0.030$ for wheel 2.

Using the lookup table, the procedure is straightforward. Plugging the dimensionless geometric quantities into the lookup table and interpolating yields normalized wheel stiffnesses of $K_{\text{norm},1} = 0.3058$ and $K_{\text{norm},2} = 1.050$. Using Equation (3.5), we obtain the true estimated wheel stiffnesses: $K_1 = 5\,811$ kN/m and $K_2 = 4\,960$ kN/m.

Figure 3.12 demonstrates the process of building the 1D polynomials which are specific to our two example wheels. Each of the first series of 9th order 1D polynomials are evaluated for the given axle/wheel radii ratio. This is represented by the vertical line drawn at the given r_A/r_W values. This provides a new set of data points, to which the second 6th order polynomials can now be fit. As the process of fitting a one dimensional polynomial is simpler than that of a two-dimensional polynomial, it was done using the MATLAB function *polyfit*. This uses the method of least squares to fit a curve to a given data set.

Equations (3.12) and (3.13) show the final 1D polynomials for each example wheel. Note that the coefficients have been rounded here for ease of display.

$$P_1(a/r_{W_1}) = \left(\frac{K}{wE}\right)_1 = -5\,506\,860(a/r_W)^6 + 1\,766\,278(a/r_W)^5 - 222\,310(a/r_W)^4 + 14\,130(a/r_W)^3 - 498(a/r_W)^2 + 12(a/r_W) + 0.2 \quad (3.12)$$

$$P_2(a/r_{W_2}) = \left(\frac{K}{wE}\right)_2 = -13\,397\,078(a/r_W)^6 + 4\,314\,984(a/r_W)^5 - 545\,898(a/r_W)^4 + 34\,857(a/r_W)^3 - 1\,177(a/r_W)^2 + 39(a/r_W) + 0.3 \quad (3.13)$$

Plugging the relative contact area half-lengths into the above equations yields normalized wheel stiffnesses of $K_{\text{norm},1} = 0.3134$ and $K_{\text{norm},2} = 1.030$. Using Equation (3.5), we obtain the true estimated wheel stiffnesses: $K_1 = 5\,954$ kN/m and $K_2 = 4\,867$ kN/m.

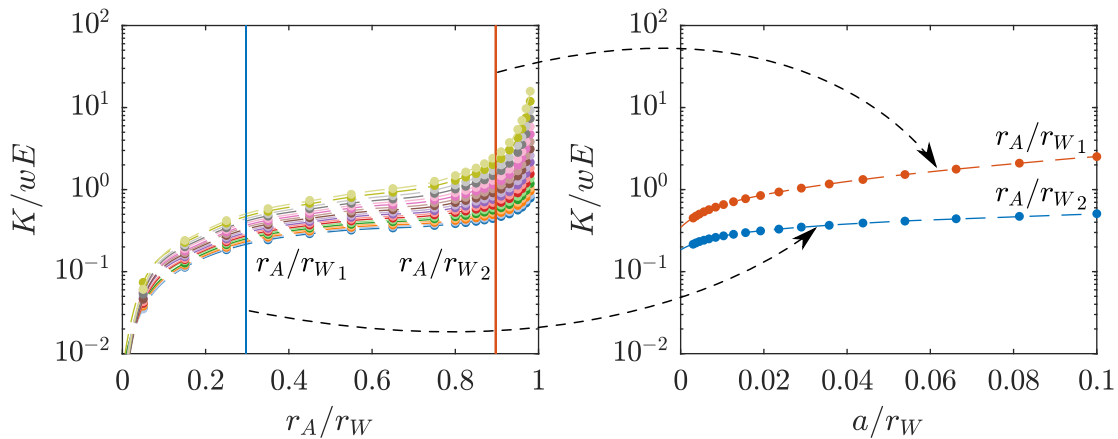


Figure 3.12: Example of the 1D polynomial characterization procedure for $r_A/r_{W_1} = 0.300$ and $r_A/r_{W_2} = 0.897$. Plotted on a logarithmic y -scale (base 10).

The process for using the 2D polynomial is also very straightforward. All that is needed is to solve Equation (3.11) for the given dimensionless geometric quantities. Doing so yields normalized wheel stiffnesses of $K_{\text{norm},1} = 0.3049$ and $K_{\text{norm},2} = 1.089$. Using Equation (3.5), we obtain the true estimated wheel stiffnesses: $K_1 = 5\,793$ kN/m and $K_2 = 5\,146$ kN/m.

Table 3.8 summarizes the results of the three methods. For wheel 1, there is a 2.4% difference between the results of the lookup table and 1D polynomials, a 0.3% difference between the lookup table and 2D polynomial, and a 2.7% difference between the 1D polynomials and 2D polynomial. For wheel 2, there is a 1.9% difference between the results of the lookup table and 1D polynomials, a 3.7% difference between the lookup table and 2D polynomial, and a 5.6% difference between the 1D polynomials and 2D polynomial. All three methods provide reasonably close results to one another.

Table 3.8: Summary of Example Results

Method	Wheel 1		Wheel 2	
	K_{norm} (-)	K (kN/m)	K_{norm} (-)	K (kN/m)
Lookup table	0.3058	5 811	1.050	4 960
1D polynomials	0.3134	5 954	1.030	4 867
2D polynomial	0.3049	5 793	1.089	5 146

The major difference in methods becomes apparent when comparing their calculation times. As an example, a simple MATLAB script was written to perform a loop of 10 000 iterations using each calculation method. Using the same computer that was used for the parametric study (described in Section 3.2.1), the 1D polynomials and the 2D polynomial methods each finished in less than 0.1 second. The lookup table method, however, took more than 9 seconds to complete. When running a Python version of the same script, the difference is even more pronounced (0.1, 0.1, and 40.4 seconds for the 1D polynomials, 2D polynomial, and lookup methods, respectively). In a time domain model implementation where the wheel stiffness is recalculated at each moment in time throughout the course of the simulation, implementation of one of the two polynomial methods would provide significant improvement over the lookup method in terms of computational efficiency. This is discussed further in Section 3.8.1.

3.7 Comparison with analytical methods

The results of the previous FE-based estimations were compared with two analytical methods to identify whether these simpler analytical solutions could be used in their place as an accurate representation of the wheel stiffness. Two analytical methods were investigated: an equivalent beam and an equivalent trapezoidal prism.

3.7.1 Equivalent beam

In the rolling noise model presented in [6], the stiffness used in the dynamic model is taken as that of an equivalent beam, whose cross-section is defined by the contact area, and whose height is defined by the distance between the floor and the axle (the presence of an axle is ignored in [6], but is included here for comparison). This may be given by

$$K_{\text{beam}} = \frac{2awE}{\sqrt{r_W^2 - a^2} - r_A} \quad (3.14)$$

This may be rearranged to have the same form as Equation (3.5) in order to achieve the normalized equivalent beam stiffness.

$$K_{\text{beam,norm}} = \frac{K_{\text{beam}}}{wE} = \frac{2(a/r_W)}{\sqrt{1 - (a/r_W)^2} - (r_A/r_W)} \quad (3.15)$$

Figure 3.13 shows the estimated wheel stiffness found using the wheel abacus and Equation (3.15), as well as the percent error of the beam curve with respect to the wheel abacus. When compared to the wheel abacus, the approximation given by the equivalent beam is not very accurate. Calculating the equivalent beam stiffnesses for the wheel geometries used in this work yields a data-set with relatively poor fit to the wheel abacus: having an average percent error of 62% (median 67%), with some values as high as 247% for extremely small axle/wheel radii ratios. The standard deviation of the percent error is 10%.

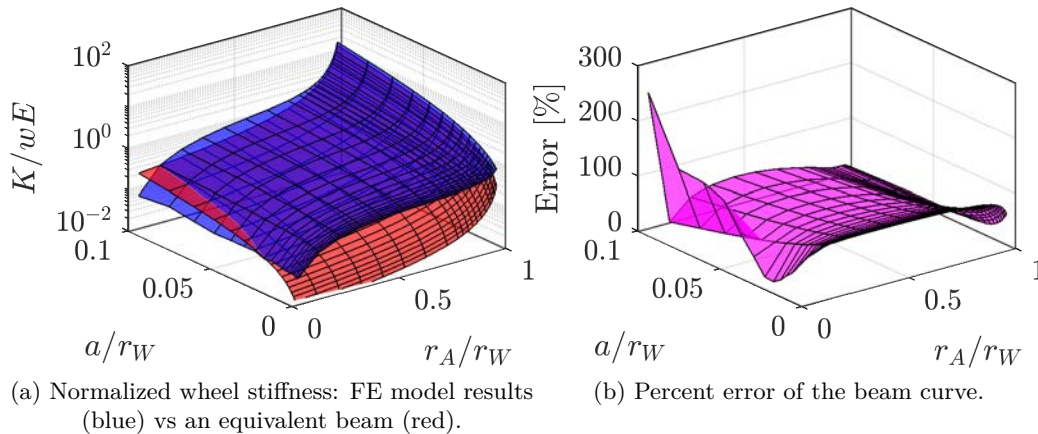


Figure 3.13: Comparison of the normalized wheel stiffness from the abacus and equivalent beam estimation.

3.7.2 Equivalent trapezoidal prism

The issue with the simple beam is that it has a constant cross-section throughout its height. The cylindrical wheel, with its two load points being the contact patch from below and the axle surface from above, is perhaps more akin to a trapezoidal prism. To that effect, an equivalent prism whose cross-sectional area changes along its height, from $2aw$ on one end to $2r_Aw$ on the other, may yield a closer approximation of the equivalent stiffness. Such a prism would have a stiffness given by

$$K_{\text{trap, norm}} = \frac{K_{\text{trap}}}{wE} = \left(\int_0^h \frac{z}{2x(z)} dz \right)^{-1} \quad (3.16)$$

where $h = \sqrt{r_W^2 - a^2} - r_A$ is the height of the prism in the z direction: the distance between the flat spot and the bottom of the axle. The half-length of the prism is given by x , which is now a function of z . The function has been inverted inside the integral (and then again outside after integration) to reflect the fact that when integrating along the height of the prism, one is essentially adding a number of springs in series, and thus requires an inverse summation.

Figure 3.14 shows the estimated wheel stiffness found using the wheel abacus and Equation (3.16), as well as the percent error of the trapezoidal prism curve with respect to the wheel abacus. This formulation, on top of being quite a bit more complicated, unfortunately yields results which are still not satisfactorily close to those given by the wheel abacus. The equivalent trapezoidal prism results have an average percent error of 67% (median 55%) with respect to the wheel abacus, with some values as high as 197% for extremely small contact area half-lengths. The standard deviation of the percent error is 9%.

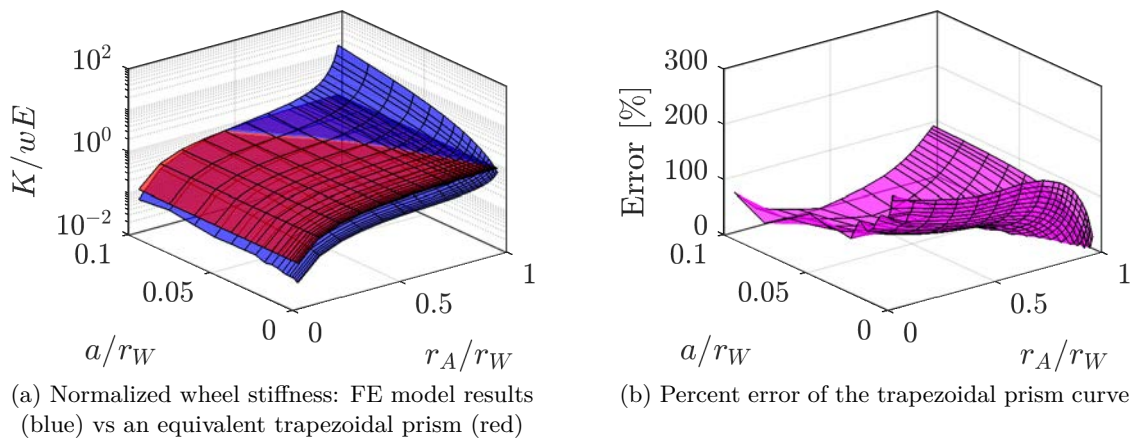


Figure 3.14: Comparison of the normalized wheel stiffness from the abacus and equivalent trapezoidal prism estimation.

While the trapezoidal prism does account for the changing cross sectional area of the equivalent shape, it still does not account for the coupling of the lateral and vertical deformations

(i.e. the Poisson's effect). It is believed that the curvature of the wheel is the source of this phenomenon, and thus cannot be captured by a trapezoidal prism.

Neither an equivalent beam nor an equivalent trapezoidal prism is sufficiently accurate to be used reliably as a replacement for the wheel abacus. On the other hand, this shows that the implementation of the wheel abacus into an indoor rolling noise model would indeed be a beneficial improvement.

3.8 Discussion

On a larger scale, the results shown in this chapter (particularly in regards to the discovery of the lack of influence of the Poisson effect) demonstrate that a similar modeling technique may be used to characterize the properties of other shapes as well. Characterizations have been performed for constant circular cross sections [104, 108] (for which the Poisson effect plays a large role), and characterizations of materials with constant square cross sections yield results which are nearly identical to those of a constant circular cross section below Poisson's ratios of about 0.47. However, analysis of other non-constant cross sections, or even more complex shapes, could potentially provide beneficial insights in applications and industries beyond rolling contact modeling.

The methods of estimating the wheel stiffness presented in this chapter were developed for use in a non-linear rolling noise model which operates in the time domain. The method is valid in the frequency domain as long as the elastic parameters do not depend on the frequency, as there is a correspondence between the time and the frequency behavior of the spring-mass system. The elastic parameters used in this model (e.g. the damping loss factor) generally deviate to the greatest extent at high frequencies, where there is little acoustic energy generated due to rolling noise. The exact validity of the frequency dependent parameters could be taken into account in future work.

3.8.1 Implementation into a rolling noise model

There are two ways in which the stiffness estimation procedures presented in this work may be implemented into a rolling noise model: pre or continuous calculation.

One option is to pre-calculate the stiffness of the wheel at the start of the model computation process. This may be used in models which operate in either the time or frequency domain. Here, Hertzian equations are used to compute the size of the contact area under static load in the absence of roughness, and the stiffness is then estimated based on this wheel geometry. Thus the wheel stiffness remains constant throughout the entire rolling model computation process.

In reality, however, the wheel stiffness is not constant. It depends on the size of the contact area, and any change in contact area half-length will result in a small change the wheel stiffness. Because the contact area half-length changes throughout the rolling event as a new roughness profile continuously “moves into” the area between the wheel and the floor, the wheel stiffness itself changes continuously as well. To account for this phenomenon, the second option is to calculate the wheel stiffness at each instant throughout the rolling event, providing a unique stiffness value for every discrete moment in time. Consequently, this may only be used in time-domain rolling noise models. It is more computationally expensive, but could potentially provide greater accuracy in the stiffness estimation. This is investigated in Chapter 5.

In the continuous-calculation method, the presence of roughness in the contact area is accounted for in calculating the size of the contact area for the purpose of estimating the wheel stiffness (This is not to be confused with the local contact stiffness between the wheel and the floor, which represents the small scale deformation due to the interpenetration of the two bodies). In the pre-calculation method, a simplifying assumption is implicitly made that the presence of roughness will change the value of a/r_W from its original static Hertzian estimation by a small enough amount that it may be ignored for the purpose of calculating the wheel stiffness. In both cases, the value of a/r_W is always calculated prior to estimating the wheel stiffness.

Which method should be used depends on the methodology of the model (time or frequency domain), the magnitude of the roughness profile, and the priorities of the user. A roughness profile which is relatively smooth may not result in a contact area which changes greatly throughout the course of the rolling event, and thus pre-calculation may be more practical. Rougher profiles however, particularly those containing large discontinuities such as floor joints or wheel flats, may benefit from continuous calculation. Finally, as continuous calculation will take longer to complete than pre-calculation, users which prioritize short computation times may still choose to implement pre-calculation instead.

3.8.2 Scope of the method’s applicability

In both phases of the parametric study, care was taken to run FE models for a wide range of parameter values. Thus, for the most part, any kind of trolley wheel which may be reasonably expected to be found in the real world can have this method applied. Due to their linear dependence, for the wheel width, radius, and Young’s modulus, any value may be used. Axle radii of 5-98% of the wheel radius are valid, which for all intents and purposes is comprehensive, as a wheel outside this range would be of no practical use. For the contact area half-length, the method is assumed to be valid for any value below 10% of the wheel radius. Again, the

wheel softness and applied load would need to be so high to achieve a contact area half-length above this limit, that in reality it is of no concern. For contact area half-length values below 0.3% of the wheel radius, the wheel stiffness is assumed to continue to follow the polynomial profile. This likely results in an overestimation of the stiffness for these extremely small contact area half-lengths. However, this is considered acceptable in order to allow for discontinuities like floor joints or wheel flats, where the size of the contact area becomes extremely small for a brief moment as the wheel rotates around the corner of the flat spot and/or floor joint.

3.9 Conclusion

This chapter presents an original technique for estimating the stiffness of a cylindrical indoor trolley wheel. A parametric study was conducted in order to identify the dependence of the wheel stiffness on each of the relevant variables. The stiffness is linearly dependent on the wheel width and Young's modulus, and largely independent from Poisson's ratio. A unique dependency exists for the axle/wheel radii ratio and contact area half-length. Using the information from these relationships, an abacus was created for estimating the stiffness of virtually any cylindrical wheel. Three methods were presented for estimating the wheel stiffness: a lookup table, a series of one-dimensional polynomials, or a single two-dimensional polynomial. The polynomials have extremely good fit to the data, and all three methods provide estimates that are reasonably close to one another. These methods may be implemented into a rolling noise model to provide either a pre-calculated or continuously updating estimation of the wheel stiffness.

THIS chapter presents the results of several experimental rolling noise tests conducted at two different laboratory locations, as well as a series of small-scale roughness measurements performed at the metrology laboratory at INSA-Lyon. An analysis of the measured roughness profiles is first presented in Section 4.1. For the rolling noise tests, the primary test trolley used in these measurements is presented in Section 4.2, followed by the methodology and results of tests performed at industrial partners in France (Section 4.3) and in the Netherlands (Section 4.4). The two locations are then compared with one another in Section 4.5. These experimental results are used further in Chapter 5 for validating the rolling noise model.

4.1 Roughness measurement

The contact model may use any kind of roughness profile in its estimation procedure, whether that be measured or artificial. In practice, a measured roughness profile will yield the most accurate results when comparing to a real-world rolling event, as well as for validation of the model. Thus, it was deemed necessary to acquire measured roughness profiles to be used as input in the model.

This presents a particularly difficult problem for indoor rolling noise. Roughness profiles measured for train wheel/rail and vehicle tire/road contact are typically done with a spatial resolution of 1 mm (e.g. as in [39]). This is acceptable for the large contact dimensions at play in these scenarios. However, due to the smaller wheel sizes and static loads with indoor trolleys, where the length of the contact area in the longitudinal direction is often on the order of 1–2 mm, a much higher spatial resolution is necessary. That is to say, both large and fine resolutions are needed for indoor rolling contact.

An advantage exists in the field of indoor rolling noise with respect to the wheel's roughness, as smaller wheel sizes make it easier to measure with a higher spatial resolution without drastically

increasing the size of the data-set. For the roughness of the floor, there are other considerations which need to be made. While floors can consist of a simple continuous surface (e.g. poured concrete), they may also be made up of repeating patterned sections, such as ceramic tiles, wood panels, or other composite material sections. In such scenarios, it is not necessary to measure the roughness of a large length of the floor[†].

In the sections that follow, the measurement and analysis of a selection of floor and wheel roughness profiles are presented. These profiles, which are used as input to the rolling model, provide a real-world link between the empirical factors which influence the generated sound and the theoretical calculations which make up the model.

4.1.1 Measurement of the small-scale roughness profile

Due to the dimensions involved in indoor rolling noise (smaller wheels and often sectioned floors), the possibility was fortunately afforded to be able to measure roughness profiles in a fixed lab setup. This is an improvement over the alternative, which would be to perform in-situ measurements using a portable device. A setup where floor and wheel samples are brought to a lab for surface roughness measurements offers improved simplicity, repeatability, and accuracy over an on-site setup, where the measurement device must instead be brought to the floor and wheel samples.

Roughness measurements were conducted at the INSA-Lyon metrology lab. Roughness samples from one cylindrical wheel and four floors were measured. This was done using a Nikon LC15DX 3D scanner with an average spatial resolution of 22 μm . The floors measured were polished concrete, a smooth PVC floor covering, a rough PVC floor covering, and ceramic tile. The two PVC floors were identical in construction, the only difference being their surface roughness. A 3.5 cm wide section was measured along the full length of each floor sample: 20 cm for the concrete, 30 cm for the tile, and 60 cm for the PVC. For the wheel measurement, the entire rolling surface was captured, giving a width equal to the wheel width (3.5 cm), and length equal to the wheel's circumference (10π cm).

Figure 4.1 below shows the measured roughness profiles. The profiles were low-pass filtered with a cut-off wavelength of 20 mm, which corresponds to a cut-on frequency of 50 Hz for a trolley speed of 1 m/s. The rough PVC floor covering is by far the roughest of the four measured profiles, having amplitudes which are an order of magnitude higher than those of the other three profiles.

[†]Provided the roughness of the floor remains consistent from section to section. While it is certainly possible that a particular section may have a different small-scale roughness than the rest of the floor (e.g. a heavily trafficked area), such a scenario is not considered here.

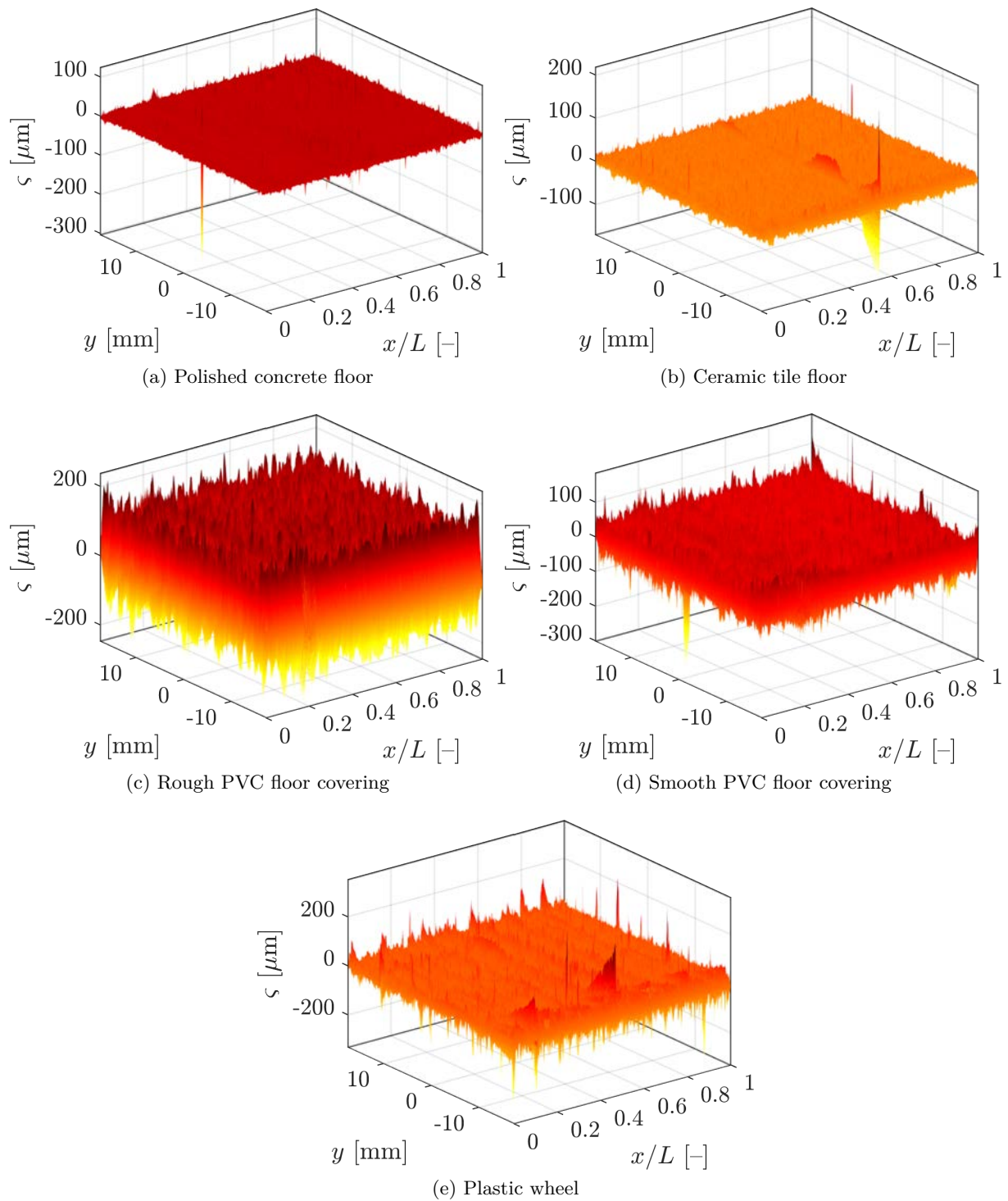
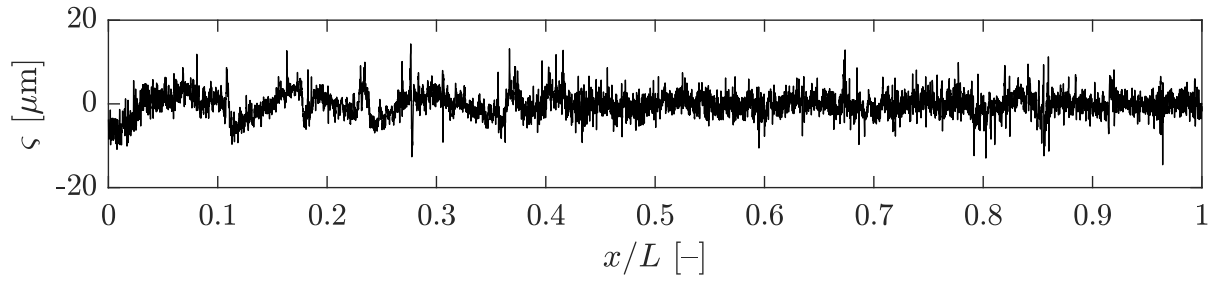


Figure 4.1: Measured roughness profiles. Low pass filtered with a cutoff wavelength of 20 mm.

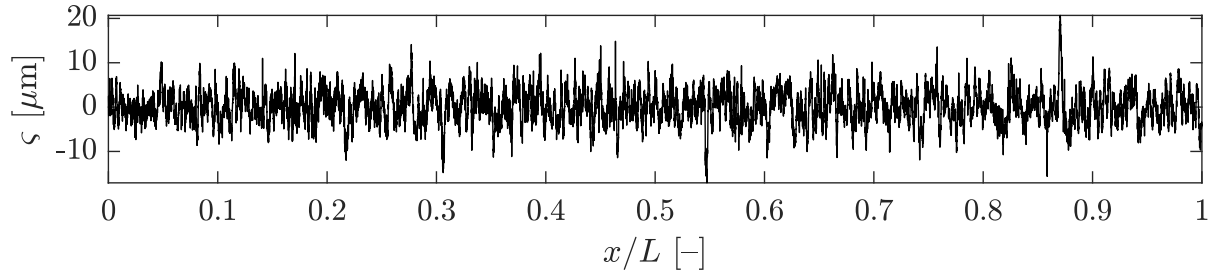
Figure 4.2 shows a single line from each of the measured roughness profiles. There does not appear to be any single wavelength which dominates in any of the roughness profiles: they all appear largely scattered. In examining the scale of each of the plots, we see that the overall magnitude of each profile varies substantially from material to material.

The relatively broadband nature of the profiles is confirmed by examining their wavelength spectra, which is shown in Figure 4.3. The profiles here were windowed with a Tukey window using a cosine fraction of $r = 0.1$. All four profiles remain remarkably broadband across the entire spectrum: with only the rough PVC profile exhibiting a substantial shift at $\lambda = 1 - 2$ mm. Note here that as the plots are showing parallel lines in the longitudinal direction, variations in the profiles in the transverse y direction are still in the spatial domain, not the wavelength domain.

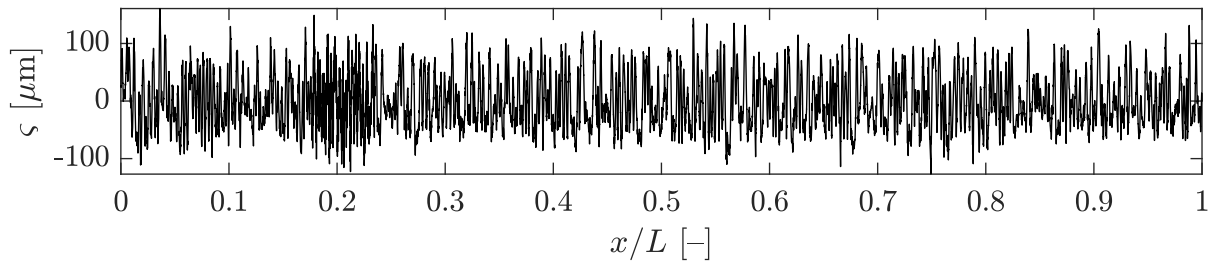
The differences in spectra may be seen more clearly in examining a single spectral line in the longitudinal direction (band averaged on a log scale), as shown in Figure 4.4. Here the rough PVC, appearing as a line of highest magnitude in the mid to long wavelength range, is essentially comprised of two zones in the wavelength domain: below 1-2 mm and above 1-2 mm. The spectra of the two PVC floor coverings are nearly identical in the shorter wavelength zone, which is to be expected considering their congruent construction. The smooth PVC still generally has more mid to long wavelength content than the non-PVC of the profiles, exhibiting the second highest magnitude curve. The plastic wheel remains the flattest of the measured curves: changing the least across the whole wavelength spectrum. The ceramic tile has a similar profile as that of the rough PVC, with a substantial change from low to high magnitude along the curve. Though here the change occurs at 0.5–1 mm rather than 1–2 mm. This may be perhaps due to similarities in the manufacturing process for these two materials. Finally, the concrete experiences a relatively low magnitude across the whole wavelength spectrum, though it does rise slightly in the longer wavelength region.



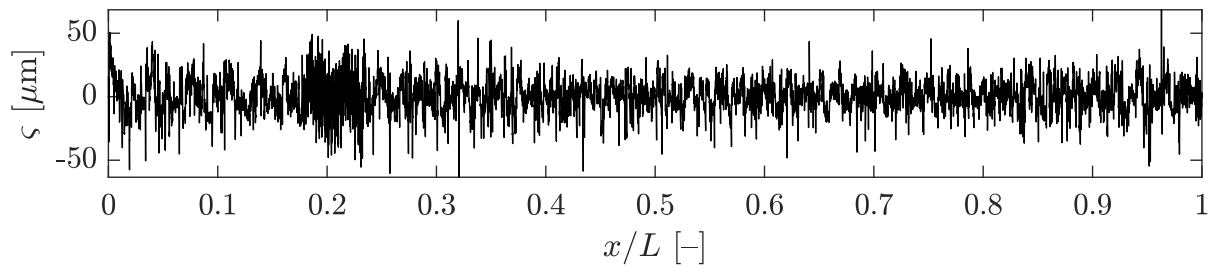
(a) Polished concrete floor



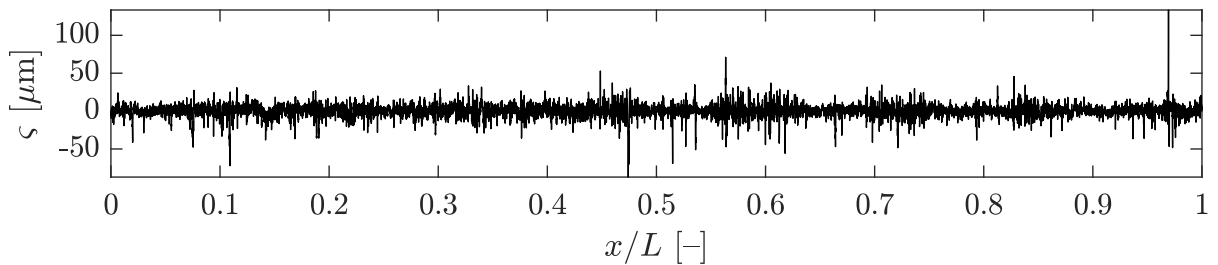
(b) Ceramic tile floor



(c) Rough PVC floor covering



(d) Smooth PVC floor covering



(e) Plastic wheel

Figure 4.2: One line from each of the measured roughness profiles. Low pass filtered with a cutoff wavelength of 20 mm.

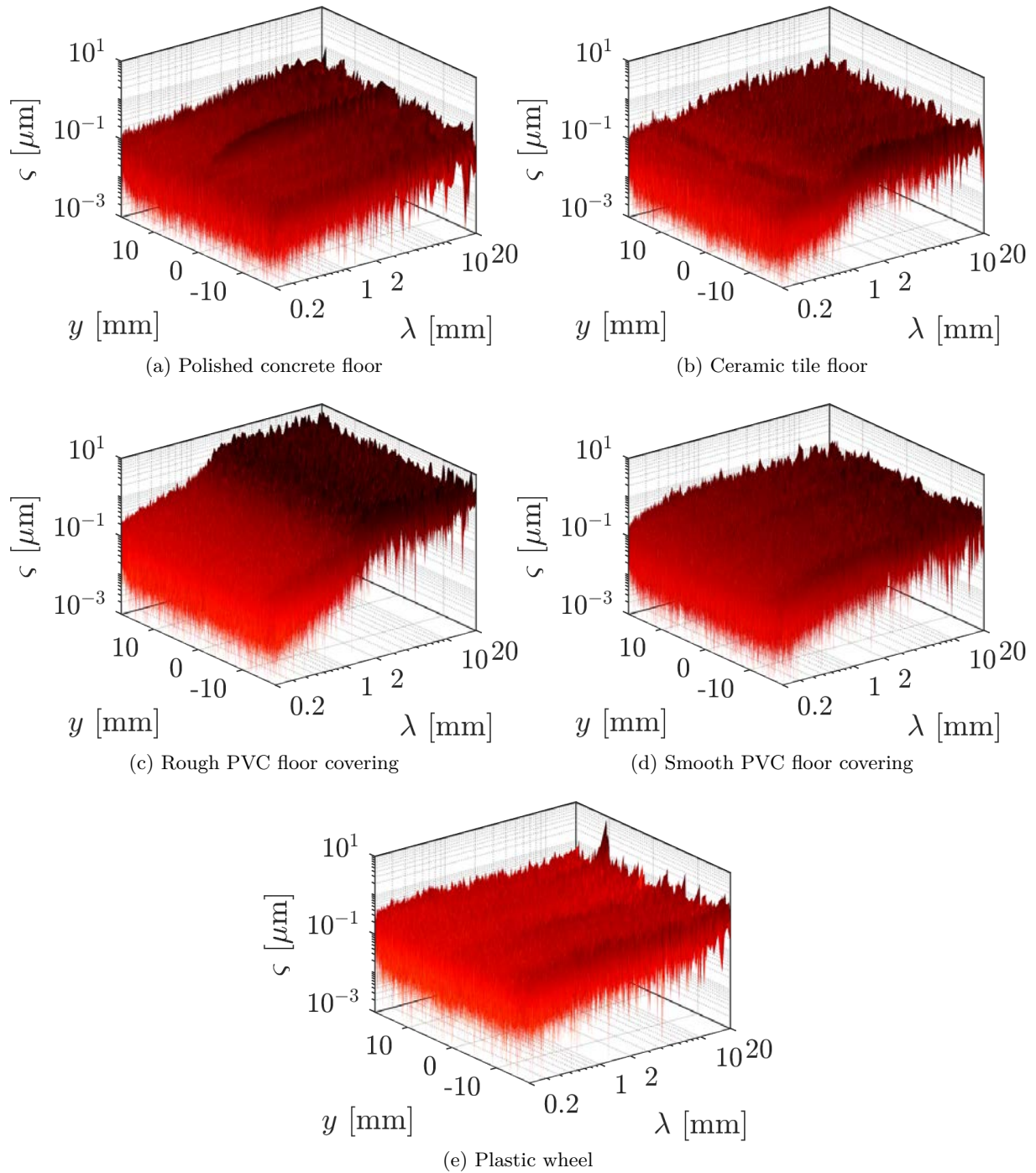


Figure 4.3: Measured roughness spectra. Windowed with a Tukey window using a cosine fraction of $r = 0.1$.

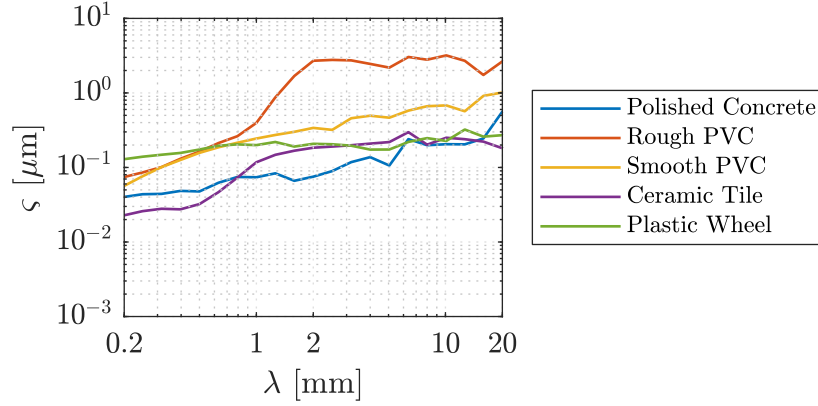


Figure 4.4: One line from each of the measured roughness spectra. Band averaged on a log scale. Windowed with a Tukey window using a cosine fraction of $r = 0.1$.

4.1.2 Roughness parameters

In the field of surface metrology, certain single-number parameters are often calculated and used to describe a surface roughness profile. These parameters, defined in ISO 4287 [109], are based on the mean-line system, meaning they all depend on some form or another on the deviations of the peaks and valleys from the mean. For 2D profiles, the convention is to use the letter R followed by an additional or series of additional lower case letter(s) to define each of the parameters. For 3D profiles, the letter S is used in place of the letter R. As the profiles measured in Section 4.1.1 are 3D profiles, the 3D roughness parameters are used from here onward.

The most commonly reported 3D parameter, Sa , is the arithmetical mean deviation of the profile.

$$Sa = \frac{1}{n} \sum_{i=1}^n |\zeta_i| \quad (4.1)$$

Where ζ_i is the i^{th} roughness profile in the longitudinal direction. A total of n parallel roughness lines are used.

This is followed closely by Sq , the root mean squared of the profile.

$$Sq = \sqrt{\frac{1}{n} \sum_{i=1}^n \zeta_i^2} \quad (4.2)$$

These two values describe the general behavior of the profile as a whole, and are good at ignoring the influence of a single large outlier asperity. On the other hand, they still have their disadvantages, as wildly different profiles can still result in identical Sa and Sq values.

The next three values describe the maxima and minima of the profile. Sv is the maximum valley depth of the profile,

$$Sv = \left| \min_i \varsigma_i \right| \quad (4.3)$$

Sp is the maximum peak height of the profile,

$$Sp = \left| \max_i \varsigma_i \right| \quad (4.4)$$

and Sz is the maximum height of the profile,

$$Sz = Sp + Sv \quad (4.5)$$

which is simply the total distance from lowest valley to highest peak. Sv , Sp , and Sz are all generally unreliable when discussing the overall behavior of the roughness profile as a whole, as a single outlier peak or valley will drastically skew these values in a way which will not necessarily represent the behavior of the majority of the profile.

Ssk is the skewness of the profile,

$$Ssk = \frac{1}{nSq^3} \sum_{i=1}^n \varsigma_i^3 \quad (4.6)$$

which is the measure of the asymmetry of the probability distribution of the profile about its mean. It may be positive, negative, zero, or undefined. In general, a negative skewness indicates that the probability distribution function has a tail which skews left of the mean, and a positive skewness indicates that the probability distribution function has a tail which skews right of the mean.

Sku is the kurtosis of the profile,

$$Sku = \frac{1}{nSq^4} \sum_{i=1}^n \varsigma_i^4 \quad (4.7)$$

which is a measure of the “tailedness” of the probability distribution of the profile about its mean. In effect, it measures the influence of the outliers of the data-set, as a standardized value which is less than one (i.e. a value close to the mean), when raised to the fourth power, will become close to zero. Similar to Sv , Sp , and Sz , Ssk and Sku can easily be skewed to deceptively high absolute values in the presence of a single outlier asperity. Thus their values should be taken with a grain of salt.

Finally, an additional parameter which is not given in ISO 4287, but which is still sometimes used in surface metrology, is the Hurst exponent or roughness exponent. It is defined in terms of the asymptotic behavior of the rescaled range of the span of a series [110],

$$\mathbb{E} \left[\frac{R(n)}{\sigma(n)} \right] = C_n^H \text{ as } n \rightarrow \infty \quad (4.8)$$

where \mathbb{E} is the expected value, $R(n)$ is the range of the first n cumulative deviations from the mean, $\sigma(n)$ is their standard deviation, and C is a constant.

The Hurst exponent may be thought of as a measure of the randomness of the profile. It describes the likelihood of a series to either regress back towards the mean or to move in a certain direction. $0.5 < H < 1$ denotes a profile with positive autocorrelation, or in other words, that a large value at point i is likely to be followed by another large value at point $i + 1$. Conversely, $0 < H < 0.5$ denotes the opposite: a profile with negative autocorrelation, which is constantly switching back and forth between large and small values, one after the other. $H = 0.5$ denotes an uncorrelated profile: the magnitude of point i provides no information about the magnitude of point $i + 1$ [111]. In practice, the Hurst exponent for the measured roughness profiles was estimated here in MATLAB using [112], which is developed from [113, 114, 115].

No one statistical parameter is adequate for fully describing the behavior of a roughness profile. Each one is useful for a different situation, provided the user has an understanding of the meaning of the parameter. This is true in the wider field of surface metrology, and it is also true in the field of rolling noise.

Table 4.1 shows the calculated statistical roughness parameters for each of the measured profiles. Comparing the results for the polished concrete with its profile in Figure 4.1, it becomes apparent that the single outlier valley in the profile dominates the results for Sv , Sz , Ssk , and Sku , giving the impression that it is much rougher of a profile than it really is. A similar phenomenon exists (though to a lesser degree) for the ceramic tile and plastic wheel as well. For comparing the overall behavior of the profile, Sa and Sq are much more useful here. These values support best what is seen in Figure 4.1. The order of profiles from least rough to most rough are: polished concrete, ceramic tile, plastic wheel, smooth PVC, and rough PVC.

The Hurst exponents indicate that all of the profiles exhibit a low degree of autocorrelation, though some more than others. The polished concrete is slightly more negatively autocorrelated, lending to its generally smoother nature. The higher Hurst exponent for the rough PVC is an artifact of the profile having a more pronounced periodic pattern. The remaining profiles, the smooth PVC, ceramic tile, and plastic wheel, are largely uncorrelated.

Table 4.1: Statistical roughness parameters

	Sa [μm]	Sq [μm]	Sv [μm]	Sp [μm]	Sz [μm]	Ssk [-]	Sku [-]	H [-]
Rough PVC	42.1	51.1	247.1	237.0	484.2	0.3	2.6	0.7
Smooth PVC	9.2	12.3	301.1	183.4	484.5	-0.4	8.5	0.5
Plastic wheel	6.6	10.5	332.2	351.6	683.8	-0.8	28.1	0.4
Ceramic tile	3.6	5.0	171.3	217.8	389.1	-1.7	67.0	0.5
Polished concrete	2.0	3.0	303.9	123.9	427.8	-8.3	668.4	0.3

So, what is the purpose of calculating these single-number parameters in the context of rolling noise? They give information about the amplitude and randomness of the various profiles, yes. However, beyond that, what means do they serve in influencing their use in a rolling noise model? The answer to this question, which is explored in the following section, has to do with the direction in which the wheel is rolling.

4.1.3 Directionality

An important consideration to be made in the context of indoor rolling noise regarding the roughness profiles is their directionality. In vehicle tire/road and train wheel/rail contact, the wheel always rolls in the same direction with respect to the road or rail: along its length. Indoor rolling noise, however, has no such restriction: as demonstrated in Figure 4.5, trolleys may move in any direction across the floor, approaching the roughness profile from any orientation. Thus it is beneficial to investigate the variation of the roughness profile in different directions.

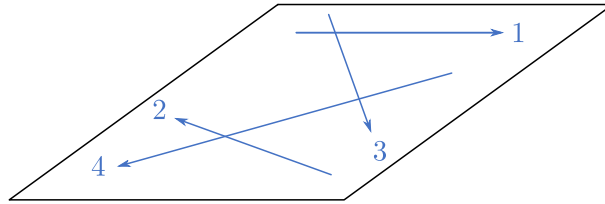


Figure 4.5: Example schematic of rolling orientation. The trolley is not restricted to a single path: it may roll in any direction across the floor.

The initial hypothesis was that, due to the way in which floors and flooring materials are manufactured, no discernible difference in direction should be seen across orientations. A polished concrete slab, for example, is assembled by simply pouring wet concrete into a mold, allowing it to partially dry, and then passing over the surface several times with a floor grinder. Neither the person pouring the wet concrete nor the person operating the floor grinder give thought as to any pattern they may place into the floor: they simply pour and polish until the floor appears level and smooth to the naked eye. Similarly for floor sections manufactured on an assembly line (e.g. ceramic tiles and PVC floor coverings), the sections are designed to be assembled together

in any orientation. Thus, in theory, care should not need to be given in discerning their direction when it comes to using their small scale roughness as input into a rolling noise model.

In addition to the roughness profiles measured in Section 4.1.1, a second set of profiles were measured for each of the four floors in an orthogonal direction. These profiles are shown in Figure 4.6. In comparing them with the previously presented profiles, one may determine if there are any discernible differences between the two. Or at least, any differences which are important to be considered for the rolling model. Indeed, in support of the initial hypothesis, these profiles appear more or less visually identical to those shown in Figure 4.1.

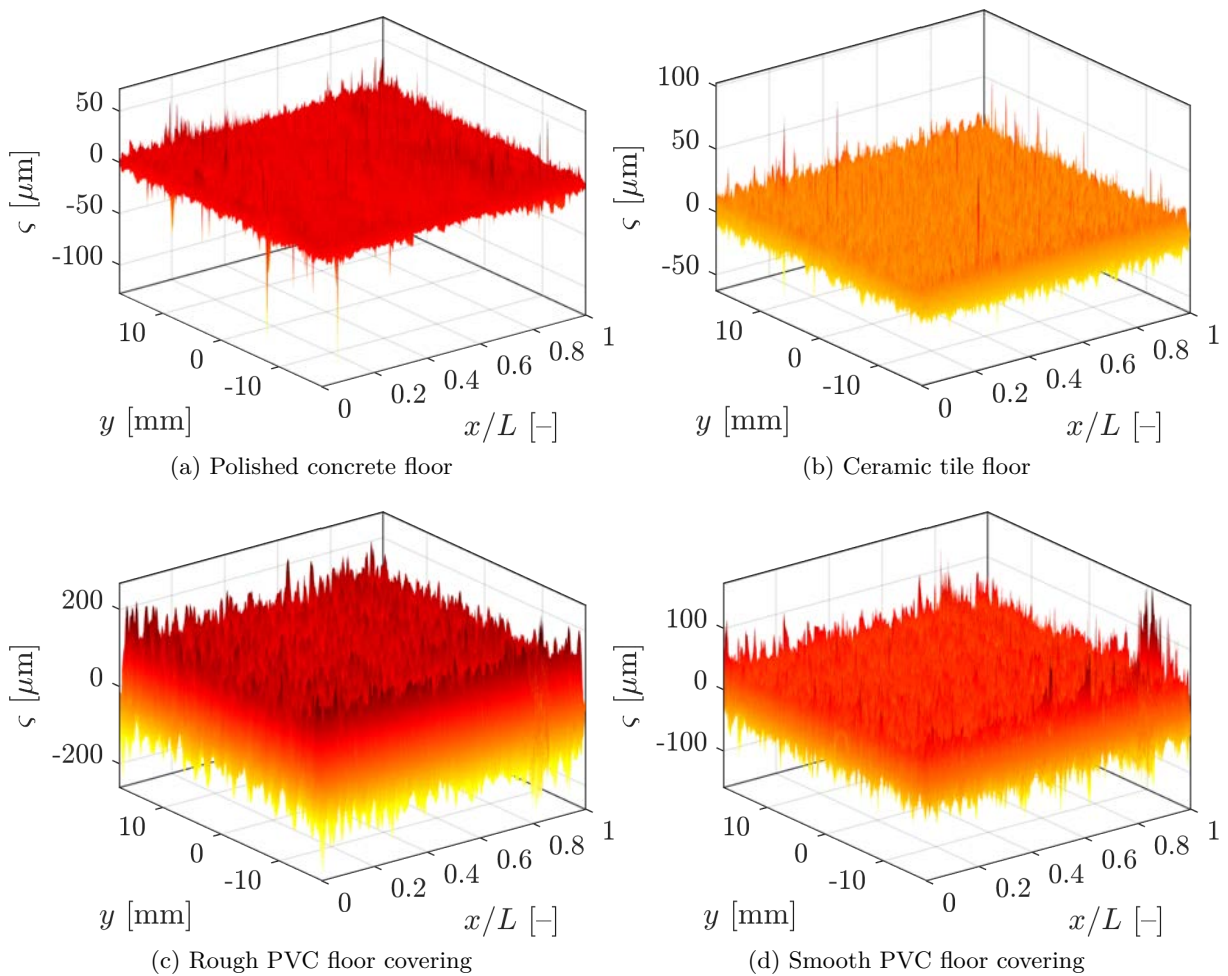


Figure 4.6: Orthogonal measured floor roughness profiles. Low pass filtered with a cutoff wavelength of 20 mm.

Similarly, Table 4.2 shows the statistical parameters for each of the orthogonal floor roughness profiles. In comparing with the values given in Table 4.1, the orthogonal profiles exhibit largely similar values for S_a , S_q , and H as their original counterparts. The others on the other hand, S_v , S_p , S_z , S_{sk} and S_{k_u} tend to vary considerably. This once again highlights the precarious natures of some of these parameters with regards to outlier asperities. However, in general, S_a ,

Sq , and H serve as further evidence to the congruency of the orthogonal profiles.

Table 4.2: Statistical roughness parameters—orthogonal direction

	Sa [μm]	Sq [μm]	Sv [μm]	Sp [μm]	Sz [μm]	Ssk [-]	Sku [-]	H [-]
Polished concrete	2.2	3.1	128.0	71.6	199.6	-0.3	22.0	0.3
Rough PVC	42.3	51.2	261.8	267.1	528.9	0.4	2.6	0.7
Smooth PVC	9.5	12.6	159.6	173.1	332.7	-0.3	5.7	0.5
Ceramic tile	3.3	4.2	62.9	102.3	165.2	0.2	4.6	0.5

Figure 4.7 compares the wavelength spectra of the measured roughness profiles with their orthogonal counterparts. The spectra have been averaged in the transverse direction for ease of comparison. The spectra in the two directions are extremely similar, if not nearly identical for each floor profile.

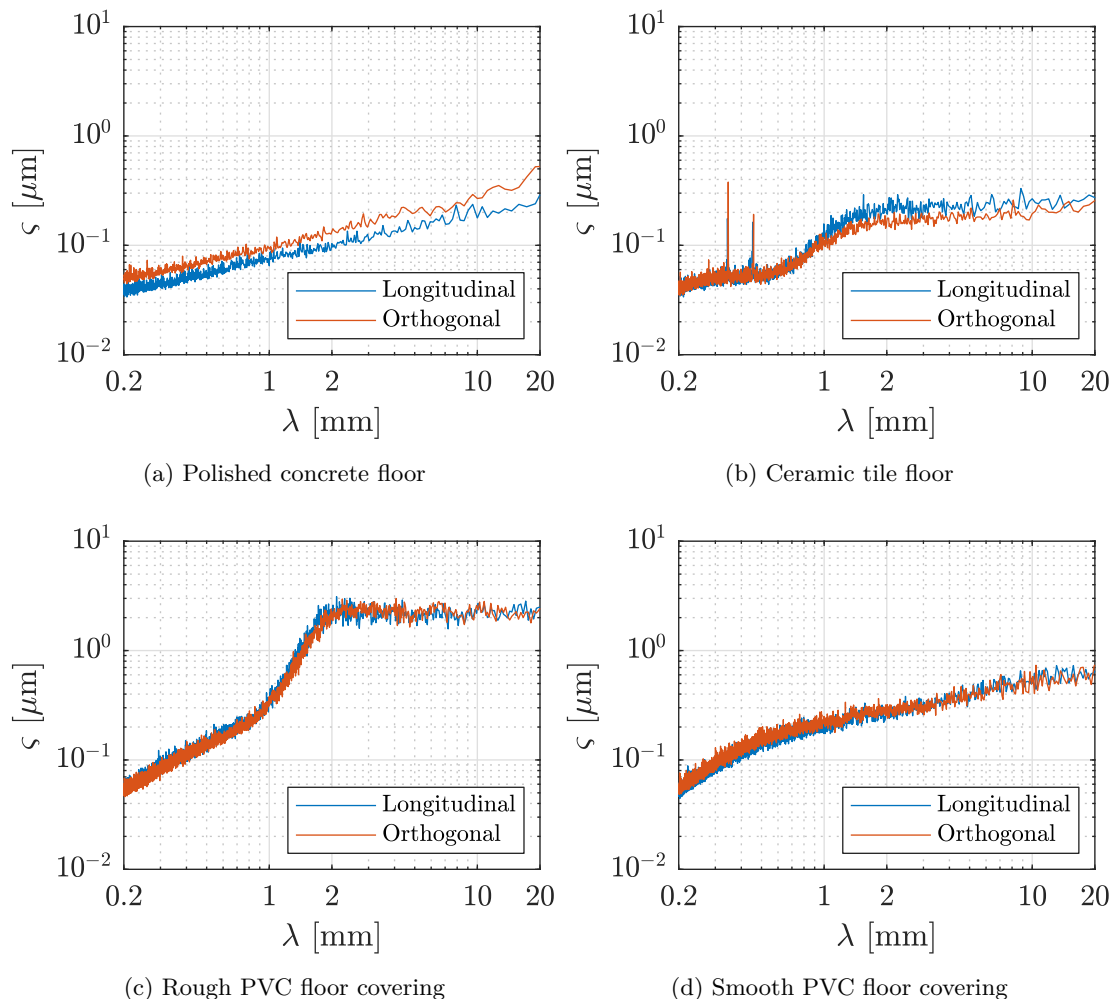


Figure 4.7: Comparison of the longitudinal and orthogonal measured floor roughness spectra. Windowed with a Tukey window using a cosine fraction of $r = 0.1$, and averaged in the transverse direction.

All the analysis in this section points to the same conclusion: that the roughness profiles measured here are, for all intents and purposes, isometric. The profile does not change in any meaningful way when changing measurement direction on the test specimen, neither in the spatial nor the wavelength domains. Thus the initial hypothesis is confirmed. This bodes well for the rolling noise model, as direction may be ignored when deciding which roughness profile to use as input.

Coherence

In exploring the literature of train wheel/rail contact modeling, it was discovered that an alternative method of quantifying the directionality of the roughness profile has been used in previous works. Pieringer et al., for example, found that the sound generated is highly dependent on the roughness correlation in the transverse direction [39]. 2D and 3D versions of the same model can differ by several decibels when correlation is low. As train rails are not omni-directional, here Pieringer et al. are referring to the correlation in the transverse direction of parallel longitudinal roughness lines, being the most appropriate definition for the given application. This correlation is quantified using the coherence of the roughness profile.

Coherence γ^2 is a statistical measure of the congruence between two signals. By definition, it always falls within the range $0 \leq \gamma^2 \leq 1$. A coherence of 0 indicates that the two signals are perfectly uncorrelated: the behavior of signal one provides no information about the behavior of signal two. A coherence of 1 indicates perfectly correlation: there is a linear relationship between the behavior of the signals.

The coherence γ^2 of the roughness profile in the transverse direction is calculated in [39] as

$$\gamma^2(f) = \frac{|S_{ij}(f)|^2}{S_{ii}(f)S_{jj}(f)} \quad (4.9)$$

where S_{ii} is the power spectral density (psd) of the central roughness line,

$$S_{ii}(f) = \text{psd}(\varsigma_i) \quad (4.10)$$

S_{jj} is the mean power-spectral density of all other roughness lines,

$$S_{jj} = \frac{1}{N} \sum_{\substack{j=1 \\ j \neq i}}^N \text{psd}(\varsigma_j) \quad (4.11)$$

and S_{ij} is the mean cross power spectral density (cpsd) between the central line and the mean of all other lines.

$$S_{ij} = \text{cpsd} \left(\zeta_i, \frac{1}{N} \sum_{\substack{j=1 \\ j \neq i}}^N \zeta_j \right) \quad (4.12)$$

Using this formulation, Pieringer et al. identify high coherence in the transverse direction at wavelengths below roughly 28 mm (corresponding to a frequency of roughly 1 000 Hz at 100 km/h, where $f = v/\lambda$) for a corrugated rail and wheel with cast iron block brakes. Two wheels with sinter block brakes were also measured, and were found to have low coherence across the entire wavelength spectrum. The authors point to this as an explanation for the discrepancies they see between the results of their 2D and 3D contact models.

The transverse coherence of the measured roughness profiles may be calculated here in a similar way. However, they will be modified slightly to account for the large spatial resolution available in the transverse direction (Pieringer et al. had 6 parallel roughness lines, whereas we have over 2 000). Instead of taking S_{ii} to be the spectrum of the central line, we shall take it to be the spectrum of the i^{th} line, and loop through the entire width of the profile, calculating a separate coherence for each parallel line. These may then be averaged together to achieve a single mean transverse coherence $\bar{\gamma}^2$ for each measured roughness profile. This is summarized by

$$\bar{\gamma}^2(f) = \frac{1}{N} \sum_{i=1}^N \frac{|S_{ij}(f)|^2}{S_{ii}(f)S_{jj}(f)} \quad (4.13)$$

where N is the total number of parallel lines.

The mean coherence of each of the roughness profiles for the measured wheels and floors are shown in Figure 4.8. In general, all of the measured roughness profiles are quite uncorrelated in the transverse direction across the whole wavelength spectrum. The two PVC floor coverings exhibit very similar coherence profiles (to be expected considering their similarity in construction), and are the most uncorrelated of the measured profiles: resting toward the bottom of the plot around $\bar{\gamma}^2 \approx 0.2$ for all wavelengths. The polished concrete is also very similar in coherence to the PVC floor coverings: deviating only slightly upward for $\lambda \geq 5$ mm. The ceramic tile and plastic wheel each exhibit a higher transverse mean coherence: approaching (and in the case of the plastic wheel, exceeding) 0.4.

Herein lies the problem with using coherence to describe the transverse variation of the roughness profile in the context of an indoor rolling noise model. Looking at Figure 4.8 alone, it would be tempting to conclude that all of the measured profiles here vary greatly in the

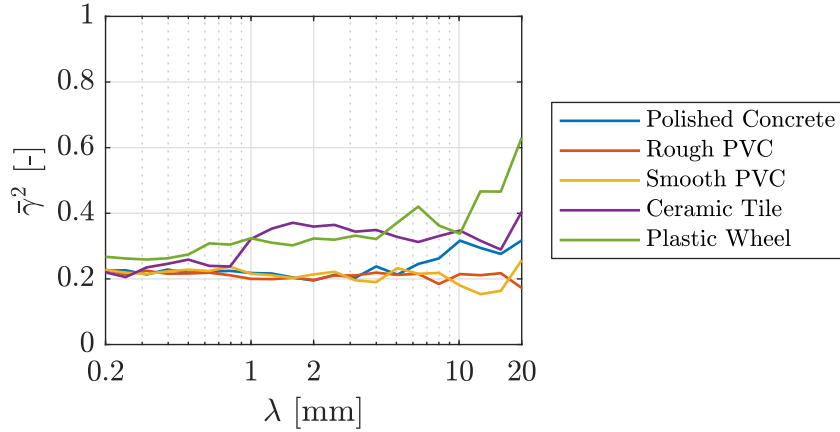


Figure 4.8: Mean coherence of the measured roughness profiles.

transverse direction[†]. However, we know from the previous analysis conducted in Section 4.1.3 that this is not the case. How do we reconcile this difference?

The problem boils down to the fact that all of these profiles are extremely broadband in nature. For example, there is little difference between the spectra of the smooth PVC and that of white noise. It is this artifact which makes the coherence a bad candidate for quantifying the profiles. In the case of Pieringer et al., the corrugated rail showed high coherence because of a dominating peak around a wavelength of 55 mm (500 Hz at 100 km/h), which was present in all the parallel lines. If, for example, the central line had had a 55 mm wavelength corrugation, but the outer lines had had corrugation at a shorter 20 mm wavelength, the coherence would have been substantially lower. This is, of course, not physically likely, as rail corrugation tends to occur equally across the whole width of the rail, but the point still stands. However, two parallel lines which are both highly broadband are still similar to one another in the sense that they are both equally random. Nevertheless, their coherence will still be low, because that's how coherence works. It is, in effect, a measure of to what degree one profile may be described as a linear function of another profile.

Does this mean that Pieringer et al. were wrong to use coherence in their analysis of train rails and wheels? Not at all. What it does mean, however, is that care must be taken if it is to be used. Just like the statistical roughness parameters, no single quantity tells the whole story. In general, the more tonal the spectrum of a roughness profile, the more informative its coherence will be. Conversely, the more random the spectrum, the more other quantities should be relied upon for analyzing the directionality of the roughness.

[†]By consequence, the orthogonal direction as well. The mean coherence may be calculated by comparing the i^{th} line of the roughness profile to the i^{th} line of its orthogonal profile, and then averaging them together. This results in largely identical values as those shown in Figure 4.8, so they are omitted for brevity.

In the field of indoor rolling noise, the types of wheels and floors likely to be encountered have a tendency to be more random in nature. Not only does this mean that they are largely independent of direction, but also that there exists the possibility of generating artificial roughness profiles representative of their real counterparts. These profiles could be created knowing only the statistical roughness parameters (i.e. Sa , Sq , and H) of the surfaces they are aiming to replicate, and could potentially yield similar results to their real counterparts when used in an indoor rolling noise model. Such a concept has not been explored in this work, but it remains a possible topic of future work in the field of indoor rolling noise.

4.2 The test trolley

As the goal of this work is to predict the sound of a rolling delivery trolley, a logical start may be to use an actual trolley for testing. However, doing so poses a problem of residual noise. Delivery trolleys often have cages and other mechanisms for holding and securing merchandise which may shake and rattle during rolling. This generates residual noise which is not the focus of this work. Thus, it was deemed necessary to develop a test trolley which is void of these extra features: generating purely rolling noise. The trolley may be used to conduct rolling tests for the purpose of validating the prediction model.

Figure 4.9 below shows the test trolley which was used for model validation. The trolley consists of two wheels which are easily interchangeable, a center post where weights may be added to increase the mass of the trolley, and a push handle for maneuvering the trolley across the floor. As the trolley body consists of a hollow metal tube, it was filled with fine grain sand to eliminate ringing due to resonance while rolling. Additionally, as the wheels of the trolley turn on a rigid axle (i.e. there are no wheel bearings involved), the axle was wrapped in Teflon tape to eliminate rattling between the wheel and axle. These two modifications ensured that the only noise being generated during rolling was the rolling noise itself. The mass of the empty trolley (with no added weights) was 7 kg.

Two types of wheels were used: one with a smooth profile, and one with flat spots positioned around the wheel's circumference. The latter was included as a means of including the effect of wheel flats on the generated rolling noise. The positions of the flat spots around the wheel's circumference were chosen so as to not generate a single periodic frequency of contact with the floor. Diagrams of the wheels can be found in Appendix B.

The two-wheel design was chosen as it is a simple means of ensuring two things: that all wheels remain in contact with the floor at all times, and that the effective load on each wheel remains the same. The drawback of this design is that the trolley must be pushed by hand,



Figure 4.9: Test trolley used for model validation tests: shown here with 20 kg added mass.

which introduces a degree of variability in the trolley speed, as well as the potential for footfall noise to be registered. Both of these concerns will be addressed in this chapter.

The question of how to design an ideal trolley brings rise to further considerations. In the world of building acoustics, a standard tapping machine has long existed for the purpose of replicating and regulating impact noise. This device, which was originally designed to mimic the sound of human footfall [85], consists of five hammers which rise and fall automatically in succession to generate impact events with the floor upon which the machine rests [82]. Just as the standard tapping machine can be used in any building and on any surface as a way of characterizing and comparing the performance of various floors with respect to impact noise, the development of a standard rolling device would enable the same evaluation and comparison to be made with respect to rolling noise. This topic is expanded upon in greater detail in Appendix A.

4.3 Rolling noise location one: Industrial partner in France

The first round of tests were conducted in a two-story reverberation room at an industrial partner in France. For each measurement, the test device was rolled in the emission room above, and the sound measured in both the emission and reception rooms. Each room had a volume of 52 m^3 , and the floor which separated the two rooms was 14 cm thick concrete. A decision was made to follow as closely as possible the existing standard for the laboratory measurement of impact noise defined by ISO 10140-3 [3]. This was done because of its simplicity: using a tried and true existing methodology is more robust than developing a brand new one.

The reverberation time of the reception room is shown in Figure 4.10. This is defined as the time it takes for a reference signal to diminish by 60 dB. This is rarely calculated directly, as it typically exceeds the measurement capabilities of most laboratories due to the extremely low

noise floor required. In practice, the reverberation time is instead calculated by measuring a 20 or 30 dB reduction, and extrapolating out to 60 dB. This is referred to as T_{20} or T_{30} , and is calculated in accordance with ISO 3382-2 [116] using the interrupted noise method.

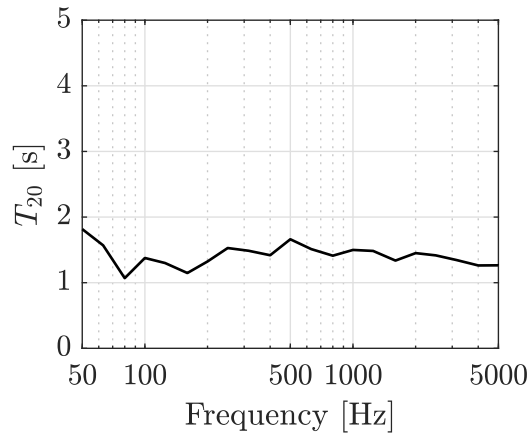


Figure 4.10: T_{20} reverberation time of the reception room at the industrial partner in France.

The benefit of using a reverberation room to conduct measurements is that the acoustic field in the room may be considered diffuse everywhere. That is, the sound level in the room is independent of microphone location or orientation. However, this is not true for all frequencies. In general, the lower the frequency, the more modal the acoustic behavior, and the less diffuse the field may be considered. The change from modal field to diffuse field is not instantaneous, but happens gradually over a range of frequencies. However, the generally accepted cutoff point where the dominant behavior switches from diffuse to modal is the Schroeder frequency. This is a factor of the room geometry and acoustic absorption, and approximated (for usual temperature and pressure conditions) by [117]

$$f_s = 2000 \sqrt{\frac{T_{20}}{V}} \quad (4.14)$$

where V is the volume of the room in cubic meters. Here the reverberation time is averaged over the whole frequency spectrum to achieve a single-number value.

Using the above formula, the Schroeder frequency of the reception room may be calculated as 322 Hz. This may seem high, and it shows an inherent difficulty in measuring rolling noise. As will be demonstrated shortly in the experimental results that follow, rolling noise is by nature very low in frequency. The vast majority of the acoustic energy generally exists below 1 000 Hz. However, while large reverberation rooms with low Schroeder frequencies exist, large two-story reverberation rooms are quite rare. The cases in which two-level reverberation rooms are typically used, measuring the transmission loss for airborne sources or impact noise, generally have much less low-frequency acoustic energy and thus do not require an extremely low Schroeder frequency to obtain meaningful results.

A Schroeder frequency of 322 Hz does not automatically mean that all results below this frequency are meaningless. It simply means that they must be taken with a grain of salt. In general, large peaks found below f_s in the experimental results may be at least partially attributed to the modal behavior of the room. Additionally, larger differences between experimental and model results are to be more expected below this frequency.

4.3.1 Rolling noise: Test trolley

The test trolley presented in Section 4.2 was used as the test device for the following measurements. A schematic of the setup is shown in Figure 4.11. The measurement procedure was as follows: the trolley would start rolling, then the sound recording would begin. The trolley would continue to roll in a linear fashion, traversing the floor in a back and forth motion, for a duration of 30 seconds. The sound recording would then finish, and the trolley would finally stop rolling. The trolley would either roll on the floor of the test room itself, or on a floor covering which was placed on top. In either case, the trolley was always rolled in a direction which did not split the room symmetrically, so as to reduce the effect of room modes. As depicted in Figure 4.11, the floor coverings (when present) only covered the section of the floor upon which the trolley rolled: they did not cover the entire room. The rolling distance in a single direction (before stopping and rolling in the reverse direction) was 2.5 m. As the trolley was pushed by hand, care was taken to ensure the operator was generating as little footfall noise as possible. A rotating boom microphone was used in both the emission and reception rooms. Both microphones were PCB 377A02 1/2 inch BNC free field standard microphones with integrated preamplifiers. Data was acquired using an OROS OR35 modular analyzer interface. The emission room from the test is shown in Figure 4.12. While measurements were recorded in the emission room, they were not used for any further analysis.

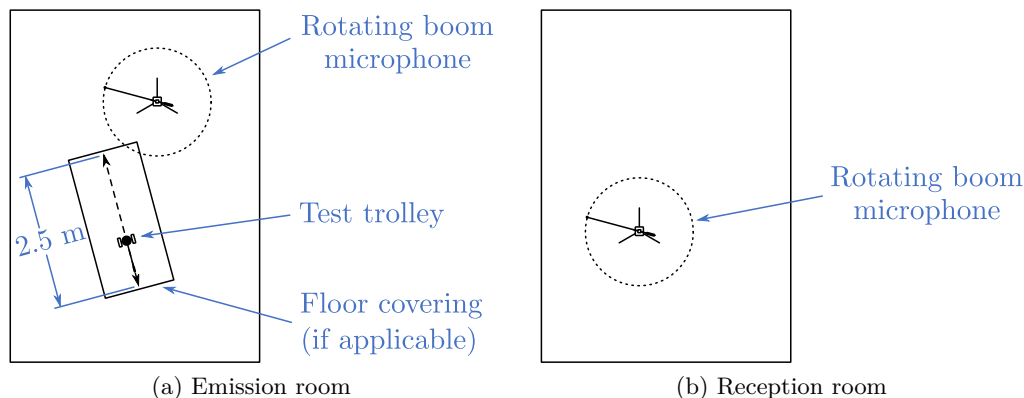


Figure 4.11: Measurement setup for the rolling test conducted at the industrial partner in France.



Figure 4.12: Emission room of the industrial partner in France.

The varying parameters of the test were the floor type, the wheel type, and the added load on the trolley. These are summarized in Table 4.3. Three different weight configurations were used: 10, 20, and 30 kg. These added loads were all in addition to the 7 kg mass of the trolley itself. The trolley was rolled on the bare concrete floor, as well as two types of PVC floor coverings: one smooth and one rough. The PVC floor coverings used for testing at the industrial partner in France were the same ones used for both the roughness measurements and the subsequent testing presented in Section 4.4 at Level Acoustics & Vibration. The trolley was rolled with two different types of plastic cylindrical wheels installed: both with a 5 cm radius and 3.5 cm width. The two types of wheels were identical in construction, with the exception that one set (denoted the “flat” wheel) had a series of flat spots (depth 0.5 mm) milled into the rolling surface of the wheel. The wheel without flat spots was denoted the “smooth” wheel. These are the same floors and wheels that had their roughness profiles measured in Section 4.1. The tile floor had its roughness profile measured, but was never used for rolling noise testing, as it was not feasible to install a full tile floor on top of the concrete. Finally, a fiberwood underlayer was added between the concrete and the rough PVC floor covering for some of the runs.

Table 4.3: Test parameters used in the rolling noise test at the industrial partner in France.

Floor	Wheel	Load
Concrete	Smooth	10 kg
Concrete + rough PVC	Flat	20 kg
Concrete + smooth PVC		30 kg
Concrete + fiberwood + rough PVC		

The first three floor types (concrete, rough PVC, and smooth PVC), both wheel types, and all three added load parameters were tested for all possible permutations at a trolley speed of 0.6 m/s. This speed was chosen as the operator found it a comfortable speed to constantly push

the trolley without too much variation. This yielded 12 test configurations. The concrete + fiberwood underlayer and rough PVC floor covering were tested for both wheel types, but only for the 10 kg added load. This yielded an additional 2 configurations. Thus a total number of 14 configurations were tested.

Influence of floor and wheel type

One of the main quantities which will be used in this chapter to quantify the sound generated by the rolling test trolley is the normalized sound pressure level L_n . This is calculated from the measured sound pressure level using

$$L_n = L_p + 10 \log \left(\frac{A}{A_0} \right) \quad (4.15)$$

where L_p is the measured sound pressure level in the room, A_0 is the reference absorption area (equal to 10 m² for a laboratory), and A is the equivalent absorption area of the room in square meters.

The equivalent absorption area in the room was calculated in accordance with ISO 10140-4 [4] using

$$A = \frac{0.16V}{T_{20}} \quad (4.16)$$

where V is the volume and T_{20} is the reverberation time of the room.

In the field of building acoustics, solutions are often quantified in terms of the benefit they provide over a reference configuration. The same can be achieved here by subtracting the normalized sound level with one of the floor coverings installed from the normalized sound level on bare concrete. Doing so allows one to visualize the relative performance of the floor covering under various conditions. This is calculated using

$$\Delta L_n = L_{n,0} - L_n \quad (4.17)$$

where $L_{n,0}$ is the normalized sound pressure level on the reference floor (here taken to be concrete) and L_n is the level with the floor covering in place. This is done not only because the benefit of a floor covering is often the primary quantity of interest, but also because doing so helps remove variations in experimental data, as well as modeling uncertainties, which may be present in the absolute level results.

Figure 4.13 shows the normalized sound pressure level L_n in the reception room due to rolling noise for all floor and wheel types. For all of these runs, the trolley speed was 0.6 m/s and the added load was 10 kg. The spectra of the background noise and noise generated due to the

walking of the operator alone are also shown. Each curve represents a single run.

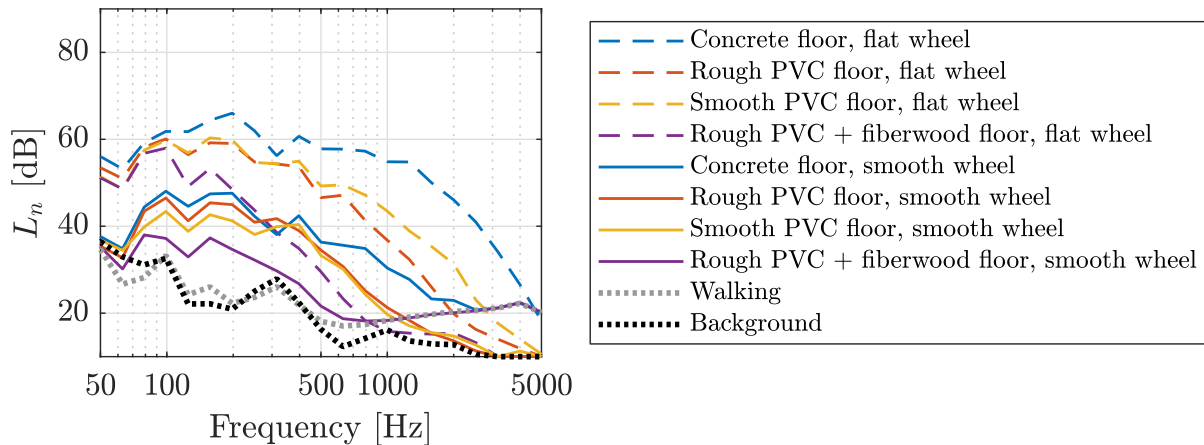


Figure 4.13: Rolling test results for varying floor and wheel type at the industrial partner in France. All runs were done with a trolley speed of 0.6 m/s and an added load of 10 kg.

Several observations may be made from this graph. The noise generated due to the walking of the operator was negligible, as it is essentially the same as the background noise level, and generally far below the rolling noise level. The quieter configurations (e.g. the smooth wheel on rough PVC + fiberwood floor) very closely approach the noise floor in the high frequency range, as most of the energy in this range is effectively absorbed by the floor covering. Both PVC floor coverings provided a mild benefit over the bare concrete alone due to their lower elasticities. This benefit was smaller for the smooth wheel, showing primarily above 500 Hz. The benefit was much more pronounced for the flat wheel, existing for nearly all frequency bands. Interestingly enough, while the difference between the rough and smooth PVC was more or less negligible with the smooth wheel (the rough PVC being a few decibels louder in the range of 70–300 Hz), the rough PVC was actually quieter than the smooth PVC with the flat wheel above 500 Hz. This may be due to uncertainties in the measurement procedure, such as the trolley speed.

The presence of wheel flats was found to have a far greater effect on the radiated sound than the type of floor used. The flat wheel rolling on the soft PVC was still significantly louder than the smooth wheel rolling on the bare concrete. Only the fiberwood underlayer provided enough damping to bring the flat wheeled trolley down to levels on par with the concrete + smooth wheel configuration. Even then, this was only the case for frequencies above 200 Hz. Because the floor coverings were only placed on the section of the floor upon which the trolley rolled, the rest of the floor was left bare. The covering and underlayer (if present) act as a spring-mass insulator in this situation. There is thus no need to cover the floor for this kind of excitation.

Figure 4.14 shows the benefit of applying the rough and smooth PVC floor coverings on bare concrete for a trolley with a 10 kg added load. Here it becomes easier to see how the

performance of the floor covering changes with frequency. Both rough and smooth PVC floor coverings provide nearly the same benefit for the smooth wheel. However, the rough PVC performs better than the smooth PVC when a flat wheel is used.

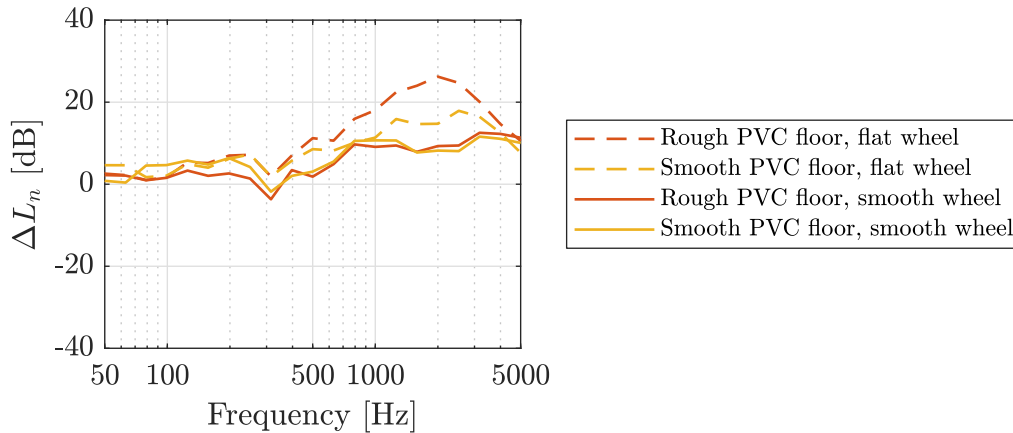


Figure 4.14: Benefit of applying the rough and smooth PVC floor coverings for a trolley with a 10 kg added load at the industrial partner in France.

Because the ΔL_n plot masks the absolute performance of each floor covering, they can sometimes suggest misleading results. Looking at Figure 4.14, one might believe that both PVC floor coverings perform significantly better for the case of the flat wheel than for the smooth wheel. However, this only appears to be so because the absolute levels in the case of the smooth wheel are so low to begin with (i.e. the smooth wheel does not ensure a sufficient signal to noise ratio (SNR) with the noise floor). Were the noise floor of the test facility much lower, it would be reasonable to expect the smooth wheel curves in Figure 4.14 to follow the upward trend exhibited by the flat wheel curves above 700 Hz. Both the absolute and the relative performance curves are beneficial in understanding the full story.

Influence of added load

Figure 4.15 shows the normalized sound pressure level in the reception room due to rolling noise for varying added loads, in the case of both a smooth and flat wheel. For all of these runs, the trolley speed was 0.6 m/s and the floor was concrete. The large difference between smooth and flat wheel for all loads can once again be seen. Interestingly enough, varying the load did not greatly change the radiated sound level. The difference between the 10 kg and 20 kg configurations was largely negligible for both smooth and flat wheel. Moving up to 30 kg reduced the sound level a bit more across the frequency spectrum: slightly more for the smooth wheel than for the flat wheel.

The fact that increasing the load can result in a decrease in sound level may seem counter-

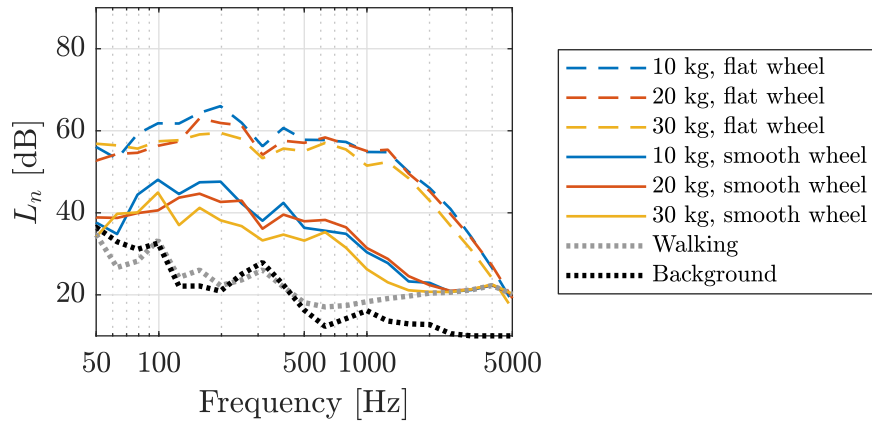


Figure 4.15: Rolling test results for varying added load at the industrial partner in France. All runs were done on the concrete with smooth PVC floor covering at a trolley speed of 0.6 m/s.

intuitive. After all, a higher load results in a higher injected force into the floor, which is what is acting as the dominant radiation source. However, increasing the load also reduces the vertical motion of the trolley, which lessens the magnitude of the injected force. The fact of the matter is that the injected force increase due to a higher static load is not sufficient to overcome the simultaneous injected force decrease due to the greater inertia of the system. The inertial effect may be slightly more dominant, resulting in a mild decrease in sound level, or the two may more or less cancel each other out, resulting in a largely similar sound level.

Additionally, as the load on the trolley increases, the roughness asperities in contact with one another between the when and floor change, as the higher load causes the two surfaces to be pushed further into one another. Thus the effective surface roughness seen by the contact area is reduced as the load increases. This causes a slight reduction in excitation, and thus a slight reduction in radiated sound level.

Among all the variables present in the rolling noise scenario, the total mass of the trolley plus added load plays the lowest role. Provided the trolley is at least sufficiently heavy to eliminate wheel rattle (which may occur for a very light trolley if there is loss of contact between the wheels and floor during rolling), increasing the load any further provides little acoustic benefit.

Figure 4.16 shows how the benefit of adding a rough PVC floor covering changes with trolley added load. The performance of the rough PVC is mostly independent of the added load on the trolley, though the benefit does drop moderately for a 30 kg added load with the smooth wheel. Once again, this does not mean that the 30 kg load and smooth wheel was *louder*, it simply means that the relative benefit diminishes slightly with increasing load. In the case of the flat wheel, the added load has less of an effect as the effect of the wheel flats already dominates.

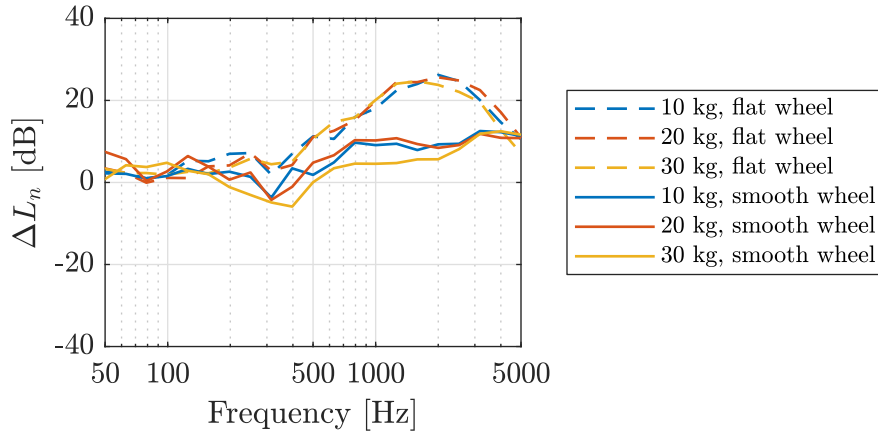


Figure 4.16: Change in benefit from applying the rough PVC floor covering due to changing trolley added load at the industrial partner in France.

Influence of trolley speed

The influence of trolley speed was not studied in this measurement campaign. It will be addressed in the second measurement campaign presented in Section 4.4.

4.3.2 Comparison with a second trolley

The modifications made to the test trolley in Section 4.2 (filling the hollow trolley frame with sand and wrapping the axles with Teflon tape) were done in order to reduce the residual rattling and ringing that would otherwise occur during rolling. In a preliminary study conducted several years prior to the current one, a previous test trolley had been manufactured which did not include the wrapped axles (the older trolley was otherwise identical in construction to the newer test trolley). The two trolleys were both fabricated by the same manufacturer using the same plans. As a way of quantifying the repeatability of the rolling noise test, a number of measurements were performed with the old test trolley and compared with those of the new one.

Figure 4.17 shows the normalized sound pressure level in the reception room due to rolling noise from the new and old trolleys on concrete. As the trolley frame, axle, and wheels themselves were all interchangeable, four permutations were tested for comparison. For all of these runs, the trolley speed was 0.6 m/s, the added load was 10 kg, and the wheels with flat spots (either new or old) were used.

The effectiveness of the Teflon in reducing axle/wheel rattle is seen in the difference in blue and orange curves above 500 Hz. The peak at 160 Hz in the purple curve is likely due to the excitation of the old trolley frame. However, in comparing the old and new trolleys (e.g. the purple vs blue curves), we see that the old trolley was overall quieter than the new trolley for

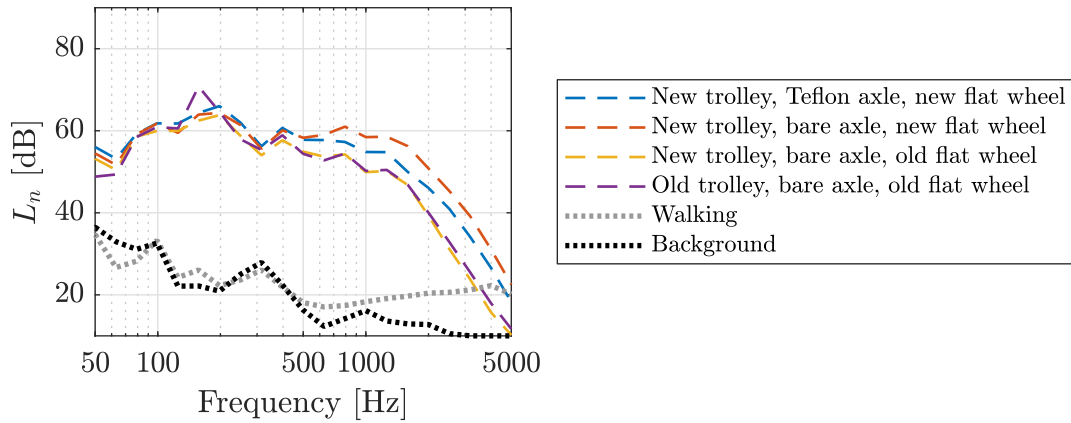


Figure 4.17: Normalized sound pressure level of the new and old two-wheeled trolleys in various wheel and axle configurations on concrete at the industrial partner in France. For all curves, the trolley speed was 0.6 m/s, the added load was 10 kg, and the wheels with flat spots (either new or old) were used.

the run tested. While the curves are largely similar, the differences which do exist among them show that repeatability and variation between identical runs can be an issue in rolling noise. This topic is explored further in Section 4.4. Because speed was not tightly controlled in these measurements, it is possible that variations in trolley speed are contributing to the differences seen in Figure 4.17.

Figure 4.18 shows how the benefit of adding a rough PVC floor covering changes with various trolley configurations. For all curves, a 10 kg added load as used. While it is shown in Figure 4.17 for the concrete floor, the configuration of the old trolley, bare axle, and old flat wheel is not shown here, as it was unfortunately not measured on the rough PVC floor covering. The performance of the rough PVC floor covering is largely the same for all configurations. The only significant deviations occur at high frequencies, where the absolute level are already quite low.

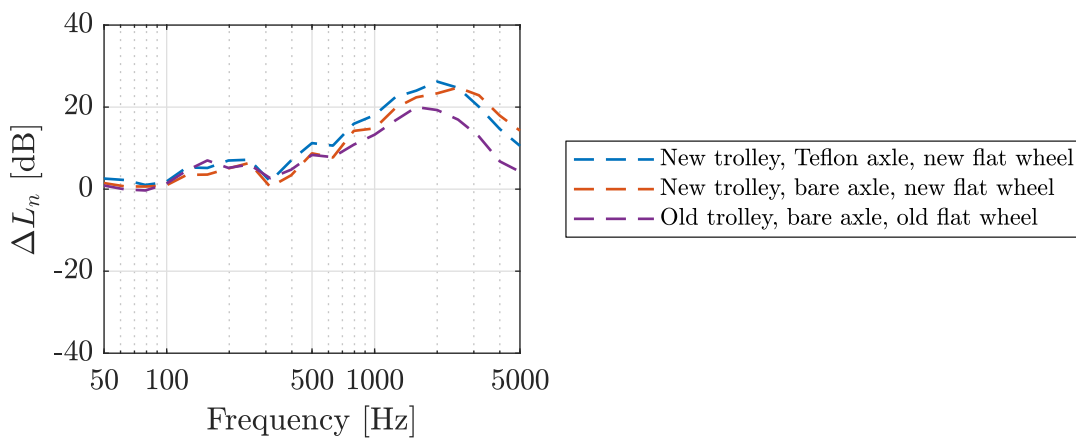


Figure 4.18: Change in benefit from applying the rough PVC floor covering for various new and old trolley configurations at the industrial partner in France. For all curves, a 10 kg added load as used.

Figures 4.14, 4.16 and 4.18 together demonstrate that the performance of the PVC floor covering is largely independent of external factors. For the most part, it provides the same benefit regardless of trolley configuration.

4.3.3 Global indicators

Often in the field of building acoustics, the performance of an acoustic solution is reduced to a single-number value. This has its drawbacks, as it greatly simplifies the story and removes any information regarding frequency dependency. However, it can still be beneficial, particularly when presenting performance data to those who are not experts in the field. For impact noise, ISO 717-2 defines the weighted normalized sound pressure level $L_{n,w}$, which is the single-number quantity derived from the normalized sound pressure level L_n [118]. An illustration of the process is shown in Figure 4.19. It is calculated by first overlaying a reference curve on top of the L_n curve for a given measurement, both in 1/3 octave band frequencies. The reference curve is continually shifted downward in 1 dB increments while the sum of unfavorable deviations remains greater than 32 dB. Once the reference curve can no longer be shifted further without violating the criterion, the value of the reference curve at 500 Hz is chosen as the $L_{n,w}$ indicator for that measurement.

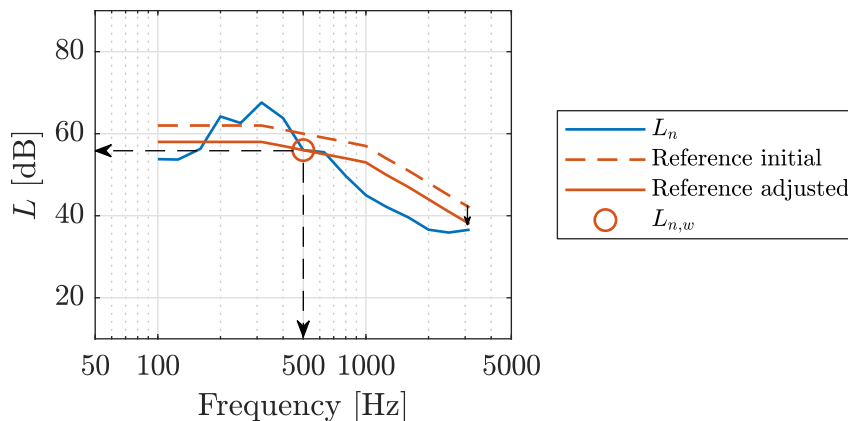


Figure 4.19: Example calculation of the weighted normalized sound pressure level indicator $L_{n,w}$ as outlined in ISO 717-2 [118].

In addition to the weighted normalized sound pressure level, ISO 717-2 also provides a procedure for calculating an adaptation term C_I . In the scope of impact noise, it is used to take into account the fact the $L_{n,w}$ indicator does not sufficiently consider level peaks at low frequencies. This can commonly occur for timber joist floors or bare concrete floors without added floor

coverings. It is calculated as

$$C_I = 10 \log \sum_{i=1}^k 10^{L_i/10} - 15 - L_{n,w} \quad (4.18)$$

where the first term indicates the log sum of the L_n curve over each 1/3 octave frequency band in the range 100–2 500 Hz. The adaptation term is designed such that a massive floor with an effective covering will have a C_I of about zero, and a floor with large low frequency peaks will have a C_I which is slightly negative. When used together, the two indicators are expressed as a sum, i.e. $L_{n,w} + C_I$.

The calculation for the adaptation term may alternatively be conducted over the enlarged range of 50–2 500 Hz, in which case it is denoted as $C_{I,50-2500}$. This is likely to be more appropriate for the case of rolling noise, due to the fact that the majority of the acoustic energy exists in this low frequency range.

Table 4.4 shows the calculated indicators for a number of the measurements conducted at the industrial partner in France using the two-wheeled trolley. The weighted normalized sound pressure level $L_{n,w}$ is shown alone, as well as with each of the two adaptation terms: $L_{n,w} + C_I$ and $L_{n,w} + C_{I,50-2500}$. The adaptation terms have a tendency to change the global indicator by ± 1 dB, though some cases (e.g. rough PVC + fiberwood) do exhibit larger modifications. Here the adaptation term is correcting for any deviations which may have been introduced into the global indicator in the low frequency range via the shape of the reference curve (particularly for $L_{n,w} + C_{I,50-2500}$).

Figure 4.20 shows $L_{n,w} + C_{I,50-2500}$ versus the added load for the different two-wheeled trolley configurations. A line of best fit has been added for each configuration to show general trends in the data. The coefficients of determination R^2 for the trend lines are also shown. The difference between flat and smooth wheels is present, as well as the relative difference of adding the rough floor covering. In comparing with Figure 4.13, we see that the global indicator does have a tendency to mask part of the story. The difference in mid to high frequency between the smooth wheel on concrete and the smooth wheel on rough PVC is hidden when only looking at the respective $L_{n,w} + C_{I,50-2500}$ values. However, this is to be expected to some degree, as it is a known drawback of single-number values: the greater the curves vary in spectral content, the less representative their global indicators will be. Configuration changes which result in a broadband change in sound level will be reflected in a proportionally changing $L_{n,w} + C_{I,50-2500}$, but configuration changes which only affect certain octave bands will not have as great an influence. This topic of global indicators will be expanded upon in the next section, which details a second round of measurements performed at a different location.

Table 4.4: Global indicators for the two-wheeled trolley rolling noise measurements at the industrial partner in France.

Floor	Wheel	Added Load [kg]	$L_{n,w}$ [dB]	$L_{n,w} + C_I$ [dB]	$L_{n,w} + C_{I,50-2500}$ [dB]
Concrete	Flat	10	58	57	57
		20	56	55	55
		30	54	53	53
Concrete	Smooth	10	39	39	40
		20	37	36	37
		30	34	34	35
Rough PVC	Flat	10	51	51	52
		20	49	50	50
		30	48	48	49
Rough PVC	Smooth	10	37	37	37
		20	34	34	35
		30	33	33	34
Smooth PVC	Flat	10	51	52	52
	Smooth	10	35	35	35
Rough PVC + fiberwood	Flat	10	43	45	47
	Smooth	10	30	28	30
Walking	–	–	28	21	24
Background	–	–	21	21	26

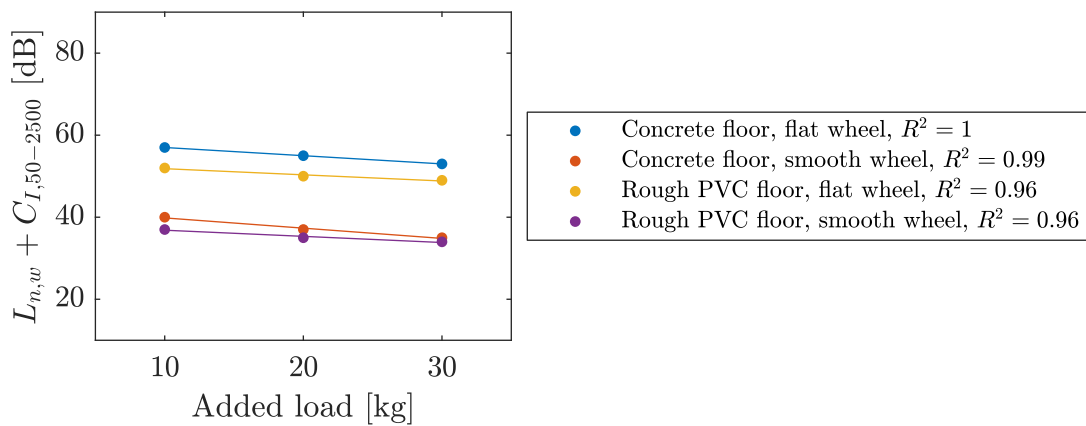


Figure 4.20: Global indicator $L_{n,w} + C_{I,50-2500}$ versus added load of the two-wheeled trolley at the industrial partner in France.

4.3.4 Test conclusion

The testing performed in the two-story reverberation room at the industrial partner in France provided not only insight into the influencing factors of rolling noise, but also guidance on how to improve the reliability of future tests. The testing provided confirmation that repeatability may be achieved when using test trolleys manufactured at different times, but following the same design. This may not seem significant, but it is important for development of a standard rolling device, where consistency and repeatability are paramount. For more on this topic, see Appendix A.

4.4 Rolling noise location two: Industrial partner in the Netherlands

The second round of tests were conducted in a two-story transmission room at Level Acoustics & Vibration in Eindhoven, the Netherlands. This provided an opportunity to not only build upon lessons learned in the first round of testing, but also acquire a second data set at a different location, which is useful for determining the measurement repeatability.

The T_{20} reverberation time of the reception room is shown in Figure 4.21. This yields a Schroeder frequency of 267 Hz, which is fortunately lower than that of the industrial partner in France (due mainly to the larger volume, which was 80 m^3 for both emission and reception rooms).

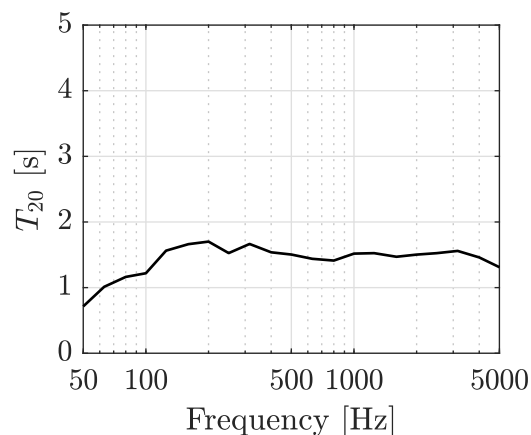


Figure 4.21: T_{20} reverberation time of the reception room at Level Acoustics & Vibration

As shown in Figure 4.22, there was an opening in between the two rooms, inside which a custom floor was installed for testing. This opening, having dimensions $3 \text{ m} \times 3 \text{ m}$, was filled with a 10 cm thick isolated concrete slab. The word “isolated” refers to the fact that the slab was supported around its perimeter by elastic supports, which effectively decoupled the slab from

the surrounding floor structure. This was done to ensure that the microphone in the reception room below was only measuring the direct structure-borne noise transferred vertically through the slab when the trolley was rolled in the emission room above. Thus, flanking transfer paths were eliminated.

Placing concrete slab on an elastic foundation essentially created a very large spring-mass-damper system. The material that was used as the elastic foundation around the perimeter of the slab was chosen such that the structure as a whole had a vertical natural resonance frequency of 10 Hz. This was deemed sufficiently low that excitation by the rolling trolley (essentially acting as a force input to the spring-mass-damper system) would not cause an erroneously large response.

4.4.1 Floor transmission loss

To ensure there was no contact between the concrete slab and the surrounding floor, a small gap was left around the perimeter. Before testing could begin, it was necessary to ensure that the construction of the slab was not allowing for sound transmission in excess of what would be expected by a normal 10 cm thick concrete floor. To verify this, the transmission loss (TL) of the slab was measured in accordance with ISO 10140-2 [4]. A pink noise signal was played in the emission room from two loudspeakers placed at non-symmetrical positions and angles (with respect to both one another and the room walls & floors). The sound pressure level in the emission and reception rooms was measured, and their difference used in order to calculate the TL due to the presence of the concrete slab. This was done in accordance with ISO 10140-2 [119] using

$$TL = L_1 - L_2 + 10 \log \left(\frac{S}{A} \right) \quad (4.19)$$

where L_1 is the measured sound pressure level in the emission room and L_2 is the measured sound pressure level in the reception room. Here A is taken as the equivalent absorption area of the reception room and S the surface area of the slab.

The TL test was performed for two floor configurations: one with just the concrete slab resting on its elastic perimeter foundation, and a second with mineral wool insulation placed in the gap formed between the slab and the floor opening. The gap with the added mineral wool can be seen in Figure 4.23. Inside this gap, the only barrier between the emission room and the reception room is the elastic foundation itself. Thus the mineral wool was added with the hypothesis that it would increase the TL between the two rooms in the event that the TL of the slab alone was insufficient to match that of a normal 10 cm concrete floor.

Similar to Equation (4.19), the benefit the mineral wool provides may be quantified using its

Concrete floor

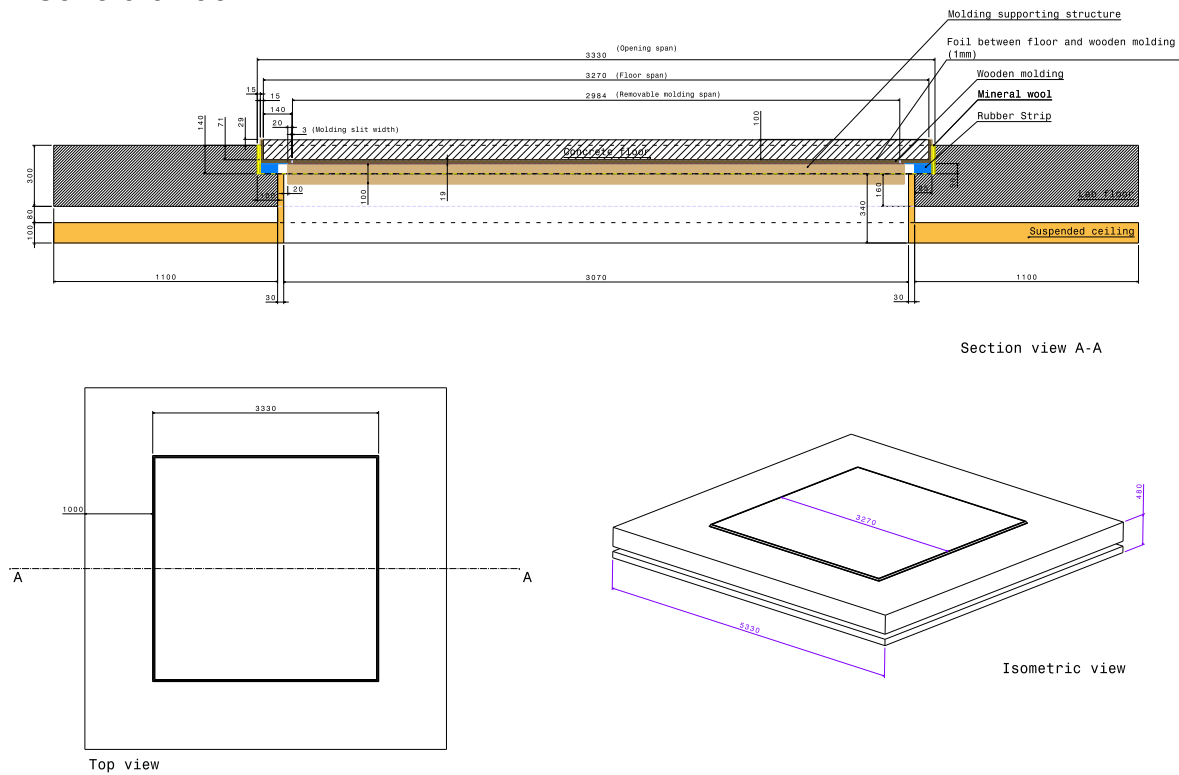


Figure 4.22: Schematic of the concrete floor installed in the two-story transmission room at Level Acoustics & Vibration. The wooden molding and molding support structure were only present while pouring the concrete and waiting for it to dry: they were removed prior to testing.



Figure 4.23: Concrete slab with mineral wool insulation placed in the gap between the perimeter of the slab and the surrounding floor at Level Acoustics & Vibration.

insertion loss (IL). This was calculated using

$$IL = TL_1 - TL_2 \quad (4.20)$$

where TL_1 and TL_2 are the TL of the concrete slab with and without the added mineral wool.

Figure 4.24 shows the TL of the two configurations, as well as the IL of the mineral wool.

With no added insulation, the concrete slab provided a roughly 40 dB benefit across the entire spectrum, varying as low as 27.5 dB and as high as 57.6 dB depending on frequency. Adding insulation increased the TL in the high frequency range up to as high as 65.8 dB. While the mineral wool provided negligible IL below 500 Hz, the IL above 500 Hz was generally greater than 10 dB.

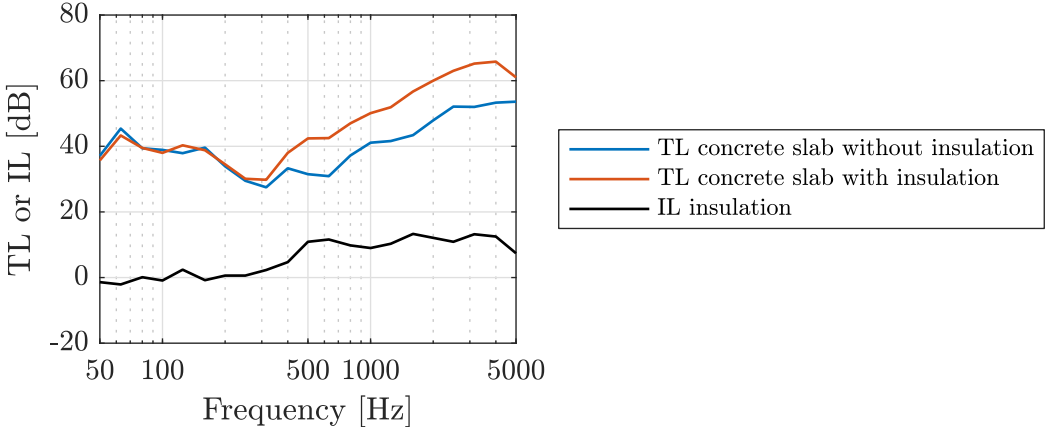


Figure 4.24: TL of the concrete slab with and without the mineral wool insulation, as well as the calculated mineral wool IL at Level Acoustics & Vibration.

Figure 4.25 shows the TL of the two configurations compared to the expected TL of a standard 10 cm concrete floor. The expected TL was estimated using Bassist.Lab, an in-house simulation software package developed by Level Acoustics & Vibration. While the concrete slab alone was not sufficient in reproducing the desired TL, the addition of the mineral wool increased the TL to be on par with that of the normal 10 cm floor. Thus, for all subsequent tests performed, the merino wool was left inserted in the gap. Note that the results in Figure 4.25 are shown in full octave bands.

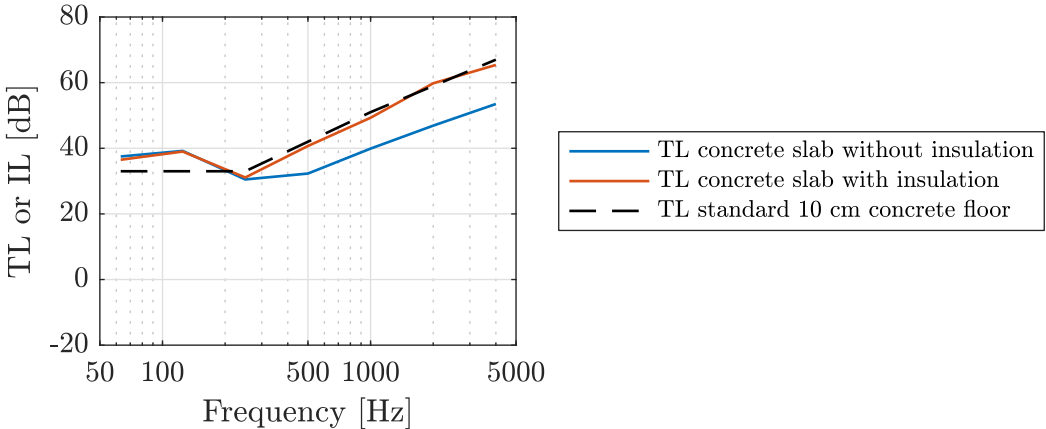


Figure 4.25: Comparison between measured and expected TL at Level Acoustics & Vibration. Results in full octave bands.

4.4.2 Rolling noise: Test trolley

A schematic of the measurement setup used for the rolling tests is shown in Figure 4.26. The same measurement procedure that was used in the previous round of testing at the industrial partner in France was again used here. Five stationary microphones were used in the emission room, and a single rotating boom microphone was used in the reception room. For each run, the recordings from the five stationary microphones were averaged together, resulting in a single sound pressure recording for the emission room and a single sound pressure recording for the reception room. The microphones in the emission room were G.R.A.S. 46AF 1/2 inch LEMO free field standard microphones with integrated preamplifiers. The microphone in the reception room was a Brüel & Kjær 4189 1/2 inch BNC free field standard microphone with integrated preamplifier. Data was acquired using a G.R.A.S 12AG 8-channel power module and RME Fireface UCX (18 I/O) interface. The emission room from the test is shown in Figure 4.27. While measurements were recorded in the emission room, they were not used for any further analysis.

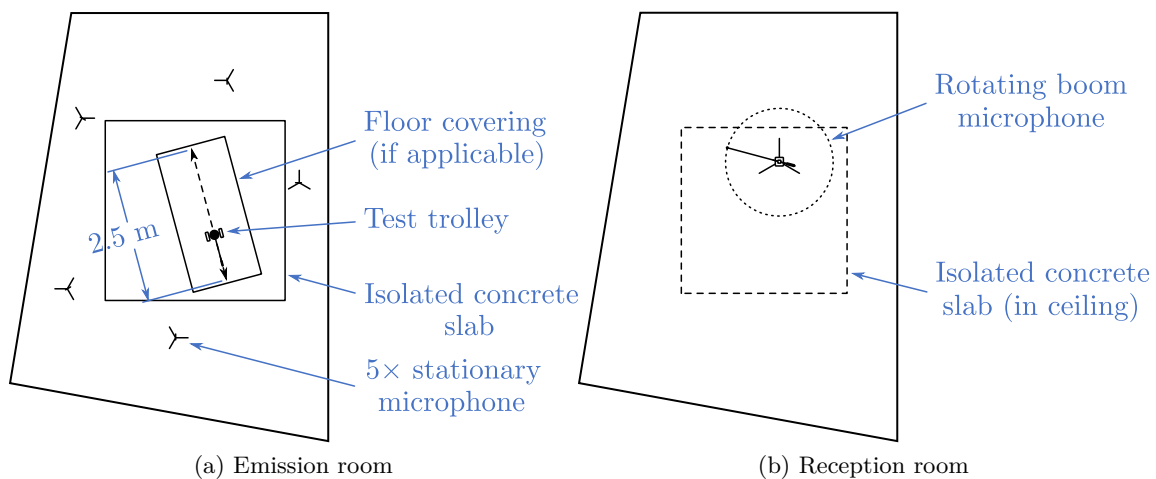


Figure 4.26: Measurement setup for the rolling test conducted at Level Acoustics & Vibration .

The varying parameters of the test were the floor type, the wheel type, the trolley speed, and the added load on the trolley. These are summarized in Table 4.5. Three different weight configurations were used: 10, 20, and 30 kg. These added loads were all in addition to the 7 kg mass of the trolley itself. The trolley was rolled on the bare polished concrete floor, as well as two types of PVC floor coverings: one smooth and one rough. The PVC floor coverings used for testing at Level Acoustics & Vibration were the same ones used for both the roughness measurements and the testing at the industrial partner in France. The trolley was rolled with two different types of plastic cylindrical wheels installed: both with a 5 cm radius and 3.5 cm width. The two types of wheels were identical in construction, with the exception that one



Figure 4.27: Emission room at Level Acoustics & Vibration.

set (denoted the “flat” wheel) had a series of flat spots (depth 0.5 mm) milled into the rolling surface of the wheel. The wheel without flat spots was denoted the “smooth” wheel. These are the same floors and wheels that had their roughness profiles measured in Section 4.1. The tile floor had its roughness profile measured, but was never used for rolling noise testing, as it was too impractical to install a full tile floor on top of the concrete slab.

Table 4.5: Test parameters used in the rolling noise test at Level Acoustics & Vibration

Floor	Wheel	Load	Speed
Concrete	Smooth	10 kg	0.5 m/s
Concrete + rough PVC	Flat	20 kg	0.9 m/s
Concrete + smooth PVC		30 kg	1.6 m/s

Three different trolley speeds were used: 0.5, 0.9, and 1.6 m/s for the tests. These were selected empirically, in an attempt to capture “low”, “medium”, and “high” speed scenarios. 0.9 m/s was first chosen as the “medium” speed, as observation showed that this was a comfortable speed to push the trolley while walking normally. Originally, the hypothesis was that the average preferred walking speed of humans should be used, which is 1.4 m/s [120]. However, in preliminary testing it was found that this was actually quite a bit higher than the speed at which an operator would naturally be inclined to push a heavy trolley. The added resistance provided by the trolley resulted in a drop in preferred walking speed. This new preferred speed was found to be around 0.9 m/s. From there, speeds slightly below and slightly above were chosen as the “low” and “high” speeds. Similar to the medium speed, these were chosen through trial and error. It was found that any lower than 0.5 m/s, and the sound level would approach the noise floor of the room, making accurate measurements difficult. Any higher than 1.6 m/s, and the trolley became difficult to operate consistently, especially with the higher added loads. Thus, the three speeds were chosen.

The floor type, wheel type, and added load parameters were tested for all possible permutations at a trolley speed of 0.9 m/s. This yielded eighteen test configurations. The low and high trolley speeds were tested for all floor and wheel types, but only for the 10 kg added load. This yielded an additional twelve configurations. Thus a total number of thirty configurations were tested.

The issue of controlling trolley speed was made even more complicated by the fact that, since the trolley was being rolled in a linear back-and-forth motion along the floor, the speed was not constant over the entire data acquisition period. Every time the operator reached the end of the rolling area, he would need to bring the trolley to a stop for an instant before beginning to roll it again in the opposite direction. Thus, the true speed of the trolley versus time was not constant, but somewhat periodic. An example is shown in Figure 4.28 for what this might look like for a trolley which performs a “down and back” trajectory across the rolling area.

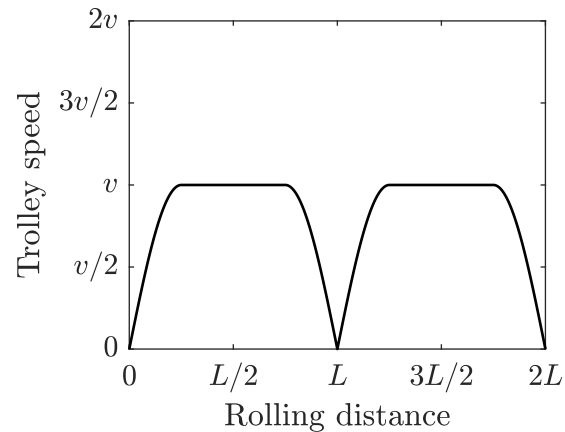


Figure 4.28: Variable speed of the trolley when rolling in a linear trajectory

To remedy this to the greatest extent possible, the operator wore a wireless earpiece which played a metronome set to a tempo which matched the desired rolling speed. By regulating the speed such that the metronome would click as the trolley reached each end of the rolling distance, as well as at the midpoint, the average speed over the course of the entire measurement would be equal to the desired trolley speed. For a rolling distance of 2.5 m and chosen speeds of 0.5, 0.9, and 1.6 m/s, this corresponded to tempos of 25, 43, and 74 beats per minute (BPM) respectively. In addition, For each configuration a total of five runs were conducted and averaged together. This allowed for further reduction of variability due to small differences in trolley speed.

Influence of floor and wheel type

Figure 4.29 shows the normalized sound pressure level in the reception room due to rolling noise for all floor and wheel types. For all of these runs, the trolley speed was 0.9 m/s and

the added load was 10 kg. The spectra of the background noise and noise generated due to the walking of the operator alone are also shown. For the rolling noise spectra, errors bars at each 1/3 octave band frequency show ± 1 standard deviation for the five repeated runs.

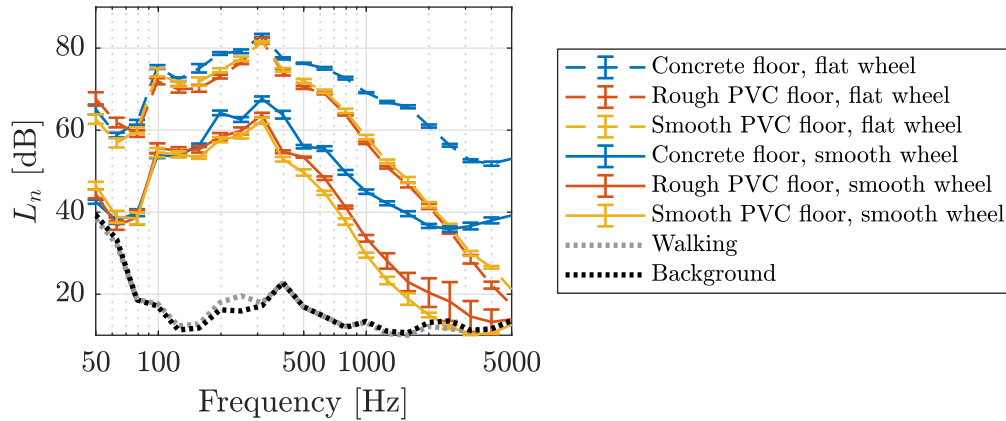


Figure 4.29: Rolling test results for varying floor and wheel type at Level Acoustics & Vibration. All runs were done with a trolley speed of 0.9 m/s and an added load of 10 kg.

Several observations may be made from this graph. The noise generated due to the walking of the operator is once again negligible. Both PVC floor coverings again provided a reasonable benefit over the bare concrete alone above 200 Hz due to their lower elasticities: this time greater than for the test at the industrial partner in France. The greater consistency in trolley speed allowed it to be revealed that the rough PVC was slightly louder than the smooth PVC, though this difference was negligible for the flat wheel. The elasticity of a given floor layer does indeed have a greater influence on the radiated sound than its surface roughness.

The presence of wheel flats was again found to have a far greater effect on the radiated sound than the type of floor used. The flat wheel rolling on the soft PVC was still significantly louder than the smooth wheel rolling on the bare concrete. For this test, the PVC provided a similar benefit over the bare concrete in the case of both smooth and flat wheels. This suggests that the effect of adding a floor covering may be more or less independent of the wheel type.

Finally, the standard deviations between the individual runs were quite low for all cases. This validated the method of using a metronome as an effective means of controlling the trolley speed.

Figure 4.30 shows the benefit of applying the rough and smooth PVC floor coverings on bare concrete for a trolley with a 10 kg added load. Once again, both PVC floor coverings provide a most or the less consistent benefit regardless of trolley configuration.

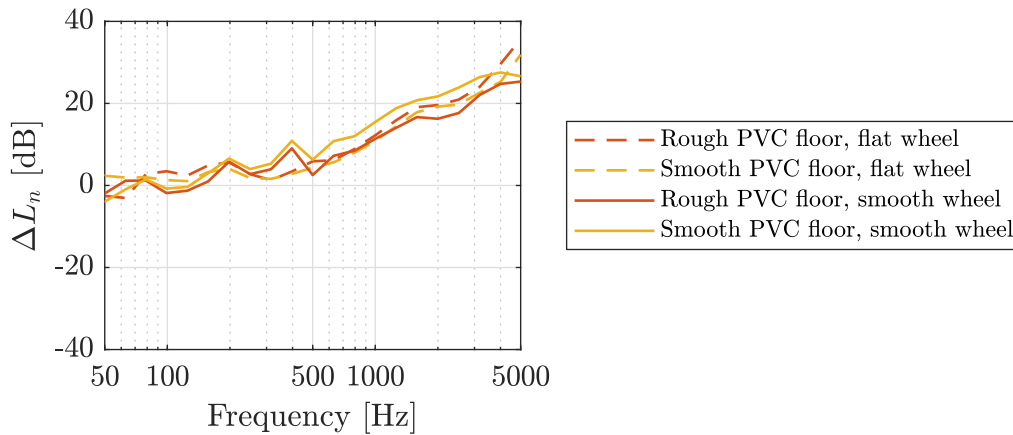


Figure 4.30: Benefit of applying the rough and smooth PVC floor coverings for a trolley with a 10 kg added load at Level Acoustics & Vibration.

Influence of added load

Figure 4.31 shows the normalized sound pressure level in the reception room due to rolling noise for varying added loads, in the case of both a smooth and flat wheel. For all of these runs, the trolley speed was 0.9 m/s and the floor was concrete. The large difference between smooth and flat wheel for all loads can once again be seen. Similar to the previous round of tests, varying the load did not greatly change the radiated sound level. For the case of the smooth wheel, increasing the load caused a small reduction in sound level at low frequencies and a small increase in sound level at high frequencies. The flat wheel exhibited essentially no noticeable change in sound level with changing load.

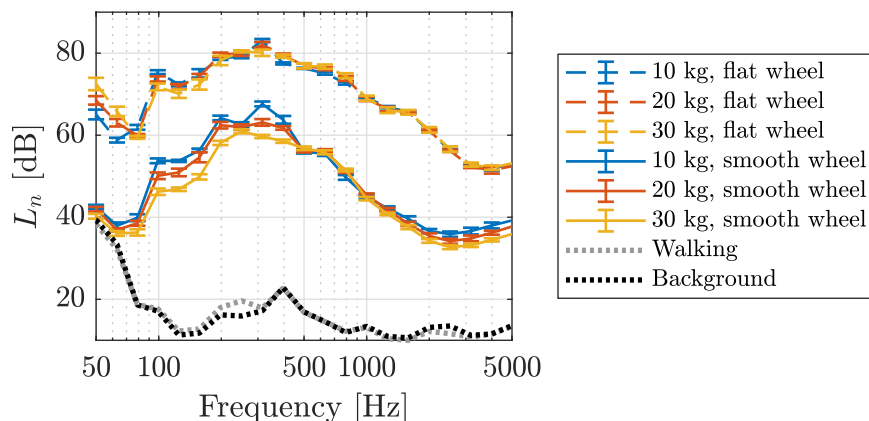


Figure 4.31: Rolling test results for varying added load at Level Acoustics & Vibration. All runs were done on the concrete floor with a trolley speed of 0.9 m/s.

Figure 4.32 shows how the benefit of adding a rough PVC floor covering changes with trolley added load. These curves show a slight link between floor covering performance and added load, though this link is actually opposite between smooth and flat wheels. The type of excitation

on the floor is different between the smooth and flat wheel: the latter exhibiting properties of impact noise as well as rolling noise. Thus the influence of a higher kinetic energy (due to a higher added load) is more pronounced in the case of the flat wheel. Nevertheless, the link between added load and floor covering performance is still small.

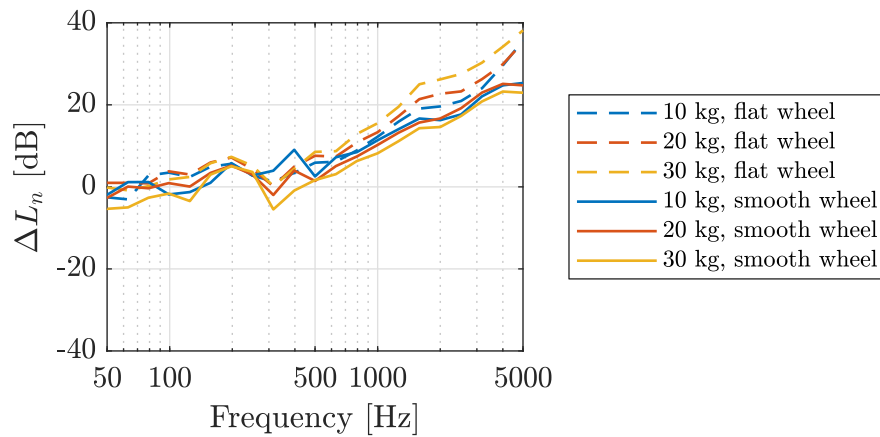


Figure 4.32: Change in benefit from applying the rough PVC floor covering due to changing trolley added load at Level Acoustics & Vibration.

Influence of trolley speed

Figure 4.33 shows the normalized sound pressure level in the reception room due to rolling noise for varying trolley speed, in the case of both a smooth and flat wheel. For all of these runs, the added load was 10 kg and the floor was concrete. The high influence that the trolley speed has on the radiated sound level becomes apparent here. The effect of the speed may even eclipse the effect of the wheel type for mid to high frequencies if the speed difference is sufficiently large: for example, when comparing the smooth wheel at 1.6 m/s to the flat wheel at 0.5 m/s. Raising the speed results in a mostly broadband increase in sound level for a given wheel type. There is a slight upward frequency shift present as well, but its effect is very minimal. In theory, changing the speed will change the roughness wavelengths which are excited in the contact area. However, because the roughness profiles are largely random in nature (as demonstrated in Section 4.1), and also possibly due to the higher than normal mobility of the 10 cm concrete slab, this effect is minimal.

Figure 4.34 shows how the benefit of adding a rough PVC floor covering changes with trolley speed for a 10 kg added load. The benefit is more or less consistent with changing speed for both smooth and flat wheels. The deviations in curves in the high frequency range are due to the absolute curves hitting the noise floor at different points in the frequency range, not due to differences in floor covering performance.

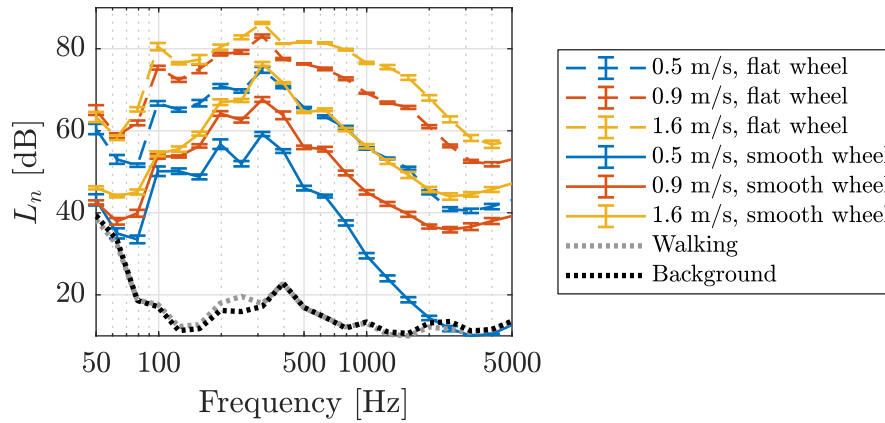


Figure 4.33: Rolling test results for varying trolley speed at Level Acoustics & Vibration. All runs were done on the concrete floor with an added load of 10 kg.

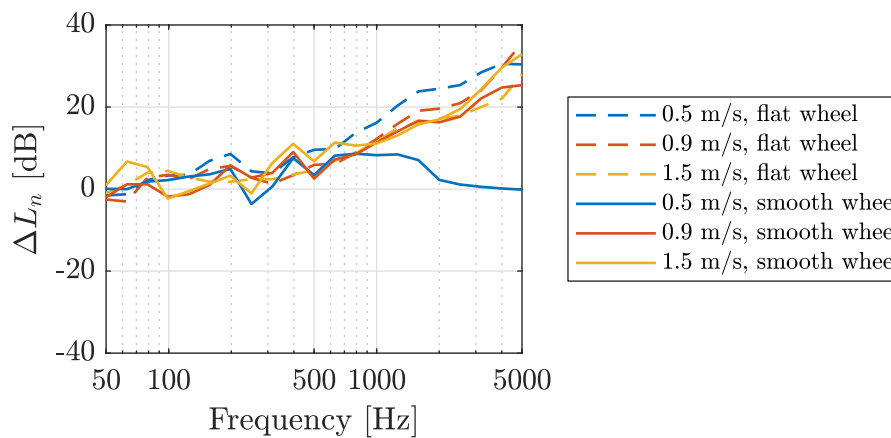
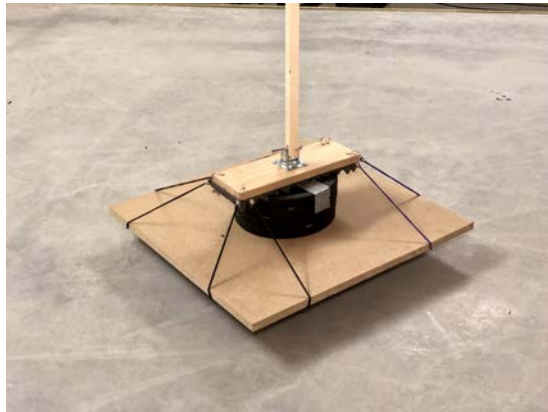


Figure 4.34: Change in benefit from applying the rough PVC floor covering due to changing trolley speed at Level Acoustics & Vibration.

4.4.3 Rolling noise: Three-wheeled trolley

In addition to the measurements performed with the two-wheeled test trolley, a different three-wheeled trolley was also built and used for a number of supplemental tests. This was done to investigate a number of parameters which were not easily modifiable on the two-wheeled trolley: the wheel spacing, wheel material, and rolling trajectory. The trolley is shown in Figure 4.35. It consisted of a simple design: three 360° swivel wheels, spaced equally apart from one another, were affixed to a solid piece of medium-density fiberwood (MDF). The distance of each of the wheels from the center of the board (and the wheels themselves) could easily be changed for measuring the effect of wheel spacing and wheel material on the radiated sound level. An additional 360° swivel joint was used to attach a push arm to the top side of the trolley. This, combined with the wheels, permitted the trolley to be pushed in along any trajectory without the need for the operator to move position: thus allowing for the effect of rolling trajectory to be measured.



(a) Top view



(b) Bottom view

Figure 4.35: Three-wheeled test trolley used for supplemental testing. The wheel type, wheel spacing, and added load were all easily interchangeable. The 360° swivel wheels allowed to smoothly change the rolling trajectory without sliding between the wheels and the floor.

Three wheels were used, all of which were the same width (2 cm) and radius (2.5 cm): wood, nylon, and aluminum. Three wheel spacings were used: placing the wheels at 12, 21, and 27 cm from the center of the MDF (the angular spacing stayed constant at 120°). The trolley was rolled in two trajectories: linear and circular. The linear trajectory was the same as the tests with the two-wheeled trolley, where the trolley was rolled forward 2.5 m, brought to a stop, and then rolled in the reverse direction 2.5 m to complete one period. This was repeated for the duration of the 15 second measurement. The only difference was that, as opposed to walking with the trolley as previous, the operator was able to stand to the side of the rolling area and remain stationary while he moved the trolley with the help of the swivel arm. This was found to be feasible at low trolley speeds and low added loads, but became more difficult to control (particularly to change direction) as speed and load increased.

For the circular trajectory, the operator stood in the center of the floor and rotated the trolley around him in a constant circular fashion at a radius of 1 m. A diagram of this setup is shown in Figure 4.36. For both linear and circular trajectories, the same metronome technique was used as before to ensure the operator was pushing the trolley at a constant speed of 0.9 m/s. This corresponded to 43 BPM for the linear trajectory (with four clicks per period) and 72 BPM for the circular trajectory (with eight clicks per period).

Influence of rolling trajectory

Figure 4.37 shows the normalized sound pressure level in the reception room due to rolling noise for linear and circular trajectory. For all of these runs, the trolley speed was 0.9 m/s, the added load was 10 kg, the wheel spacing was 21 cm, and the wheel material was nylon.

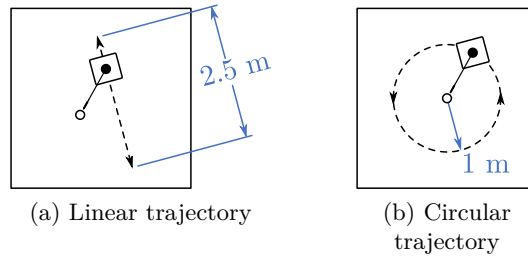


Figure 4.36: Diagrams of the three-wheeled test trolley trajectories.

The spectra of the background noise and noise generated due to the walking of the operator alone are also shown. As it was already determined that walking in the linear trajectory had no noticeable effect, here the spectrum from walking in the circular trajectory is shown. This is less-so walking and more-so stepping, as the operator needed to continuously rotate his body in place to keep facing the trolley as it traversed the circular path. Once again, for the rolling noise spectra, errors bars at each 1/3 octave band frequency show ± 1 standard deviation for the five repeated runs.

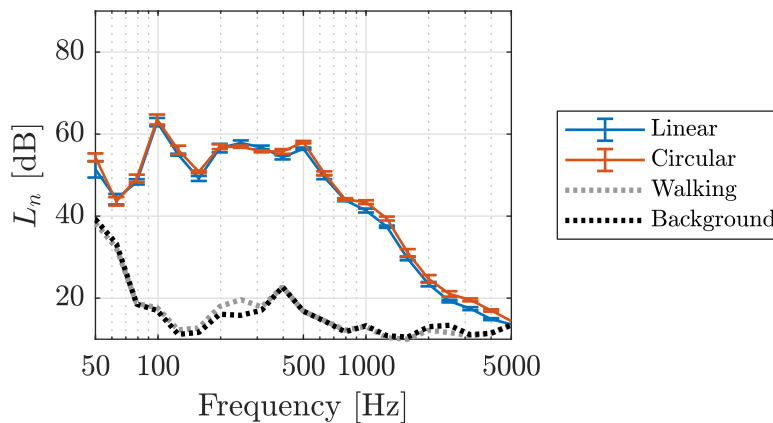


Figure 4.37: Rolling test results for varying rolling trajectory of the three-wheeled test trolley. All runs were done on the concrete floor with a 10 kg added load, 0.9 m/s trolley speed, 21 cm wheel spacing, and nylon wheel material.

There is very little difference between the sound spectra for the linear and circular trajectories: they are nearly identical. This justifies the use of a linear trajectory as a suitable replacement in standardized testing. In the velocity range at play here, there is a direct relationship between the speed of the trolley and its radiated sound level. Thus, as long as the average speed over a set measurement duration is the same, it may be assumed that amount of acoustic energy will be the same as well. The circular trajectory may still provide a benefit in some cases from a pragmatic perspective, as it is easier in this case to replace the operator by a rotating system (for the purpose of automating the rolling process).

Influence of wheel material

Figure 4.38 shows the normalized sound pressure level in the reception room due to rolling noise for the nylon, wood, and aluminum wheels. For all of these runs, the trolley speed was 0.9 m/s, the added load was 10 kg, the wheel spacing was 21 cm, and the rolling trajectory was circular.

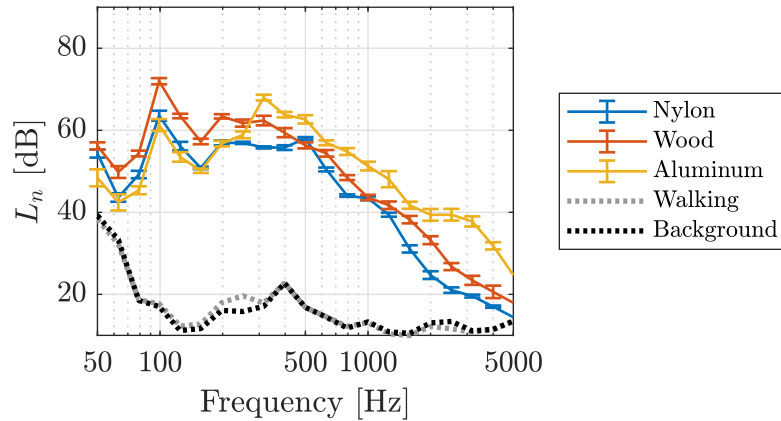


Figure 4.38: Rolling test results for varying wheel material of the three-wheeled test trolley. All runs were done on the concrete floor with a 10 kg added load, 0.9 m/s trolley speed, 21 cm wheel spacing, and circular rolling trajectory.

The relationship between wheel material and radiated sound level is well established. More specifically, what matters is the apparent Young's modulus E' , being a function of the Young's moduli and Poisson's ratio of both the wheel and floor. A higher E' causes a greater injected force into the floor, leading to a higher excitation. As the elasticity of the wheel increases, the radiated sound level should increase proportionally: this is exactly what is demonstrated here ($E_{\text{aluminum}} \approx 70$ GPa, $E_{\text{wood}} \approx 10$ GPa, and $E_{\text{nylon}} \approx 2$ GPa). However, while the effect is realized across the entire frequency spectrum for the wood and nylon wheels, the same cannot be said for the aluminum wheel. The aluminum wheel has a greater amount of acoustic energy above 250 Hz, but is more or less equivalent to the nylon wheel at low frequencies. It is possible that this discrepancy may be explained by the differences in roughness profiles, which unfortunately were not measured for these wheels. If the long wavelength asperities of the aluminum wheel's roughness profile are less significant than those of the wood and nylon wheel, less acoustic energy would be radiated in the low frequency range. Additionally, modification of the stiffness of the wheel implies a modification of the spring-mass system, which will change the response of the trolley as a result of the contact force.

Figure 4.39 shows how the benefit of adding a rough PVC floor covering changes with wheel material. For all curves, a 10 kg added load, 21 cm wheel spacing, and circular trajectory were used. Out of all the ΔL_n plots, this one shows the greatest deviation between curves. Indeed,

because the elasticity and roughness of each wheel is different, they all excite the floor covering differently. The rough PVC provides a greater benefit for the aluminum and wood wheels than it does for the nylon wheel.

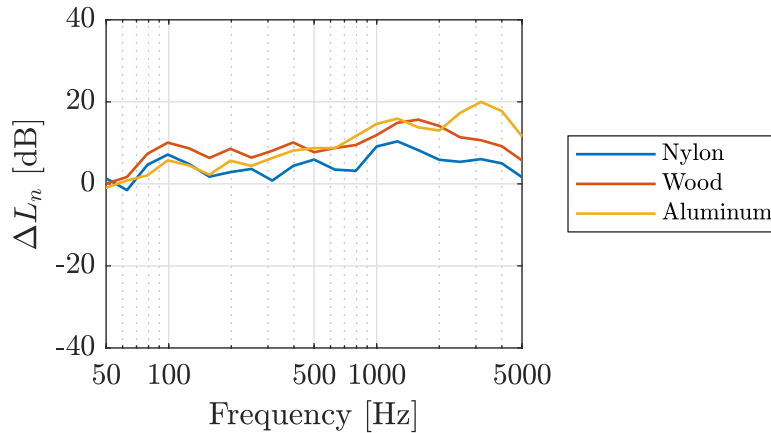


Figure 4.39: Change in benefit from applying the rough PVC floor covering due to changing wheel material.

Influence of wheel spacing

Figure 4.40 shows the normalized sound pressure level in the reception room due to rolling noise for the 12, 21, and 27 cm wheel spacings. For all of these runs, the trolley speed was 0.9 m/s, the added load was 10 kg, the wheel material was nylon, and the rolling trajectory was circular. The original hypothesis was that wheel spacing would not play a significant role in the radiated sound level. This turned out to not entirely be the case: enlarging the wheel spacing did mildly increase the radiated sound level in the range of 100–300 Hz. The opposite effect occurred below 100 Hz, though this result is less reliable considering the high modality of the room in this frequency range. Changing the wheel spacing changes the modes being excited on the floor and the trolley body. This change is slight, but in some cases, such as this one, it is enough to cause a difference in radiated sound level. These results show that modal behavior becomes increasingly influential as frequency decreases: both due to the structure-borne excitation of the trolley and the airborne room modes. Increasing the rigidity of the trolley would help to alleviate this problem.

4.4.4 Influence of floor mobility

As the concrete slab using in the rolling noise tests in the two-story transmission room is essentially a large spring-mass-damper system, it has its own frequency response function, which may influence its sound power radiation due to excitation by the rolling trolley. In order to

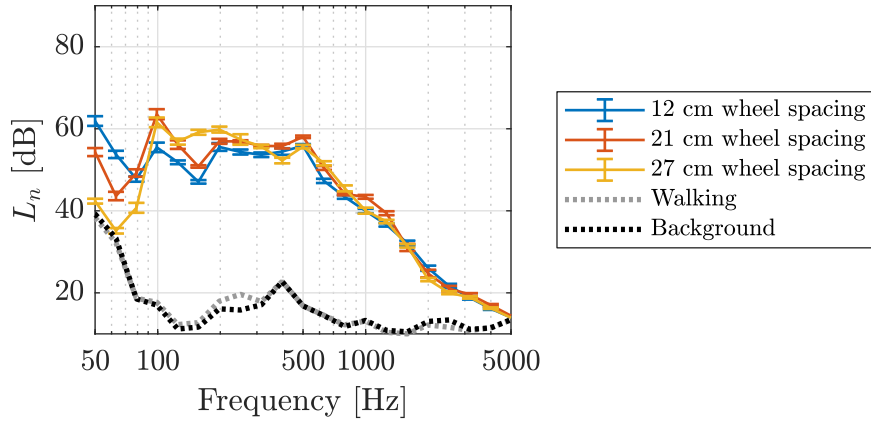


Figure 4.40: Rolling test results for varying wheel spacing of the three-wheeled test trolley. All runs were done on the concrete floor with a 10 kg added load, 0.9 m/s trolley speed, nylon wheel material, and circular rolling trajectory.

investigate this, the results from the rolling noise tests may be compared to the slab’s mobility, which was measured following the measurement procedure outlined in ISO-7626-2 [121]. Being the inverse of mechanical impedance, the mobility Y of a structure is a measure of the structure’s velocity response v to a force input F .

$$Y(f) = \frac{v(f)}{F(f)} \quad (4.21)$$

Figure 4.41 shows the measured magnitude and phase of the mobility of the 10 cm thick concrete slab in both narrow band and 1/3 octave bands, as well as the theoretical mobility of an infinite concrete plate of equal thickness. Comparing to Figures 4.29, 4.31, 4.33, 4.37, 4.38 and 4.40, the peaks at 100, 200, and 315 Hz align closely between sound level and floor mobility for many of the configurations. This helps to explain the elevated levels at these frequencies. The peaks in the mobility at 63 and 150 Hz, however, do not tend to reveal themselves in the sound pressure level results.

4.4.5 Global indicators

Table 4.6 shows the calculated global indicators for the measurements conducted at Level Acoustics & Vibration using the two-wheeled test trolley. Similar to the results from the industrial partner in France, the adaptation terms tend to provide a ± 1 dB correction to the weighted normalized sound pressure level.

Figure 4.42 shows the global indicator $L_{n,w} + C_{I,50-2500}$ versus the added load and trolley speed for the different two-wheeled trolley configurations. A line of best fit has been added for each configuration to show general trends in the data. The coefficients of determination R^2 for

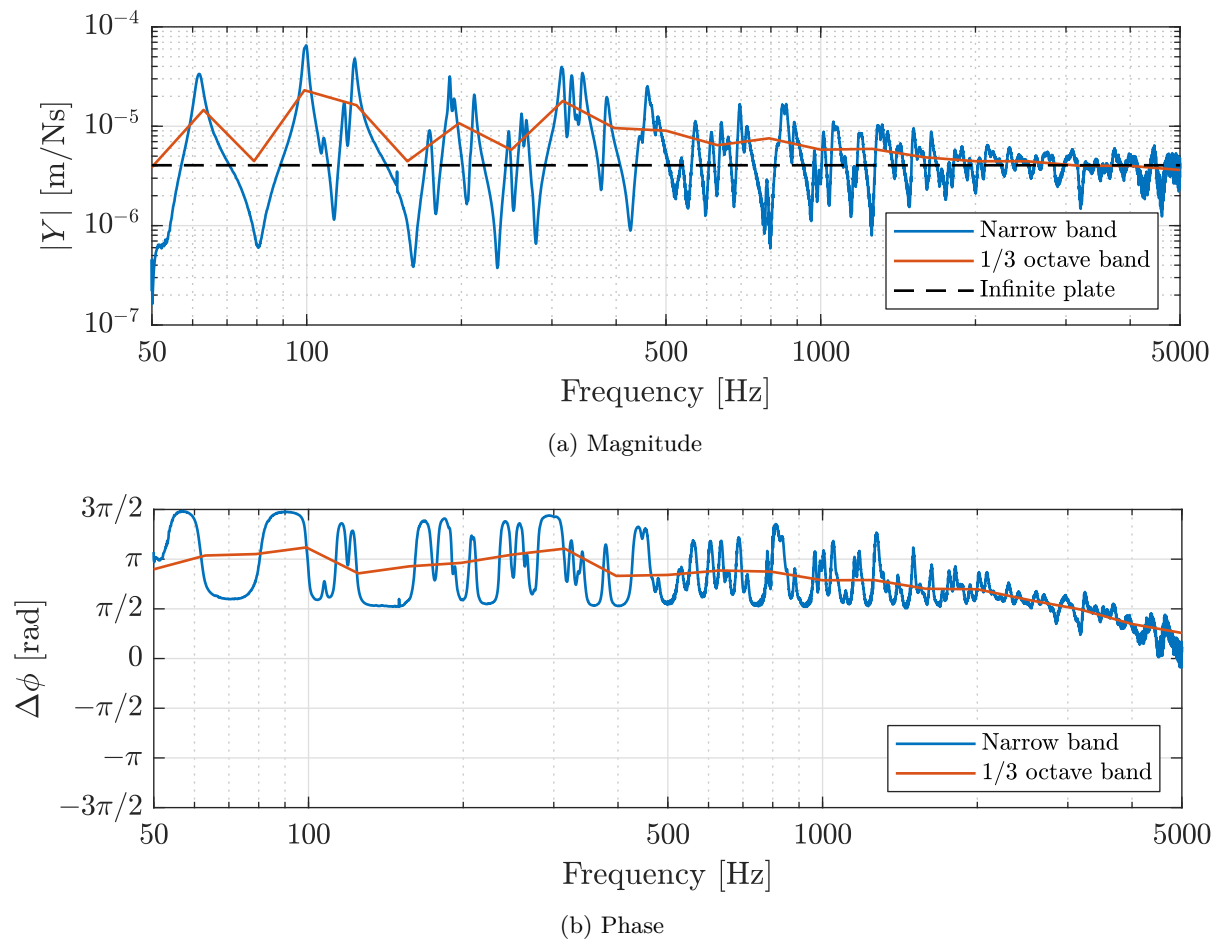
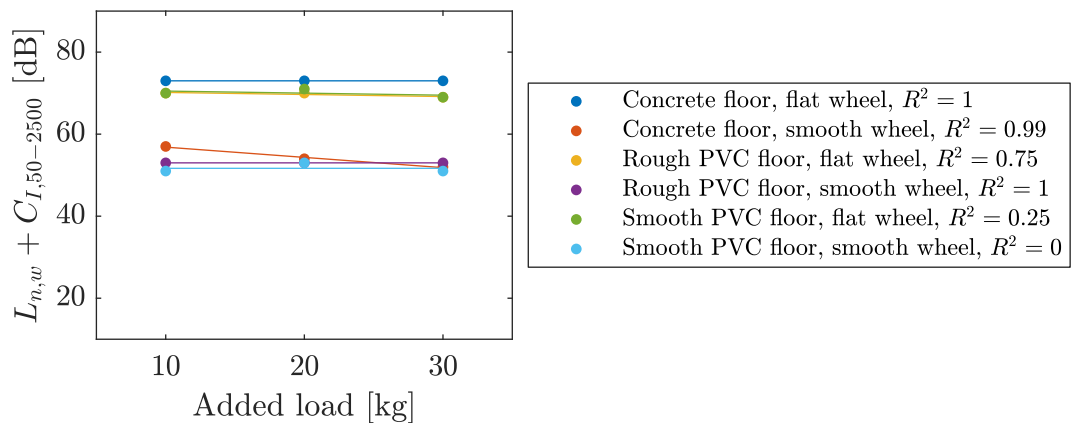


Figure 4.41: Measured mobility of the 10 cm thick concrete slab (narrow band and 1/3 octave band), as well as that of an equivalent infinite plate

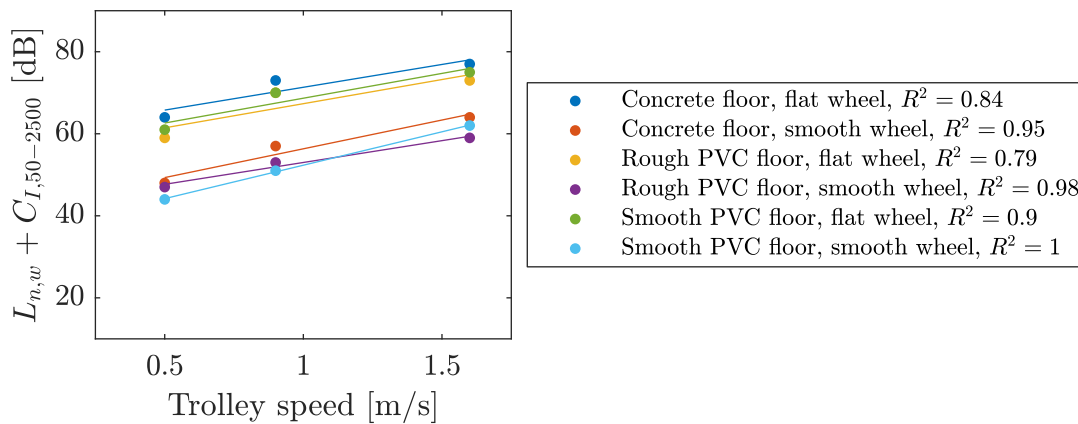
Table 4.6: Global indicators for the rolling noise measurements with the two- wheeled test trolley at Level Acoustics & Vibration

Floor	Wheel	Speed [m/s]	Added Load [kg]	$L_{n,w}$ [dB]	$L_{n,w} + C_I$ [dB]	$L_{n,w} + C_{I,50-2500}$ [dB]
Concrete	Flat	0.5	10	64	64	64
		0.9	10	73	73	73
		1.6	10	79	77	77
		0.9	20	74	73	73
		0.9	30	74	72	73
Concrete	Smooth	0.5	10	47	48	48
		0.9	10	56	57	57
		1.6	10	63	64	64
		0.9	20	54	54	54
		0.9	30	53	52	52
Rough PVC	Flat	0.5	10	58	59	59
		0.9	10	69	70	70
		1.6	10	73	73	73
		0.9	20	68	69	70
		0.9	30	67	68	69
Rough PVC	Smooth	0.5	10	45	47	47
		0.9	10	52	52	53
		1.6	10	57	59	59
		0.9	20	52	53	53
		0.9	30	51	53	53
Smooth PVC	Flat	0.5	10	60	61	61
		0.9	10	70	70	70
		1.6	10	75	75	75
		0.9	20	69	70	71
		0.9	30	67	68	69
Smooth PVC	Smooth	0.5	10	42	44	44
		0.9	10	50	51	51
		1.6	10	60	62	62
		0.9	20	52	53	53
		0.9	30	50	51	51
Walking	–	–	–	18	13	25
Background	–	–	–	19	13	26

the trend lines are also shown. The difference between flat and smooth wheels is once again present, as well as the relative difference of adding the rough and smooth PVC floor coverings. The benefit of adding a floor covering is more pronounced here than it was in Figure 4.20, as is the lack of difference between the smooth and rough PVC, perhaps due to a more robust test method and consequential more reliable data-set. The change in $L_{n,w} + C_{I,50-2500}$ also tracks well with the change in trolley speed: being more or less consistent across all configurations. The exception to this is the smooth wheel on smooth PVC, which exhibited a relatively greater increase in global indicator at the higher trolley speed compared to the other configurations.



(a) Added load



(b) Trolley speed

Figure 4.42: Global indicator $L_{n,w} + C_{I,50-2500}$ versus various configurations of the two-wheeled trolley at Level Acoustics & Vibration

Table 4.7 shows the calculated global indicators for the measurements conducted at Level Acoustics & Vibration using the three-wheeled test trolley. The adaptation terms here are roughly the same as those shown in Tables 4.4 and 4.6 for the two-wheeled trolley.

Figure 4.43 shows the global indicator $L_{n,w} + C_{I,50-2500}$ versus the added load and trolley speed for the different three-wheeled trolley configurations. A line of best fit has been added for each configuration to show general trends in the data. The coefficients of determination R^2

Table 4.7: Global indicators for the three-wheeled trolley rolling noise measurements at Level Acoustics & Vibration

Trajectory	Floor	Wheel	Added Load [kg]	Wheel spacing [cm]	$L_{n,w}$ [dB]	$L_{n,w} + C_I$ [dB]	$L_{n,w} + C_{I,50-2500}$ [dB]		
Circle	Concrete	Nylon	10	12	49	48			
			10	21	52	52	51		
			10	27	52	52	53		
			20	21	51	53	52		
			30	21	50	52	53		
		Wood	10	21	57	59	59		
			Aluminum	10	21	56	57	57	
		Rough PVC	Nylon	10	28	48	48	48	
				Wood	10	21	49	50	51
				Aluminum	10	21	49	50	50
Line	Concrete	Nylon	10	21	51	52	52		
Walking	–	–	–	–	18	13	25		
Background	–	–	–	–	19	13	25		

for the trend lines are also shown. The difference between changes in low and high frequencies when changing wheel material is again lost when comparing single-number values. However, the other two plots adequately demonstrated the relative effects that each one has: slight in the case of wheel spacing, and negligible in the case of rolling trajectory.

In comparing global indicators from the measurements conducted at both test locations, $L_{n,w} + C_{I,50-2500}$ appears to be a modestly accurate means of characterizing a given rolling noise configuration. However, differences which are present for certain frequency bands, but not others, will have a tendency to skew the single-number results. For this reason, comparison of the full normalized sound level spectra should first be compared to check for these differences before relying on $L_{n,w} + C_{I,50-2500}$.

4.4.6 Test conclusion

The testing performed in the two-story transmission room at Level Acoustics & Vibration in Eindhoven, the Netherlands was able to build upon lessons learned during previous tests. An isolated concrete floor, a highly regulated trolley speed, and repetitive runs all allowed for a data set which may be considered highly reliable. As such, these are the experimental results which will be used primarily for comparing against model results in Chapter 5.

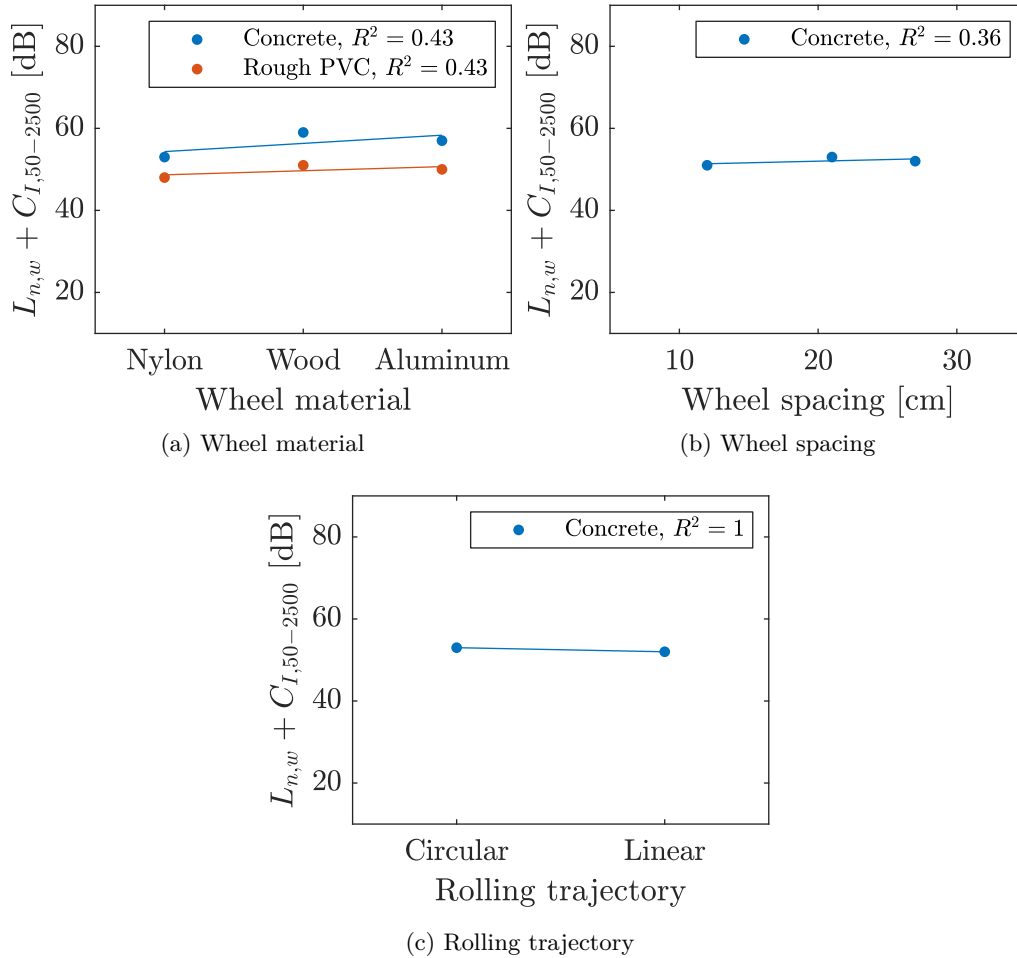


Figure 4.43: Global indicator $L_{n,w} + C_{I,50-2500}$ versus various configurations of the three-wheeled trolley at at Level Acoustics & Vibration

4.5 Test location comparison

In order to assess the repeatability of the rolling noise measurements, the results of the two-wheeled test trolley from both locations may be compared. This unfortunately cannot be an exact one-to-one comparison. Not only are the floors different thicknesses (14 cm in France vs 10 cm in the Netherlands), but the isolated nature of the floor in the Netherlands means that flanking conditions will differ between the two locations as well. Finally there is the issue of trolley speed: the tests in France were conducted (as best as possible) at speed of 0.6 m/s, whereas the tests in the Netherlands were done at speeds of 0.5, 0.9, and 1.6 m/s. For these reasons, the results should not be expected to be perfectly identical. Nevertheless, some degree of congruency should theoretically be able to be drawn from their comparison.

Figure 4.44 shows the normalized sound pressure level in the reception room due to rolling noise of the two-wheeled test trolley with a 10 kg added load at both laboratories. Both the

smooth and flat wheel spectra are shown for three floor conditions: concrete, rough PVC, smooth PVC. Surprisingly, the results from the two labs for each floor condition agree remarkably well with one another. The curves from the Netherlands are higher in the mid frequency range for both smooth and flat wheels for all three floor configurations, but only by a few decibels. It is not possible to determine the exact influence of each parameter individually. However it is possible that the effect of decreasing the speed from 0.6 m/s to 0.5 m/s (which would yield a lower radiated sound level) and decreasing the floor thickness from 14 cm to 10 cm (which would yield a higher radiated sound level) effectively canceled one another out. The largest deviations occur at 100 and 315 Hz, which also correspond to maxima in the floor mobility at Level Acoustics & Vibration in the Netherlands. Thus it would be recommended to use a thicker concrete slab (e.g. 140 mm) in future tests to reduce the influence of the floor mobility.

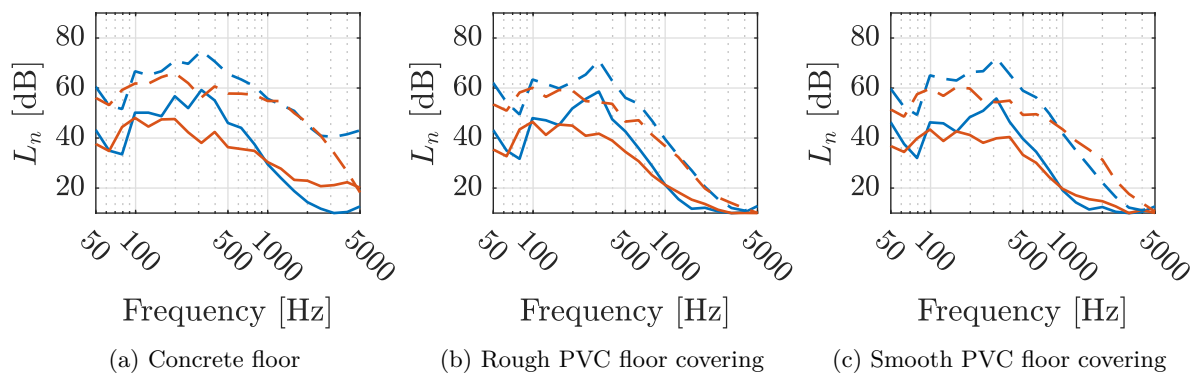


Figure 4.44: Comparison of rolling noise results from two different lab tests using the two-wheeled trolley with a 10 kg added load. — The Netherlands, smooth wheel, 0.5 m/s, — France, smooth wheel, 0.6 m/s, - - - The Netherlands, flat wheel, 0.5 m/s, - - - France, flat wheel, 0.6 m/s.

It should be noted that a 140 mm thick concrete floor is already the standard thickness in buildings, as well as for test laboratories. 100 mm concrete floors are typically not used in real buildings without support joists for added rigidity. Furthermore, if the trolley is rolling on the ground floor, the damping could be even higher due to an increased slab thickness, and/or the presence of the ground beneath.

Figure 4.45 shows the benefit of adding a rough and smooth PVC floor covering at each of the test locations for both a smooth and flat wheel. The benefit provided by the rough and smooth PVC is very similar between locations. For the flat wheel, the rough and smooth PVC provided largely the same benefit in both lab locations. The smooth wheel saw slightly less agreement between locations, though this is likely due to the fact that, because of the lower excitation provided by the smooth wheel, external factors (such as the construction of the test lab, which are different between locations) have a higher relative influence.

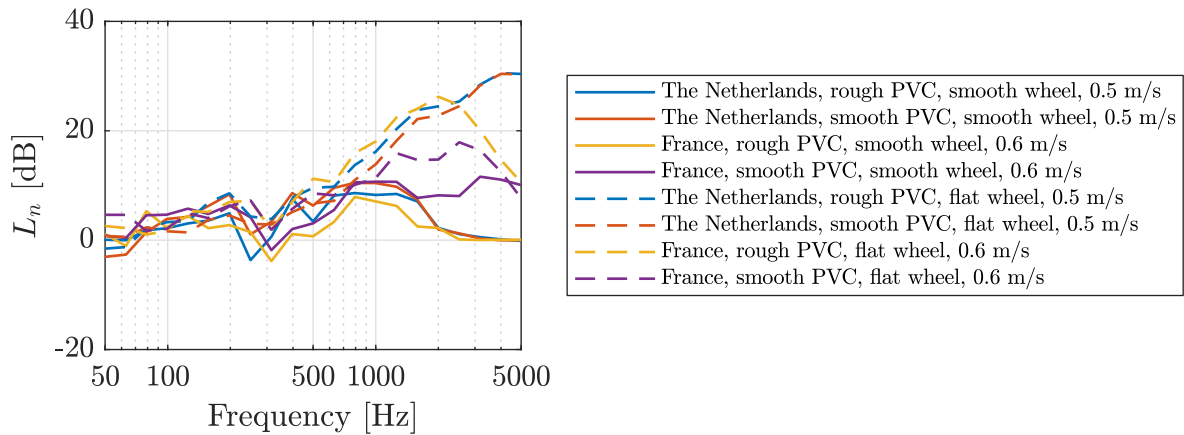


Figure 4.45: Comparison of the benefit of adding smooth and rough PVC floor coverings from two different lab test using the two wheeled trolley with a 10 kg added load.

4.6 Conclusion

This chapter presents the experimental results of two rounds of testing conducted at acoustics laboratories in France and the Netherlands, as well as the small-scale roughness profiles measured at the metrology lab at INSA–Lyon. The measured roughness profiles are used in Chapter 5 as input into the rolling noise model for estimating the radiated sound level of the rolling trolley. Four floors and one wheel was measured for a total of five three-dimensional roughness profiles: polished concrete, rough PVC, smooth PVC, ceramic tile, and a plastic cylindrical wheel. The profiles as a whole were found to be largely broadband in nature, exhibiting little variation in amplitude across the wavelength spectrum. In addition, the coherence of the profiles was not found to be an ideal means of assessing the transverse correlation of the roughness due to their random nature.

For both rolling test locations, a two-wheeled test trolley was used as the primary device for generating a consistent rolling noise excitation in either a two-story reverberation or two-story transmission room. A former iteration of the two-wheeled test trolley which did not have modifications done to it to prevent excess rattling and ringing was also tested at the industrial partner in France. Additionally, a three-wheeled test trolley was tested at Level Acoustics & Vibration for analysis of the effect of wheel material, wheel spacing, and rolling trajectory.

The experimental results presented in this chapter demonstrate not only the spectral content of indoor rolling noise, but also how it changes with varying influencing parameters. The trolley speed has a high influence on the radiated sound level, as does the presence (or not) of wheel flats, and the type of floor covering used (if any at all). The wheel material has a moderate effect on the radiated sound level, while the added load and wheel spacing have a minor (though non-negligible) effect. The effect of the rolling trajectory, however, is negligible.

The consistency of results demonstrated between the two test locations shows that the rolling test procedure used, combined with the modified measurement method for impact noise described in ISO 10140-3 [3], are adequate for generating reproducible results. Care must be taken to regulate the speed of the test trolley to the highest degree possible, but this is manageable through the use of a metronome.

The global indicator $L_{n,w} + C_{I,50-2500}$ appears modestly suitable for describing the overall performance of a given rolling noise configuration, though there can be a tendency to mask information in situations where there are large peaks in the radiated sound spectra.

The experimental results presented here provide adequate basis for comparison with model results. The results from the two-wheeled trolley tests conducted at Level Acoustics & Vibration in the Netherlands will be used primarily, as they were determined to be more robust due to the increased focus put on regulating trolley speed during testing. This comparison will be presented in Chapter 5. The results with the two and three wheeled trolleys are very encouraging, but there is still work to be done to increase the reproducibility of the results.

THIS chapter presents the results of the rolling noise model. Comparisons are made both between the experimental results from Chapter 4 as well as the results of the preliminary model presented in Chapter 2. While the primary means of comparison is the estimated normalized sound pressure level (being the primary goal of the model), comparisons are also made with other calculated quantities, such as the contact force and vertical wheel displacement. This is done in order to investigate model and physical phenomena which are not directly apparent from looking at the sound spectra alone.

5.1 Default parameters

In the sections that follow, a number of comparisons will be made between model and experimental results. There are a large number of variables which may change from run to run, so for the purpose of brevity, several default values will be first declared here. Unless otherwise stated, the parameters shown in Table 5.1 are used for the results shown in this chapter. If a particular run deviates from these default parameters (e.g. if a 20 kg added load is used instead of a 10 kg added load), it will be specified as such. The wheel damping ratio ζ and the viscous damping factor C are related by Equation (2.72).

The plastic test wheel and four flooring materials (polished concrete, rough PVC, smooth PVC, and ceramic tile) have material properties given in Table 5.2. They were obtained from the respective material manufacturers. These material characteristics are known to provide good results (measured vs calculated) when evaluating impact noise.

Table 5.1: Default parameters used for the results shown in Chapter 5, unless otherwise specified.

Parameter	Variable	Unit	Value
Wheel radius	r_x	(mm)	50
Wheel transverse radius	r_y	(mm)	∞
Wheel axle radius	r_A	(mm)	6.5
Wheel width	w	(mm)	35
Wheel damping ratio	ζ	(-)	0.4
Wheel flat depth (if applicable)	h_W	(mm)	0.5
Floor joint length (if applicable)	l_F	(mm)	10
Trolley speed	v	(m/s)	0.9
Rolling distance	L	(mm)	1000
Added load	M_l	(kg)	10
Trolley mass	M_t	(kg)	7

Table 5.2: Material properties for the wheel and floors used for the results shown in Chapter 5.

Material	Young's modulus E (GPa)	Poisson's ratio ν (-)	Mass density ρ (kg/m ³)
Plastic wheel	0.2	0.3	1428
Polished concrete floor	33	0.3	2150
PVC floor covering	0.75	0.3	1556
Ceramic tile floor	109	0.2	2400

5.2 Floor admittance

The propagation model presented in Chapter 2 uses the floor admittance Y_F to calculate the sound level in the reception room via the TMM. As stated previously, in practice this is done by using a unit injected force of 1 N to obtain the floor impedance before multiplying by the blocked force calculated in the rolling model to obtain the true injected force. Figure 5.1 shows the unit admittance of 100 and 140 mm thick concrete floors, representing the floors found at the two test locations presented in Chapter 4. In addition, the unit admittance of the multi-layer floor systems formed by placing a 6 mm thick PVC floor covering on top of each concrete floor is also shown. Finally, the thin plate approximation of the 100 mm and 140 mm concrete slabs are also shown for comparison [77]. This can be seen as a flat curve which does not change with frequency. As the unit floor impedance does not depend on the surface roughness, there is no difference here between the smooth and rough PVC. These admittances were calculated using AlphaCell: a software based on the TMM which predicts the vibro-acoustic response of multi-layer systems [89].

The 140 mm thick concrete, being more massive, provides a slightly lower admittance than the 100 mm thick concrete. The admittance rises significantly above 100 Hz when the PVC floor covering is added, as seen in the top curves in the figure. Here less energy is transferred through

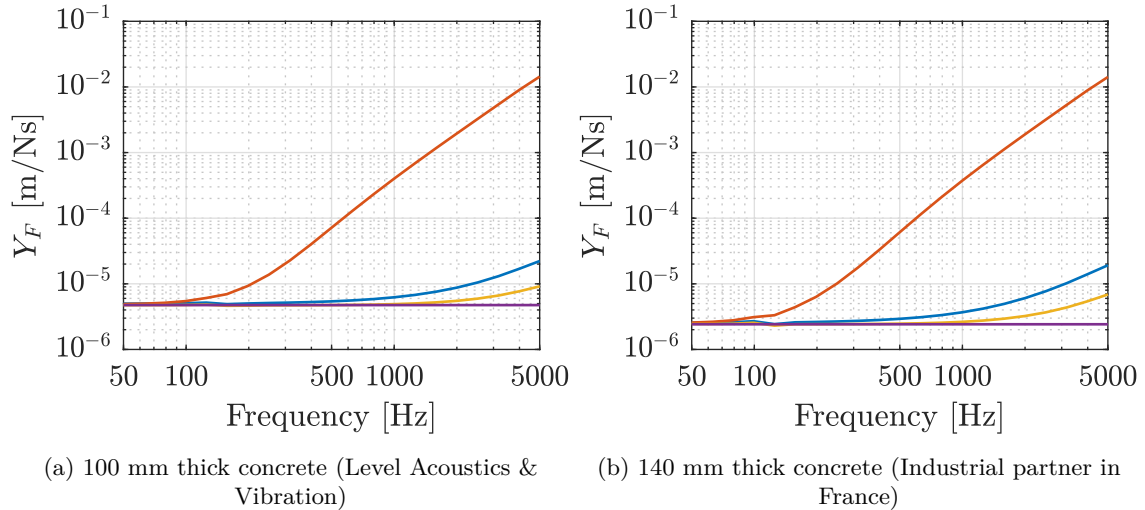


Figure 5.1: Unit admittance of the bare concrete floor and concrete floor with PVC floor covering. — concrete, — concrete + 6 mm thick PVC floor covering, — concrete + 8 mm thick ceramic tile floor covering, — concrete thin plate estimation [77].

the system: reducing the radiated sound level as was demonstrated in Chapter 4, and as one would logically expect with the addition of a softer floor covering. Conversely, adding tiles on top of the concrete yields a lower admittance due to their high stiffness and mass, as seen in the curves which rise only slightly in the high frequency region. While using admittance of a thin plate is largely appropriate for the bare concrete slab (under certain frequency and thickness conditions), the addition of a softer floor covering immediately causes the admittance to deviate strongly from the thin plate approximation for all but the lowest of frequencies. Thus it would not be an appropriate representation in the case of a multi-layer system.

5.3 Wheel stiffness: comparison of the proposed methods

In Chapter 3, three methods were proposed for estimating the stiffness of the wheel used in the dynamic model: a look-up table, a series of one-dimensional polynomials, or a single two-dimensional polynomial. Before continuing with further model validation, it is first useful to observe how each of these methods affects the results of the rolling noise model.

To make this comparison, the model was run for three floor types (polished concrete, rough PVC, and smooth PVC) and three wheel types (smooth, ideal flat, and rounded flat). As the PVC is a floor covering, those floor types also included the polished concrete as a base layer underneath, thus mimicking a floor covering condition. All three methods of estimating the wheel stiffness were used for both initial and continuous calculation (i.e. estimating the wheel stiffness once at the start of the rolling event versus re-calculating it at each time step based on

the newly updated contact area half-length). This allows one to observe not only how the three methods differ from one another in their estimation, but also how much the changing contact area half-length affects the estimation.

Figure 5.2 shows the normalized sound pressure level calculated by the rolling noise model for the test wheel rolling on a concrete floor for three different wheel stiffness calculation methods: the pre-calculation using the 2D polynomial, continuous calculation using the 2D polynomial, and pre-calculation using an equivalent beam approximation. The lookup and 1D polynomial methods were found to produce L_n curves which were not visibly different than the 2D polynomial method, whether using pre-calculation or continuous calculation. They have thus been omitted here for brevity. There is little difference between the methods developed in Chapter 3. Similar results were observed for the rough and smooth PVC floor coverings. The equivalent beam, which is used in the preliminary model, has a tendency to overestimate the wheel stiffness. As such, this results in slightly elevated sound levels in the low frequency range for the smooth wheel, and over the whole frequency range for the ideal flat wheel. Even so, the difference in sound level is still minimal (e.g. 4–6 dB at 100 Hz).

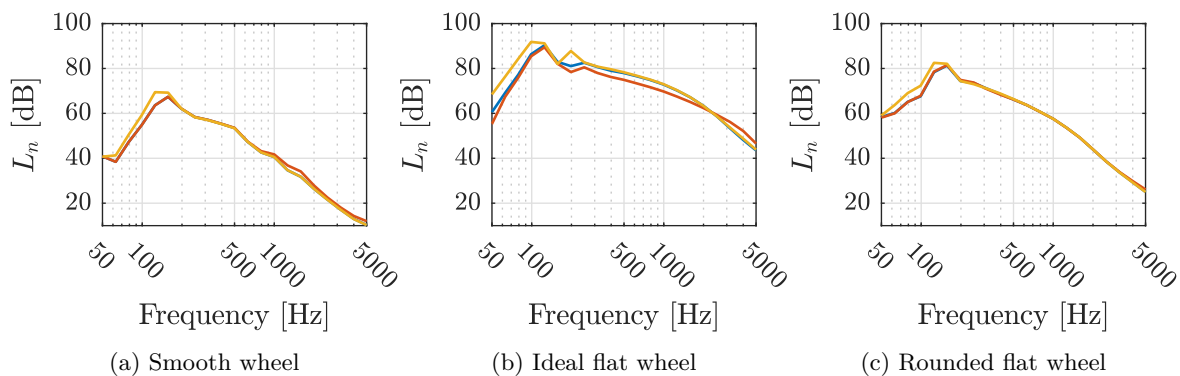


Figure 5.2: Normalized sound pressure level calculated by the rolling noise model as a function of wheel stiffness calculation method: — pre-calc, 2D polynomial, — continuous-calc, 2D polynomial, — equivalent beam approximation.

In order to observe what is occurring during the rolling event to cause the results to be so close to one another, we may plot the contact area half-length a as a function of the rolling distance x . For the pre-calculation method it will be constant for all x . For the continuous calculation methods, it will change throughout the rolling event. An example of this comparison using the 2D polynomial method is shown in Figure 5.3 for the smooth test wheel rolling on a concrete floor. The size of the contact area indeed changes throughout the rolling event as a new roughness profile continuously moves through the contact area. However, this change is not large enough to translate to a noticeable effect on the radiated sound level. Similar results were also observed for the flat wheels and PVC floor coverings.

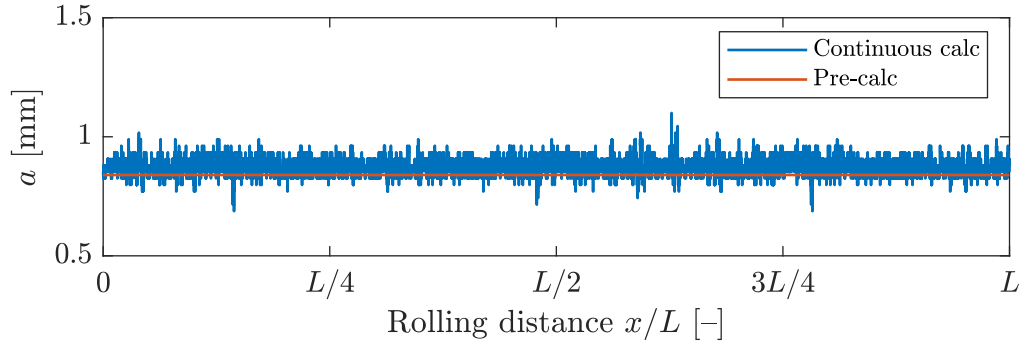


Figure 5.3: Contact area half-length a as functions of rolling distance x for the smooth test wheel rolling on a concrete floor.

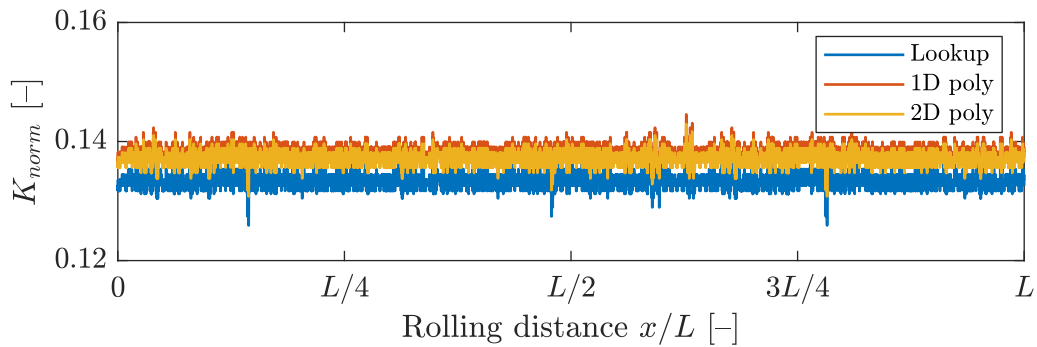


Figure 5.4: Normalized wheel stiffness K_{norm} as functions of rolling distance x for the smooth test wheel rolling on a concrete floor.

Figure 5.4 shows the normalized wheel stiffness K_{norm} as a function of rolling distance x for the three abacus methods (lookup, 1D polynomial, 2D polynomial) due to the smooth wheel rolling on a concrete floor. All curves are for the continuous calculation method. All three methods return largely similar results, and exhibit little change throughout the rolling event. While the continuous calculation method does technically provide a more accurate means of estimating the wheel stiffness, the change that it experiences throughout the rolling event is not significant enough to result in a substantial change in radiated sound level.

The contact force depends on the wheel stiffness, but to a small enough degree that the modulation which occurs in the continuous calculation method may be considered negligible. For the results presented in the remaining sections of this chapter, the decision was made to use the 2D polynomial, pre-calculation method. This provides a faster calculation time with a negligible reduction in accuracy. Overall it appears that a small variation in the wheel stiffness does not have a strong influence on the estimated sound level.

5.4 Roughness profiles

Because the wheel profile ξ_W changes with (x', z) for every position x in the global coordinate system (i.e. along the rolling trajectory), it is not possible to plot the wheel profile as only a function x . If however, we use the equivalent 1D profile used in the one-dimensional version of the model, we may visualize a coarse approximation of the profile. Recall that the process for obtaining the 1D profile involves taking the value of the 2D profile $\xi_W(x', x)$ at $x' = 0$ for each x . The same may be done for the floor profile ξ_F and the roughness profiles ς_W & ς_F .

Figure 5.5 shows the equivalent relative 1D profile for the case of the ideal flat wheel rolling on tile. The wheel flat spots and floor joints appear as negative dips in the relative 1D profile: both of which are far greater in magnitude than either the wheel or floor roughness profiles. Recall that because the flat spots on the wheel were designed to be non-periodic (see Appendix B for a diagram), the positive bumps in Figure 5.5 are non-periodic as well.

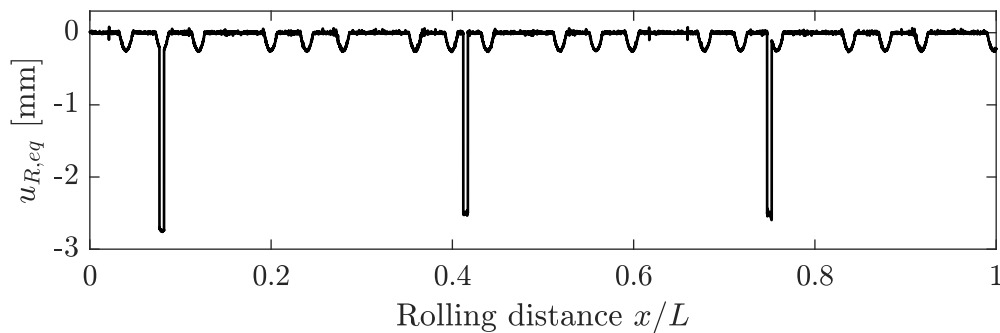


Figure 5.5: One-dimensional representation of the relative combined wheel profile, floor profile, wheel roughness, and floor roughness.

Figure 5.6 shows the frequency spectra of the equivalent relative 1D profile in 1/3 octave bands. Here the trolley speed is 0.9 m/s. Extending the low frequency range of the plot shows that the influence of the frequency of wheel flat and floor joint impacts serve to elevate the overall roughness level in the low frequency range. However, these fundamental impact frequencies are still not clearly present in the plot. It is also worth noting here that the magnitude of the floor profile spectra is overestimated here: in reality the wheel will not contact the bottom of the 2.5 mm deep floor joint.

5.5 Radiated sound level: Model versus experimental results

In the plots that follow, we shall switch from the convention used in Chapter 4 of displaying the smooth wheel with a solid line and the flat wheel with a dashed line to instead displaying the model results with a solid line and the experimental results with a dashed line. Thus in a

each plot, the comparison of interest shall be that between a solid and dashed line of a given color.

5.5.1 Level Acoustics & Vibration

The measurements conducted at Level Acoustics & Vibration in the Netherlands allow for comparisons between the model and experimental results for varying floor type, wheel type, added load, and trolley speed. Considering each of these variables has been previously shown to have an influence on the radiated sound level, the models ability to capture them should be investigated. This is done in the sections that follow.

Influence of floor and wheel type

Figure 5.7 shows the model versus experimental results of the normalized sound pressure level in the reception room due to the two-wheeled rolling test trolley for the smooth wheel, ideal flat wheel, and rounded flat wheel on multiple floors. The concrete floor generally yields higher levels than the rough and smooth PVC floors, which are similar to one another in shape and magnitude. Model results agree well above 300 Hz for the ideal flat wheel. The smooth wheel and rounded flat wheel tend to under-predict across the whole frequency range, however their general shapes are still congruent with those of their respective experimental curves. The background noise level for the measurement was set to 10 dB, so any values below this were corrected to this level. This can be seen particularly in the results for the smooth wheel above 1 000 Hz.

Just as the benefit provided by adding a floor covering was computed in Chapter 4 via ΔL_n using experimental data, the same may be done with the model results. Figure 5.8 shows the

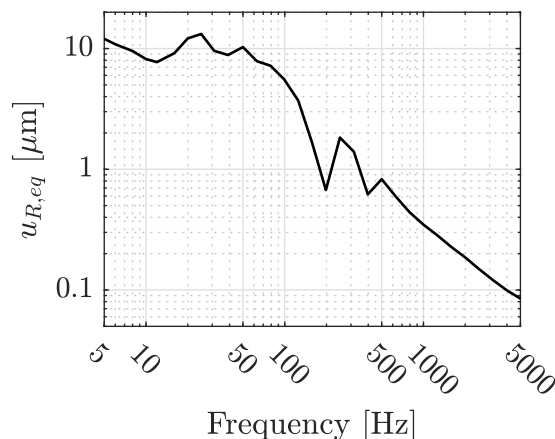


Figure 5.6: Frequency spectra of the one-dimensional representation of the combined wheel profile, floor profile, wheel roughness, and floor roughness.

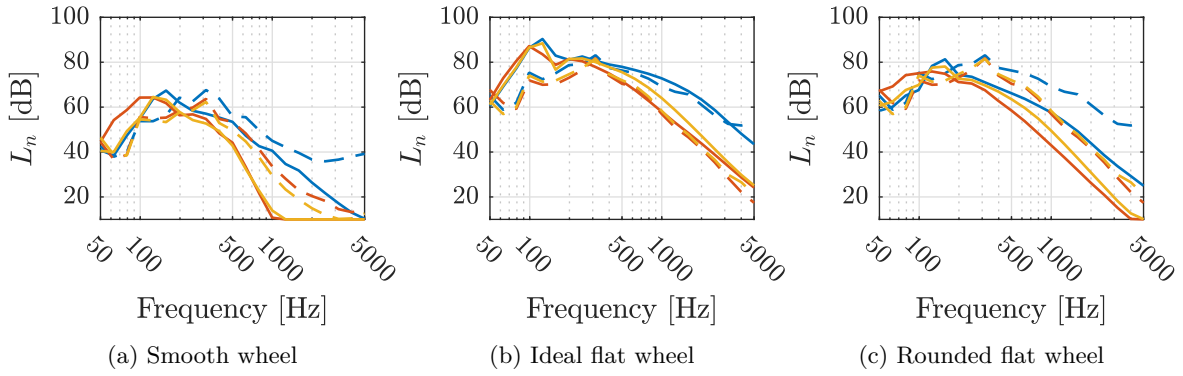


Figure 5.7: Normalized sound pressure level in the reception room for varying floor covering: model versus experiment. For all curves, the trolley speed was 0.9 m/s and the added load was 10 kg. — model concrete floor, - - - experiment concrete floor, — model, rough PVC floor, - - - experiment, rough PVC floor, — model smooth PVC floor, - - - experiment, smooth PVC floor.

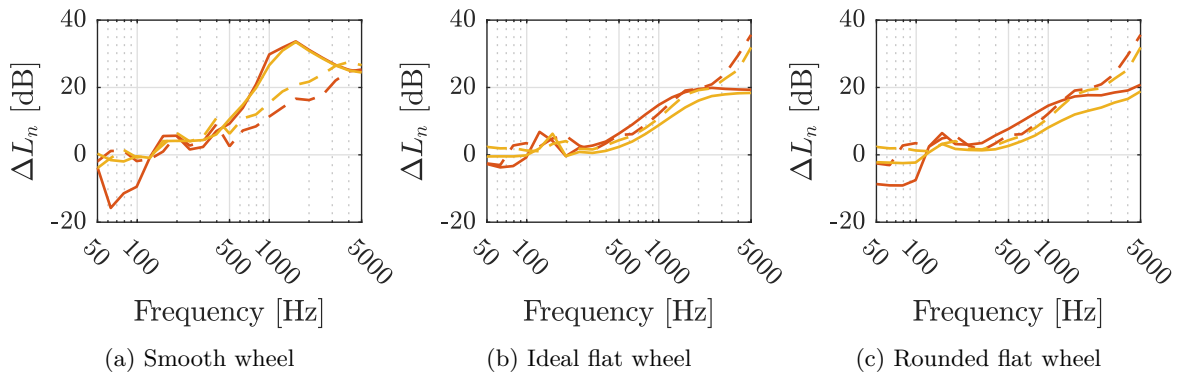


Figure 5.8: Benefit from applying the rough and smooth PVC floor coverings: model versus experiment. For all curves, the trolley speed was 0.9 m/s and the added load was 10 kg. — model concrete floor, - - - experiment concrete floor, — model, rough PVC floor, - - - experiment, rough PVC floor, — model smooth PVC floor, - - - experiment, smooth PVC floor.

benefit of adding a floor covering, as computed with both model and experimental data. There is quite a bit less difference between the three wheel types in the ΔL_n plots than in the L_n plots, indicating that the floors provide more or less a similar benefit regardless of wheel type. Additionally, while the model is not perfectly accurate at estimating the absolute sound level L_n , it is much more accurate at estimating the relative sound level ΔL_n . A greater deviation occurs in the high frequency range for the smooth wheel, where the model has a tendency to over-predict above 500 Hz. This is due to the weak excitation of the smooth wheels. The curves shown here were not corrected to the background noise level of 10 dB, so the behavior of the curves in the high frequency range are accurate.

Influence of added load

Figure 5.9 shows the model versus experimental results of the normalized sound pressure level in the reception room due to the two-wheeled rolling test trolley for the smooth wheel, ideal flat wheel, and rounded flat wheel for multiple added loads. For all curves, the trolley speed was 0.9 m/s and the floor was concrete. The model correctly predicts only a slight change in sound level with changing wheel load. However in the low frequency range, where an inverse relationship is expected (i.e. a slight decrease in sound level with increasing added load), the effect is not seen in the model results. Instead, a positive relationship is predicted: the heavier 30 kg configuration has the highest curve (followed by 20 kg and then 10 kg in decreasing magnitude). This is possibly due to the fact that the modal behavior of the slab is not being taken into account, which would manifest itself at the low frequencies seen here. The inverse relationship in the high frequency range is however represented in the model for the ideal and rounded flat wheel.

The model predicts a frequency shift towards lower frequencies with increasing load. This agrees with the expected phenomena for a static mechanical source. However, this shift is not seen in the experimental results. It is possible that, as the load increases, the true roughness profile in the contact area changes, as the higher load causes new roughness asperities to come into contact with one another. This changing roughness profile may be overriding the low frequency shift which is otherwise expected.

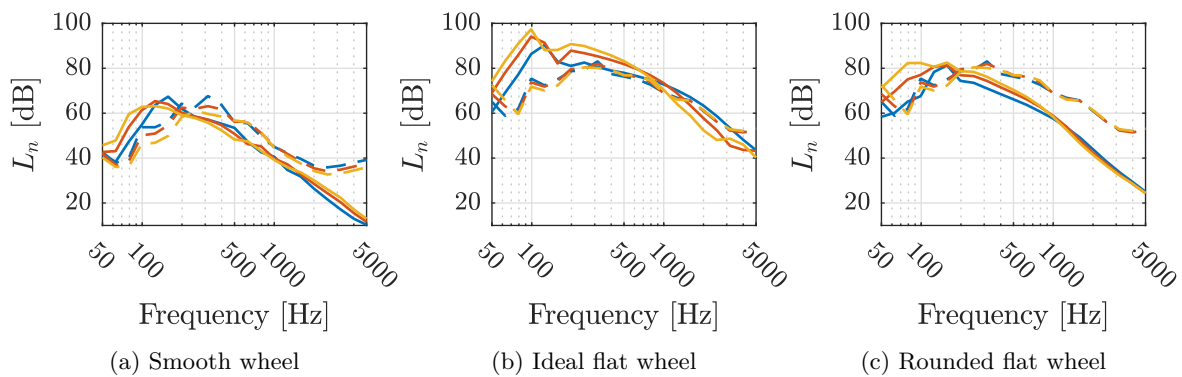


Figure 5.9: Normalized sound pressure level in the reception room for varying added load: model versus experiment. For all curves, the trolley speed was 0.9 m/s and the floor was concrete. — model, 10 kg, - - - experiment, 10 kg, — model, 20 kg, - - - experiment, 20 kg, — model, 30 kg, - - - experiment, 30 kg

Figure 5.10 shows how the benefit of adding a rough floor covering changes with trolley added load, as computed with both model and experimental data. The results are similar to those shown in Figure 5.8, with a tendency to deviate from experimental results in the high

frequency range. Model results in the low and mid frequencies, however, remain quite good. Here we see that the model predicts that the floor covering will perform slightly worse as the load increases for the case of the flat wheel: the 30 kg load being slightly lower than the 20 kg load, and the 20 kg load being slightly lower than the 10 kg load). However, this is the region where results are closely approaching the noise floor, and thus results are not necessarily expected to agree well. The mid and low frequency regions, which are of greater interest as they contain the majority of the acoustic energy, tend to agree well with experimental results.

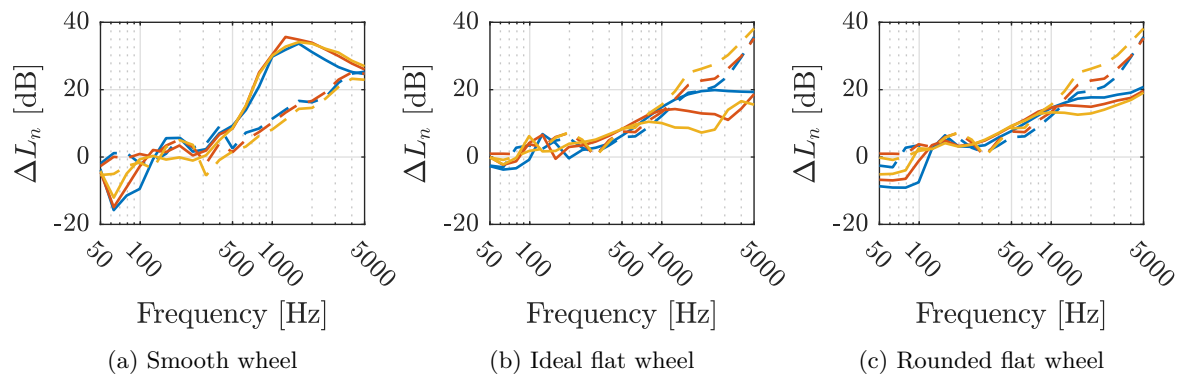


Figure 5.10: Benefit from applying the rough PVC floor covering for varying added load: model versus experiment. For all curves, the trolley speed was 0.9 m/s. — model, 10 kg, - - - experiment, 10 kg, — — — model, 20 kg, - - - experiment, 20 kg, — — — model, 30 kg, - - - experiment, 30 kg

Influence of trolley speed

Figure 5.11 shows the model versus experimental results of the normalized sound pressure level in the reception room due to the two-wheeled rolling test trolley for the smooth wheel, ideal flat wheel, and rounded flat wheel for multiple trolley speeds. The tendency of the sound level to increase with increasing speed is present in the model results, as seen by the 1.6 m/s curve yielding the highest magnitude for all three wheel types (followed by the 0.9 m/s and 0.5 m/s speed curves having decreasing magnitudes). The degree of change in sound level also appears to be more or less similar between experimental and model results, though the absolute levels remain reduced (for the smooth and rounded flat wheel) and elevated (for the ideal wheel) from the model.

Figure 5.12 shows how the benefit of adding a rough floor covering changes with trolley speed, as computed with both model and experimental data. Here what was observed in the previous figure is confirmed: the model is largely capable of handling changes in the relative sound level ΔL_n with changes in trolley speed. The results are however still slightly more accurate for the flat wheel rather than the smooth wheel. Similar to the added load, the model predicts

that the benefit of the floor covering will drop slightly as the trolley speed increases for the flat wheels. The 1.6 m/s curve has the lowest magnitude, followed by the 0.9 m/s and 0.5 m/s curves (though the differences are still quite small). It is interesting to note that while the trolley speed greatly affects the absolute sound level, the relative relationship between floor covering and trolley speed remains quite small. That is to say, the benefit provided by a given floor covering is largely independent of trolley speed.

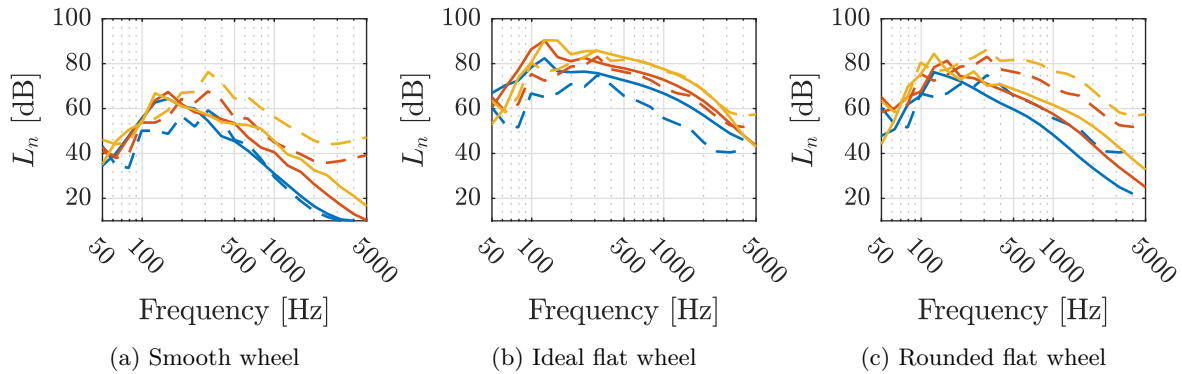


Figure 5.11: Normalized sound pressure level in the reception room for varying trolley speed: model versus experiment. For all curves, the added load was 10 kg and the floor was concrete. — model, 0.5 m/s, - - - experiment, 0.5 m/s, — model, 0.9 m/s, - - - experiment, 0.9 m/s, — model, 1.6 m/s, - - - experiment, 1.6 m/s.

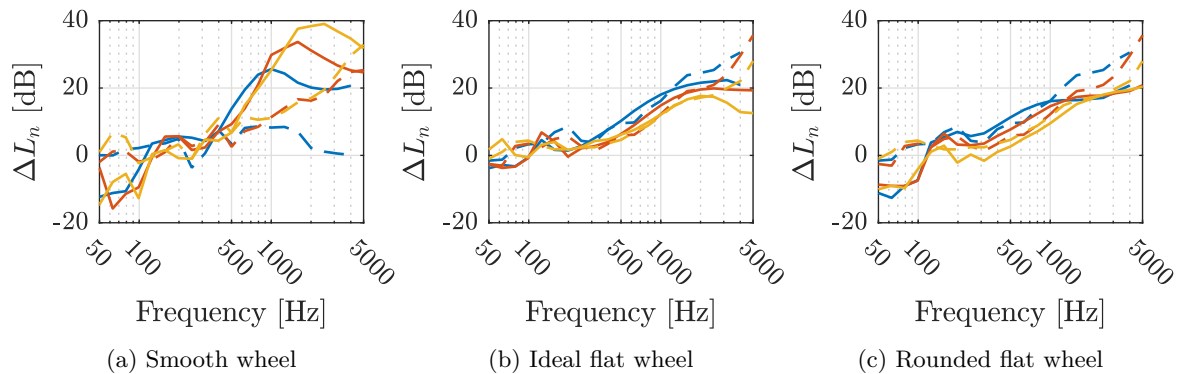


Figure 5.12: Benefit from applying the rough PVC floor covering for varying trolley speed: model versus experiment. For all curves, the added load was 10 kg. — model, 0.5 m/s, - - - experiment, 0.5 m/s, — model, 0.9 m/s, - - - experiment, 0.9 m/s, — model, 1.6 m/s, - - - experiment, 1.6 m/s.

5.5.2 Industrial partner in France

The experimental tests conducted at the laboratory in France, while less robust (and not allowing for a comparison of the trolley speed), provide an opportunity to observe the applicability of the rolling noise model for data gathered at multiple locations. For all runs in this

section, the trolley speed was 0.6 m/s.

Influence of floor and wheel type

Figure 5.13 shows the model versus experimental results of the normalized sound pressure level in the reception room due to the two-wheeled rolling test trolley for the smooth wheel, ideal flat wheel, and rounded flat wheel on multiple floors. Values below the background noise level of 10 dB were corrected here just as they were in the previous results. The concrete floor again yields higher levels, followed by the two PVC floor coverings. The rough PVC is slightly quieter than the smooth PVC in both model and experimental results for the flat wheels. The two are essentially identical for the smooth wheel. While the model had a tendency to under-predict when compared to the results from Level Acoustics & Vibration, it has a tendency to over-predict when compared to the results from the industrial partner in France. Thus it is the rounded flat wheel rather than the ideal flat wheel which corresponds better to the experimental results here. This reveals the difficulty in modeling noise sources in buildings, and why the relative sound level ΔL_n is often used instead of the absolute level L_n . There are many factors which contribute to what the sound level of a source in a given environment will be, several of which are not congruent between laboratories. These differences are removed when comparing ΔL_n .

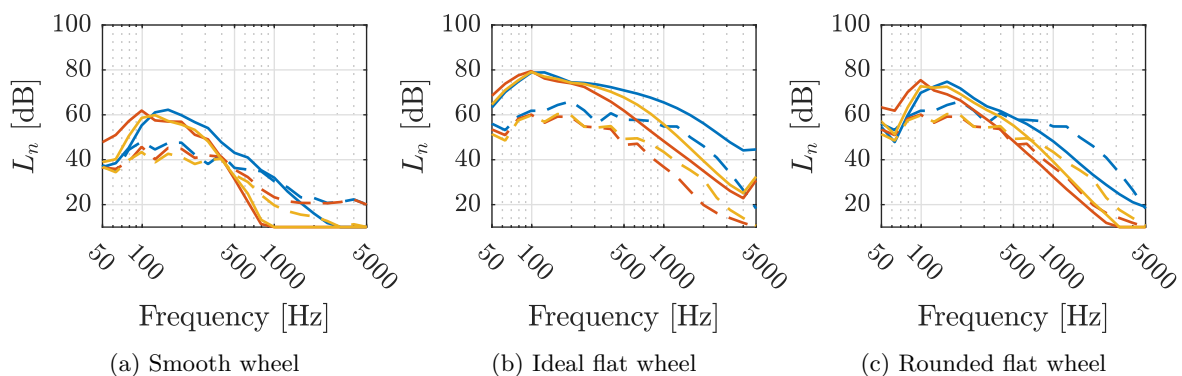


Figure 5.13: Normalized sound pressure level in the reception room for varying floor covering: model versus experiment. For all curves, the trolley speed was 0.6 m/s and the added load was 10 kg. — model concrete floor, - - - experiment concrete floor, — model, rough PVC floor, - - - experiment, rough PVC floor, — model smooth PVC floor, - - - experiment, smooth PVC floor.

Figure 5.14 shows the benefit of adding a floor covering, as computed with both model and experimental data. The results for the smooth wheel are similar here compared to those given in Figure 5.8 from Level Acoustics & Vibration, with the rough PVC providing a slightly higher benefit than the smooth PVC for the flat wheels. Model results were nearly identical for the smooth wheel. The model under-predicts slightly in the high frequency range for the ideal and

rounded flat wheels when compared to the results from the industrial partner in France, which was less-so the case for the results from Level Acoustics & Vibration. A tendency to over-predict above 500 Hz is again present for the smooth wheel due to its low excitation.

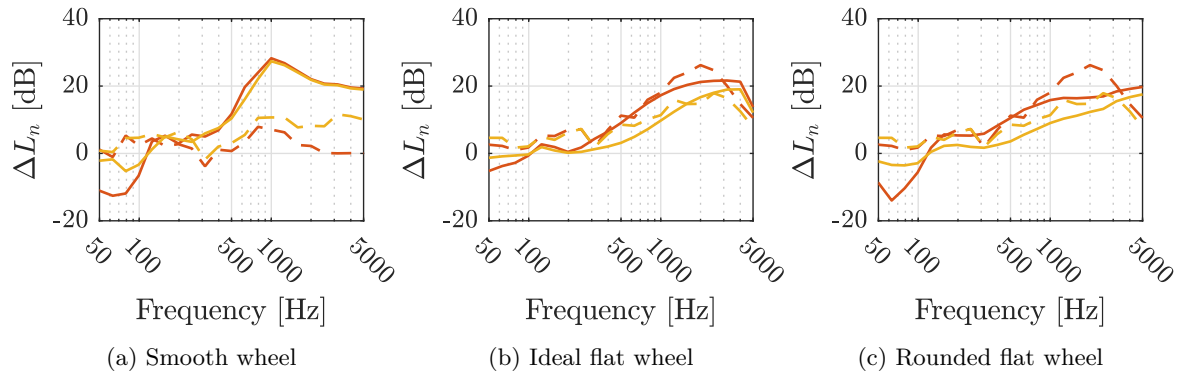


Figure 5.14: Benefit from applying the rough and smooth PVC floor coverings: model versus experiment. For all curves, the trolley speed was 0.6 m/s and the added load was 10 kg.
— model, rough PVC floor, - - - experiment, rough PVC floor,
— model, smooth PVC floor, - - - experiment, smooth PVC floor.

Influence of added load

Figure 5.15 shows the model versus experimental results of the normalized sound pressure level in the reception room due to the two-wheeled rolling test trolley for the smooth wheel, ideal flat wheel, and rounded flat wheel for multiple added loads. For all curves, the trolley speed was 0.6 m/s and the floor was concrete. The tendency of the model to over-predict when compared to the results from the industrial partner in France is once again present, as are the previously identified physical phenomena (i.e. the positive relationship in the low frequency range and the inverse relationship in the high frequency range between sound level and added load). The 30 kg load has the highest magnitude curve in the low frequency range for all three wheels, followed by the 20 kg and then 10 kg curves in descending order.

Figure 5.16 shows how the benefit of adding a rough floor covering changes with trolley added load, as computed with both model and experimental data. The model again over-predicts above 500 Hz for the smooth wheel, but predictions for the flat wheel agree well with experimental results. The largest deviations occur in the regions where the model is known to be less accurate due to either the low noise floor (above 1 000 Hz) or the high modality (below 100 Hz).

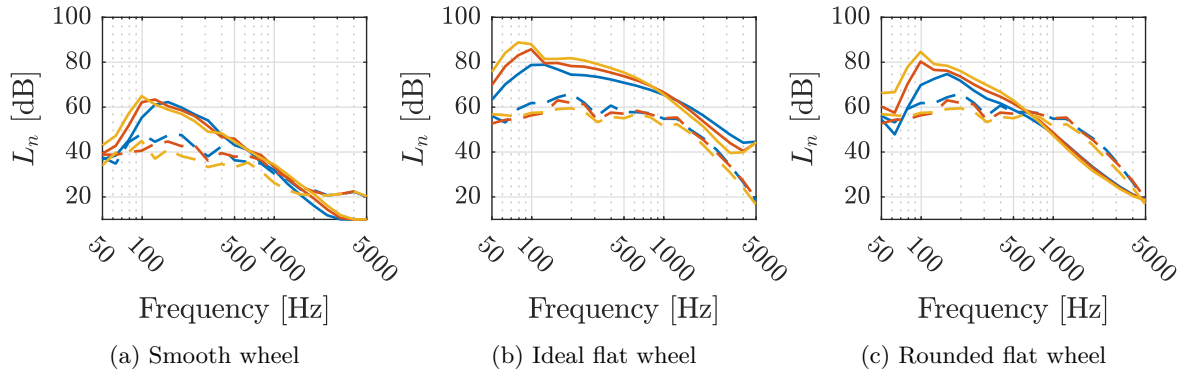


Figure 5.15: Normalized sound pressure level in the reception room for varying added load: model versus experiment. For all curves, the trolley speed was 0.6 m/s and the floor was concrete. — model, 10 kg, - - - experiment, 10 kg, — model, 20 kg, - - - experiment, 20 kg, — model, 30 kg, - - - experiment, 30 kg

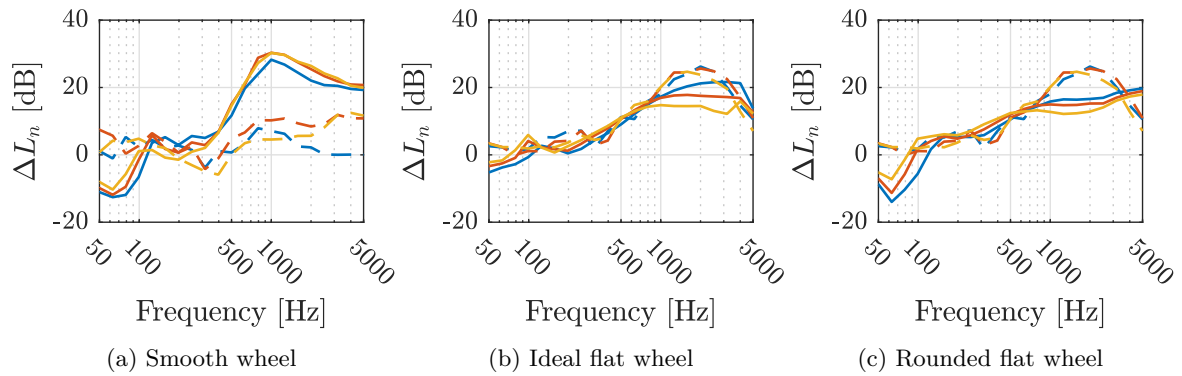


Figure 5.16: Benefit from applying the rough PVC floor covering for varying added load: model versus experiment. For all curves, the trolley speed was 0.6 m/s. — model, 10 kg, - - - experiment, 10 kg, — model, 20 kg, - - - experiment, 20 kg, — model, 30 kg, - - - experiment, 30 kg

5.6 Global indicators: Model versus experimental results

In Chapter 4, the weighted normalized sound pressure level plus adaptation term $L_{n,w} + C_{I,50-2500}$ was demonstrated to be a modest indicator of floor performance when large tonal components are not present. Global indicators may be calculated using the results of the rolling noise model as well. A comparison between model and experimental weighted normalized sound pressure level is presented in the following sections.

5.6.1 Level Acoustics & Vibration

Table 5.3 shows the global indicator $\Delta L_{n,w} + \Delta C_{I,50-2500}$ for both model and experimental results for the measurements conducted at Level Acoustics & Vibration using the two-wheeled test trolley. Similar to how the relative normalized sound pressure level ΔL_n is computed by

subtracting the L_n of a given floor covering from the L_n of concrete, this global indicator is computed via

$$\Delta L_{n,w} + \Delta C_{I,50-2500} = (L_{n,w,0} + C_{I,50-2500,0}) - (L_{n,w} + C_{I,50-2500}) \quad (5.1)$$

where $L_{n,w,0} + C_{I,50-2500,0}$ is the value of the reference configuration (concrete) and $L_{n,w} + C_{I,50-2500}$ is the value of the floor covering (rough or smooth PVC).

Table 5.3: Comparison of global indicators between model and experimental results: Level Acoustics & Vibration

Floor covering	Wheel	Speed [m/s]	Added load [kg]	Model	Experiment
				$\Delta L_{n,w} + \Delta C_{I,50-2500}$ [dB]	$\Delta L_{n,w} + \Delta C_{I,50-2500}$ [dB]
Rough PVC	Smooth	0.5	10	-1	3
		0.9	10	-2	5
		1.6	10	-2	6
		0.9	20	-1	4
		0.9	30	1	2
	Ideal flat	0.5	10	5	7
		0.9	10	5	5
		1.6	10	6	6
		0.9	20	6	7
		0.9	30	6	6
	Rounded flat	0.5	10	-1	7
		0.9	10	1	5
		1.6	10	0	6
		0.9	20	3	7
		0.9	30	4	6
Smooth PVC	Smooth	0.5	10	6	4
		0.9	10	6	6
		1.6	10	7	2
		0.9	20	7	3
		0.9	30	7	2
	Ideal flat	0.5	10	4	7
		0.9	10	4	6
		1.6	10	5	5
		0.9	20	5	6
		0.9	30	5	7
	Rounded flat	0.5	10	4	7
		0.9	10	4	6
		1.6	10	2	5
		0.9	20	4	6
		0.9	30	4	7

Similar to the results for ΔL_n , the model has a tendency to under-predict $\Delta L_{n,w} + C_{I,50-2500}$ by a few decibels for the smooth and rounded flat wheels, but to be more accurate for the ideal flat wheel. For the case of smooth PVC, however, there is a slight over-prediction for the smooth wheel. It is also worth noting that the differences between runs are not always correctly predicted by the model $\Delta L_{n,w}$. For example, comparing the first two rows in Table 5.3, increasing the trolley speed from 0.5 to 0.9 m/s (all else equal) results in a 2 dB increase in the experimental $\Delta L_{n,w} + C_{I,50-2500}$, from 3 to 5 dB, but a 1 dB decrease in the model $\Delta L_{n,w} + C_{I,50-2500}$ from -1 to -2 dB. This discrepancy in model $\Delta L_{n,w}$ is present when comparing several other runs as well in Table 5.3.

Figures 5.17 and 5.18 visualize how the model and experimental $\Delta L_{n,w} + C_{I,50-2500}$ change with changing trolley speed and added load. Here the under and over predictions of the model results (blue bar, shown on the left of each pair) compared to the experimental results (orange bar, shown on the right of each pair) are more easily visualized.

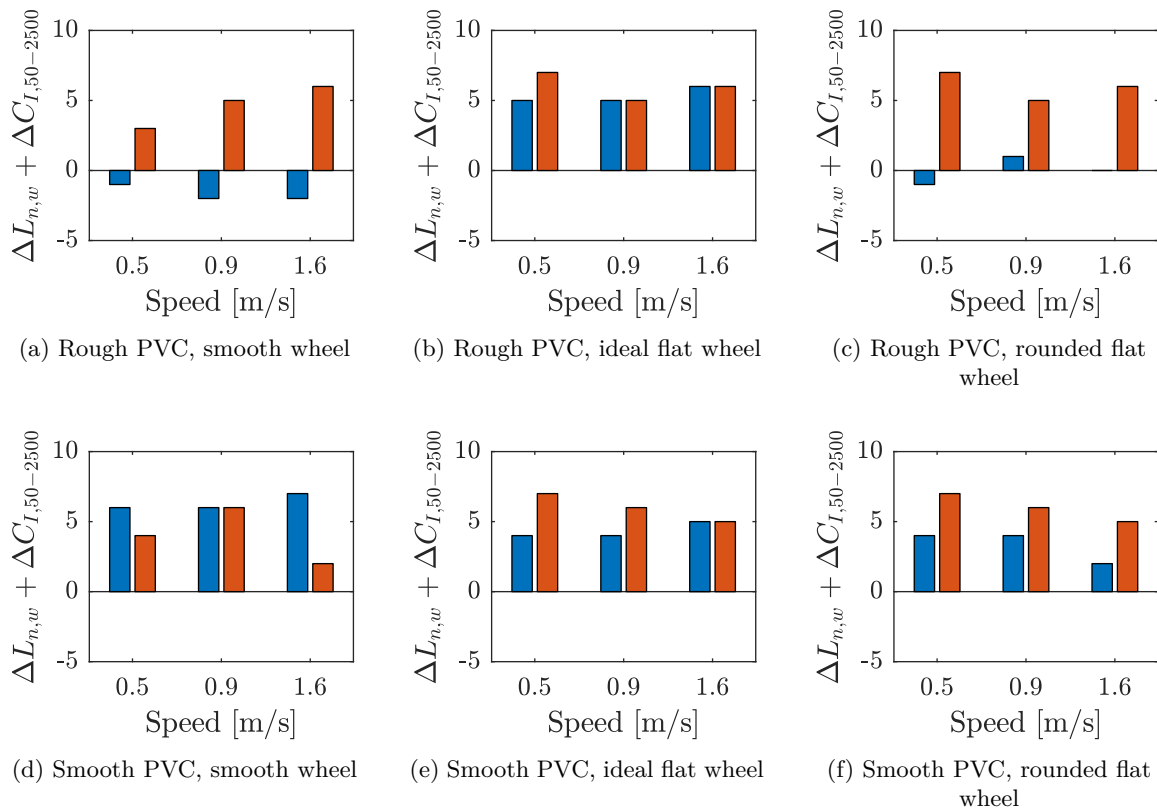


Figure 5.17: Comparison of how the global indicator $\Delta L_{n,w} + C_{I,50-2500}$ changes with trolley speed for the model and experimental results from Level Acoustics & Vibration. ■ model, ■ experiment.

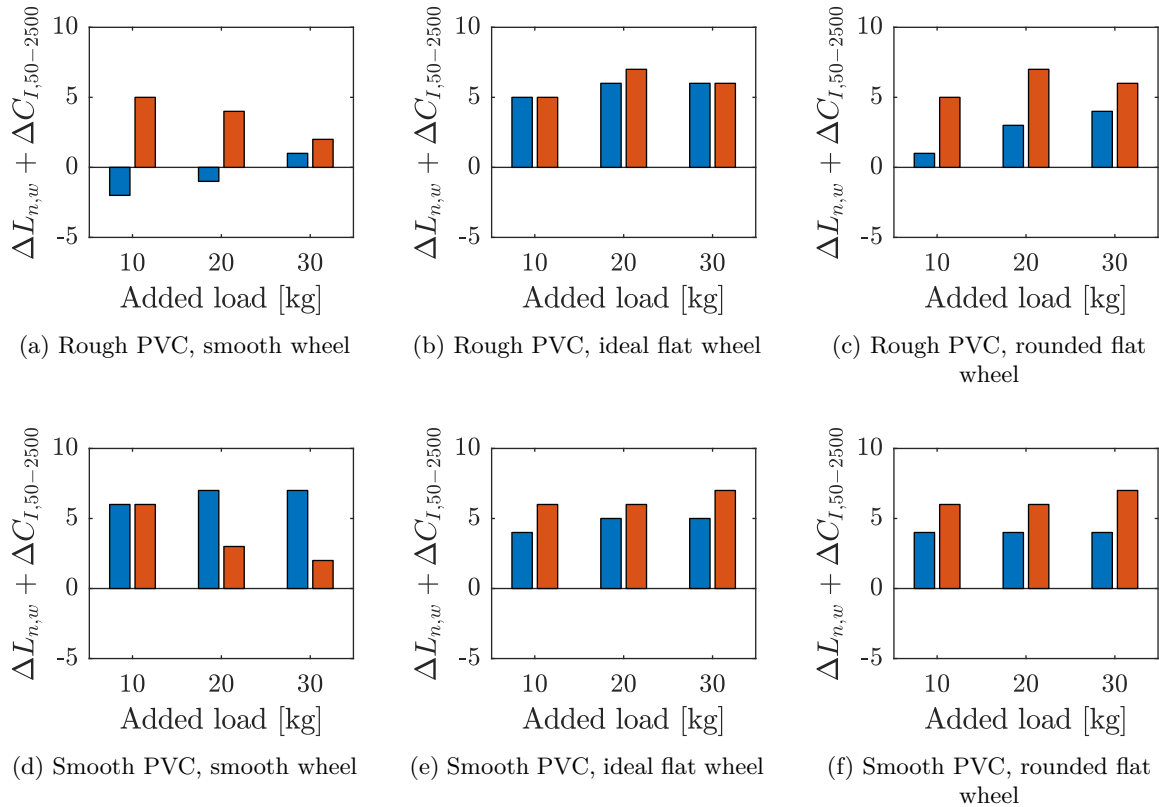


Figure 5.18: Comparison of how the global indicator $\Delta L_{n,w} + C_{I,50-2500}$ changes with added load for the model and experimental results from Level Acoustics & Vibration. ■ model, ■ experiment.

5.6.2 Industrial partner in France

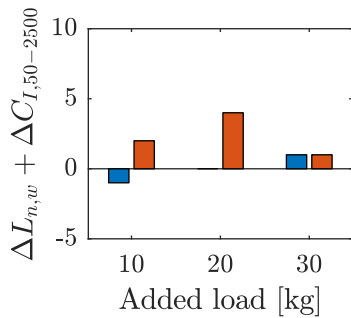
Table 5.4 shows the global indicator $\Delta L_{n,w} + \Delta C_{I,50-2500}$ for both model and experimental results for the measurements conducted at the industrial partner in France using the two-wheeled test trolley. Here the model continues to generally under-predict for the smooth and rounded flat wheel. The idea flat wheel is also slightly under predicted here, though to a much smaller degree than the other wheel configurations.

Figure 5.19 visualizes how the model and experimental $\Delta L_{n,w} + \Delta C_{I,50-2500}$ change with changing added load. The model results (shown on the left of each pair) again have a general tendency to under-predict compared to the experimental results (shown on the right of each pair).

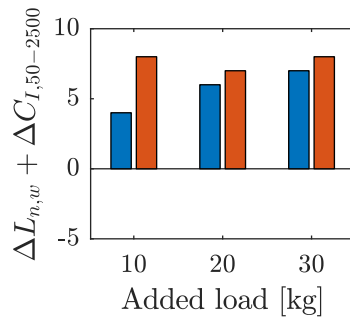
The model can predict the global indicator $\Delta L_{n,w} + \Delta C_{I,50-2500}$ with modest accuracy for many cases. Rolling noise contains more low frequency energy and less high frequency energy than impact noise, which spurred the use of the $C_{I,50-2500}$ adaptation term. Future work which serves to develop a unique reference curve (and by consequence, a unique global indicator) for rolling noise may help improve the usefulness of such single-number values.

Table 5.4: Comparison of global indicators between model and experimental results: industrial partner in France

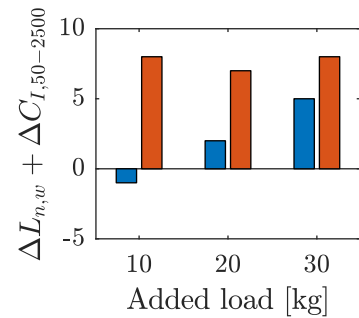
Floor covering	Wheel	Added load [kg]	Model	Experiment
			$\Delta L_{n,w} + \Delta C_{I,50-2500}$ [dB]	$\Delta L_{n,w} + \Delta C_{I,50-2500}$ [dB]
Rough PVC	Smooth	10	-1	4
		20	0	4
		30	1	1
Rough PVC	Ideal flat	10	4	8
		20	6	7
		30	7	8
Rough PVC	Rounded flat	10	-1	8
		20	2	7
		30	5	8
Smooth PVC	Smooth	10	5	5
	Ideal flat	10	4	8
	Rounded flat	10	4	8



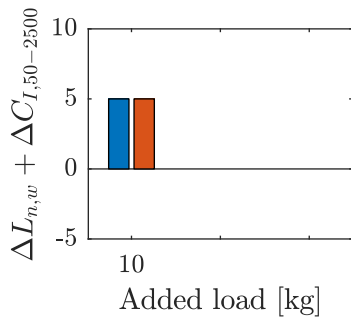
(a) Rough PVC, smooth wheel



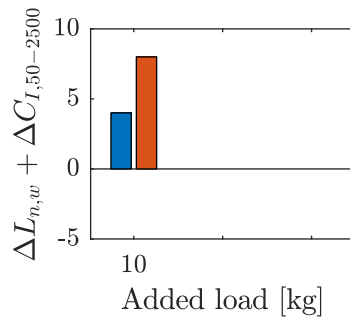
(b) Rough PVC, ideal flat wheel



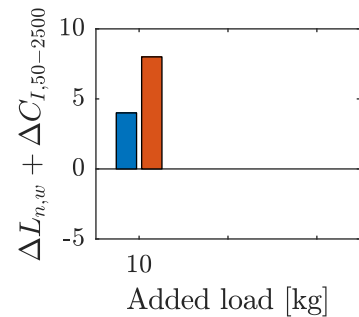
(c) Rough PVC, rounded flat wheel



(d) Smooth PVC, smooth wheel



(e) Smooth PVC, ideal flat wheel



(f) Smooth PVC, rounded flat wheel

Figure 5.19: Comparison of how the global indicator $\Delta L_{n,w} + C_{I,50-2500}$ changes with added load for the model and experimental results from the industrial partner in France. ■ model, ■ experiment.

5.7 Investigation of the contact force

As a wheel flat moves through the vicinity of contact, the longitudinal position of the contact area relative to the wheel center will shift: first backwards as the wheel flat enters the vicinity of contact, and then forwards as the wheel flat exits the vicinity of contact. As the face of the wheel flat impacts the floor, a spike in the contact force will occur, and the position of the wheel center will drop momentarily. All of these phenomena may be visualized via the rolling model.

Figure 5.20 shows the vertical displacement of the wheel, contact force, and contact force distribution as a cylindrical wheel rolls through an ideal flat spot on a concrete floor. Here the force distribution plot is showing slices of the contact stress profile for each discretized moment along the rolling distance x . Recall that x' is the local coordinate system in the vicinity of contact, centered at the wheel center position. The magnitude of the contact stress appears very high because the size of a given discretized cell $\Delta x \times \Delta y$ is very small ($\Delta x = \Delta y = 55 \mu\text{m}$).

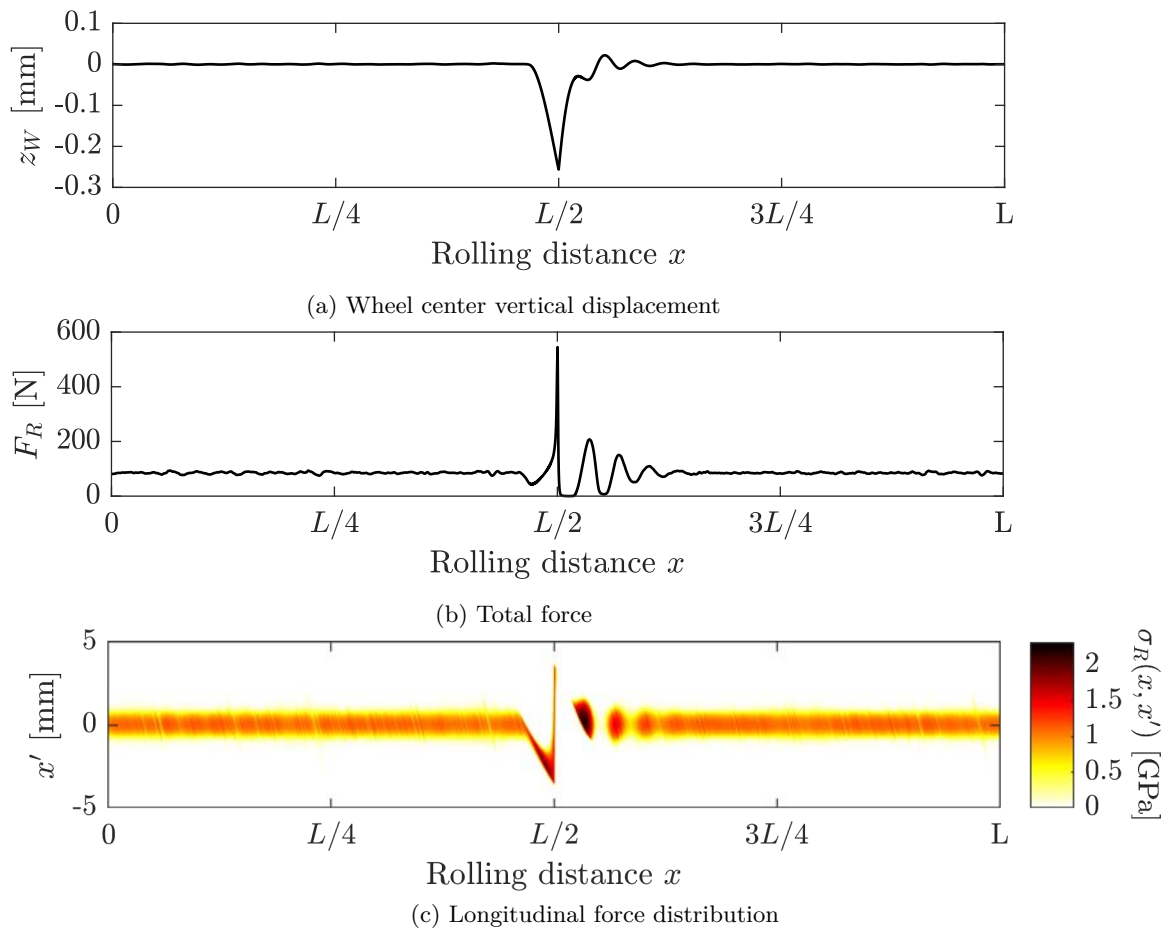


Figure 5.20: Response of a wheel rolling through a single ideal wheel flat

For this simulation, the wheel ($r_x = 50 \text{ mm}$) was given a single ideal flat spot ($h_W = 0.5 \text{ mm}$) located at $\theta = \pi$, and the rolling distance was set to the circumference of the wheel. As such,

the face of the wheel flat impacts the floor at half the rolling distance, which can be clearly seen in all three plots. The wheel center drops a height approximately equal to the wheel flat depth (with small deviations from that value being due to the small scale roughness), and then returns to its previous position as the wheel flat leaves the vicinity of contact. At the moment of impact, a force is generated which is $6.4\times$ the static load (this factor is not universal and changes depending on the influencing factors such as the wheel flat geometry and trolley speed).

Figure 5.21 shows the vertical displacement of the wheel, contact force, and contact force distribution as a cylindrical wheel rolls through a rounded wheel flat on a concrete floor. The same parameters were used as before, with only the type of wheel flat being changed from ideal to rounded flat. The impact force can once again be seen, though its magnitude is noticeably lower than that of the ideal wheel flat, at only $2.3\times$ the static load. The contact force distribution also exhibits a more “smeared” appearance, as the hard corner of the ideal wheel flat is no longer present.

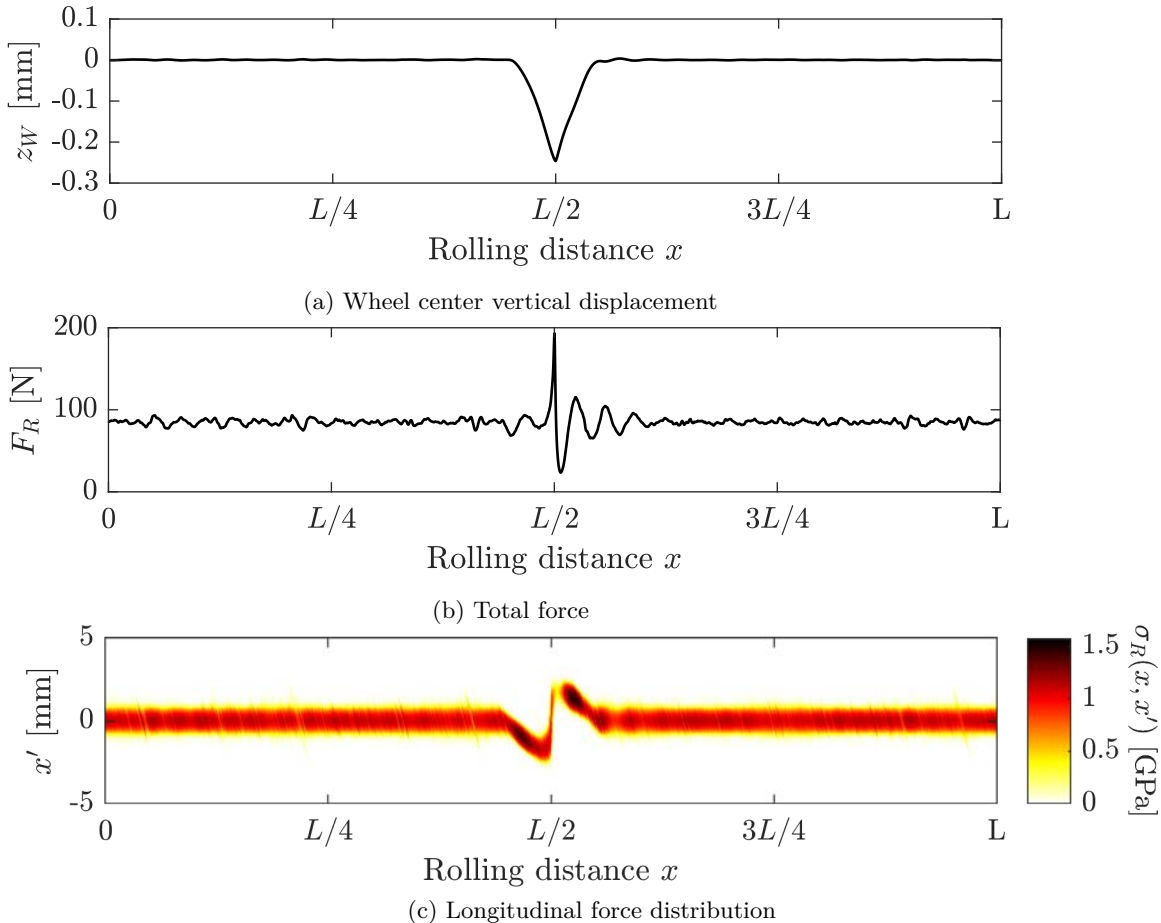


Figure 5.21: Response of a wheel rolling through a single rounded wheel flat

When the wheel flat is replaced by a floor joint, a similar behavior occurs. The wheel center

drops until the leading face of the wheel strikes the far side of the floor joint[†]. Figure 5.22 shows the vertical displacement of the wheel, contact force, and contact force distribution for a smooth wheel rolling over a tile floor joint. The wheel here ($r_x = 50$ mm) encountered a single floor joint ($l_F = 1$ cm) located half the rolling distance (which was again set to the circumference of the wheel). The drop in wheel center is once again visible as the wheel traverses the floor joint. The fact that the area of contact jumps from behind to in front of the wheel center can be seen in the contact force distribution. This differs from the behavior of a wheel flat, as the wheel does not contact the bottom of the floor joint. There is, however, no large spike in the contact force at the moment of impact with the far side of the floor joint. The spike instead comes slightly afterward at $2.9\times$ the static load, as the wheel moves up and out of the far side of the floor joint. A very small spike can be seen at the moment of impact (at $L/2$), but its magnitude is not much larger than that which would be caused by a large roughness asperity.

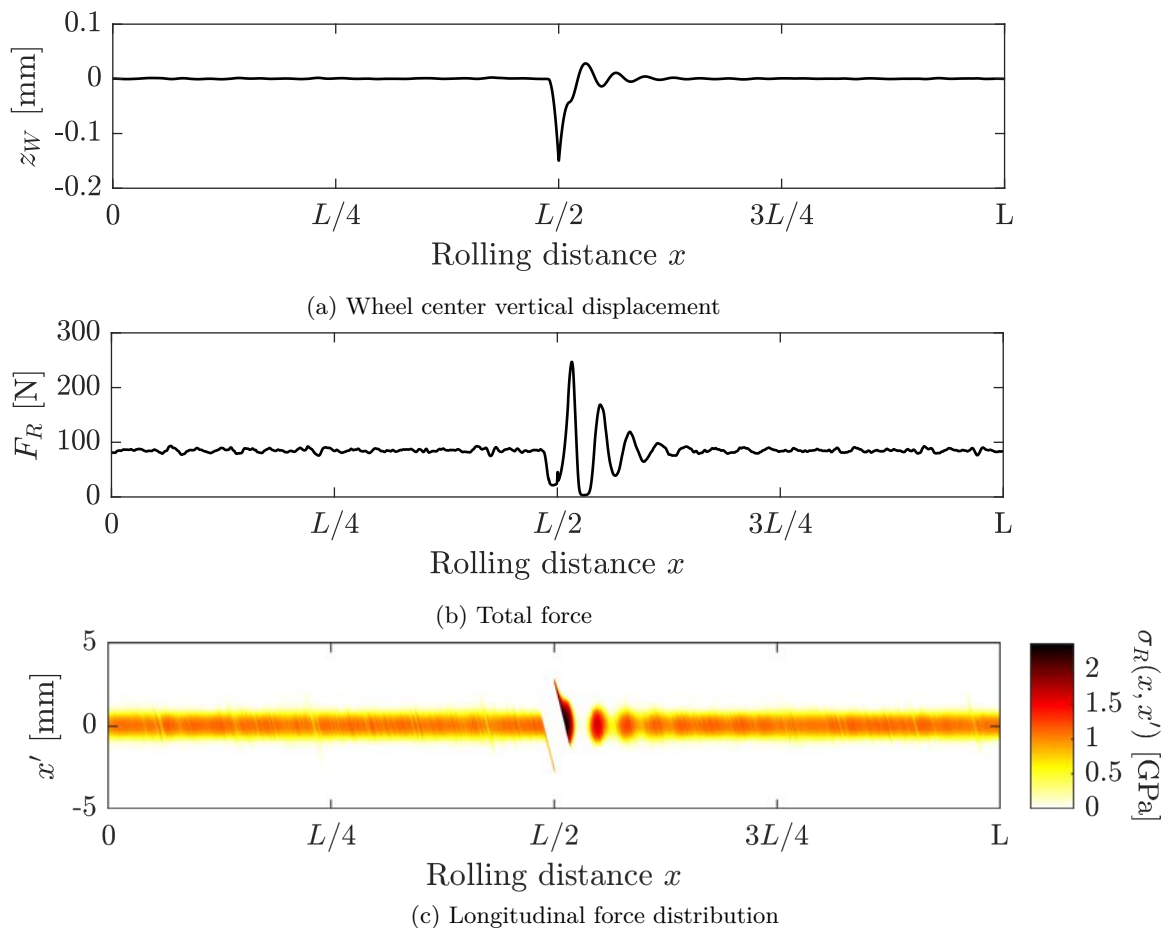


Figure 5.22: Response of a wheel rolling through a single floor joint

[†]A wheel which strikes the bottom of the floor joint before striking the far side is not investigated here. Such a joint would be impractically long, and would not occur in a real built environment

5.7.1 Contact force spectrum

Figure 5.23 shows the contact force spectra $F_R(f)$ for each of the three wheels. The shape of the curves are similar to those in Figure 5.7, which is expected, considering there is a direct link between the contact force spectra and the normalized sound pressure level. The concrete yields the highest magnitude force, followed by the two PVC floor coverings. In the case of the smooth wheel, the two PVC floor coverings have essentially identical force spectra. In the case of the flat wheel, the smooth PVC has a slightly higher force spectrum in the mid frequency range than the rough PVC. This matches the trend seen in the normalized sound pressure level data.

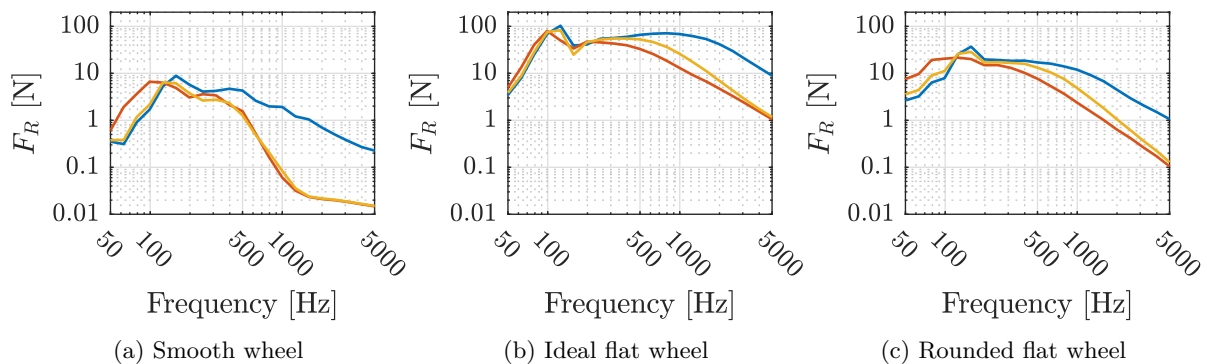


Figure 5.23: Contact force spectra calculated by the rolling noise model. — concrete floor, — rough PVC floor, — smooth PVC floor

5.7.2 Wheel impedance

Figure 5.24 shows the wheel impedance spectra $Z_W(f)$ for each of the three wheels. The impedance is calculated by dividing the contact force spectrum by the wheel vertical velocity spectrum. For comparison, the impedance of a simple rigid mass ($i\omega M$) is also shown (e.g. as is the case for the hammer of a tapping machine). The impedance of the smooth wheel follows that of a simple mass, deviating only above 1 000 Hz where damping and elastic effects play a greater role. The curve of the simple mass continues upward from there. The impedance is significantly lower for the flat wheels, and much flatter across the frequency spectrum as well. While using the impedance of a simple mass would be mostly appropriate for a smooth wheel, the unique wheel impedance calculated by the model is necessary in the presence of discrete irregularities. In all cases, the wheel impedance on concrete is slightly higher than smooth PVC, which is in turn slightly higher than rough PVC. Because the wheel response (e.g. vertical velocity) depends on the type of floor it is rolling on, its impedance is dependent on the type of floor as well.

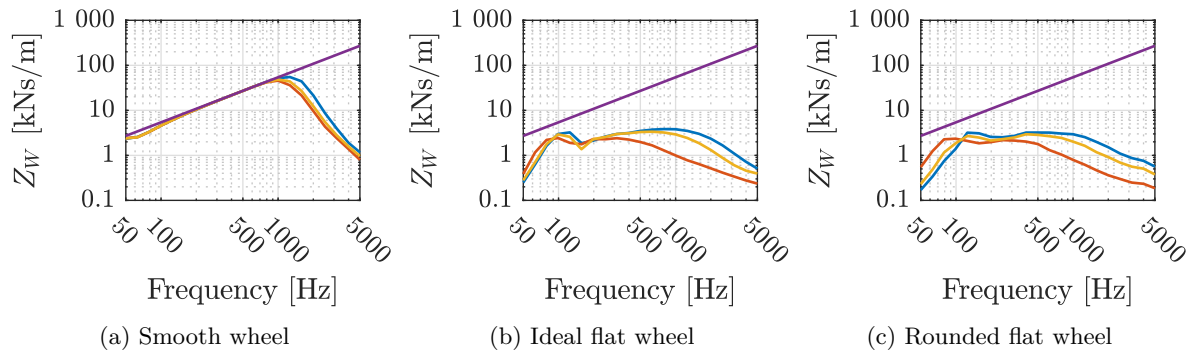


Figure 5.24: Wheel impedance spectra calculated by the rolling noise model.
— concrete floor, — rough PVC floor, — smooth PVC floor, — simple mass: $i\omega M$

5.8 Contact dimensionality

In Chapter 2 it was explained how the rolling model, which normally operates in three dimensions (x, y, z) , may be reduced to a two or one dimensional model. To demonstrate the effect that the dimensionality of the model has on the calculated results, the model was run for an example condition of the smooth, ideal flat, and rounded flat test wheel rolling on a 100 mm thick concrete floor. The results of this comparison are shown in Figure 5.25. Looking first at the one dimensional model compared to the others, we see the effect of the contact filter. Because the contact area is reduced to a single point in the one dimensional model, no filtering of the roughness occurs. The two (line contact) and three dimensional (surface contact) models, on the other hand, naturally filter out the components of the roughness profile with wavelengths shorter than the dimensions of the contact area. Thus the one dimensional model should be expected to over-predict at higher frequencies, as it will calculate an influence of short-wavelength roughness components which is not present in real life. This is exactly what is seen in the model results: the one dimensional curve is significantly elevated in the high frequency region.

Comparing the two and three dimensional models, we see that they yield similar results for the two flat wheel conditions: with the three dimensional model being slightly lower in magnitude. However, the difference is much more pronounced for the smooth wheel, with the predictions of the three dimensional model being noticeably quieter. What is occurring here is likely an over-dependence on the small scale roughness in the one and two dimensional models. Because the effect of the wheel flat impact dominates the force spectra for the flat wheel, the relative influence of the small-scale roughness is diminished. In the absence of wheel flats, the small-scale roughness plays the primary role.

The one and two dimensional models do not over-estimate the static force. The mean contact force over the entire rolling event for the smooth wheel is approximately equal to the static load

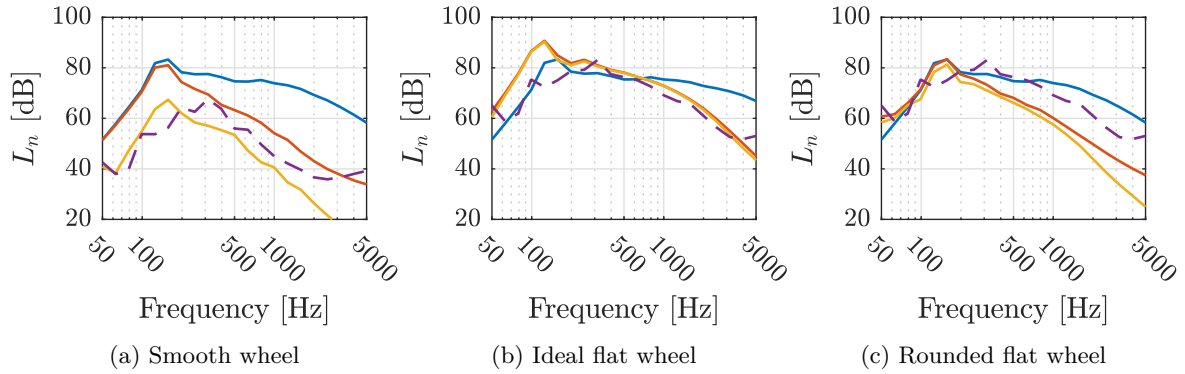


Figure 5.25: Normalized sound pressure level calculated by the rolling noise model in one, two, and three dimensions. Compared with experimental results from Level Acoustics & Vibration.
— model 1D, — model 2D, — model 3D, - - - experiment

Q : this is true for all three dimensions. Figure 5.26 shows the wheel response and contact force calculated by the rolling noise model in one, two, and three dimensions. While the mean value of the contact force stays the same, the variation becomes higher and higher as the dimensionality drops from three to two and then two to one. This is what results in the higher force spectra and consequently higher radiated sound level. The 3D model has the lowest magnitude of the three, modulating only slightly for the vertical scaling shown. The 2D model modulates even more, and the 1D model modulates the most across the whole rolling distance. Particularly for the contact force, the 1D curve is significantly higher in magnitude than the 2D and 3D curves.

Another artifact worth noting in Figure 5.26 is the lower mean wheel displacement for the one dimensional model versus the two and three dimensional models. This is a result of the absence of the wheel curvature in the contact calculation. The two and three dimensional models are able to account for the curvature of the wheel in the direction of rolling, which affects the interpenetration profile u_R between the wheel and floor. As the one dimensional profile has no way to account for this curvature, the difference manifests itself as a greater static vertical displacement of the wheel center.

5.9 Comparison with the preliminary model

A major difference between the preliminary and improved model is the expansion from one dimensional contact to three dimensional contact via the use of a Winkler bedding. Not only does this allow for variations in the roughness profile in the transverse direction to be taken into account, it also provides a natural way of implementing the effect of the contact filter. The preliminary model also cannot not account for the curvature of the wheel, thus discrete

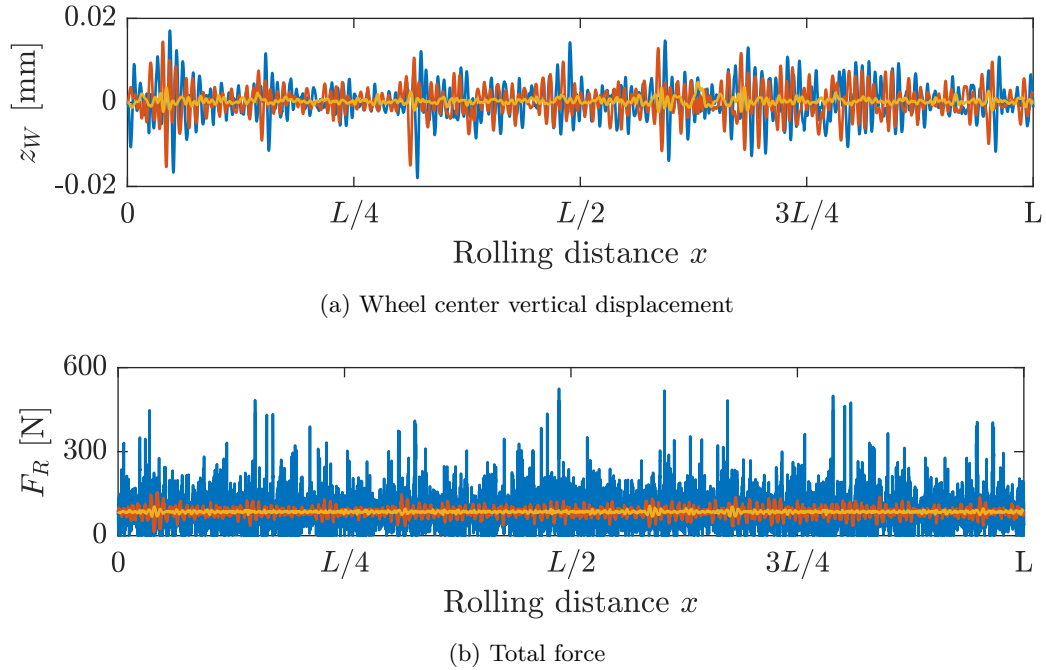


Figure 5.26: Wheel response and contact force calculated by the rolling noise model in one, two, and three dimensions for a smooth wheel rolling on 100 mm thick concrete.

— model 1D, — model 2D, — model 3D

irregularities must be included in the roughness profile rather than being implemented separately through the terms ξ_W and ξ_F .

A second major difference is the improved model's use of Green's functions to calculate the response of the wheel, versus the preliminary model's use of the FDTD method. Green's functions provide a more robust model which has a lower dependence on both the small scale roughness and the wheel damping factor. This avoids the problem of the model estimating that, for example, the rough PVC will result in a significantly higher radiated sound level than the smooth PVC due to the larger roughness asperities, when in reality the difference between the two is minimal.

The two models also differ in the method used to calculate the wheel stiffness: the preliminary model using an equivalent beam and the improved model using polynomial relations derived from finite element models. While this results in a more accurate estimation of the wheel stiffness itself, as was discovered in Section 5.3, this does not translate to a largely different radiated sound level. Nevertheless, other discoveries made in Chapter 3 while conducting the wheel stiffness parametric study (e.g. the lack of Poisson's effect for complex cross sections) still validates the usefulness of study.

Figure 5.27 shows the results of the improved and preliminary rolling noise models in comparison with experimental results for the test wheel rolling on 100 mm thick concrete. The same roughness profiles were used as input to both models. Right away, one of the greatest drawbacks

of the preliminary model becomes apparent: it cannot account for negative irregularities like wheel flats. There is little discernible difference between the curves for the preliminary model between the smooth, ideal flat, and rounded flat wheel: the preliminary model curve appears nearly identical across all three plots in Figure 5.27. The profile of the wheel with flat spots included is indeed used in the preliminary model. However, due to how the model operates, it registers a flat spot moving through the contact area as the wheel center continuing straight and effectively floating above the floor, rather than falling down to remain in contact. When the flat spot profile moves through the contact area in the model, a negative contact force is calculated, which is then set to zero. The preliminary model views flat spots not as impact events, but as moments of loss of contact.

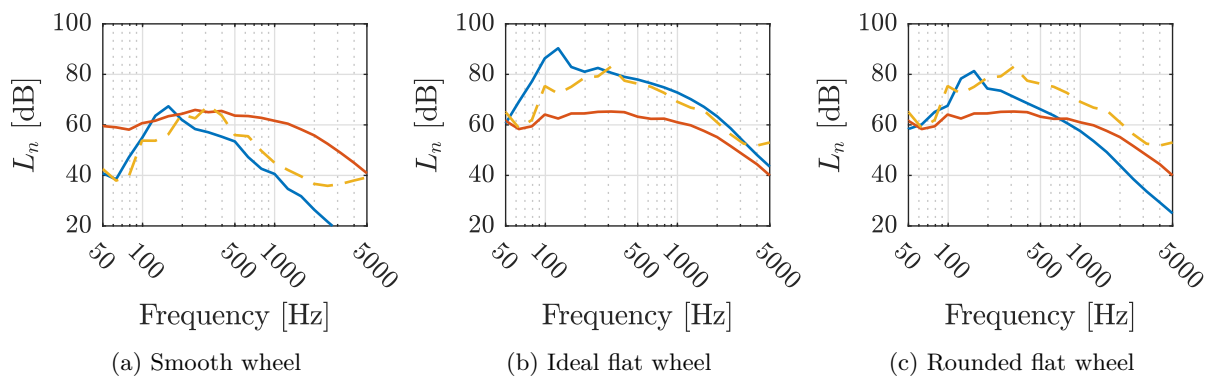


Figure 5.27: Comparison of the normalized sound pressure level calculated by the improved and preliminary models for various wheels rolling on 100 mm thick concrete.

— improved model, — preliminary model, - - - experimental results

Looking at the case of the smooth wheel, even with the use of a real roughness profile, the preliminary model yields less accurate results than the improved model. The over-estimation which occurs at high frequencies in the case of the smooth wheel can be attributed to the lack of contact filter.

Figure 5.28 shows the benefit of adding the rough PVC floor covering to 100 mm thick concrete as calculated by the improved and preliminary rolling noise models in comparison with experimental results. The new model is much better at predicting ΔL_n for both smooth and flat wheels. The preliminary model has a tendency to significantly under-estimate the relative benefit of adding a floor covering below 1 000 Hz, and significantly over-estimate above 1 000 Hz. The overestimation in the high frequency range is once again mainly due to the lack of contact filter. The preliminary model fails to filter out the roughness components with wavelength shorter than the dimensions of the contact area which in reality do not play a role in the generated rolling noise. Though even below 1 000 Hz where the contact filter has no effect, large deviations are still seen.

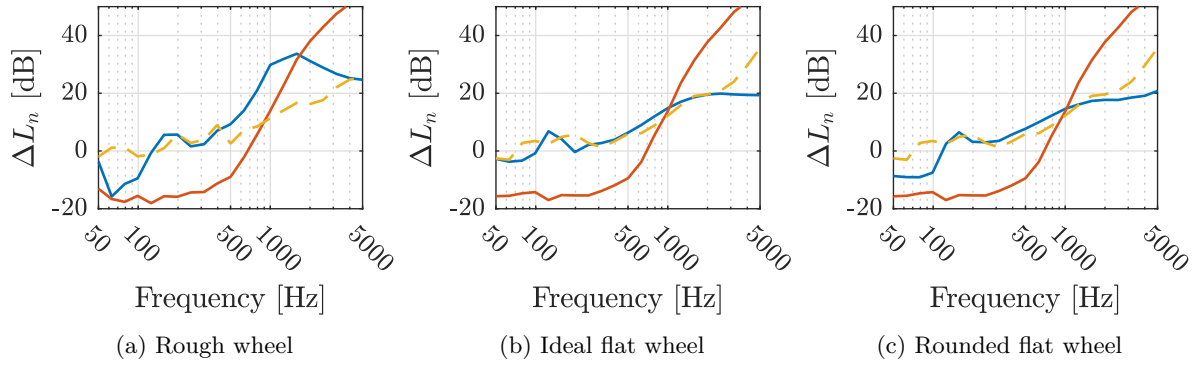


Figure 5.28: Comparison of the the benefit of adding the rough PVC floor covering to 100 mm thick concrete as calculated by the improved and preliminary models for various wheels.
— improved model, — preliminary model, - - - experimental results

In visualizing the contact force in the time domain, we can identify another important advantage that the improved model has over the preliminary model: the accurate estimation of the wheel response and contact force. Figure 5.29 shows a comparison of the wheel response and contact force calculated by the improved and preliminary models for a smooth wheel rolling on 100 mm thick concrete. The improved model correctly estimates a contact force of magnitude which is on par with the excitation present in the smooth wheel configuration. The preliminary model, on the other hand, erroneously estimates a contact force with significantly greater fluctuations: often reaching a magnitude on par or even greater than that which is seen by the impact of a rounded wheel flat in the improved model (see Figure 5.21 for example). Furthermore, the contact force in the improved model fluctuates around the static load Q (84.7 N for this scenario), while the preliminary model fluctuates around a mean value of zero. This implies that the preliminary model is predicting loss of contact between the wheel and the floor continuously throughout the rolling event, which does not happen in reality.

The high excitation is also seen in the vertical wheel center displacement. The improved model estimates small wheel fluctuations on the order of a few micrometers, while the preliminary model predicts much greater wheel displacement due to its over-estimation of the contact force. This is due to multiple factors. The high contact force will directly result in a higher wheel response. Though furthermore, the use of the FDTD method in the preliminary model for calculating the response of the wheel makes the model more sensitive to the wheel stiffness K and damping factor C . Here we see that this too causes greater wheel vertical movement.

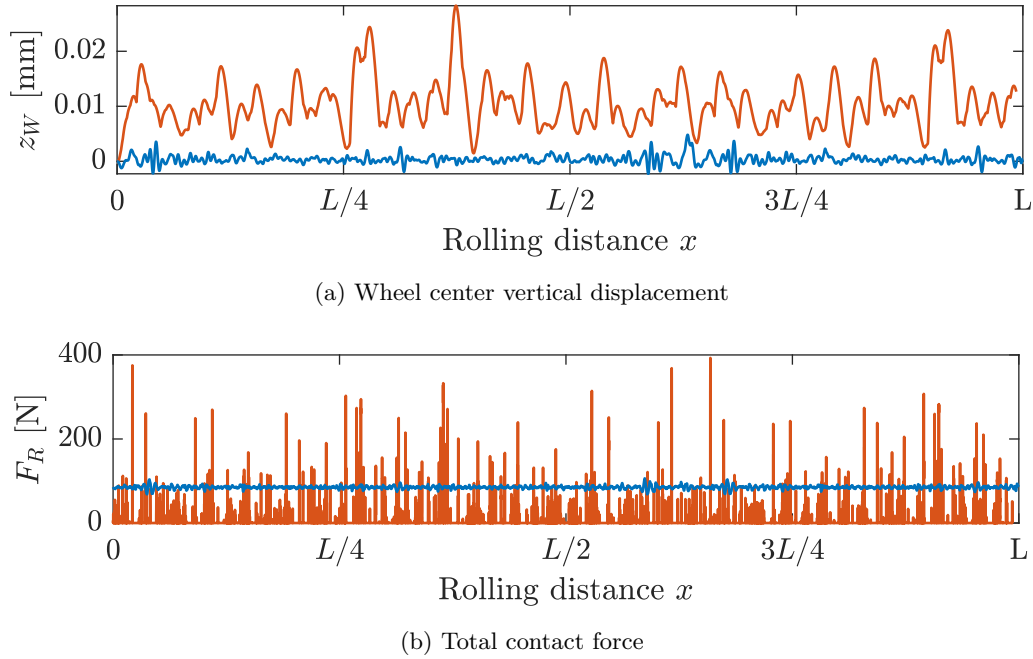


Figure 5.29: Comparison of the wheel response and contact force calculated by the improved and preliminary models for a smooth wheel rolling on 100 mm thick concrete.
— improved model, — preliminary model

As a final comparison, Figure 5.30 shows the wheel response and contact force calculated by the improved and preliminary models for an ideal flat wheel rolling on 100 mm thick concrete. The wheel flats are not visible in the curve for the preliminary model. Every time a wheel flat passes through the contact area, instead of the wheel center falling to stay in contact with the floor (and eventually impacting), the two simply lose contact with one another and the wheel stays floating above the floor.

Due to the high values of F_R and z_W in Figure 5.29, one might expect the preliminary model to predict sound levels even higher than those in Figure 5.27. The fact that the preliminary model sometimes predicts a contact force of zero at certain moments appears to partially balance out the other moments of extremely high force. The moderate agreement between preliminary model and experimental results which is sometimes present for certain frequency regions (e.g. 200–400 Hz for the smooth wheel in Figure 5.27) appears to be mere coincidence.

For this reason, the rolling noise model developed and presented in this thesis provides a substantial improvement over the previous preliminary model. While by no means perfect, it provides more accurate representation of the underlying phenomena present in indoor rolling contact. The forcing and wheel excitation predicted by the improved model are far more realistic and in-line with the real physical characteristics which they represent than those of the preliminary model. The improved model is also able to capture the effects of discrete irregularities: an important feature that the preliminary model fails to have.

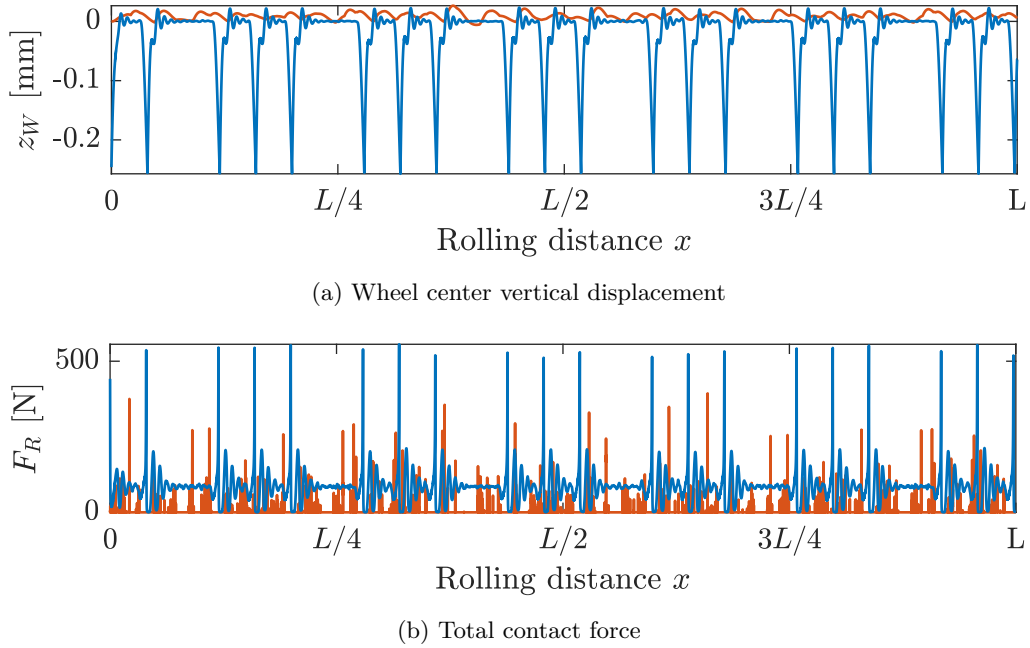


Figure 5.30: Comparison of the wheel response and contact force calculated by the improved and preliminary models for an ideal flat wheel rolling on 100 mm thick concrete.
— improved model, — preliminary model

5.10 Conclusion

This chapter presents a comparison between model and experimental results for the purpose of model validation. The model has been shown to yield moderately accurate results for a multitude of wheel/floor configurations, including the presence of wheel flats. Most importantly, the model is able to predict the relative benefit of adding a floor covering to a reference floor with modest accuracy. Model predictions are particularly close to experimental results for the case of the flat wheel. The new rolling noise model was shown to be a decided improvement over the preliminary model: not only in sound level predictions, but also in its ability to account for discrete irregularities and estimate the physical response of the rolling wheel itself.

In the case of a soft floor, the relative surface roughness between the wheel and floor plays a minor role in the resulting sound pressure level (e.g. the similarity between rough and smooth PVC conditions). The material properties of the two bodies, as well as the mobility of the floor, play a much larger role instead. The addition of a soft floor covering reduces the sound level to a far greater extent, particularly in the high frequency range.

The wheel stiffness plays an important role in determining the correct response of the wheel. However, its variation has a low influence. Thus small fluctuations in the wheel stiffness yield mostly negligible changes in the wheel response and resulting sound level.

While the magnitude of the surface roughness may not play a large role in the case of indoor

rolling noise for soft floors, the contact filter still has a high influence. The one dimensional version of the improved model (and the preliminary model), which lack this contact filter, overestimate the influence of the short roughness wavelengths compared to the two and three dimensional versions.

The added load on the trolley plays a minor role in changing the radiated sound level, and the improved model reflects this. Increasing the mass results in only a slight decrease in sound pressure level. Conversely, the speed of the trolley plays a major role. However, this influence on speed is mostly present in absolute sound levels. Differences between relative sound levels when comparing the benefit of adding a floor covering are smaller.

The greatest influencing factor is the presence of discrete irregularities, which the improved model is able to capture. Model results in general were more accurate for both the ideal and rounded flat wheel when comparing to experimental results versus the smooth wheel, due to the low excitation of the smooth wheels. Considering the fact that the presence of even a small wheel flat has the potential to outweigh the effect of most other influencing factors, being able to capture this effect in the model is very important.

General Conclusions and Perspectives

Conclusion

This thesis concerns the development of a numerical model for predicting the normalized sound pressure level generated by a rolling trolley in an indoor building environment.

The literature review presented in the first chapter allowed for an identification of several techniques which have been used with success in train wheel/rail and vehicle tire/road contact modeling, and which could be adapted to be applicable to indoor rolling noise as well. The use of a bed of independent springs for estimating the contact force between the wheel and floor, the transfer matrix method for calculating the sound radiation to an adjacent room due to said contact force, and identification of the contact filter as a phenomena which should be addressed via either explicit (one dimension) or natural (two and three dimensions) filtering, were all techniques identified throughout the course of this literature review.

The primary objective of this thesis was to develop a rolling noise model that can capture the physical phenomena present in indoor rolling contact, as well as predict the sound level benefit of adding a floor covering to a given floor. The model which was developed has been specifically adapted for the characteristics of rolling in multi-story buildings, such as highly elastic wheels, multi-layer floors, and sound propagation via vertical structure-borne transfer paths. This is a domain which has hereto been left unexplored. As such, this thesis serves as a ground-breaking look into the problem of indoor rolling noise. This thesis serves as a platform which may spur further exploration into the field of indoor rolling noise by other researchers.

The rolling model presented in this thesis, based on Hertzian contact mechanics, has been demonstrated to accurately predict the contact force between a rolling trolley wheel and a multi-layered floor as a function of the geometric and material properties of the two bodies in contact, as well as their small-scale roughness profiles. The inclusion of discrete irregularities such as

wheel flats and floor joints widens the range of scenarios in which the model may be used. Because the model does not take into account the modal behavior of the floor, estimations at very low frequencies have a tendency to deviate from measured results. This is thus an area which could benefit from further research in the future: the implementation of modal estimation techniques into an indoor rolling noise model could serve to increase the accuracy of the model in the low frequency region.

The three developed methods of estimating the wheel stiffness were found to yield largely similar results. Considering its ease and speed of implementation, the two-dimensional polynomial method was chosen for use in the rolling noise model. Furthermore, continuously calculating the wheel stiffness as a function of changing contact area throughout the rolling event was found to yield a mostly negligible benefit. This allows for the pre-calculation method to be used instead, which improves model performance due to its reduced calculation time.

The unique relationship between wheel stiffness and Poisson's ratio which was identified in the finite element parametric study is particularly interesting. The Poisson effect is known to have a high influence on the deformation of other shapes with simpler cross sections, so its absence in the case of a cylindrical wheel was an unexpected discovery. Considering this, it could be beneficial to use the same method (i.e. a finite element parametric study) to investigate the behavior of other complex cross sections in order to see if the effect (or others) are present elsewhere.

The measured small-scale roughness profiles provided a high quality input to the rolling noise model. Roughness profiles with high spatial resolutions (particularly in the transverse direction) are often a large hurdle in rolling noise modeling due to the difficulty and cost of procuring them. Their presence provides a vital link between the numerical model and the real world excitation source which is responsible for the rolling noise being estimated. The discovery that the coherence of the roughness profile in the transverse direction can sometimes yield misleading results may be beneficial to the field of rolling noise as a whole. Multiple parameters should be investigated when studying the behavior of the small-scale roughness in order to form a more complete picture of how they will interact in rolling.

The experimental tests conducted at two industrial partners provided not only meaningful data with which to validate the model, but also valuable insight into the physical phenomena behind indoor rolling noise. Moving forward, performing rolling tests in the field (as opposed to a lab) could provide even further insight into how the sound profile of a rolling device changes depending on the more complex features of the built environment.

While the model can predict the global indicator $\Delta L_{n,w} + C_{I,50-2500}$ in many cases with modest accuracy, the trends of how the global indicators change when changing different influencing parameters of the model (e.g. added load or trolley speed) are not always correct. Future work which serves to develop a unique reference curve (and by extension, unique global indicators and adaptation terms) for rolling noise may help improve the usefulness of such single-number values.

Perspectives

The rolling noise model presented in this thesis has shown its potential to be used in designing acoustic solutions for building applications. With such a model, the acoustic performance of various floor systems may be estimated in order to identify which ones yield the greatest benefit for rolling noise. This is a technique which already exists for other sources of indoor structure-borne noise, such as the tapping machine. However, because impact noise is starkly different than rolling noise, floor systems which have been developed for reducing impact noise will not necessarily exhibit high performance with rolling noise as well. This model may serve as a complement to the existing indoor structure-borne noise modeling solutions, yielding building materials which have better acoustic performance for a wider range of sound sources. The proposition given in Appendix A for a standard rolling device would help in this endeavor.

Until now, the field of rolling noise has stayed largely separated from the wider domain of building acoustics. The focus on rolling noise existed exclusively for outdoor applications such as train wheel/rail and vehicle tire/road contact. This focus is justified, to be sure, as these are both areas where rolling noise poses a significant annoyance to the general public. The indoor rolling noise model developed in this thesis serves as a means of bridging this gap. There are other techniques currently in use in the field of building acoustics which have the potential to be implemented into an indoor rolling noise model, such as lateral and upward transmission of structure-borne noise in multi-story buildings [84]. The implementation of these techniques was outside the scope of this thesis. However, bridging the gap between these acoustic phenomena which have typically only seen focus from more classical sound sources (e.g. airborne or impact structure-borne) could not only serve to further improve the applicability of indoor rolling noise modeling, but also broaden the field of building acoustics as a whole.

Bibliography

- [1] J. Forssén, W. Kropp, J. Brunskog, S. Ljunggren, D. Bard, G. Sandberg, F. Ljunggren, A. Ågren, O. Hallström, H. Dybro, K. Larsson, K. Tillberg, K. Jarnerö, L.-G. Sjökvist, B. Östman, K. Hagsberg, Å. Bolmsvik, A. Olsson, C.-G. Ekstrand, and M. Johansson, “Acoustics in Wooden Buildings, State of the Art 2008,” Tech. Rep. 2008:16, SP Technical Research Institute of Sweden, 2008.
- [2] “ISO 10140-1:2016 - Acoustics – Laboratory Measurement of Sound Insulation of Building Elements – Part 1: Application Rules for Specific Products,” 2016.
- [3] “ISO 10140-3:2010 - Acoustics – Laboratory Measurement of Sound Insulation of Building Elements – Part 3: Measurement of Impact Sound Insulation,” 2010.
- [4] “ISO 10140-4:2010 - Acoustics – Laboratory Measurement of Sound Insulation of Building Elements – Part 4: Measurement Procedures and Requirements,” 2010.
- [5] M. Edwards, F. Chevillotte, L. Jaouen, F.-X. Bécot, and N. Totaro, “Rolling Noise Modeling in Buildings,” in *Internoise 2018*, (Chicago, IL USA), Aug. 2018.
- [6] F. Chevillotte, F.-X. Bécot, and L. Jaouen, “Rolling noise model for building acoustics purposes,” in *Eurnoise 2015*, (Maastricht, The Netherlands), 2015.
- [7] F. Chevillotte, “Rolling Noise Modeling in Buildings,” in *Acoustics '17*, (Boston, MA, USA), June 2017.
- [8] F. Wullens and W. Kropp, “A Three-Dimensional Contact Model for Tyre/Road Interaction in Rolling Conditions,” *Acta Acustica United with Acustica*, vol. 90, pp. 702–711, 2004.

- [9] P. B. U. Andersson and W. Kropp, “Time Domain Contact Model for Tyre/Road Interaction Including Nonlinear Contact Stiffness due to Small-Scale Roughness,” *Journal of Sound and Vibration*, vol. 318, pp. 296–312, Nov. 2008.
- [10] R. J. Pinnington, “Tyre–Road Contact Using a Particle–Envelope Surface Model,” *Journal of Sound and Vibration*, vol. 332, pp. 7055–7075, Dec. 2013.
- [11] P. Remington and J. Webb, “Estimation of Wheel/Rail Interaction Forces in the Contact Area due to Roughness,” *Journal of Sound and Vibration*, vol. 193, pp. 83–102, May 1996.
- [12] D. J. Thompson, B. Hemsworth, and N. Vincent, “Experimental Validation of the TWINS Prediction Program for Rolling Noise, Part 1: Description of the Model and Method,” *Journal of Sound and Vibration*, vol. 193, pp. 123–135, May 1996.
- [13] D. J. Thompson, P. Fodiman, and H. Mahé, “Experimental Validation of the TWINS Prediction Program for Rolling Noise, Part 2: Results,” *Journal of Sound and Vibration*, vol. 193, pp. 137–147, May 1996.
- [14] O. E. Lundberg, S. Finnveden, S. Björklund, M. Pärssinen, and I. Lopez Arteaga, “A Non-linear State-Dependent Model for Vibrations Excited by Roughness in Rolling Contacts,” *Journal of Sound and Vibration*, vol. 345, pp. 197–213, June 2015.
- [15] H. Hertz, D. E. Jones, and G. A. Schott, *Miscellaneous Papers*. London: Macmillan, New York, Macmillan and co., 1896.
- [16] A. E. H. Love and F. R. S., “IX. The Stress Produced in a Semi-Infinite Solid by Pressure on Part of the Boundary,” *Phil. Trans. R. Soc. Lond. A*, vol. 228, pp. 377–420, Jan. 1929.
- [17] S. Timoshenko and J. N. Goodier, *Theory of Elasticity*. New York: McGraw-Hill, 1951.
- [18] J. Boussinesq, “Application des Potentiels à l’Étude de l’Équilibre et du Mouvement des Solides Élastiques, Principalement au Calcul des Déformations et des Pressions que Produisent, dans ces Solides, des Efforts Quelconques Exercés sur une Petite Partie de leur Surface ou de leur Intérieur : Mémoire Suivi de Notes Étendues sur Divers Points de Physique Mathématique et d’Analyse,” *Lilliad - Université de Lille - Sciences et technologies*, 1885.
- [19] K. L. Johnson, *Contact Mechanics*. Cambridge University Press, Aug. 1987.
- [20] J. J. Kalker, *Three-Dimensional Elastic Bodies in Rolling Contact*. Place of publication not identified: Springer, 1991.

- [21] P. J. Remington, “Wheel/Rail Rolling Noise: What do we know? What don’t we know? Where do we go from here?,” *Journal of Sound and Vibration*, vol. 120, pp. 203–226, Jan. 1988.
- [22] P. J. Remington, “Wheel/Rail Noise—Part I: Characterization of the Wheel/Rail Dynamic System,” *Journal of Sound and Vibration*, vol. 46, pp. 359–379, June 1976.
- [23] M. J. Rudd, “Wheel/Rail Noise—Part II: Wheel Squeal,” *Journal of Sound and Vibration*, vol. 46, pp. 381–394, June 1976.
- [24] I. L. Vér, C. S. Ventres, and M. M. Myles, “Wheel/Rail Noise—Part III: Impact Noise Generation by Wheel and Rail Discontinuities,” *Journal of Sound and Vibration*, vol. 46, pp. 395–417, June 1976.
- [25] P. J. Remington, “Wheel/Rail Noise—Part IV: Rolling Noise,” *Journal of Sound and Vibration*, vol. 46, pp. 419–436, June 1976.
- [26] P. J. Remington, “Wheel/Rail Rolling Noise, II: Validation of the Theory,” *The Journal of the Acoustical Society of America*, vol. 81, pp. 1824–1832, June 1987.
- [27] J. Feldman, “Impedance Considerations in the Structure-Borne Behavior of a Simple Rolling Model,” in *Fortschritte der Akustik DAGA ‘84*, 1984.
- [28] J. Feldman, “A Model of Structure-Borne Excitation by Rolling,” in *Fortschritte der Akustik DAGA ‘85*, 1985.
- [29] D. Thompson, “Wheel-rail Noise Generation, Part I: Introduction And Interaction Model,” *Journal of Sound and Vibration*, vol. 161, pp. 387–400, Mar. 1993.
- [30] D. Thompson, “Wheel-rail Noise Generation, Part II: Wheel Vibration,” *Journal of Sound and Vibration*, vol. 161, pp. 401–419, Mar. 1993.
- [31] D. Thompson, “Wheel-rail Noise Generation, Part III: Rail Vibration,” *Journal of Sound and Vibration*, vol. 161, pp. 421–446, Mar. 1993.
- [32] D. Thompson, “Wheel-rail Noise Generation, Part IV: Contact Zone And Results,” *Journal of Sound and Vibration*, vol. 161, pp. 447–466, Mar. 1993.
- [33] T. Wu and D. Thompson, “Theoretical Investigation of Wheel/Rail Non-Linear Interaction due to Roughness Excitation,” *Vehicle System Dynamics*, vol. 34, pp. 261–282, Oct. 2000.
- [34] D. J. Thompson, “On the Relationship Between Wheel and Rail Surface Roughness and Rolling Noise,” *Journal of Sound and Vibration*, vol. 193, pp. 149–160, May 1996.

- [35] E. Winkler, *Der Eisenbahn-Overbau*. Dominicus, Prag, 1871.
- [36] F. D. Fischer and E. Gamsjäger, “Beams on Foundation, Winkler Bedding or Halfspace – A Comparison,” *Technische Mechanik*, vol. 28, no. 2, pp. 152–155, 2008.
- [37] O. E. Lundberg, A. Nordborg, and I. Lopez Arteaga, “The Influence of Surface Roughness on the Contact Stiffness and the Contact Filter Effect in Nonlinear Wheel–Track Interaction,” *Journal of Sound and Vibration*, vol. 366, pp. 429–446, Mar. 2016.
- [38] R. A. J. Ford and D. J. Thompson, “Simplified Contact Filters in Wheel/Rail Noise Prediction,” *Journal of Sound and Vibration*, vol. 293, pp. 807–818, June 2006.
- [39] A. Pieringer, W. Kropp, and D. J. Thompson, “Investigation of the Dynamic Contact Filter Effect in Vertical Wheel/Rail Interaction using a 2D and a 3D Non-Hertzian Contact Model,” *Wear*, vol. 271, pp. 328–338, May 2011.
- [40] T. Mazilu, “Green’s Functions for Analysis of Dynamic Response of Wheel/Rail to Vertical Excitation,” *Journal of Sound and Vibration*, vol. 306, pp. 31–58, Sept. 2007.
- [41] A. Nordborg, “Wheel/Rail Noise Generation due to Nonlinear Effects and Parametric Excitation,” *The Journal of the Acoustical Society of America*, vol. 111, pp. 1772–1781, Apr. 2002.
- [42] J. C. O. Nielsen and A. Igeland, “Vertical Dynamic Interaction Between Train and Track Influence of Wheel and Track Imperfections,” *Journal of Sound and Vibration*, vol. 187, pp. 825–839, Nov. 1995.
- [43] O. E. Lundberg, *On the Influence of Surface Roughness on Rolling Contact Forces*. PhD thesis, Royal Institute of Technology, 2016.
- [44] F. Wullens, *Excitation of Tyre Vibrations Due to Tyre/Road Interaction*. PhD thesis, Chalmers University of Technology, Göteborg, 2004.
- [45] T. Fujikawa, H. Koike, Y. Oshino, and Y. Tachibana, “Generation Mechanism of Tire/Road Noise, Part 1: Tire Vibration Caused by Road Roughness,” *INTER-NOISE and NOISE-CON Congress and Conference Proceedings*, vol. 1999, no. 4, 1999.
- [46] T. Clapp, A. Eberhardt, and C. Kelley, “Development and Validation of a Method for Approximating Road Surface Texture-Induced Contact Pressure in Tire-Pavement Interaction,” *Tire Science and Technology*, vol. 16, no. 1, pp. 2–17, 1988.

- [47] G. Dubois, J. Cesbron, H. P. Yin, and F. Anfosso-Lédée, “Numerical Evaluation of Tyre/Road Contact Pressures Using a Multi-Asperity Approach,” *International Journal of Mechanical Sciences*, vol. 54, pp. 84–94, Jan. 2012.
- [48] G. Dubois, J. Cesbron, H. P. Yin, F. Anfosso-Lédée, and D. Duhamel, “Statistical Estimation of Low Frequency Tyre/Road Noise from Numerical Contact Forces,” *Applied Acoustics*, vol. 74, pp. 1085–1093, Sept. 2013.
- [49] A. von Meier, G. van Blokland, and G. Descornet, “The Influence of Texture and Sound Absorption on the Noise of Porous Road Surfaces,” in *PIARC 2nd International Symposium on Road Surface Characteristics*, pp. 7–19, 1992.
- [50] P. Klein and J. F. Hamet, “Road Texture and Rolling Noise: An Envelopment Procedure for Tire-Road Contact,” 2004.
- [51] T. Clapp, *Spectral Correlation of the Surface Profile in the Development of a Tire and Pavement Interaction Force Model*. Master, Raleigh, 1984.
- [52] H. B. Pacejka and R. S. Sharp, “Shear Force Development by Pneumatic Tyres in Steady State Conditions: A Review of Modelling Aspects,” *Vehicle System Dynamics*, vol. 20, no. 3-4, pp. 121–175, 1991.
- [53] T. Beckenbauer, P. Klein, J.-F. Hamet, and W. Kropp, “Tyre/Road Noise Prediction: A Comparison Between the SPERoN and HyRoNE Models - Part 1,” *The Journal of the Acoustical Society of America*, vol. 123, p. 3388, June 2008.
- [54] P. Klein, T. Beckenbauer, J.-F. Hamet, and W. Kropp, “Tyre/Road Noise Prediction: A Comparison Between the SPERoN and HyRoNE Models - Part 2,” *The Journal of the Acoustical Society of America*, vol. 123, p. 3389, June 2008.
- [55] F. Wullens and W. Kropp, “Wave Content of the Vibration Field of a Rolling Tyre,” *Acta Acustica United with Acustica*, vol. 93, pp. 48–56, 2007.
- [56] C. Hoever and W. Kropp, “A Model for Investigating the Influence of Road Surface Texture and Tyre Tread Pattern on Rolling Resistance,” *Journal of Sound and Vibration*, vol. 351, pp. 161–176, Sept. 2015.
- [57] W. Kropp, P. Sabiniarz, H. Brick, and T. Beckenbauer, “On the Sound Radiation of a Rolling Tyre,” *Journal of Sound and Vibration*, vol. 331, pp. 1789–1805, Apr. 2012.

- [58] P. J. Remington, “Wheel/Rail Rolling Noise, I: Theoretical Analysis,” *The Journal of the Acoustical Society of America*, vol. 81, pp. 1805–1823, June 1987.
- [59] T. X. Wu and D. J. Thompson, “A Hybrid Model for the Noise Generation due to Railway Wheel Flats,” *Journal of Sound and Vibration*, vol. 251, pp. 115–139, Mar. 2002.
- [60] W. Keulen and M. Duškov, *Inventory Study of Basic Knowledge on Tyre/Road Noise*. Jan. 2005.
- [61] E. K. Bender and P. J. Remington, “The Influence of Rails on Train Noise,” *Journal of Sound and Vibration*, vol. 37, pp. 321–334, Dec. 1974.
- [62] “BS EN 15610:2019 - Railway applications - Acoustics - Rail and wheel roughness measurement related to noise generation.”
- [63] A. Johansson and J. C. O. Nielsen, “Out-of-round railway wheels—wheel-rail contact forces and track response derived from field tests and numerical simulations:,” *Proceedings of the Institution of Mechanical Engineers, Part F: Journal of Rail and Rapid Transit*, Jan. 2006.
- [64] D. J. Thompson and C. J. C. Jones, “Sound Radiation from a Vibrating Railway Wheel,” *Journal of Sound and Vibration*, vol. 253, pp. 401–419, May 2002.
- [65] E. Schneider, K. Popp, and H. Irretier, “Noise Generation in Railway Wheels due to Rail-Wheel Contact Forces,” *Journal of Sound and Vibration*, vol. 120, pp. 227–244, Jan. 1988.
- [66] D. J. Thompson, “Predictions of Acoustic Radiation from Vibrating Wheels and Rails,” *Journal of Sound and Vibration*, vol. 120, pp. 275–280, Jan. 1988.
- [67] J. Rayleigh, *Theory of Sound*. Dover Publications, second ed., 1945.
- [68] X. Zhang and H. G. Jonasson, “Directivity of Railway Noise Sources,” *Journal of Sound and Vibration*, vol. 293, pp. 995–1006, June 2006.
- [69] P. Kindt, P. Sas, and W. Desmet, “Development and Validation of a Three-Dimensional Ring-Based Structural Tyre Model,” *Journal of Sound and Vibration*, vol. 326, pp. 852–869, Oct. 2009.
- [70] K. Larsson and W. Kropp, “A High-Frequency Three-Dimensional Tyre Model Based on Two Coupled Elastic Layers,” *Journal of Sound and Vibration*, vol. 253, pp. 889–908, June 2002.

- [71] M. Brinkmeier, U. Nackenhorst, S. Petersen, and O. von Estorff, “A Finite Element Approach for the Simulation of Tire Rolling Noise,” *Journal of Sound and Vibration*, vol. 309, pp. 20–39, Jan. 2008.
- [72] J. A. González and R. Abascal, “Using the Boundary Element Method to Solve Rolling Contact Problems,” *Engineering Analysis with Boundary Elements*, vol. 21, pp. 385–392, June 1998.
- [73] L. E. Kinsler, A. R. Frey, A. B. Coppens, and J. V. Sanders, *Fundamentals of Acoustics*. New York: Wiley, 4th ed ed., 2000.
- [74] D. Thompson, *Railway Noise and Vibration : Mechanisms, Modelling and Means of Control*. Elsevier Science, 2009.
- [75] T. X. Wu and D. J. Thompson, “A Double Timoshenko Beam Model for Vertical Vibration Analysis of Railway Track at High Frequencies,” *Journal of Sound and Vibration*, vol. 224, pp. 329–348, July 1999.
- [76] F.-X. Bécot, S. Barrelet, and W. Kropp, “On the Sound Radiation from Tyres,” in *Inter-noise 2000*, (Nice, France), p. 6, 2000.
- [77] L. Cremer, M. Heckl, and B. A. T. Petersson, *Structure-Borne Sound: Structural Vibrations and Sound Radiation at Audio Frequencies*. Berlin Heidelberg: Springer-Verlag, third ed., 2005.
- [78] M. M. Späh and B. M. Gibbs, “Reception Plate Method for Characterisation of Structure-Borne Sound Sources in Buildings: Assumptions and Application,” *Applied Acoustics*, vol. 70, pp. 361–368, Feb. 2009.
- [79] M. M. Späh and B. M. Gibbs, “Reception Plate Method for Characterisation of Structure-Borne Sound Sources in Buildings: Installed Power and Sound Pressure from Laboratory Data,” *Applied Acoustics*, vol. 70, pp. 1431–1439, Dec. 2009.
- [80] B. Brouard, D. Lafarge, and J.-F. Allard, “A General Method of Modelling Sound Propagation in Layered Media,” *Journal of Sound and Vibration*, vol. 183, pp. 129–142, May 1995.
- [81] D. Rhazi and N. Atalla, “Transfer Matrix Modeling of the Vibroacoustic Response of Multi-Materials Structures Under Mechanical Excitation,” *Journal of Sound and Vibration*, vol. 329, pp. 2532–2546, June 2010.

- [82] “ISO 10140-5:2010 - Acoustics – Laboratory Measurement of Sound Insulation of Building Elements – Part 5: Requirements for test facilities and equipment,” 2010.
- [83] “BS EN 16205:2013+A1:2018 - Laboratory measurement of walking noise on floors.”
- [84] B. Asmussen, “Definition of appropriate procedures to predict exposure in buildings and estimate annoyance Deliverable D1.6,” 2012.
- [85] H. Reiher, “über den Schallschutz durch Baukonstruktionsteile (Sound Isolation by Building Construction Elements),” *Beiheft zue Gesundh.-Ing.*, vol. 2, no. 11, pp. 2–28, 1932.
- [86] C. Guigou-Carter and M. Villot, “Study of Simulated Rainfall Noise on Multi-layered System,” in *Euronoise 2003*, (Naples, Italy), May 2003.
- [87] C. Guigou-Carter and M. Villot, “Predicting the Acoustic Performance of Multilayered Structures Submitted to Structural Excitation,” in *DAGA 2007*, (Stuttgart, Germany), Mar. 2007.
- [88] J.-B. Chéné, C. Guigou-Carter, R. Foret, and M. L. Larsen, “Mesure et prédiction du bruit de pluie sur des systèmes multicouches,” in *10ème Congrès Français d’Acoustique*, (Lyon, France), Apr. 2010.
- [89] L. Jaouen, F.-X. Bécot, and F. Chevillotte, “AlphaCell.” Matelys Research Lab, Mar. 2020. ver 12.0.
- [90] A. Pieringer, W. Kropp, and J. Nielsen, “A time domain model for the wheel/rail interaction aiming to include non-linear contact stiffness and tangential friction,” *Proceedings of the 9th International Workshop on Railway Noise (IWRN9), Munich, Germany, 2007 (published on CD)*, 2007.
- [91] T. A. Harris, *Rolling Bearing Analysis*. New York: Wiley, 4th ed ed., 2001.
- [92] A. Pieringer and W. Kropp, “A fast time-domain model for wheel/rail interaction demonstrated for the case of impact forces caused by wheel flats,” *7th European Conference on Noise Control 2008, EURONOISE 2008; Paris; France; 29 June 2008 through 4 July 2008*, pp. 2643–2648, 2008.
- [93] L. Baeza, A. Roda, J. Carballeira, and E. Giner, “Railway Train-Track Dynamics for Wheel flats with Improved Contact Models,” *Nonlinear Dynamics*, vol. 45, pp. 385–397, Aug. 2006.

- [94] A. Pieringer, *Modelling of Wheel/Rail Interaction Considering Roughness and Discrete Irregularities*. PhD thesis, Chalmers University of Technology, 2008.
- [95] D. L. Folds and C. D. Loggins, “Transmission and reflection of ultrasonic waves in layered media,” *The Journal of the Acoustical Society of America*, vol. 62, pp. 1102–1109, Nov. 1977.
- [96] J. Allard and N. Atalla, *Propagation of Sound in Porous Media: Modelling Sound Absorbing Materials*. Wiley, second ed., 2009.
- [97] N. Atalla, “An overview of the numerical modeling of poroelastic materials,” in *Congress Symposium on the Acoustics of Poro-Elastic Materials*, (France), 2004.
- [98] M. Villot, C. Guigou, and L. Gagliardini, “Predicting the Acoustical Radiation of Finite Size Multi-Layered Structures by Applying Spatial Windowing on Infinite Structures,” *Journal of Sound and Vibration*, vol. 245, pp. 433–455, Aug. 2001.
- [99] D. Rhazi and N. Atalla, “A simple method to account for size effects in the transfer matrix method,” *The Journal of the Acoustical Society of America*, vol. 127, pp. EL30–EL36, Feb. 2010.
- [100] O. Dazel, B. Brouard, J.-P. Groby, and P. Göransson, “A normal modes technique to reduce the order of poroelastic models: Application to 2D and coupled 3D models,” *International Journal for Numerical Methods in Engineering*, vol. 96, no. 2, pp. 110–128, 2013.
- [101] F. Fahy and P. Gardonio, *Sound and Structural Vibration: Radiation, Transmission and Response*. Amsterdam ; Boston: Elsevier/Academic, 2nd ed ed., 2007.
- [102] M. Edwards, F. Chevillotte, F.-X. Bécot, L. Jaouen, and N. Totaro, “Polynomial relations for cylindrical wheel stiffness characterization for use in a rolling noise prediction model,” *Acta Acustica*, vol. 4, no. 2, p. 4, 2020.
- [103] E. Rustighi and S. J. Elliott, “Stochastic Road Excitation and Control Feasibility in a 2D Linear Tyre Model,” *Journal of Sound and Vibration*, vol. 300, pp. 490–501, Mar. 2007.
- [104] S. Sim and K. J. Kim, “A method to determine the complex modulus and poisson’s ratio of viscoelastic materials for FEM applications,” *Journal of Sound and Vibration*, vol. 141, pp. 71–82, Aug. 1990.
- [105] T. Paviot, “pythonOCC,” June 2007. ver 0.16.0.

- [106] H. Si, “Tetgen,” 2013. ver 1.5.
- [107] F. Hecht, O. Pironneau, and A. Le Hyaric, “FreeFem++,” July 2017. ver 3.56.
- [108] “ISO 18437-5:2011 - Mechanical vibration and shock – Characterization of the dynamic mechanical properties of visco-elastic materials – Part 5: Poisson ratio based on comparison between measurements and finite element analysis,” 2014.
- [109] “ISO 4287:1997- Geometrical Product Specifications (GPS) - Surface texture: Profile method - Terms, definitions and surface texture parameters.”
- [110] J. Feder, *Fractals. Physics of Solids and Liquids*, New York: Plenum Press, 1988.
- [111] H. Hurst, “The Long-Term Storage Capacity of Reservoirs,” *Transactions of the American Society of Civil Engineers*, vol. 116, pp. 770–799, 1951.
- [112] T. Aste, “Generalized Hurst Exponent.” MATLAB Central File Exchange, 2020. ver 1.2.0.0.
- [113] T. Di Matteo, T. Aste, and M. Dacorogna, “Scaling behaviors in differently developed markets,” *Physica A: Statistical Mechanics and its Applications*, vol. 324, pp. 183–188, June 2003.
- [114] T. D. Matteo, T. Aste, and M. M. Dacorogna, “Long-term memories of developed and emerging markets: Using the scaling analysis to characterize their stage of development,” *Journal of Banking & Finance*, vol. 29, pp. 827–851, Apr. 2005.
- [115] T. Di Matteo, “Multi-scaling in finance,” *Quantitative Finance*, vol. 7, pp. 21–36, Feb. 2007.
- [116] “ISO 3382-2:2008 - Acoustics – Measurement of room acoustic parameters – Part 2: Reverberation time in ordinary rooms,” 2008.
- [117] M. R. Schroeder, “Statistical parameters of the frequency response curves of large rooms,” *J. Audio Eng. Soc.*, vol. 35, no. 5, pp. 299–306, 1987.
- [118] “ISO 717-2:2013 - Acoustics – Rating of sound insulation in buildings and of building elements – Part 1: Impact sound insulation,” 2013.
- [119] “ISO 10140-2:2010 - Acoustics – Laboratory Measurement of Sound Insulation of Building Elements – Part 2: Measurement of airborne sound insulation,” 2010.

- [120] R. C. Browning, E. A. Baker, J. A. Herron, and R. Kram, "Effects of obesity and sex on the energetic cost and preferred speed of walking," *Journal of Applied Physiology*, vol. 100, pp. 390–398, Feb. 2006.
- [121] "ISO 7626-5:2019 - Mechanical vibration and shock – Experimental determination of mechanical mobility – Part 5: Measurements using impact excitation with an exciter which is not attached to the structure," 2019.
- [122] K. Jarnerö, D. Bard, and C. Simmons, "Vibration Performance of Apartment Buildings with Wooden Lightweight Frame-Work – Residents Survey and Field Measurements. AkuLite Report 6," Tech. Rep. 2013:17, SP - Sveriges Tekniska Forskningsinstitut, SP Trä, 2013.
- [123] T. J. Schultz, "Impact Noise Testing and Rating - 1980," Final NBS-GCR-80-249, Bolt Beranek and Newman Inc., Cambridge MA, USA, Jan. 1981.
- [124] "Field and Laboratory Measurements of Airborne and Impact Sound Transmission," 1960. Recommendation R-140 (International Organization for Standardization), Geneva.
- [125] V. L. Chrisler and W. F. Snyder, "Transmission of Sound Through Wall and Floor Structures," Tech. Rep. 48, J. Research NBS 2, 1929.
- [126] "DIN 4110, 1938: Technischen Bestimmungen für die Zulassung neuer Bausweisen (Technical Recommendations for Licencing of Building Constructions)," Tech. Rep. Deutsche Industrie Normen 4110, Abschnitt D 11 (Schallschutz) (Section D11 - Sound Protection), 1938.
- [127] C. Hopkins, *Sound Insulation*. Amsterdam: Elsevier / Butterworth-Heinemann, 1st ed ed., 2007.
- [128] "National Physical Laboratory Annual Report," Tech. Rep. III - Sound A.-General Research and Maintenance of Standards, (1) Measurement of Sound Transmission Through Building Structures (b) Floors, 1935.
- [129] A. Gastell, "Schalldämm-Messungen in der Praxis und Vorschläge zur Normung des Schallschutzes von Wohnungstrennwänden und Decken (Sound Isolation Measurements in Practice and Proposals for Standardization of Sound Protection of Walls and Floors in Dwellings)," *Akustische Zeitschrift*, vol. 1, pp. 24–35, 1936.
- [130] W. Schule, W. Bausch, and R. Seeger, "Wärme- und Schalltechnische Untersuchungen an der Versuchssiedlung Stuttgart-Weissenhof (Thermal and Acoustical Researches at the

- Weissenhof Housing Development, Stuttgart),” *Gesundheits-Ingenieur*, vol. 60, pp. 709–713, Nov. 1937.
- [131] G. Hofbauer, “Der Schallschutz von Decken (The Sound Isolation of Floors),” *Gesundheits-Ingenieur*, vol. 54, no. 42, pp. 562–566, 1934.
- [132] W. Bausch, “Senalldämmungsmessungen im Laboratorium und in fertigen Gebäuden (Sound Isolation Measurements in the Laboratory and in Finished Buildings),” *Beiheft zue Gesundh.-Ing.*, vol. 2, no. 20, 1939.
- [133] E. Meyer, “Schallisolation und Schallabsorption: Verfahren zu ihrer Messung (Sound Isolation and Sound Absorption: Procedures for their Measurement),” *Zeitschr, VDI*, vol. 74, pp. 273–279, Mar. 1930.
- [134] E. Meyer, “Schallschutz in Hochbauten (Sound Protection in High Buildings),” *Zeitschr, VDI*, vol. 57, no. 1, pp. 563–566, 1931.
- [135] “Measurement of Sound, Noise Abatement, Acoustics of Buildings, Sound Transmission Through Walls, Floors, and Pipes,” Tech. Rep. Engineering 148, National Physical Laboratory, England, Nov. 1939.
- [136] R. Lindahl and H. J. Sabine, “Measurement of Impact Sound Transmission Through Floors,” *The Journal of the Acoustical Society of America*, vol. 11, pp. 401–405, Apr. 1940.
- [137] F. M. Osswald, “Method for Measuring Sound Isolation, in Particular of Impact Sound,” *The Journal of the Acoustical Society of America*, vol. 7, pp. 261–264, Apr. 1936.
- [138] P. Kipfer, “Insulation Measurement of Footstep Noises,” tech. rep., The Physical Society, London, 1949.
- [139] C. Kosten and J. van den Eijk, “Comparative Impact Sound Measurements,” tech. rep., The Physical Society, London, 1949.
- [140] P. Parkin, “Provisional Code for Field and Laboratory Measurements of Airborne and Impact Sound Insulation,” tech. rep., The Physical Society, London, 1949.
- [141] T. Mariner, “Comments on Impact-Noise Measurement,” *The Journal of the Acoustical Society of America*, vol. 35, pp. 1453–1453, Sept. 1963.
- [142] T. Mariner, “Criticism of the ISO Impact-Noise Test,” *The Journal of the Acoustical Society of America*, vol. 36, pp. 1024–1024, May 1964.

- [143] T. J. Schultz, “Alternative test method for evaluating impact noise,” *The Journal of the Acoustical Society of America*, vol. 60, pp. 645–655, Sept. 1976.
- [144] J. J. LoVerde and D. W. Dong, “A dual-rating method for evaluating impact noise isolation of floor-ceiling assemblies,” *The Journal of the Acoustical Society of America*, vol. 141, pp. 428–440, Jan. 2017.
- [145] W. Scholl, “Impact Sound Insulation: The Standard Tapping Machine Shall Learn to Walk!,” *Building Acoustics*, vol. 8, pp. 245–256, Dec. 2001.
- [146] K. Sippell, “Schallschutz durch Baukonstruktionsteile (Sound Protection by Building Construction Elements),” *Gesundheits-Ingenieur*, vol. 55, pp. 535–540, 1940.
- [147] L. Cremer, “Stand der Forschung im Baulichen Schallschutz (Status of Research of Noise Control in Buildings),” *VDI-Zeitschrift*, vol. 91, pp. 199–205, May 1949.
- [148] D. Dal Palù, E. Buiatti, G. E. Puglisi, O. Houix, P. Susini, C. De Giorgi, and A. Astolfi, “The use of Semantic Differential Scales in Listening Tests: A Comparison Between Context and Laboratory Test Conditions for the Rolling Sounds of Office Chairs,” *Applied Acoustics*, vol. 127, pp. 270–283, Dec. 2017.
- [149] R. N. Hamme, “Sound Transmission Through Floor-Ceiling Structures: I. Evolution of New Impact Test Method,” Tech. Rep. IBI-1-I (unpublished), from Geiger and Hamme Laboratories, Anne Arbore, MI, to Insulation Board Institute, New York, NY, Nov. 1965.
- [150] “ISO 6395:2008 - Earth-moving machinery – Determination of sound power level – Dynamic test conditions,” 2008.

A.1 Recommendation for a standard rolling noise machine

A.1.1 Introduction

In the world of building acoustics, a standard tapping machine has long existed for the purpose of replicating and regulating impact noise. This device was originally designed to mimic the sound of human footfall [85], and while this is indeed the strongest source of annoyance among survey responders (in regards to strictly floors) [122], there still exist other kinds of structure-borne noise (whose primary transfer path is through the floor) which could benefit from being considered when designing a building. One of these types of sources is rolling noise.

When it comes to assessing the performance of flooring construction in multi-story buildings, the tapping machine is by far and away the most widely used device. This use is justified, to be sure, as impact noise is often given as one of the greatest sources of annoyance to multi-story building inhabitants [1]. Other sources of noise exist, however, such as rolling noise. This is often talked about in regards to outdoor sources such as trains and automobiles, but there are a plethora of indoor rolling sources which can cause annoyance for building inhabitants as well: delivery trolleys in commercial spaces, rolling desk chairs in offices (both personal and commercial), children's toys, and suitcases, for example. As shown in Figure A.1, these items generate noise due to the small-scale roughness between the floor and wheels, which causes structure-borne noise to propagate through the building as they roll across the floor.

Figure A.2 shows the spectra of a typical tapping machine and rolling noise on a classical concrete floor, as well as the attenuation of a classical floating floor. The sound signature of impact noise is quite different than that of rolling noise in both the temporal and spectral domains. Considering the prevalence of tapping machines, this mismatch means that focus is rarely given to the effects of rolling noise when designing acoustic treatment systems for floors,

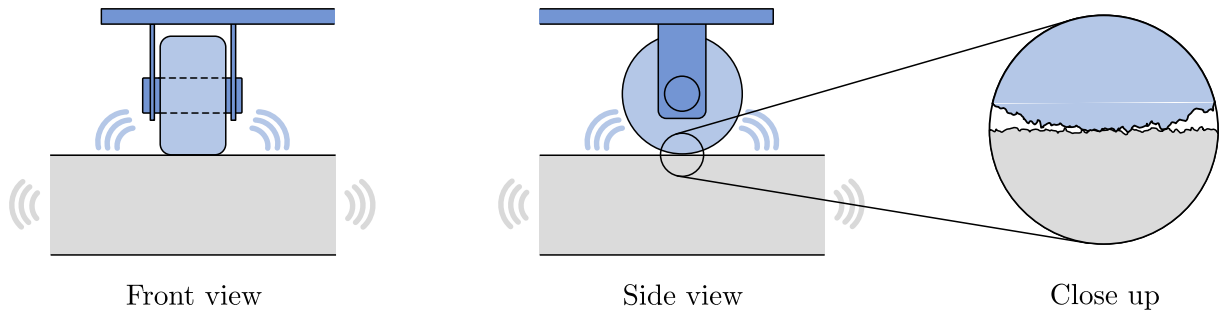


Figure A.1: A typical rolling noise schematic. The small-scale roughness between the floor and wheel generates structural vibrations as the wheel rolls across the floor.

resulting in a gap in performance. There is no guarantee that the techniques which are developed to reduce impact noise will necessarily be effective at reducing rolling noise. Furthermore, without a repeatable way of replicating and measuring this kind of noise, the processes to go about finding solutions to it will remain impeded and incongruent.

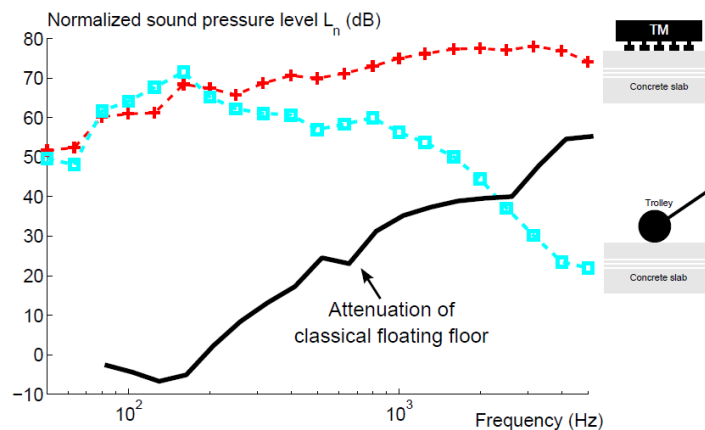


Figure A.2: Comparison of the spectra of tapping noise and rolling noise of a classical concrete floor, as well as the attenuation of a classical floating floor (140 mm concrete slab + a decoupling layer + 40 mm screed). [5]

This report details a proposal for defining a standard rolling noise machine. Just as the standard tapping machine can be used in any building and on any surface as a way of characterizing and comparing the performance of various floors with respect to impact noise, the development of a standard rolling device would enable the same evaluation and comparison to be made with respect to rolling noise. It should be noted that, should the proposal be carried forth to the development of a prototype itself, this device should be treated as just that: a prototype. The development of a rolling noise machine that is robust enough to satisfy all the necessary requirements of being deemed “the standard” is no simple task. As such, one should not expect to accomplish such a lofty goal on the first attempt. Rather, the hope is that such a prototype may serve as a launch pad for further development, spurring future discussion and criticism on the

topic by others who may wish to aid in the pursuit of a truly standardized rolling noise machine. If such a device is intended to be as to rolling noise as a tapping machine is to impact noise, then analyzing how the tapping machine came to be should serve as a good way to inspire its development.

A.1.2 The standard tapping machine: A history

The purpose of this section is not to present a comprehensive overview of the history of the tapping machine. In fact, something of the sort has already been accomplished by Theodore J. Schultz in his extensive report “Impact Noise Testing and Rating – 1980” [123]. On the contrary, this section shall discuss the aspects of the development of the tapping machine which have been deemed relevant to providing insight into how one may go about developing an equivalent device for rolling noise. The history of how the tapping machine become the standard for impact noise may be used as inspiration for how to go about setting a standard for rolling noise.

The tapping machine as it exists today

The modern tapping machine, a schematic of which is shown in Figure A.3, is defined by ISO 10140-5 [82]. It has remained essentially unchanged since its first recommendation in 1960 [124]. It consists of five hammers, controlled by an AC motor on a cam system, which rise and fall in succession to generate impact events with the floor upon which the machine rests. The hammers each have a mass of 500 g ($\pm 2.5\%$), a fall height of 4 cm ($\pm 2.5\%$), and are dropped once every 100 ± 5 ms. Each hammer is supposed to strike the floor only once each time it is dropped (though this has been shown to not always be the case in reality [123]). The hammer material may be either brass or steel, with a third option to use a rubber hammer head (the properties of which are tightly controlled) on fragile floor surfaces. The hammer heads are to be 3 cm in diameter with slightly rounded faces, with a radius of curvature of 50 cm.

How we got to now

The story of how the tapping machine as we know it today came to become the standard for measuring impact noise in buildings is a long and winding one. Starting in 1927 with the first recorded study of footfall noise at the National Bureau of Standards in the United States, and reaching international agreement in January 1960 with the first adoption of the standard by the International Organization for Standardization (ISO), one may hasten to call the process by which the design of the tapping machine was settled upon to be 10% scientific and 90% political. Schultz summed up the major issue that was at hand rather nicely when he stated:



Figure A.3: A typical tapping machine. The five hammers repeatedly drop in succession to generate impacts with the floor at a rate of 10 Hz.

“It is worthwhile to recall here that, in acoustical testing, we sometimes have to choose between making worthless measurements or making meaningless measurements. For example, in the case of impact noise: If we do our measurement in the field, using some kind of real-life excitation such as walking, the resulting impact sound level may be so low compared to the background noise that it cannot be accurately measured; therefore, the measurement is worthless. On the other hand, if we hammer harder (as with the hammer machine), so that the impacts can be readily measured, then the measurement is meaningless, because it tells us nothing about how the floor behaves under actual use.” [123]

Many of the decisions that were made in the design of the tapping machine erred towards being worthwhile (what exactly this means will be discussed later). As a result, the final product is often regarded by critics as yielding results which are meaningless. Nonetheless, the tapping machine we have is the tapping machine that we have: it is the device for measuring impact noise in buildings, and while there exists much contention over its usefulness, there still appears to be some agreement that it is still better to have a poor standard than no standard at all.

Physical machine construction

The mid 1900’s saw a plethora of different tapping machines being developed and tested by various teams across Europe and North America. Most of these drew inspiration from one another in some form, and as the years progressed, a regression towards the mean developed, as the various tapping machines became more and more similar, finally culminating in the standard we know today. Even from the very first impact test, the design has changed remarkably little. The original tapping machine, developed by the United States National Bureau of Standards,

consisted of five rods which could be controlled by a DC motor with a cam system to rise and fall at separate times, roughly once every fifth of a second [125]. From there, other teams developed their own versions of the device; with the next significant event coming in 1938, when Germany standardized their own tapping device (DIN 4110, 1938) [126]. The differences across these devices were found in the varying hammer masses, drop heights, hammer head materials, and frequency of impacts. However, the general construction and methodology (i.e. a device which automatically raises and lowers hammers for impacting the floor) remained essentially unchanged from the start. Perhaps this is not terribly surprising, as it is a relatively straightforward and intuitive way to generate impacts remotely while conducting measurements in the room below. Nevertheless, it begs the question of whether other designs were not given credence simply because of the strong mentality of “this is the way we have always done it” that tends to overpower group decision making, especially in a bureaucratic scenario such as that of writing an international standard.

As a matter of fact, other variations in the tapping machine design were indeed developed and tested. Furthermore, methodologies for reproducing impact noise which have nothing to do with the tapping machine at all have even been developed, some of which are currently in use today in some parts of the world. Perhaps the most well-known example of this is the rubber ball test (Also defined in ISO 10140-5 [82]), which is used in some eastern countries like Japan in place (or in addition to) the tapping machine, due to its ability to better replicate the sound of bare feet walking across a floor (a more common occurrence in some eastern cultures). Just as the name implies, this involves dropping a standardized rubber ball of mass 2.5 kg and diameter 18 cm from a height of 1 m multiple times, and recording the resulting impact sound in the room below. It can also be used in scenarios where low frequency impact performance is of concern, as it generates an impact noise which has more acoustic energy in the low frequencies than the tapping machine, as exemplified in Figure A.4 [127].

In setting out to investigate the story of how the tapping machine came to be, we began with some sort of an expectation that the development process would have been rooted in deep mathematical analysis. We were hoping to find some sort of documentation throughout the research process which detailed the complex theoretical methodologies employed by these early researchers to develop the various tapping machine iterations that were designed throughout history: with vast numerical explanations which depicted how they arrived at their final prototypes. The reality was surprisingly (or perhaps not at all, depending on one’s familiarity with the matter) nothing of the sort. As far as we could find, the early tapping machines were developed almost completely by trial and error, with researchers simply trying different materials,

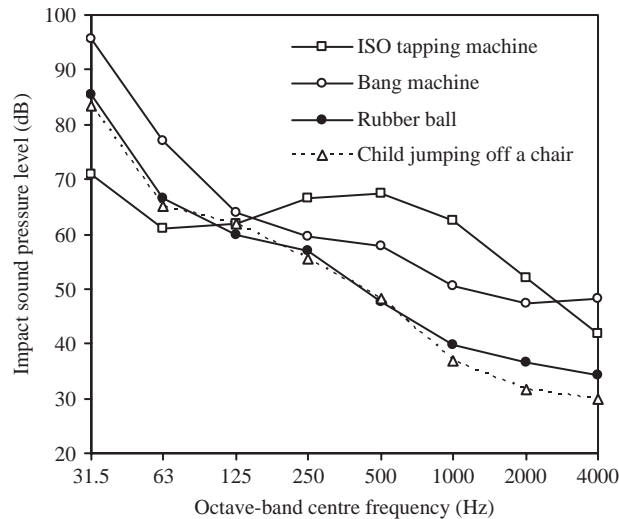


Figure A.4: Impact sound pressure level on a timber floor from various impact devices, including the standard tapping machine and rubber ball. Reproduced from [127].

weights, drop heights, and methodologies, until they found the one that sounded the best when listened to from the room below. There was a small amount of theoretical analysis involved, to be fair. For example, two parameters, fall energy (e.g. in [128, 129, 130]) and hammer momentum (e.g. in [131, 132]), were discussed in several of these early designs. Fall energy is usually expressed in terms of gram-centimeters, and is defined simply by multiplying the hammer mass by the hammer fall height. Hammer momentum on the other hand is defined by multiplying the hammer mass by the square root of the fall height. These values were discussed, and a bit of argument went back and forth over the years over which one was more accurate at describing the loudness of a given impact noise (with hammer momentum eventually winning out and being accepted as the more correct term [132])). However, by far and away, these machines appear to have been designed experimentally. It is also worth noting that some of the early test devices were sparse in their details, neglecting to specify aspects of the test procedure (e.g. [133]), or even making no mention of whether or not they were designed to replicate human footfall noise (e.g. [134]).

The variations to the tapping machine itself that were tested during this gestation period mostly came in the form of differing hammer materials, impact frequencies, and fall energies. The most common materials used started out as wood, rubber, and leather, then migrated towards brass and steel as the years progressed. Anywhere from between one and six hammers were used, impacting at frequencies ranging from 4 Hz to 10 Hz. Hammer masses tended to be in the range of 100–1 000 g [123]. Hammer drop heights observed the greatest range of variability, mostly due to the experimentation that was done with measurement procedures which involved hammer machines with variable drop heights (more on that in the following section).

Measurement procedures

The divide between low and high fall energy tapping machines is linked to the types of measurement procedures which were tried throughout its infancy. The procedure used today involves placing the tapping machine on the floor of the room above and measuring the sound pressure level in the room below. Thus, the performance depends solely on the sound level in the reception room. However, many early researchers experimented with using a transmission loss style approach, where the sound in both the emission and reception rooms was measured (e.g. in [125, 135, 136]), and the difference between the two used to categorize the performance of the floor. Eventually researchers did move towards only measuring the sound level (or loudness level) in the reception room. Comparative tests do exist today: typically for evaluating the performance of a floor covering. Here the sound pressure level in the reception room is measured with and without the floor covering installed on a concrete slab, and the difference between the two calculated as the sound attenuation. Nevertheless, the measurements typically remain conducted solely in the reception room.

Subjective listening was also used in place of objective sound level or loudness measurements in many early studies. This was partially due to the fact that accurate objective measurement equipment had not really been invented yet, but also due to the belief that subjective measurements would yield results closer to reality. The two most common subjective methods were the reference sound method and the just audible method. In the reference sound method, the listener listened to the tapping machine sound in the reception room and compared it to a calibrated reference sound. This calibrated reference sound could have been anything from a pure tone (the frequency content of which was often never stated in these early reports) to an impulse caused by passing a voltage spike through a loudspeaker, with the voltage itself measured as the quantifying value. Examples of this can be found in [128] and [134]. The just audible method involved using a tapping machine capable of dropping the hammers from varying heights, and having the listener listen to the impact events over several of these height cycles. By counting the number of impacts heard between periods of silences (i.e. when the impacts occurring were below the threshold of audibility), they could identify the lowest audible drop height. Examples of this can be found in [85, 131, 137, 138]. It is worth noting that in essentially all of these early subjective tests, there was still a degree of calibration involved in the listening. Listeners did not judge the impact sound while standing in the reception room directly, but listened to it instead through an earpiece which was transmitting the sound from the reception room, and which had been calibrated so that the loudness of the sound through the receiver was perceived to be the same as the loudness of the impacts while standing directly in the reception room [123].

In the wake of World War II in the late 1940's, a group of research teams met from England, France, Denmark, and the Netherlands to compare test procedures for impact noise [139]. They used the same kind of tapping machine and the same test procedure in each of their respective labs, but with different measurement equipment (i.e. they each used the measurement equipment available at their respective labs, and did not try to expressly ensure they were identical in calibration). The results were surprising, deviating 10–15 dB from one another, even after correcting for the absorptions of the various lab reception rooms. A second round of comparative testing was then done, this time using a single tapping machine in a single lab, but each of the research groups bringing their own measurement equipment to perform the same measurement procedure with. This time results were much closer to one another, staying within a range of ± 2.5 dB after absorption correction. Nevertheless, such a range in the very same lab with the very same tapping machine was still found to be alarming to the researchers themselves, and a cause for concern about the validity of the tapping machine as a reliable test apparatus [123].

Final approval

Despite the concerns raised, representatives from Denmark, France, the Netherlands, Sweden, and the United Kingdom met in 1948 to discuss adopting an international standard tapping machine. They agreed to use the already existing German standard tapping machine (defined in DIN 4110 1938 [126]), with the only major change being to use brass rather than wood hammers, with an alternative option to use rubber hammers on fragile floors. This decision was made based on a desire to reduce as much as possible the variability in measurements, as the material properties of brass and rubber can be controlled tighter than wood [123]. The recommendation was brought to a symposium of 32 countries later that year, with comments on the symposium code being submitted in 1949. A final document on the recommendation for an international tapping machine was approved shortly thereafter at a meeting in Copenhagen [140]. Schultz also points out the peculiarity that the German standard was agreed upon being recommended internationally despite the fact that no representative from Germany was present at the 1948 meeting. This could perhaps lead credence to the “this is the way we’ve always done it” theory being a powerful driver in the decision-making process that ultimately resulted in an international standard being adopted in 1960 which was based on a design created in 1938, despite the fact that numerous alternatives were developed, tested, and proposed during the two decades that separated the two.

As bureaucratic dealings tend to go, the process was still rather slow in reaching the ISO. The recommendation first came before a committee of the ISO in 1955, with the final draft being

voted upon in 1958. Of the twenty member countries, this final draft was approved by sixteen, receiving three abstentions and one opposition (from Canada). Finally, in January 1960, the ISO officially adopted ISO standard R 140 for conducting impact noise testing (among other things), cementing the tapping machine's standardization in international history [123].

Teach the controversy?

Today there are acousticians who strongly criticize the use of the tapping machine as an effective means of replicating impact noise in buildings. This is not a recent phenomenon, as criticisms of the tapping machine have existed since the very beginning [141, 142]. Alternatives have been proposed [143, 144, 145], but nothing has been adopted. Schultz points out however, that at the time the German DIN 4110 1938 standard was made, we already knew essentially all of the same problems that we know today, yet they still decided to make the tapping machine the way that they did. This does not mean that criticisms of the tapping machine are moot; perhaps it instead serves as evidence to how heavily politics influence the decision-making process. In regards to using live walkers as a way to more accurately create standard footfall noise, Schultz states: "It is assumed without question in each study that any machine at all would be preferable to using live people to excite the test floor (Only in Sippell's paper (1932) [146] is there a suggestion that live walkers were used, and even then the evidence is far from certain)." Ultimately, the international symposium in 1948 decided to do what they did because they wanted a way to be able to compare lab tests to one another across locations, and the standard they came up with, however lacking, was the best way to do it.

Design criteria of a standard rolling noise machine

In this section we shall draw on what was learned from the development of the tapping machine to inspire the conditions for a standard rolling noise machine. At its most basic level, a standard rolling noise machine should perform a simple function: it should roll across the floor of the emission room while generating a noise that can be measured in the reception room below. There are countless ways by which this can be achieved. The goal here is not to come up with the design for the prototype itself, but rather to propose a methodology for creating one, and present a discussion of what the priorities should be in the engineering process in order to ensure that, when the times comes, the device that ends up being developed is worthwhile.

Lessons learned from the tapping machine

So, with all of that being said regarding the history of the tapping machine, how does any of it help inform the decision on how to go about designing a standard rolling noise machine? Looking at the history of the development of the tapping machine, some trends start to emerge. First and foremost, there is a clear preference for repeatability over accuracy. If the device yields wildly different results when tested repeatedly in the same scenario, then its usefulness as a standard is hardly justifiable. Thus, a rolling device should follow suit. A rolling device rolling across a standard concrete floor in one lab should yield similar measured results to the same device rolling across a similar concrete floor in a different lab.

A second preference can be seen for a machine which requires little or no modification from location to location. Today's tapping machine generates impacts which, for a lightweight floor, have the capacity to be quite a bit louder than real footfall noise. If one wishes to have a device which is standard across all floor environments, this is an unavoidable reality. However, this has been deemed to be preferable to the alternative: a device which replicates real footfall noise perfectly, but is therefore so quiet when being tested on high impedance floor structures that the results provide no beneficial meaning. The same should be true of a standard rolling machine. The device should be capable of generating rolling noise levels which are sufficiently above the background noise level for a wide range of flooring constructions, from thick concrete to lightweight timber.

During the development of the tapping machine, much focus was placed on choosing the right hammer material. This is a consideration that depends not only on sound, as a leather tipped hammer will generate a slightly different impact noise than a brass tipped one, but also on repeatability (linking it with the first point made above). Brass, steel, and rubber can be controlled much easier than wood or leather, making them more appropriate (in the eyes of the 1948 committee) as materials to be used in an international standard device. When looking at rolling noise, such a consideration is equally as important, if not more. The wheels of such a device should be chosen such that they can be used repeatedly, and for a long lifetime, without degrading to the point of significantly changing the noise being produced. This may prove difficult, as the rolling noise depends on the roughness of the wheel, so any change in the wheel surface will result in a change in sound. Though perhaps the use of a sufficiently hard material, such as brass or steel, may be able to mitigate these problems to an acceptable degree. This also has the added benefit of generating a higher overall sound level, reducing the likelihood that the results will be too close to the background noise level.

Perhaps the most important lesson that can be learned from the development of the tapping machine is that, no matter what the case, sacrifices will always have to be made. In an ideal world, one could create an impact noise device which perfectly replicates footfall noise in every possible scenario, while also being repeatable, easily measurable, and standardized. We do not live in an ideal world: concessions will always be necessary. However, a device which is perhaps less accurate than one would like is better than no device at all. After the end of the second world war, acousticians in Europe were eager to establish standards for noise in buildings as quickly as possible, as they did not want buildings which were being constructed to be done so hastily, and with no regards to acoustic quality [139, 147, 148]. Furthermore, they recognized that “more reliable test methods would have to be developed to permit widespread testing of new buildings” [123]. Today, the time-sensitive pressure to develop standards quickly no longer exists, but the need for test methods which can be used easily in widespread cases remains. A device which is so complex or so modular that it is rendered no longer useful for quick validation tests is hardly worth developing, even if it may satisfy the desires of the most purist of acousticians. With rolling noise, just as with impact noise, the difficulty lies in choosing which corners are worth cutting for the sake of simplicity and which ones are worth preserving for the sake of accuracy.

Specific considerations for the standard rolling noise machine

The parameters which dictate the impact sound of a tapping machine are the hammer mass, hammer material, hammer drop height, frequency of impacts, and floor construction. With rolling noise, the governing parameters are the roughness of the floor and wheel, material properties of the floor and wheel, floor construction, speed of the device, and load on the device. In both cases, the parameters related to the floor are the dependent variables of the equation, as the whole purpose is to assess their acoustical performance. This may cause an issue for rolling noise. Because the rolling noise depends not only on the intrinsic material properties and the macro construction of the floor, but also on its surface roughness, two identical floors with different surface finishes can yield different noise levels for the same source rolling across them. For example, in the case of rolling office chairs, subjective testing has shown there to be a noticeable difference in the sound produced when changing the flooring material upon which the chair rolls [148].

As an example, suppose we have a basic two-story structure with a simple concrete slab separating the two floors, such as the one shown in Figure A.5. In the west half of the room, the concrete remains as it was when it was poured (i.e. relatively rough). In the east half of the room, a polisher was used to polish the surface of the concrete during drying, resulting in

a much smoother surface. The two halves of the floor remain identical in material composition and in construction, all that has changed is the surface roughness. In this scenario, a trolley rolling across the floor from east to west will exhibit a change in sound profile as soon as it crosses from rolling on the smooth concrete to rolling on the rough concrete (or vice versa). A tapping machine, on the other hand, will sound the same on both surfaces. All else being equal, whether this difference in rolling noise could be large enough to be detectable by a listener in the room below, or to raise concern for the feasibility of a standard rolling device, is yet to be known. Nevertheless, it is something that will need to be taken into consideration in the design process.

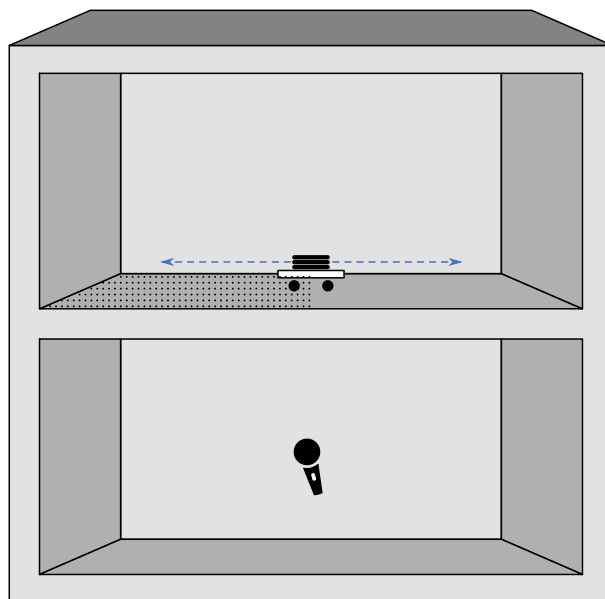


Figure A.5: Example of a simple two-story concrete structure with varying surface roughness on the top floor.

In turning next to the wheel (or rather, wheels) which will be used on this rolling device, the obvious question is that of what material they should be. While it is true that no single wheel material will be able to encompass the entire realm of possibility, the goal here is to replicate the “worst case scenario”, developing a device which generates as loud a rolling noise as possible (so that levels on massive floors are still sufficiently high). To this end, a metallic wheel would likely be the best candidate. Alternatively, just as the tapping machine standard has the option for a rubber hammer to be used on fragile surfaces, perhaps two types of wheels may be specified for a rolling device: one soft and one hard.

It has been observed through rolling noise measurements that the presence of wheel flats can dominate over all other influencing factors in rolling noise. A wheel with flat spots rolling on a soft floor covering will generally still be louder than a smooth wheel rolling on bare concrete. Thus it may be considered beneficial to use wheels with flat spots on the standard rolling

machine. An additional benefit is that the profile of a wheel is easier to control (from a standardization perspective) than a roughness profile.

While use of a flat wheel does have the benefit of generating a louder, more consistent sound, the risk is that the presence of flat spots causes the sound to shift away from sounding like rolling noise and towards sounding like impact noise. This is perhaps analogous to the discussion surrounding the tapping machine on whether or not it is truly representative of footfall noise. Use of flat wheels should remain an option in the case that a sufficiently high signal to noise ratio cannot be achieved with a smooth wheel, or that a roughness profile is considered too difficult to tightly control. However, its drawbacks should still be kept in mind.

The question of what load should be placed on the rolling device may seem to draw parallels to the question of what the hammer momentum (or fall energy) should be for the tapping machine. However, as it has been discovered that the load on the trolley has little influence on the generated sound level, this is actually only a minor design criteria. The sound level has a tendency to decrease slightly with increasing load. The trolley need only be heavy enough to ensure that no rattling or other secondary noise is emitted. Beyond that, it may be kept as light as possible to both increase sound level and reduce the difficulty of moving it around.

In a similar vein, the rolling device should be constructed in such a way so as to ensure all wheels always remain in constant contact with the ground. This can be achieved with an either two or three-wheeled device. As shown in Figure A.6, moving up to four wheels introduces the possibility that the device may wobble as it rolls, if a perfect plane is not formed between the floor and the four contact points. In the interest of automation, a three wheeled device may be considered preferable over one with two wheels, as the latter would need to be supported by some other means (likely a person) to avoid falling over (technically gyroscopic stabilization could be used on a two-wheel device, but that hardly fulfills the requirement that the design be *simple*). A three-wheeled, motorized design would allow the same flexibility offered by the tapping machine, where it could be set, turned on, and recorded without human interaction. Though considerations would still need to be made to ensure the device does not run into a wall.

Fortunately, it has been shown through rolling noise tests that trajectory and the presence of a human operator provide a negligible change in the radiated sound level. Thus the decision is greatly simplified as to whether to use two or three wheels, and whether to have the trolley automated or manually pushed.

The final variable to consider is speed. The sound level and frequency content of the rolling noise will change with the speed of the rolling device; thus this is a parameter which should be intentionally chosen. Following the goal of replicating a worst case scenario, the speed should

be reasonably high such that a high radiated sound level is generated, but not so great as to make the rolling device unstable or difficult to operate reliably. A speed of around 1 m/s, which is slightly below the preferred human walking speed of 1.4 m/s [120], may be an ideal balance point.

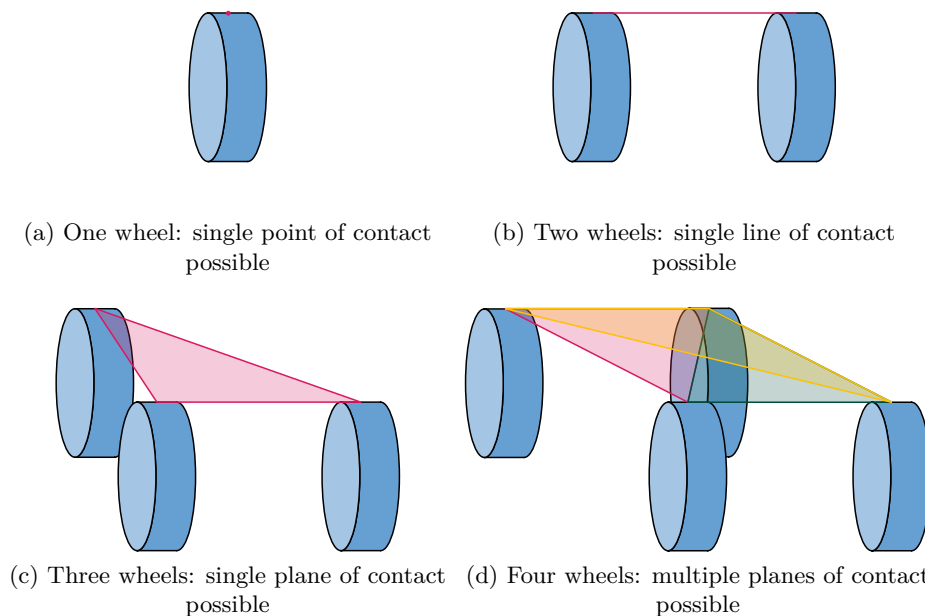


Figure A.6: Different contact scenarios based on the number of wheels. With four wheels and above, it is possible to have more than one plane of contact, introducing wobble.

Rolling noise measurement methodology

While the focus of this paper is on the development of the device itself, consideration will also need to be made in generating the method used to measure the rolling noise produced by said device. One option would be to use the same ISO standard process already established for measuring impact noise. This has the benefit of being about as straightforward as possible. There is no need to generate a brand new methodology, and rolling noise results may more easily be compared with those of a tapping machine.. However, it is worth pointing out that even the existing method of measuring root mean square (RMS) sound levels in the reception room does not accurately represent the subjective perception of impact noise either [143, 149]. This is not to say that we may take the opinion of, “well their method has flaws, so it’s okay to put the same flaws in our method too.” On the contrary, this may serve as an opportunity to correct the mistakes of yesteryear.

Measuring RMS sound levels should in theory provide a better representation of rolling noise than impact noise, as the former is more homogeneous in nature. Considering the movement

of the rolling source across the floor above (contrasted with a stationary tapping machine), directivity may play a role in the perception of the sound in the room below. This is dealt with in the standards surrounding the sound emission of earth moving equipment by having the machine drive through a microphone hemisphere at a constant speed, and measuring the average sound power level of the hemisphere from the time the center of the machine enters one side of the hemisphere to the time it exits the opposite side [150]. Additionally, for testing in reverberant rooms, a microphone on a rotating boom is often used. While the presence of a multi-floor setup with indoor rolling noise prohibits the use of a microphone hemisphere around the rolling source (not to mention the headache that would cause for acousticians, should such a method be adopted), the fact remains that averaging of the recorded sound level over the duration of the rolling event as the device moves from one side of the floor to the other may serve well to remove any discrepancies caused by directivity. Fortunately, this is precisely what is done in ISO 10140-5: either a number of microphones spaced apart or a single microphone on a rotating boom are used in the reception room. Nevertheless, a perceptive test which compares rolling noise recordings captured with different methods could yield beneficial information about how well these methods correspond to what humans actually perceive..

Finally, in order for measurements to remain comparable across laboratory locations, it is advised that a consistent thickness be used for the base concrete slab upon which the floor rolls. As 140 mm is a typical thickness for concrete floors in multi-story buildings, specifying that all rolling noise laboratory measurements be conducted using a base floor of 140 mm concrete would allow for easy comparison across a number of laboratories.

A.1.3 Proposed development process

With all the above being said, the proposed development process for a standard rolling machine prototype could be considered as follows:

1. Conduct a series of tests on various rolling products in a two-story reverberation chamber in order to gain a wide range of audio samples for the different kinds of rolling noise which may be found in indoor scenarios, thus complimenting the existing indoor rolling test data.
2. Perform a subjective study to identify how varying the measurement method of the above tests changes the perceived rolling sound compared with what a listener actually hears.
3. Use the results of the rolling product tests to aid in the development of specific design requirements for the prototype. Choose dimensional and material criteria in such a way as to provide “worst case scenario” representation of the range of sound profiles observed.

4. Develop a theoretical prototype design using a computer-aided design (CAD) software.
5. Fabricate first prototype. Test the device in a two-story reverberation chamber, comparing the results to those of the previous tested rolling products. Compare both the sound generated by the prototype, as well as the applicability of the measurement method decided upon in step 2.
6. Revise the prototype design and measurement method as necessary based on the outcomes of the test.
7. Disseminate results.

A.1.4 Conclusion

This report details a proposal for defining a standard rolling noise machine. Just as the standard tapping machine can be used in any building and on any surface as a way of characterizing and comparing the performance of various floors with respect to impact noise, the development of a standard rolling device would enable the same evaluation and comparison to be made with respect to rolling noise. Throughout the research process, it was discovered that a preference for high repeatability over high accuracy was continuously made in the decisions that went into the standard tapping machine design. These decisions may be used as guidance and inspiration in the future development of a standard rolling machine, with a possible goal being to develop a prototype which may be used as a reference device for conducting rolling noise measurements in buildings.

A.1.5 Acknowledgments

The work which went into this report was conducted as part of the Acoutect program in conjunction with NCC during the demonstrator group 3 secondment, November 5–16, 2018. The authors would like to thank NCC for hosting the team during the duration of the secondment: notably Linda Cusumano, Christina Claeson-Jonsson, and Birgitta Berglund. This project has received funding from the European Union’s Horizon 2020 research and innovation programme under grant agreement No 721536.

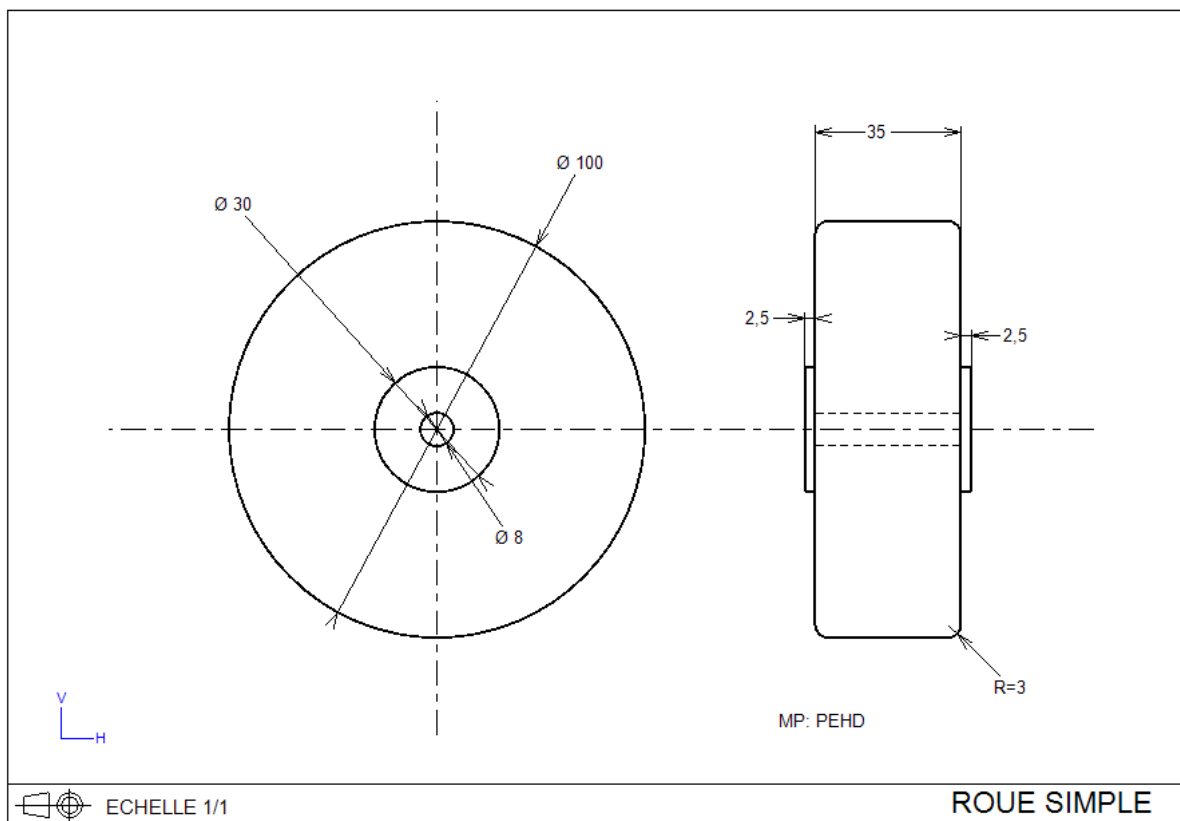


Figure B.1: Diagram of the smooth test wheel.

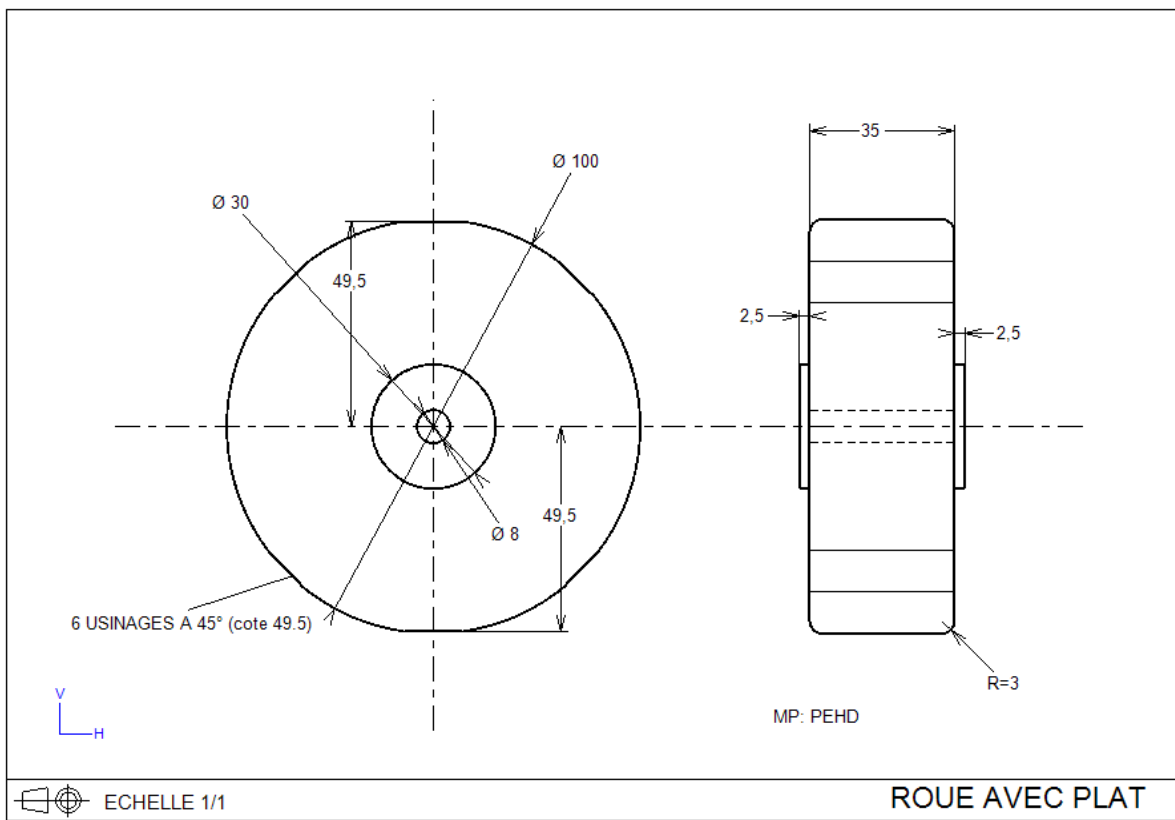


Figure B.2: Diagram of the test wheel with flat spots.

C.1 Parametric study

Table C.1 shows the values investigated in the parametric study from Chapter 3.

Table C.1: Parametric study investigated values from Chapter 3

u_0 (mm)	E (GPa)	ν (-)	r_W (mm)	r_A/r_W (-)	w/r_W (-)	a/r_W (-)
0.1	0.01	0.0	10	0.05	0.10	0.003
0.6	0.02	0.1	15	0.10	0.15	0.004
1.1	0.03	0.2	20	0.15	0.20	0.005
1.7	0.05	0.3	25	0.20	0.25	0.010
2.2	0.08	0.4	30	0.25	0.30	0.015
2.7	0.14	0.45	35	0.30	0.35	0.020
3.2	0.23	0.46	40	0.35	0.40	0.025
3.7	0.38	0.47	45	0.40	0.45	0.030
4.3	0.65	0.48	50	0.45	0.50	0.035
4.8	1.09	0.49	55	0.50	0.55	0.040
5.3	1.84	0.495	60	0.55	0.60	0.045
5.8	3.09		65	0.60	0.65	0.050
6.4	5.21		70	0.65	0.70	0.055
6.9	8.77		75	0.70	0.75	0.060
7.4	14.76		80	0.75	0.80	0.065
7.9	24.86		85	0.80	0.85	0.070
8.4	41.87		90	0.85	0.90	0.075
9.0	70.52		95	0.90	0.95	0.080
9.5	118.76		100	0.95	1.00	0.085
10.0	200			0.96		0.090
				0.97		0.095
				0.98		0.1
				0.99		

C.2 Lookup table

Table C.2 shows the values of K_{norm} from the wheel stiffness abacus used as a lookup table in Chapter 3.

Table C.2: Wheel stiffness abacus from Chapter 3: K_{norm} [-]

		a/r_W [-]					
		0.003	0.0037	0.0045	0.0056	0.0068	0.0084
r_A/r_W [-]	0.05	0.036	0.035	0.038	0.04	0.041	0.041
	0.15	0.113	0.115	0.12	0.124	0.127	0.136
	0.25	0.185	0.191	0.198	0.205	0.213	0.222
	0.35	0.244	0.254	0.263	0.274	0.284	0.296
	0.45	0.29	0.301	0.313	0.326	0.339	0.354
	0.55	0.321	0.333	0.347	0.362	0.377	0.395
	0.65	0.341	0.356	0.371	0.389	0.406	0.426
	0.75	0.365	0.382	0.399	0.418	0.441	0.463
	0.8	0.385	0.403	0.421	0.443	0.467	0.495
	0.825	0.395	0.416	0.435	0.46	0.484	0.517
	0.85	0.41	0.432	0.454	0.481	0.508	0.541
	0.87	0.426	0.448	0.472	0.502	0.531	0.567
	0.89	0.444	0.469	0.496	0.528	0.561	0.601
	0.91	0.47	0.497	0.527	0.563	0.601	0.647
	0.93	0.505	0.537	0.571	0.615	0.658	0.714
	0.95	0.562	0.6	0.641	0.698	0.753	0.826
	0.96	0.609	0.653	0.703	0.775	0.839	0.927
	0.97	0.685	0.74	0.806	0.889	0.974	1.086
	0.98	0.786	0.853	0.959	1.052	1.183	1.361

		$a/r_W [-]$					
		0.0103	0.0127	0.0156	0.0192	0.0236	0.029
$r_A/r_W [-]$	0.05	0.041	0.043	0.047	0.049	0.046	0.056
	0.15	0.14	0.144	0.152	0.158	0.165	0.171
	0.25	0.231	0.24	0.251	0.263	0.276	0.291
	0.35	0.309	0.323	0.338	0.355	0.374	0.395
	0.45	0.37	0.389	0.408	0.43	0.454	0.481
	0.55	0.415	0.435	0.459	0.486	0.515	0.548
	0.65	0.449	0.473	0.502	0.532	0.567	0.608
	0.75	0.492	0.522	0.554	0.596	0.638	0.689
	0.8	0.526	0.559	0.6	0.644	0.695	0.757
	0.825	0.548	0.586	0.629	0.679	0.737	0.804
	0.85	0.577	0.619	0.667	0.723	0.787	0.865
	0.87	0.607	0.654	0.707	0.768	0.842	0.93
	0.89	0.645	0.697	0.759	0.829	0.914	1.02
	0.91	0.698	0.761	0.83	0.916	1.015	1.136
	0.93	0.776	0.854	0.941	1.047	1.175	1.331
	0.95	0.911	1.011	1.135	1.284	1.464	1.694
	0.96	1.024	1.144	1.293	1.489	1.73	2.026
0.97	1.192	1.364	1.572	1.846	2.183	2.598	
0.98	1.555	1.821	2.154	2.61	3.127	3.829	

		$a/r_W [-]$					
		0.0357	0.0438	0.0539	0.0662	0.0814	0.1
$r_A/r_W [-]$	0.05	0.055	0.055	0.053	0.061	0.074	0.061
	0.15	0.179	0.19	0.201	0.213	0.227	0.24
	0.25	0.305	0.326	0.342	0.366	0.391	0.419
	0.35	0.418	0.444	0.474	0.506	0.542	0.586
	0.45	0.511	0.545	0.584	0.629	0.68	0.739
	0.55	0.586	0.628	0.679	0.735	0.801	0.878
	0.65	0.653	0.706	0.767	0.841	0.929	1.03
	0.75	0.75	0.817	0.899	1.001	1.123	1.263
	0.8	0.828	0.913	1.016	1.14	1.293	1.48
	0.825	0.885	0.979	1.098	1.242	1.422	1.638
	0.85	0.957	1.064	1.198	1.362	1.569	1.832
	0.87	1.034	1.16	1.314	1.507	1.752	2.07
	0.89	1.143	1.292	1.478	1.708	2.014	2.407
	0.91	1.284	1.468	1.701	1.998	2.387	2.898
	0.93	1.527	1.771	2.09	2.499	3.036	3.749
	0.95	1.987	2.36	2.839	3.472	4.301	5.412
	0.96	2.406	2.892	3.54	4.376	5.491	6.954
0.97	3.149	3.842	4.761	5.93	7.515	9.699	
0.98	4.726	5.838	7.325	9.28	11.923	15.805	

C.3 One-dimensional polynomials

Table C.3 shows the coefficients used in the 1D polynomials given in Chapter 3 with respect to the axle/wheel radii ratio r_A/r_W , which correspond to the following formulation

$$P_{a/r_W}(r_A/r_W) = \frac{K}{wE} = C_9(r_A/r_W)^9 + C_8(r_A/r_W)^8 + C_7(r_A/r_W)^7 + C_6(r_A/r_W)^6 + C_5(r_A/r_W)^5 + C_4(r_A/r_W)^4 + C_3(r_A/r_W)^3 + C_2(r_A/r_W)^2 + C_1(r_A/r_W)^1 + C_0(r_A/r_W) \quad (\text{C.1})$$

Table C.3: 1D polynomial coefficients with respect to the wheel/axle radii ratio r_A/r_W from Chapter 3

	a/r_W [-]			
	0.003	0.0037	0.0045	0.0056
C_9	3486.753	3975.390	5341.971	5022.300
C_8	-15 936.356	-18 344.279	-24 651.353	-23 199.422
C_7	31 085.712	36 145.616	48 479.527	45 692.990
C_6	-33 823.930	-39 726.807	-53 036.281	-50 085.839
C_5	22 546.316	26 716.825	35 363.785	33 473.624
C_4	-9535.668	-11 363.191	-14 823.393	-14 065.655
C_3	2574.738	3064.430	3900.020	3709.498
C_2	-442.707	-519.238	-632.442	-603.188
C_1	50.288	56.712	63.882	61.386
C_0	-5.001	-5.210	-5.288	-5.166

	a/r_W [-]			
	0.0068	0.0084	0.0103	0.0127
C_9	5485.424	6730.952	7399.380	8271.061
C_8	-25 203.250	-31 123.440	-34 273.417	-38 280.238
C_7	49 315.313	61 360.523	67 667.198	75 483.875
C_6	-53 620.879	-67 329.255	-74 314.179	-82 738.102
C_5	35 477.703	45 044.494	49 714.958	55 179.844
C_4	-14 723.056	-18 939.734	-20 872.138	-23 049.426
C_3	3824.743	4986.772	5474.981	5994.313
C_2	-611.608	-801.352	-873.107	-941.604
C_1	61.435	77.520	83.120	87.337
C_0	-5.133	-5.585	-5.736	-5.781

	$a/r_W [-]$			
	0.0156	0.0192	0.0236	0.029
C_9	9281.122	9853.289	10426.109	10896.373
C_8	-42937.615	-45449.746	-48161.529	-50067.375
C_7	84597.834	89261.120	94777.700	97849.976
C_6	-92595.299	-97355.325	-103661.532	-106045.008
C_5	61608.980	64518.002	68965.837	69681.344
C_4	-25636.602	-26721.982	-28722.086	-28527.416
C_3	6623.647	6864.866	7436.577	7211.482
C_2	-1027.503	-1057.149	-1157.151	-1085.880
C_1	92.766	94.522	104.273	94.435
C_0	-5.813	-5.809	-6.170	-5.633

	$a/r_W [-]$			
	0.0357	0.0438	0.0539	0.0662
C_9	11216.637	10860.163	11022.125	10104.188
C_8	-51609.655	-49824.566	-50807.432	-46303.708
C_7	101079.033	97299.377	99841.010	90410.144
C_6	-109884.126	-105477.946	-109119.135	-98109.423
C_5	72518.559	69441.218	72597.814	64749.346
C_4	-29866.402	-28558.768	-30258.326	-26743.058
C_3	7610.072	7284.794	7845.675	6866.598
C_2	-1156.965	-1115.018	-1222.537	-1061.154
C_1	101.269	99.396	110.086	96.060
C_0	-5.857	-5.835	-6.198	-5.657

	$a/r_W [-]$	
	0.0814	0.1
C_9	9664.066	10964.283
C_8	-44098.210	-50439.149
C_7	85664.094	98897.812
C_6	-92368.420	-107813.757
C_5	60462.720	71521.697
C_4	-24702.956	-29717.541
C_3	6250.649	7684.947
C_2	-947.801	-1196.832
C_1	84.577	108.514
C_0	-5.108	-6.026

C.4 Two-dimensional polynomial

Table C.4 shows the coefficients used in the 2D polynomial given in Chapter 3, which correspond to the following formulation.

$$\begin{aligned}
 P(f, g) = \frac{K}{wE} = \exp & \left(C_{50}f^5 + C_{41}f^4g + C_{32}f^3g^2 + C_{23}f^2g^3 + C_{14}fg^4 + C_{05}g^5 \right. \\
 & + C_{40}f^4 + C_{31}f^3g + C_{22}f^2g^2 + C_{13}fg^3 + C_{04}g^4 + C_{30}f^3 + C_{21}f^2g \\
 & \left. + C_{12}fg^2 + C_{03}g^3 + C_{20}f^2 + C_{11}fg + C_{02}g^2 + C_{10}f + C_{01}g + C_{00} \right)
 \end{aligned} \quad (\text{C.2})$$

For ease of display, the expressions for axle/wheel radii ratio and contact area half-length have been replaced by functions f and g , such that

$$f = r_A/r_W \quad (\text{C.3})$$

$$g = a/r_W \quad (\text{C.4})$$

Table C.4: 2D polynomial coefficients from Chapter 3.

$C_{i,j}$	$C_{i,j}$
C_{50}	95.448
C_{41}	280.369
C_{32}	-1319.105
C_{23}	4004.448
C_{14}	-9965.202
C_{05}	1052707.575
C_{40}	-249.304
C_{31}	-351.973
C_{22}	1108.967
C_{13}	75.910
C_{04}	-305716.234
C_{30}	246.535
C_{21}	123.059
C_{12}	-453.953
C_{03}	33012.778
C_{20}	-116.952
C_{11}	7.302
C_{02}	-1625.255
C_{10}	28.714
C_{01}	42.606
C_{00}	-4.643



FOLIO ADMINISTRATIF

THESE DE L'UNIVERSITE DE LYON OPEREE AU SEIN DE L'INSA LYON

NOM : EDWARDS

DATE de SOUTENANCE : 3/11/2020

Prénoms : Matthew Ryan

TITRE : Prediction and Control of Rolling Noise in Buildings

NATURE : Doctorat

Numéro d'ordre : 2020LYSEI097

Ecole doctorale : MEGA (Mécanique, Energétique, Génie Civil, Acoustique)

Spécialité : Acoustique

RESUME : Les nouveaux bâtiments dans les zones urbaines sont divisés en zones commerciales et en zones habitables. Les magasins commerciaux se trouvent généralement au rez-de-chaussée, les résidences privées aux étages supérieurs. Cette utilisation a révélé des perturbations critiques dues au bruit généré par les chariots de livraison lorsque les bâtiments sont principalement occupés (par exemple tôt le matin). Ces chariots génèrent des vibrations à basse fréquence (moins de 100 Hz) qui se propagent facilement dans la structure du bâtiment et aux étages supérieurs, perturbant les habitants qui s'y trouvent. Si des travaux ont été réalisés pour étudier le bruit d'impact, peu de recherches ont été menées dans le domaine du bruit de roulement dans les bâtiments. Cette thèse présente un modèle original du bruit de roulement dans les bâtiments, prenant en compte les facteurs d'influence tels que la rugosité de la roue & du sol, les propriétés matérielles de la roue & du sol, la vitesse du chariot, et la charge sur le chariot. Les irrégularités discrètes, telles que les méplats des roues et les joints de sol, sont également prises en compte. Le modèle est capable de saisir les phénomènes physiques présents dans le contact de roulement à l'intérieur, ainsi que d'estimer l'avantage relatif du niveau sonore de l'ajout d'un revêtement de sol à un système de plancher donné. Le modèle peut être utilisé comme un outil pour étudier comment différents systèmes de revêtement de sol (y compris les systèmes multicouches) réagissent à l'excitation par roulement, dans le but de développer des solutions de construction à plusieurs étages qui sont mieux équipées pour combattre ce type de source de bruit.

MOTS-CLÉS : roulement, bruit, modèle, acoustique, son, hertzien, contact, multicouche, bâtiment à plusieurs étages

Laboratoire de recherche : Laboratoire Vibrations Acoustique (LVA) de l'INSA – Lyon

Directeur de thèse : TOTARO Nicolas

Président de jury : LE BOT Alain

Composition du jury :

KROPP, Wolfgang, Professeur des Universités, Université de Chalmers,
DUHAMEL, Denis, Professeur des Universités, École des Ponts ParisTech,
GUIGOU-CARTER, Catherine, Docteur, CSTB,
LE BOT, Alain, Directeur de Recherche, École Centrale de Lyon,

Rapporteur
Rapporteur
Examinatrice
Examineur

TOTARO, Nicolas, Professeur des Universités, INSA–Lyon,

Directeur de thèse

CHEVILLOTTE, Fabien, Ingénieur de Recherche, Matelys Research Lab,

Invité